

AN ABSTRACT OF THE DISSERTATION OF

Michael Lamar Dennis for the degree of Doctor of Philosophy in Civil Engineering presented on December 5, 2018.

Title: Of Planes and Plumblines: Map Projections and Differential Leveling in a GNSS-based 3D Geodetic Framework.

Abstract approved: _____

Christopher E. Parrish

Modern geospatial data are frequently represented in some type of three-dimensional (3D) coordinate system, for example geodetic latitude, longitude, and ellipsoid height (φ, λ, h) derived from Global Navigation Satellite Systems (GNSS). But for engineering and surveying work, φ, λ, h coordinates are usually converted to a topocentric system consisting of a horizontal coordinate pair—for example northing and easting (N, E)—combined with an “elevation” (often orthometric height, H). The N, E, H components are treated as mutually orthogonal, even though in physical reality the horizontal plane represented by N, E is generally not perfectly perpendicular to the H plumbline. However, it is a reasonable and practical approximation, and one that is enforced mathematically by determining horizontal separately from height. The components can then be combined into a coordinate triplet, which, by convention, is often ordered so as to represent a left-handed N, E, H system.

For GNSS-derived positions, a commonly used approach is to compute N, E , from φ, λ using a map projection, and to compute H from h using a geoid model. That approach will continue in the future, when the National Geodetic Survey (NGS) transitions to new Terrestrial Reference Frames and the associated State Plane Coordinate System of 2022 (SPCS2022), along with the North American-Pacific Geopotential Datum of 2022 (NAPGD2022). These systems will

replace the existing U.S. “horizontal” (geometric) and vertical datums. This research investigates methods that could be applied to either or both the horizontal and vertical components of the 2022 systems.

For the horizontal component, two approaches are presented for developing conformal projected coordinate systems that could be incorporated into SPCS2022. Both are concerned with reduction of linear distortion, which is the difference in distance between a pair of projected (grid) coordinates and the actual horizontal distance at the topographic surface (ground). One is design of low distortion projections (LDPs) that minimize linear distortion for specific areas of interest such that the difference between grid and ground distances is negligible, typically within ± 20 parts per million (ppm). The other is design of SPCS2022 zones for entire states and to replace existing SPCS zones. These areas are so large that they have too much distortion to serve as LDPs. Thus, population distribution is also considered in the design process, so that distortion can be minimized more effectively where the majority of people are located.

For the vertical component, a method was developed for integrating GNSS and leveling observations into a single 3D network for simultaneous least-squares adjustment. The purpose was to determine the role of spirit leveling in NAPGD2022, which will be primarily accessed using GNSS and a gravimetric geoid model. This is important, because leveling is more accurate vertically than GNSS over distances of less than a few kilometers. A key element was developing a geoid slope error model, to correctly weight the transformed leveling observations. The high redundancy of GNSS and its accuracy over long distances compensated for the low redundancy of leveling and its rapid error growth with distance. Conversely, the high relative accuracy of leveling offset the lower vertical accuracy of GNSS over short distances. The combined network yielded residuals and error estimates that were smaller than those of the separate networks.

©Copyright by Michael Lamar Dennis
December 5, 2018
All Rights Reserved

Of Planes and Plumblines:
Map Projections and Differential Leveling in a GNSS-based 3D Geodetic Framework

by
Michael Lamar Dennis

A DISSERTATION

submitted to

Oregon State University

in partial fulfillment of
the requirements for the
degree of

Doctor of Philosophy

Presented December 5, 2018
Commencement June 2019

Doctor of Philosophy dissertation of Michael Lamar Dennis presented on December 5, 2018.

APPROVED:

Major Professor, representing Civil Engineering

Head of the School of Civil and Construction Engineering

Dean of the Graduate School

I understand that my dissertation will become part of the permanent collection of Oregon State University libraries. My signature below authorizes release of my dissertation to any reader upon request.

Michael Lamar Dennis, Author

ACKNOWLEDGEMENTS

An effort of this magnitude cannot be done alone. It is my honor to acknowledge the support received from the many people and organizations that made this endeavor possible.

I begin by thanking my advisor, Chris Parrish. He provided a Graduate Research Assistantship from the time I arrived at OSU through the duration of my time on campus. Chris was unfailingly supportive in other ways as well. He was always willing to engage in discussions on a broad range of research topics, giving thoughtful perspective and guidance. Chris also has a keen eye for detail, and my research (and this dissertation) are better for it.

I would like to thank all other members of my committee—Mike Olsen, Dan Gillins, Tracy Arras, and Robert Kennedy—for allowing me the freedom to pursue a range of ideas and helping select the ones that ultimately led to this dissertation. I would be remiss not to mention that it was Mike Olsen who first kindled my interest in graduate study at OSU, when we met some years before I enrolled. His enthusiasm for the Geomatics Engineering graduate program shone through from the start, and that (along with his great talent) has undoubtably contributed to its current success. I would also like to express specific thanks to Dan Gillins. He is a committee member who has become a deeply valued colleague at the place where we both now work, the National Geodetic Survey (NGS). I believe the work done with Dan in this dissertation is but the beginning of many future collaborations.

The research performed for Chapter 4 (manuscript #3) benefited from support provided by a number of organizations and individuals. It was funded by NGS as a cooperative agreement with the Cooperative Institute for Marine Resources Studies (CIMRS), award number

NA11OAR4320091A. Leica Geosystems and David Evans & Associates provided most of the hardware and software used for the survey campaign in Oregon. In addition, the Oregon Department of Transportation (ODOT) Geometrics Unit provided one of the GNSS receivers, and ODOT surveyors Ken Bays and Randy Oberg assisted with connecting to the Oregon Real-Time GNSS Network. NGS employees Mark Armstrong and Dave Zilkoski (retired) gave helpful recommendations and insight on height modernization surveys, OPUS-Projects, and ASTA. NGS employees Brian Shaw and Tim Hanson provided the NGS leveling data used for analysis.

I would like to thank my NGS supervisor, Vicki Childers, for her support, both administrative and personal. I also extend my gratitude to my many other NGS colleagues who provided their support, advise, and good spirits. There are too many to thank individually, but that does not diminish the positive impact. It had a larger effect than they may even realize.

Lastly, but perhaps most importantly I thank my wife, Jami Dennis. Her unwavering support, patience, and love made it possible to see this effort through to the end.

CONTRIBUTION OF AUTHORS

Dr. Chris Parrish and Dr. Dan Gillins contributed as co-authors to Chapter 4 (manuscript #3) of this dissertation. Dr. Gillins performed independent adjustments of the GNSS, leveling, and combined GNSS+leveling networks using the *STAR*NET* software package, and wrote initial drafts of the introduction and conclusions sections. Dr. Parrish wrote initial drafts of the background section. Perhaps most importantly, both contributed substantially to every part of the chapter, including problem statement, description of data, and analysis and interpretation of results.

TABLE OF CONTENTS

	<u>Page</u>
1 Introduction	1
1.1 Problem Statement	2
1.2 Research Objectives	4
1.3 Outline of Dissertation	6
2 Ground Truth: Low Distortion Map Projections for Engineering, Surveying, and GIS	9
2.1 Abstract	9
2.2 Introduction and Background.....	9
2.2.1 Linear distortion.....	10
2.2.2 Conformality	11
2.2.3 Magnitude of linear distortion	12
2.3 Methods for Reducing Linear Distortion	15
2.4 Low Distortion Projection Design Example	18
2.4.1 Step 1: Determine representative ellipsoid height, h_0 (not elevation)	18
2.4.2 Step 2: Choose projection type and place axis near center of design area	19
2.4.3 Step 3: Scale projection axis to representative ground height, h_0	20
2.4.4 Step 4: Compute distortion throughout project area and refine parameters	20
2.4.5 Step 5: Keep the definition simple and clean.....	22
2.4.6 Step 6: Explicitly define linear unit and geometric reference system	22
2.5 Discussion and Conclusions.....	23
2.6 References	26
3 A New Approach for Designing State Plane Coordinate System Zones.....	29
3.1 Abstract	29
3.2 Introduction and Background.....	29
3.2.1 A Brief History of the State Plane Coordinate System.....	29
3.2.2 A New State Plane Coordinate System for 2022	30
3.3 Objectives and Definitions	32

TABLE OF CONTENTS (Continued)

	<u>Page</u>
3.3.1 Linear Distortion and the Projection Axis	33
3.3.2 Related Work	35
3.3.3 Justification	36
3.4 Zone Design Methodology.....	38
3.4.1 Select a Projection Type and Establish a Distortion Design Criterion	38
3.4.2 Determine Projection Axis Location and Scale Based on Topography.....	44
3.4.3 Modify Projection Axis Scale Based on Population Distribution	48
3.4.4 Evaluate and Refine Design to Achieve Optimal Performance for Zone.....	49
3.5 Application of Design Method to State Plane Zones	50
3.5.1 Datasets and Software Used for Analysis and Design.....	54
3.5.2 Design Example 1: Arizona Central Zone (Transverse Mercator)	56
3.5.3 Design Example 2: California Zone 5 (Lambert Conformal Conic)	65
3.5.4 Design Example 3: Hawaii Statewide Zone (Oblique Mercator)	72
3.6 Evaluation of Designs	76
3.7 Summary and Conclusions.....	84
3.8 References	87
4 Integration of GNSS and Differential Leveling Observations in a 3D Geodetic Model.....	92
4.1 Abstract	92
4.2 Introduction and Objectives	93
4.3 Study Area and Datasets	96
4.3.1 GNSS Data.....	97
4.3.2 Leveling Data.....	100
4.3.3 Gravimetric Geoid Model	101
4.3.4 Mixing Old and New Observations	103
4.4 Mathematical Model for Combined GNSS and Leveling Observations.....	105
4.4.1 GNSS Observation Geometry and Reference System	105
4.4.2 Transformation of the Gravimetric Geoid to NAD 83 and NAVD 88	106
4.4.3 Transformed Leveling Observations.....	108

TABLE OF CONTENTS (Continued)

	<u>Page</u>
4.5 Weighting of Observations.....	112
4.5.1 GNSS Observation Errors.....	112
4.5.2 Leveling Observation Errors.....	113
4.5.3 Geoid Slope Errors.....	117
4.6 Combined 3D Adjustments of GNSS and Leveling Observations	130
4.6.1 Minimally Constrained Separate and Combined Adjustments.....	131
4.6.2 Fully Constrained Separate and Combined GNSS+Leveling Adjustments.....	135
4.6.3 Final Heights from Combined GNSS and Leveling Adjustments	143
4.7 Summary and Conclusions.....	151
4.8 References	156
5 Conclusions and Future work	162
5.1 Conclusions	162
5.2 Future Work	164
6 Bibliography	167
Appendices.....	175
Appendix A. Projection Scale Factor and Convergence Angle Computation	176
Appendix B. Methods for Computing Horizontal “Ground” Distance.....	179
Appendix C. Datasets Used for SPCS Zone Design and Analysis	181
Appendix D. SPCS2022 Zone Parameters and Comparisons to Existing Systems	184
Appendix E. Adjustment Constraints and Final Adjusted Heights and Accuracies.....	187

LIST OF FIGURES

<u>Figure</u>	<u>Page</u>
Figure 2.1. Secant map projection with respect to ellipsoid and topography.....	13
Figure 2.2. Comparison of (a) SPCS, (b) “modified” SPCS, and (c) LDP.....	17
Figure 2.3. LDP design area, showing topographic ellipsoid heights of towns.....	19
Figure 2.4. Areas with ± 20 ppm linear distortion in example for initial and final LDP designs.....	24
Figure 2.5. Areas with ± 20 ppm linear distortion in design example for original and “modified” SPCS 83 OR South Zone.	25
Figure 3.1. Overview map of the State Plane Coordinate Systems of 1927 and 1983.	31
Figure 3.2. Range in linear distortion (log scale) as a function of zone width perpendicular to projection axis.....	43
Figure 3.3. Schematic representing how linear distortion can be reduced by changing projection axis location.	46
Figure 3.4. Existing SPCS 83 zones used for default SPCS2022 designs.	52
Figure 3.5. Effect of central meridian location on distortion range and standard deviation (top), and on minimum and maximum distortion and percent balance of positive distortion areas east and west of central meridian (bottom), for Arizona Central Zone.....	58
Figure 3.6. Effect of central meridian scale on percent population, cities, and area within design criterion and east-west balance of positive distortion (top), and on min, max, and mean distortion of cities weighted by population, all cities, and entire zone (bottom), for Arizona Central Zone.....	61
Figure 3.7. Arizona Central Zone linear distortion maps, SPCS2022 (top), SPCS 83 (bottom).....	64
Figure 3.8. Effect of central parallel location (a) on distortion range and standard deviation, and (b) on minimum and maximum distortion and percent balance of positive distortion areas north and south of central parallel (California Zone 5).....	67
Figure 3.9. Effect of central parallel scale (a) on percent population, cities, and area within design criterion and north-south balance positive distortion, and (b) on min, max, and mean distortion of cities weighted by population, all cities, and entire zone (California Zone 5).	68

LIST OF FIGURES (Continued)

<u>Figure</u>	<u>Page</u>
Figure 3.10. California Zone 5 SPCS2022 linear distortion maps: initial (top), final (bottom).....	70
Figure 3.11. California Zone 5 linear distortion map for existing SPCS 83 (2-parallel LCC).	71
Figure 3.12. Hawaii SPCS linear distortion maps, SPCS2022 (top) and SPCS 83 (bottom).....	75
Figure 3.13. Distortion map of UTM Zone 4N used as a statewide zone in Hawaii.	76
Figure 3.14. Percent of population, all cities and towns, and total zone area within design criterion for 28 SPCS zones.....	80
Figure 3.15. Percent of population, all cities and towns, and total zone area within design criterion for 14 SPCS2022 and UTM statewide zones.	81
Figure 3.16. Linear distortion range, weighted mean, and overall mean for selected SPCS zones.	83
Figure 4.1. a) Overview map showing GNSS vector ties to six distant CORS, and b) project area map of GNSS and leveling networks in Willamette Valley region of Oregon.	98
Figure 4.2. GNSS and leveling networks in vicinity of a) Corvallis and Albany and b) OSU.....	99
Figure 4.3. Order and class of leveling observation for network used in this study.....	102
Figure 4.4. Age of leveling observations for network used in this study.	104
Figure 4.5. NAVD 88 bias and tilt based on linear regression of xGEOID16B (NAD 83) GNSS BM residuals (meters) to create transformed model TxGEOID16B.	107
Figure 4.6. Standard deviation of unit weight of minimally constrained adjustments of leveling network corresponding to vector rejections for various normalized residual rejection criteria.	116
Figure 4.7. Observation a priori error estimates for the constant geoid slope error model.	121
Figure 4.8. Observation a priori error estimates for distance-dependent geoid slope error models.	122

LIST OF FIGURES (Continued)

<u>Figure</u>	<u>Page</u>
Figure 4.9. Combined leveling and GNSS network in main project area, showing stations constrained for adjustments (labeled).	132
Figure 4.10. Up residuals for minimally constrained adjustments of GNSS-only, leveling-only, and GNSS+leveling networks.	135
Figure 4.11. Median ellipsoid height network and local accuracies from constrained adjustments for stations in GNSS-only, leveling-only, and GNSS+leveling networks, grouped by connecting observation type.	138
Figure 4.12. Map showing leveling network ellipsoid height accuracies for leveling-only (green) and GNSS+leveling (orange) constrained adjustments.....	140
Figure 4.13. Network and local accuracies of the 34 local GNSS station in Table 6.12 (top map) and 37 (of 1022) selected leveled-only stations in Table 6.13 (bottom map).	142
Figure 4.14. Changes in adjusted ellipsoid heights from leveling-only to GNSS+leveling network for minimally (top) and fully (bottom) constrained adjustments.....	146

LIST OF TABLES

<u>Table</u>	<u>Page</u>
Table 2.1. Linear distortion of projected coordinates due to Earth curvature (k).....	14
Table 2.2. Linear distortion of projected coordinates due to ellipsoid height.	15
Table 2.3. Distortion performance for six different LCC projection alternatives.	21
Table 3.1. Characteristics of SPCS zones used for default designs.....	53
Table 3.2. Characteristics of statewide SPCS2022 zones designed as part of this study.	54
Table 3.3. Summary of linear distortion performance for 28 default and 14 statewide preliminary SPCS2022 zone designs.....	79
Table 4.1. Summary of the leveling observations in the network used for this research.	102
Table 4.2. Scalars ($s_{\Delta L}$) used for computing a priori standard deviations of leveling observations as a function of square root of distance.....	114
Table 4.3. Results of minimally constrained adjustments of the leveling network with no geoid model and with geoid model TxGEOID16B.....	123
Table 4.4. Summary of minimally constrained and fully constrained GNSS-only, leveling-only, and GNSS+leveling network adjustments.....	133
Table 4.5. Adjusted ellipsoid height accuracies for final minimally and fully constrained combined leveling and GNSS adjustments.....	137
Table 4.6. Change in ellipsoid height and horizontal coordinates from separate to combined minimally and fully constrained adjustments.....	144

LIST OF APPENDIX TABLES

<u>Table</u>	<u>Page</u>
Table D.1. Design results and performance statistics for SPCS zones in 25 states and territories	184
Table D.2. Design results and performance statistics for 14 statewide preliminary SPCS2022 zone designs and 15 nearest UTM zones within state boundaries	186
Table E.1. Station ellipsoid heights for the GNSS, leveling, and combined networks.	187
Table E.2. Final adjusted ellipsoid and orthometric heights for the 34 local GNSS stations (6 distant CORS excluded), with network and median local accuracies	188
Table E.3. Final adjusted ellipsoid and orthometric heights for 37 (of 1022) selected leveling-only stations, with network and median local accuracies (at 95% confidence).	189

LIST OF ABBREVIATIONS

3D	Three-dimensional
3DEP	3D Elevation Program
BM	Bench Mark
CNMI	Commonwealth of Northern Mariana Islands
CONUS	CONterminous United States
CORS	Continuously Operating Reference Station
DEM	Digital Elevation Model
ECEF	Earth-Centered, Earth-Fixed
EGM2008	Earth Gravitation Model of 2008
GLOPOV	General Law Of Propagation Of Variance
GNSS	Global Navigation Satellite System
GRS 80	Geodetic Reference System of 1980
HTDP	Horizontal Time Dependent Positioning (<i>software</i>)
IGS08	International GNSS Service of 2008 (<i>reference frame</i>)
ITRF2008	International Terrestrial Reference Frame of 2008
LCC	Lambert Conformal Conic (<i>map projection</i>)
LDP	Low Distortion Projection
LGH	Local Geodetic Horizon
NAD 83	North American Datum of 1983
NAPGD2022	North American-Pacific Geopotential Datum of 2022
NASA	National Aeronautics and Space Administration
NAVD 88	North American Vertical Datum of 1988
NGA	National Geospatial-Intelligence Agency
NGS	National Geodetic Survey
NGSIDB	National Geodetic Survey Integrated Data Base
NSRS	National Spatial Reference System
OM	Oblique Mercator (<i>map projection</i>)
RMSE	Root Mean Square Error
SLOPOV	Special Law Of Propagation Of Variance
SPCS 27	State Plane Coordinate System of 1927
SPCS 83	State Plane Coordinate System of 1983
SPCS2022	State Plane Coordinate System of 2022
SRTM	Shuttle Radar Topography Mission
TM	Transverse Mercator (<i>map projection</i>)
TRF	Terrestrial Reference Frame
USGS	United States Geological Survey
UTM	Universal Transverse Mercator (<i>projected coordinate system</i>)
WGS 84	World Geodetic System of 1984
WKT	Well-Known Text (<i>format</i>)

1 INTRODUCTION

Many modern geospatial activities create and consume what can nominally be considered three-dimensional (3D) coordinates. Often they are represented in some type of local topocentric system, consisting (at least conceptually) of a “horizontal” plane with a vertical “up” direction perpendicular to that plane. A common generic example is using northing (N) and easting (E) “grid” coordinates for the horizontal plane, and “elevation” for the up component.

Coordinates are derived quantities. Specific meaning of the terms “horizontal,” “vertical,” “up,” and “elevation” depend on the methods and assumptions used in their derivation. While coordinates can be determined from other existing coordinates (through transformation or conversion), initially they must be derived from observations. The rapid adoption of 3D coordinates is propelled by the widespread use of technologies that provide 3D observations, including Global Navigation Satellite Systems (GNSS), total stations, and laser scanning systems.

GNSS is of particular interest because it can be readily and accurately georeferenced, either by relative positioning with respect to other GNSS receivers in an existing geodetic framework, or directly from satellite ephemerides. GNSS observations can thus be used to derive accurate 3D geodetic coordinates that are consistent with an established geometric reference frame (datum). These 3D coordinates are commonly provided as geodetic latitude, longitude, and ellipsoid height (φ, λ, h). For most practical applications, these must be converted to make them useful. Often that is done by handling φ and λ separately from h .

A common method for converting curvilinear φ, λ into “planar” horizontal topocentric coordinates is by using a map projection. There are many types, and the ones most commonly

used for engineering and surveying are large-scale and conformal. These types of projections have the desirable property of small scale error (linear distortion) that does not vary with direction, a characteristic that also locally preserves shapes and angles.

For deriving a useful up component from GNSS, h can be converted to an orthometric height, H , (“elevation”) using a geoid model. High-resolution geoid models are commonly available as rasters, and they are interpolated to provide a geoid height based on horizontal location. H can then be obtained by simply subtracting the geoid height from h .

Thus, for GNSS, the local topocentric triplet N, E, H can be obtained from φ, λ, h using a map projection with a geoid model. And this in fact is how the problem is often approached today. An example is using GNSS to determine North American Datum of 1983 (NAD 83) geodetic coordinates, and then applying a State Plane Coordinate System of 1983 (SPCS 83) map projection algorithms to get N, E from φ, λ . For the vertical component, a (hybrid) geoid model such as GEOID12B can be used to convert a NAD 83 h to a North American Vertical Datum of 1988 (NAVD 88) H .

1.1 PROBLEM STATEMENT

Although commonly used, the approach described above is not without pitfalls, especially for high-accuracy applications. SPCS 83 grid coordinates usually exhibit fairly high linear distortion, typically on the order of -100 to -200 parts per million (ppm), or 1:10,000 to 1:5000 (and the distortion magnitude can be significantly greater). The result is that distance between grid coordinates are systematically shorter than true horizontal “ground” distances, usually by 10-20 cm/km. Such discrepancies are large enough that they cannot be ignored. They must be

dealt with in some way, such as by providing linear distortion metadata (e.g., as “combined factors”), or by scaling the coordinates to reduce the difference between grid and ground.

The GNSS-derived H is also susceptible to relative errors, although from a different source. For typical GNSS engineering surveys, h accuracies usually range from 2 to 6 cm (at 95% confidence), both as relative height differences mark-to-mark (“local” accuracies) and with respect to the geodetic frame (“network” accuracies). The error of H is greater than this, because the geoid model itself has error, typically of about the same magnitude as h error. Treating the combined error as uncorrelated, this leads to GNSS-derived H errors of about $2\sqrt{2}$ to $6\sqrt{2} \approx 3$ to 8 cm. While this may be sufficient for certain applications, it is about an order of magnitude greater error than can be routinely achieved with spirit or differential leveling over distances of less than a few km. This presents a problem when trying to use GNSS for engineering and surveying projects that require small local vertical accuracies. Although leveling can be used to improve vertical accuracies, it can also be difficult to integrate with GNSS.

A significant motivation for pursuing this research is that the U.S. National Geodetic Survey (NGS) is in the process of modernizing the National Spatial Reference System (NSRS). This consists of replacing NAD 83 and NAVD 88 with the 2022 Terrestrial Reference Frames (TRFs) and the North American-Pacific Geopotential Datum of 2022 (NAPGD2022). A new SPCS will be created to accompany the 2022 TRFs, and the primary access to NAPGD2022 orthometric heights will be via GNSS using a gravimetric geoid model. This research is aimed at developing methods that can contribute to the modernized NSRS, through design of SPCS2022 zones that will reduce linear distortion, and through integration of GNSS with differential leveling to allow the determination of H that is more accurate than with GNSS alone. The net result of the

combined processes is derivation of N , E , H coordinates that can support high-accuracy and fully georeferenced 3D positioning applications.

1.2 RESEARCH OBJECTIVES

To address the issues with relative errors horizontally (due to map projection linear distortion) and vertically (due to accuracy limitations of GNSS and geoid models), this research explores methods for reducing both, as separate processes. There are three main objectives, all of which are relevant to the modernized NSRS.

1. Reduce map projection linear distortion to a level where horizontal ground distances represented by the projected coordinates differ by a negligibly small amount (usually within ± 20 ppm). This objective is pursued through optimized design of “low distortion projections” (LDPs). Projected N , E coordinates of an LDP give conditions “at ground” within the tolerance of most terrestrial positioning methods. Thus LDP-derived distances, areas, and volumes in engineering plans, survey plats, as-built surveys, and legal descriptions are close to the actual values based on direct measurement at the surface of the Earth. At the same time, the LDP coordinates are rigorously georeferenced so that they are correctly located and orientated within the geometric geodetic frame. This last item is critical, because it makes it possible for NGS to allow the use of LDPs as part of SPCS2022. Although LDPs are effective at reducing distortion, one limitation is that they cover relatively small geographic areas, usually less than 100 km in extent.
2. Develop a method for designing conformal projected coordinate systems that cover much larger areas than LDPs but have significantly less linear distortion than traditional large-area systems, such as existing SPCS 83 and Universal Transverse Mercator (UTM). The

goal is to develop a method for designing SPCS2022 zones that will replace existing SPCS 83 zones, as well as for developing an SPCS2022 zone for each state. Because many of these zones tend to be very large, the design process places greater emphasis on reducing distortion in populated areas (point locations nominally identified as cities and towns), than on the entire zone area. The objective is to preferentially reduce distortion in populated areas, since that is where such systems will be most heavily used, especially for applications where distortion is a more important consideration (in contrast to more remote, rural areas).

3. Determine a method for integrating GNSS and leveling observations, specifically in the context of NAPGD2022, where GNSS with a gravimetric geoid will be the primary means of computing H . The intent is for the strength of one observation type to compensate for the weakness of the other. More specifically, the objective is for the high redundancy and accuracy of GNSS over long distances to make up for the low redundancy and rapid increase in error with distance of leveling. Conversely, the high relative accuracy of leveling is intended to offset the greater vertical error of GNSS over short distances. To accomplish this objective, GNSS and leveling observations were combined in a 3D geodetic network and simultaneously adjusted. Using a gravimetric geoid model, leveling observations were transformed into the same geometric frame as the GNSS observations. An essential element was determining a realistic geoid slope error model as part of correctly weighting the transformed leveling observations.

The overall objective of this research is to develop methods that yield coordinates suitable for high-accuracy 3D applications and are compatible with NSRS modernization in 2022. Important

parts of the goal are that the coordinates be rigorously georeferenced, while representing the horizontal and vertical components in a way that preserves the intrinsic accuracy of the observations. That objective is pursued by unifying the horizontal plane represented by N , E with the plumbline of H into a single ordered triplet of N , E , H , resulting in 3D coordinates that can be used directly in engineering and surveying applications.

1.3 OUTLINE OF DISSERTATION

The dissertation follows the manuscript format as specified below, which includes a summary for each manuscript chapter:

Chapter 2 (Manuscript #1), “Ground Truth: Low Distortion Map Projections for Engineering, Surveying, and GIS,” presents a method for designing conformal map projections that optimally minimize linear distortion at the topographic surface (“ground”). This is accomplished by using existing projection types and determining their parameters to create low distortion projections (LDPs). Background and definitions are provided on linear distortion and conformal map projections. A detailed example from the Bend-Redmond-Prineville area of central Oregon is given for design of an LDP, showing how topographic slope can be used to reduce distortion more than might otherwise be achieved. Comparisons are made with SPCS 83 and with the traditional method of reducing distortion by scaling existing SPCS 83 coordinates.

Chapter 3 (Manuscript #2), “A New Approach for Designing State Plane Coordinate System Zones,” proposes an approach for designing conformal projection zones that also minimize linear distortion, but over much larger areas than LDPs. The intent is that this approach be used for designing SPCS2022 zones to replace those of SPCS 83. A design methodology is proposed that includes consideration of population distribution. Three detailed design examples are given for

zones based on the three projection types that will be used for SPCS2022: Lambert Conformal Conic, Transverse Mercator, and Oblique Mercator. The results for replacing SPCS 83 zones are compared to SPCS83, and results for statewide zones are compared to UTM, for 24 U.S. states and territories.

Chapter 4 (Manuscript #3), “Integration of GNSS and Differential Leveling Observations in a 3D Geodetic Model,” develops a method for combining GNSS and leveling observations into a 3D geodetic network for simultaneous least-squares adjustments. This chapter is concerned with two main things: 1) transforming the GNSS and leveling observations into a consistent geometry and 2) correctly weighting the observations. An important part of the process is determining an error model for relative geoid heights (geoid slope), since the geoid is used to transform leveling observations into a frame consistent with GNSS. Using a GNSS and leveling network in the vicinity of Corvallis, Oregon, combined adjustments results are compared to separately adjusted minimally and fully constrained networks, and the adjusted height accuracies (both local and network) are estimated by formal error propagation.

Chapter 5 provides general conclusions, overall contributions, and future work relevant to this dissertation.

The dissertation includes supplemental information in the following appendices:

Appendix A. Projection Scale Factor and Convergence Angle Computation.

Appendix B. Methods for Computing Horizontal “Ground” Distance.

Appendix C. Datasets Used for SPCS Zone Design and Analysis

Appendix D. SPCS2022 Zone Parameters and Comparisons to Existing Coordinate Systems

Appendix E. Ellipsoid Height Constraints and Final Adjusted Ellipsoid and Orthometric Heights

Manuscript #1

GROUND TRUTH: LOW DISTORTION MAP PROJECTIONS
FOR ENGINEERING, SURVEYING, AND GIS

Michael L. Dennis

Proceedings of the Pipelines 2016 Conference, Utility Engineering and Surveying Institute of the American Society of Civil Engineers, July 17–20, 2016 Kansas City, Missouri, U.S.A.

2 GROUND TRUTH: LOW DISTORTION MAP PROJECTIONS FOR ENGINEERING, SURVEYING, AND GIS

2.1 ABSTRACT

Map projection linear distortion is manifested as a difference in distance between a pair of projected (map grid) coordinates and the true horizontal distance at the surface of the Earth. Such differences often exceed a few hundred parts per million (ppm) for published coordinate systems (such as State Plane and UTM). It can be problematic for various geospatial products and services, such as engineering plans, construction staking, as-built surveys, property boundary plats, and facilities management systems. Although this distortion cannot be eliminated, it can be optimally reduced using *low distortion projections* (LDPs): conformal map projections for minimizing linear distortion. A method for designing LDPs is shown that yields optimal results even for large areas of variable elevation, and it can provide distortion more than an order of magnitude lower than the traditional method of scaling State Plane coordinates “to ground.” Importantly, LDPs are based on common existing projection types, so they are fully compatible with engineering, surveying, and GIS data (an additional advantage over scaled State Plane). Because they are rigorously georeferenced, LDP datasets can directly represent conditions “at ground” in GIS and CAD platforms without resorting to best-fit approximate transformations.

2.2 INTRODUCTION AND BACKGROUND

Map projection distortion is an unavoidable consequence of representing a curved surface on a flat surface. It is a change in the relationship between points located on the Earth’s surface and the representation of their relationship on a plane. Distortion cannot be eliminated; the best that can be done is to minimize its effect.

The problem of distances represented by projected coordinates being different (usually shorter) than true horizontal distances at the ground surface is well known. Often it is called the “grid versus ground” problem by surveyors and engineers. A common method for reducing the effect is to multiply coordinates from an existing conformal projection by a scale factor to represent conditions “at ground.” This method has existed for decades, and an approach utilizing the State Plane Coordinate System (SPCS) was included in training provided by the National Geodetic Survey (NGS) beginning in the 1960s (Zilkoski, 2015; Dracup, 1974).

2.2.1 Linear distortion

Although differences in finite distances are often used to describe linear distortion, it is formally defined at a point using infinitesimal (differential) distances. In this paper linear distortion is defined as

$$\delta = k \left(\frac{R_G}{R_G + h} \right) - 1 \quad (2.1)$$

where k is the *grid point (scale) factor* and can be considered the part due to Earth curvature.

The quantity in parentheses is the *elevation or height (scale) factor* and, as the name suggests, is the part due to ellipsoid height. The value of k is calculated from the mapping equations as a function of position only. Algorithms for k used in this paper are mainly from Stem (1990), augmented by those from Snyder (1987). Equations for computing k are given in Appendix A for the Lambert Conformal Conic and Transverse Mercator projections.

The product of the two scale factors is often called the *combined (scale) factor*, which represents total linear distortion. Typically linear distortion is small, and so the combined factor is usually

very close to 1. To facilitate evaluation of distortion, 1 is subtracted from the combined factor to give a value that can be represented in parts per million (e.g., a combined factor of 0.99998 is –20 ppm distortion). Linear distortion can be positive or negative. Negative distortion means the projected (map grid) length is shorter than the horizontal ground length. Positive distortion means the projected (map grid) length is longer than the ground length.

Within the height scale factor part of Eq. 2.1, h is the ellipsoid height and R_G is the geometric mean (or Gaussian) radius of curvature,

$$R_G = \frac{a\sqrt{1-e^2}}{1-e^2\sin^2\varphi} \quad (2.2)$$

where, for the reference ellipsoid used, φ is the geodetic latitude, a is the semi-major axis, and e^2 is the first eccentricity squared. For this paper, values for the GRS 80 ellipsoid are used:

$a = 6,378,137$ m (exact) and $e^2 = 0.0066943800229$.

2.2.2 Conformality

Minimizing linear distortion only makes sense for *conformal* map projections. For all non-conformal projections (such as equal area projections), linear distortion (scale error) generally varies with direction, so there is no unique value at a point. In conformal projections, linear distortion at a point is unique (i.e., the same in every direction). There are many types of conformal projections, although only a few are of practical use for low distortion projections (LDPs). Inappropriate conformal projections include those that cover large portions of the Earth and ones that are not widely available in commercial software. The following four types can be used for LDPs and are available in most geospatial software:

1. Transverse Mercator, TM (*cylindrical*). A common implementation is also called the Gauss-Krüger projection.
2. Lambert Conformal Conic, LCC (*conic*). Includes both the one-parallel and two-parallel versions (they are mathematically identical to one another).
3. Oblique Mercator, OM (*cylindrical*). A common implementation is known as the Hotine OM (also called Rectified Skew Orthomorphic).
4. Stereographic (*azimuthal*). Includes polar and oblique aspects; also known as Double Stereographic (for a specific implementation). For large areas, its performance is almost always inferior to TM, LCC, or OM because it does not curve with the Earth in any direction.

The term “projection axis” is used in this paper for the line along which projection scale (i.e., distortion with respect to the ellipsoid) is minimum and constant. It is the central meridian for the TM, the central parallel for the LCC, and the skew axis for the OM (actually scale is not constant along the skew axis but changes slowly with distance from its local origin). The stereographic projection does not have a projection axis *per se* but rather a single point of minimum scale at its origin.

2.2.3 Magnitude of linear distortion

One can think of linear distortion as the unavoidable consequence of the projection *developable surface* (plane, cone, or cylinder) departing from the reference ellipsoid. Although no ellipsoidal forms of conformal projections are “perspective” (i.e., cannot be created geometrically), it can be useful to think of linear distortion increasing as the “distance” between the developable surface and the ellipsoid increases, as shown in Figure 2.1. This diagram is for a typical secant map

projection, such as SPCS and Universal Transverse Mercator (UTM). The projection surface is “below” (inside) the ellipsoid for the middle ~71% of the zone and “above” (outside) the ellipsoid for the outer ~14.5%. This distribution balances positive and negative distortion (with respect to the ellipsoid). The diagram also shows the topographic surface. Typically it is above both the ellipsoid and projection surface, which is why linear distortion with respect to the ground surface is usually of greater magnitude (more negative) than with respect to the ellipsoid.

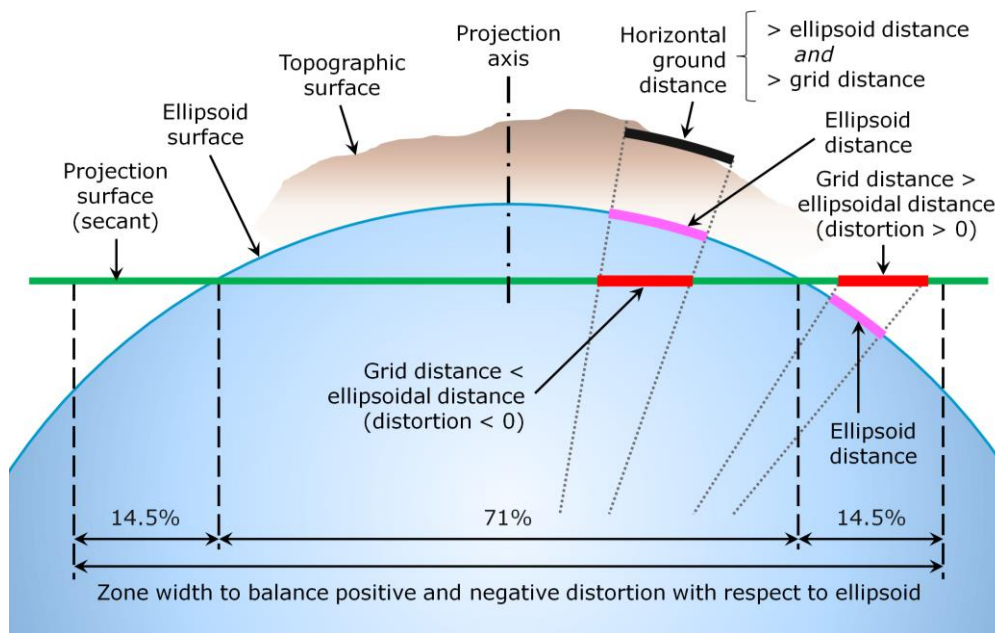


Figure 2.1. Secant map projection with respect to ellipsoid and topography.

Although total linear distortion is a combination of distortion due to curvature and to ellipsoid height, it is instructive to consider the two components separately. Distortion values for each component are given in Table 2.1 and Table 2.2. Table 2.1 gives the zone width corresponding to various maximum magnitudes of linear distortion. Distortion is expressed in ppm (mm/km); in ft/mile; and as a unitless ratio. The row in bold is for 20 ppm (0.1 ft/mile) distortion, which is

a common “low distortion” criterion. A zone can be up to 114 km (71 miles) wide and achieve ± 20 ppm distortion (with respect to the ellipsoid). The second to last row in the table gives a nominal zone width of 254 km (158 miles) for SPCS, corresponding to its well-known nominal scale error of 1:10,000 (± 100 ppm). The last row is for UTM, which can have a zone 510 km (317 miles) wide for its allowable distortion of 1:2500 (± 400 ppm).

Table 2.1. Linear distortion of projected coordinates due to Earth curvature (k).

Maximum zone width for secant projections*	Maximum linear distortion, $\delta + 1 = k$		
	Parts per million	Feet per mile	Ratio (absolute)
25 km (16 miles)	± 1	± 0.005	1 : 1,000,000
57 km (35 miles)	± 5	± 0.026	1 : 200,000
81 km (50 miles)	± 10	± 0.053	1 : 100,000
114 km (71 miles)	± 20	± 0.11	1 : 50,000
180 km (112 miles)	± 50	± 0.26	1 : 20,000
255 km (158 miles) e.g., SPCS	± 100	± 0.53	1 : 10,000
510 km (317 miles) e.g., UTM	± 400	± 2.11	1 : 2500

*Computed for TM projection at 40° latitude; for latitudes $< 70^\circ$ zone widths agree within ± 2 km for $\delta \leq 100$ ppm and within ± 10 km for $\delta = 400$ ppm for other conform projections

Table 2.2 gives linear distortion for various ranges of ellipsoid heights with respect to the projection surface. As in Table 2.1, the row with 20 ppm distortion is in bold, and it corresponds to a height range of 250 m (± 125 m). This is a modest variation in topographic height for many areas, such as most of the western US. In such situations, topographic relief is often the controlling factor for minimizing distortion. However, it will be shown that in some circumstances LDPs can be designed that achieve lower distortion than Table 2.2 indicates.

Table 2.2. Linear distortion of projected coordinates due to ellipsoid height.

Height below (–) and above (+) projection surface	Maximum linear distortion, $\delta + 1 = R_G / (R_G + h)$		
	Parts per million	Feet per mile	Ratio (absolute)
±30 m (±100 ft)	±4.7	±0.025	~1 : 213,000
±125 m (±410 ft)	±20	±0.10	~1 : 51,000
±300 m (±980 ft)	±47	±0.25	~1 : 21,000
+600 m (+2000 ft)*	–94	–0.50	~1 : 10,600
+1000 m (+3300 ft)**	–157	–0.83	~1 : 6,400
+4400 m (+14,400 ft)†	–690	–3.6	~1 : 1,500

*Approximate mean topographic height of North America

** Approximate mean topographic height in coterminous U.S. west of 100°W longitude

† Approximate maximum topographic height in coterminous U.S.

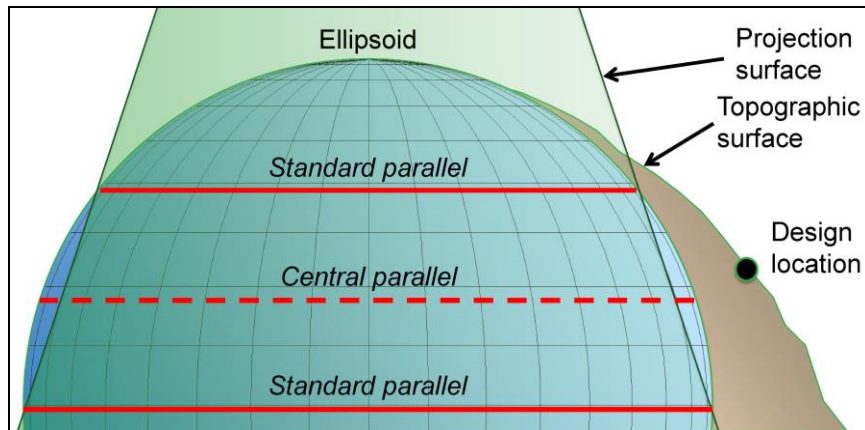
2.3 METHODS FOR REDUCING LINEAR DISTORTION

Conformal map projection linear distortion is minimized when the projection developable surface is at the topographic surface. As mentioned previously, one means for accomplishing this is to scale an existing map projection “to ground”. This approach is often called “modified” State Plane (when an SPCS projection definition is used), and it is the most commonly used method for reducing linear distortion. The main reason it is so common is historical; prior to microcomputers there was no simple way to compute projected coordinates. The only practical method was to scale existing projected coordinates. Although this approach can work well for certain applications, it has several drawbacks. The most important is that the projection type and its axis location cannot be changed. This can severely reduce the extent of the area where low distortion can be achieved. Performance can be significantly compromised when the projection axis is distant from the design area and the projection axis orientation is unfavorable.

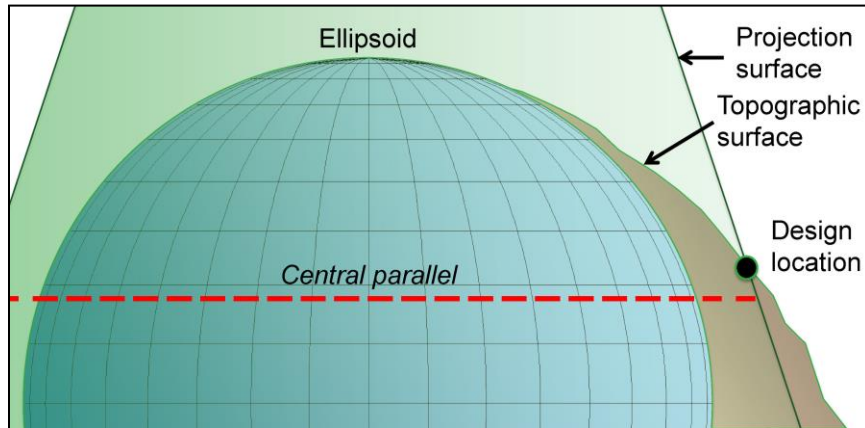
Figure 2.2 illustrates this situation for scaling an existing LCC projection, and compares it to an LCC LDP design. The top diagram (a) in the figure is a secant LCC as used for SPCS, with an implicitly defined central parallel based on the spacing between a north and south standard parallels where the cone “intersects” the ellipsoid. The middle diagram (b) is that same LCC scaled “to ground” at the indicated design location.

Scaling “to ground” is performed by dividing the coordinates by $\delta + 1$ (i.e., the combined factor). Where the developable surface intersects topography (at the design location in Figure 2.2), linear distortion is at or near zero. But elsewhere the distortion is not optimally minimized, which is particularly the case for the situation illustrated, with the topography generally sloping. The bottom diagram (c) shows an LDP design that takes advantage of the topographic slope to increase the area of low distortion coverage. To accomplish this, the projection axis (central parallel) is moved north and its scale is adjusted until the projection surface coincides with topography. The same process can be used with other conformal projections, depending on the direction of overall topographic slope. The following design example illustrates this approach using the LCC projection, directly analogous to Figure 2.2 (c).

(a) Typical SPCS situation (for LCC projection). Projection is secant to ellipsoid, with developable surface below topographic surface for most areas.



(b) SPCS scaled “to ground” at design location. Central parallel in same location as original SPCS; note developable surface inclined with respect to topographic surface.



(c) LDP design. Note central parallel moved north to align developable surface with topographic surface, thereby reducing distortion over a larger region.

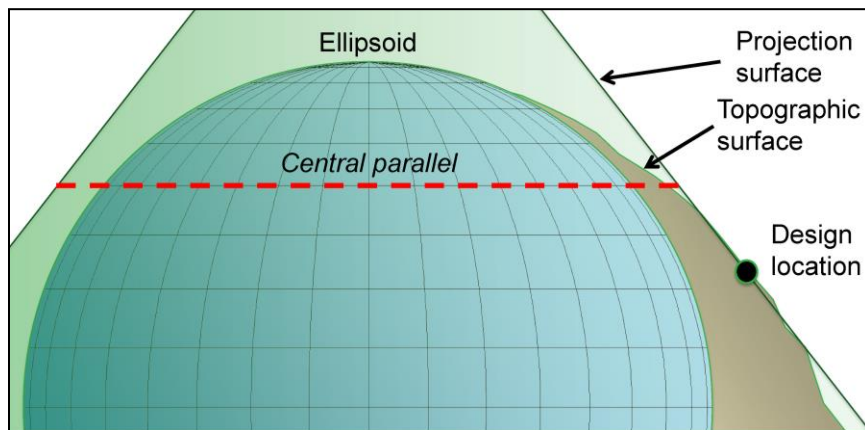


Figure 2.2. Comparison of (a) SPCS, (b) “modified” SPCS, and (c) LDP.

2.4 LOW DISTORTION PROJECTION DESIGN EXAMPLE

Figure 2.3 shows the region used to illustrate the LDP design process: the southern Deschutes River valley of central Oregon. This example follows the design of the Bend-Redmond-Prineville zone in the Oregon Coordinate Reference System (OCRS), a statewide system of LDPs (Armstrong *et al.*, 2017). The design process is illustrated in the six steps below. The first three steps are mainly to initiate the design; step 4 is where the design is optimized to minimize distortion over the largest area possible. The overall design objective is ± 20 ppm for the region and ± 10 ppm within the three largest towns (Bend, Redmond, and Prineville). Distortion in three additional towns (Sisters, Culver, and Madras) is used to represent the overall region.

2.4.1 Step 1: Determine representative ellipsoid height, h_0 (not elevation)

To start the design process, the ellipsoid heights shown in Figure 2.3 were obtained at arbitrary locations in the six towns using NAVD 88 orthometric heights (elevations) from the 1/3 arc-second USGS National Elevation Dataset (Dean *et al.*, 2002) with GEOID12B hybrid geoid heights (NGS, 2016). The mean ellipsoid height of the towns is taken as “representative” for initial design, $h_0 = 871 \text{ m (2860 ft)}$.

The design area is about 70 km (~45 miles) north-south and about 60 km (~35 miles) east-west. Based on Table 2.1, distortion can be limited to ± 10 ppm for a zone width of 80 km, so it appears the distortion criterion can be achieved, at least with respect to Earth curvature. The height range is 422 m, i.e., ± 211 m. This range corresponds to ± 33 ppm based on the ± 4.7 ppm per ± 30 m in Table 2.2; not an encouraging observation, considering the design objective of ± 20 ppm overall.

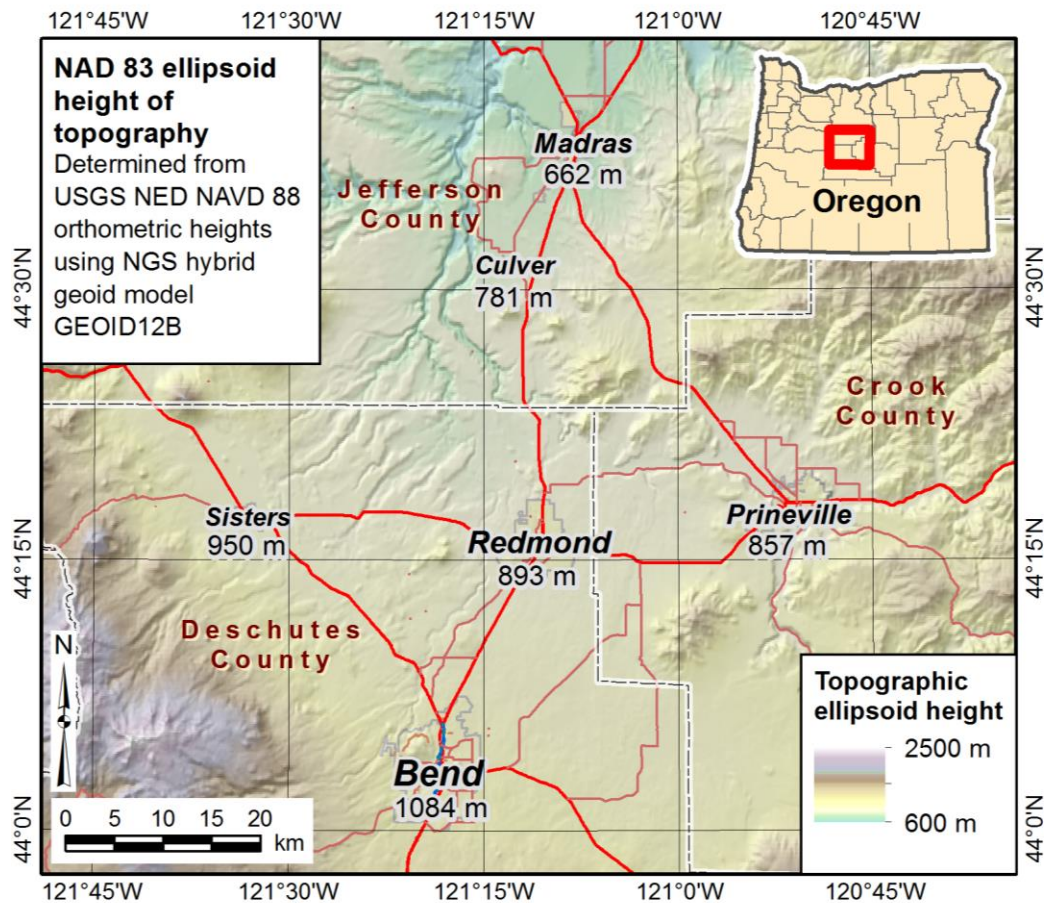


Figure 2.3. LDP design area, showing topographic ellipsoid heights of towns.

2.4.2 Step 2: Choose projection type and place axis near center of design area

Because the design area is somewhat longer north-south than east-west, one may be tempted to use a TM projection for LDP design. On the other hand, topographic height overall decreases from south to north, and such slope tends to favor the LCC projection as illustrated schematically in Figure 2.2. In the actual design for this OCRS zone, both projection types were evaluated. But the LCC provided low distortion over a substantially larger area, and in the interest of brevity only the LCC is evaluated in this example. To initiate the design process, the projection axis (LCC central parallel) is placed near the center of the region, at $\varphi_c = 44^{\circ}20'00''\text{N}$.

2.4.3 Step 3: Scale projection axis to representative ground height, h_0

The projection developable surface is brought to the topographic surface by computing an initial projection axis scale as

$$k_0 = 1 + \frac{h_0}{R_G} \quad (2.3)$$

Using the initial central parallel of $\varphi_c = 44^\circ 20' \text{N}$, Eq. 2.2 gives $R_G = 6,377,600 \text{ m}$ (20,923,900 ft). Thus the projection axis scale factor is $k_0 = 1.00013$ (rounded down so that mean distortion is within $\pm 5 \text{ ppm}$).

2.4.4 Step 4: Compute distortion throughout project area and refine parameters

Eq. 2.1 is used to compute total linear distortion at specific points for a given LDP. Distortion values for the initial LDP design are in the left column of Table 2.3. The distortion for Bend (the largest town in the region) is -28.5 ppm . Despite assigning a projection scale that gives a mean distortion of -1.3 ppm , the distortion magnitude exceeds both the $\pm 10 \text{ ppm}$ criterion for Bend and the overall target of $\pm 20 \text{ ppm}$. This could be fixed in Bend by increasing the projection scale by 30 ppm, to $k_0 = 1.00016$, which would change its distortion to $+1.5 \text{ ppm}$. However, this would also increase distortion at all other points by 30 ppm, yielding a maximum in Madras of $+69.9 \text{ ppm}$, much greater than the target maximum of 20 ppm.

Changing projection scale has essentially no effect on distortion variability; the range and standard deviation will be essentially the same regardless of the scale. For a given projection, variability can only be changed by changing the location of the projection axis (and skew axis azimuth for OM projection). The result of doing that is shown in Table 2.3 (the axis scale was also changed so that mean distortion is within $\pm 5 \text{ ppm}$ for all cases). The range and standard deviation decrease from 68.4 and $\pm 24.6 \text{ ppm}$, respectively, to minimums of 19.5 and $\pm 7.6 \text{ ppm}$

for $\varphi_c = 44^\circ 45' \text{N}$. The design with $\varphi_c = 44^\circ 40' \text{N}$ has slightly greater variability, but it has $\delta < 10$ ppm in Bend, Redmond, and Prineville, and the variability is also less in these towns.

Table 2.3. Distortion performance for six different LCC projection alternatives.

LCC axis scale	<i>Initial</i> 1.00013	1.00013	1.00012	<i>Final</i> 1.00012	1.00011	1.00010
Axis latitude	44°20' N	44°30' N	44°35' N	44°40' N	44°45' N	44°50' N
Location	Linear distortion (parts per million)					
Bend	-28.5	-10.4	-8.2	6.1	12.4	20.9
Redmond	-9.5	-2.2	-5.4	3.5	4.5	7.6
Prineville	-4.2	1.7	-2.2	6.0	6.3	8.7
Sisters	-18.7	-12.3	-16.0	-7.6	-7.0	-4.4
Culver	13.2	7.6	-2.0	0.6	-4.8	-8.1
Madras	39.9	28.9	16.6	16.4	8.3	2.3
Mean	-1.3	2.2	-2.9	4.2	3.3	4.5
Range	68.4	41.2	32.6	23.9	19.5	29.0
Std deviation	±24.6	±15.0	±10.8	±7.8	±7.6	±10.4

Evaluating distortion values at discrete points is typically not sufficient for optimizing an LDP design. A more comprehensive evaluation can be done by computing distortion on a regular grid. Distortion can then be visualized and analyzed everywhere, as shown in the maps in Figure 2.4 for both the initial and final LDP designs. All areas within ± 20 ppm are shaded green, and the zero distortion contour is shown. Substantial improvement in performance is achieved by moving φ_c north by 20 arc-minutes. After inspection of performance in other areas of the design region, a design with $\varphi_c = 44^\circ 40' \text{N}$ and $k_0 = 1.00012$ was selected for the final design (highlighted in Table 2.3).

2.4.5 Step 5: Keep the definition simple and clean

When designing LDPs (or any map projections), it is good practice to use simple and “clean” values for the defining parameters. This is consistent with how SPCS and UTM were defined. The only values that affect distortion are the projection axis scale and location (and axis orientation for the OM projection). Although the other parameters for geodetic origin and false northing and easting have no effect on distortion, they still must be specified. Below are recommendations for defining these values:

- Define the projection axis scale using no more than six decimal places (five decimal places were used in this example).
- Define the geodetic origin (e.g., central parallel, central meridian) to nearest whole (or nearest five) arc-minutes. Values with non-repeating decimal equivalents are also recommended, if it does not compromise performance.
- Use whole numbers for the grid origin (false northing and easting) in the defining linear unit such that projected coordinates are distinct from other systems in the design area (such as SPCS and UTM). Many other options for the grid origin can be used, based on preference and convenience.

2.4.6 Step 6: Explicitly define linear unit and geometric reference system

Specifying the linear unit is essential, and if feet are used it is vital that the type of foot be explicitly stated (international or U.S. survey). An LDP is not a coordinate system unless it is associated with a geometric reference system (geodetic datum). For the OCRS, the datum was specified as the North American Datum of 1983 (NAD 83).

2.5 DISCUSSION AND CONCLUSIONS

As mentioned previously, despite the popularity of “modified” SPCS, the performance is usually inferior to a carefully designed LDP. To illustrate, distortion maps are shown in Figure 2.5 for the SPCS 83 Oregon South Zone, both original and “modified” by scaling “to ground” such that it gives the same distortion in Bend as the final LDP design (+6 ppm). The difference in performance with LDPs is striking, even though all are based on the LCC projection. Even the initial LDP design covers a far larger area with low distortion than does SPCS scaled to ground.

For both original and scaled SPCS, low distortion (± 20 ppm) is only achieved in a narrow band more-or-less parallel to the projection axis (located 100 km south of Bend). Scaling SPCS has essentially no effect on the width of the band; it merely shifts it so that it is centered on Bend. This is a vivid example of how changing the projection scale has virtually no impact on variability. Indeed, the range and standard deviation for both original and scaled SPCS are 274 and ± 97 ppm, respectively (versus range of 24 ppm and standard deviation of ± 8 ppm for the final LDP).

Optimally designed LDPs have been increasingly utilized to create coordinate systems. In addition to the OCRS, a statewide system has been adopted by Iowa (Dennis *et al.*, 2014), several Indian reservations and other areas in Montana and Wyoming (Dennis, 2014), and in many more locations throughout the U.S.

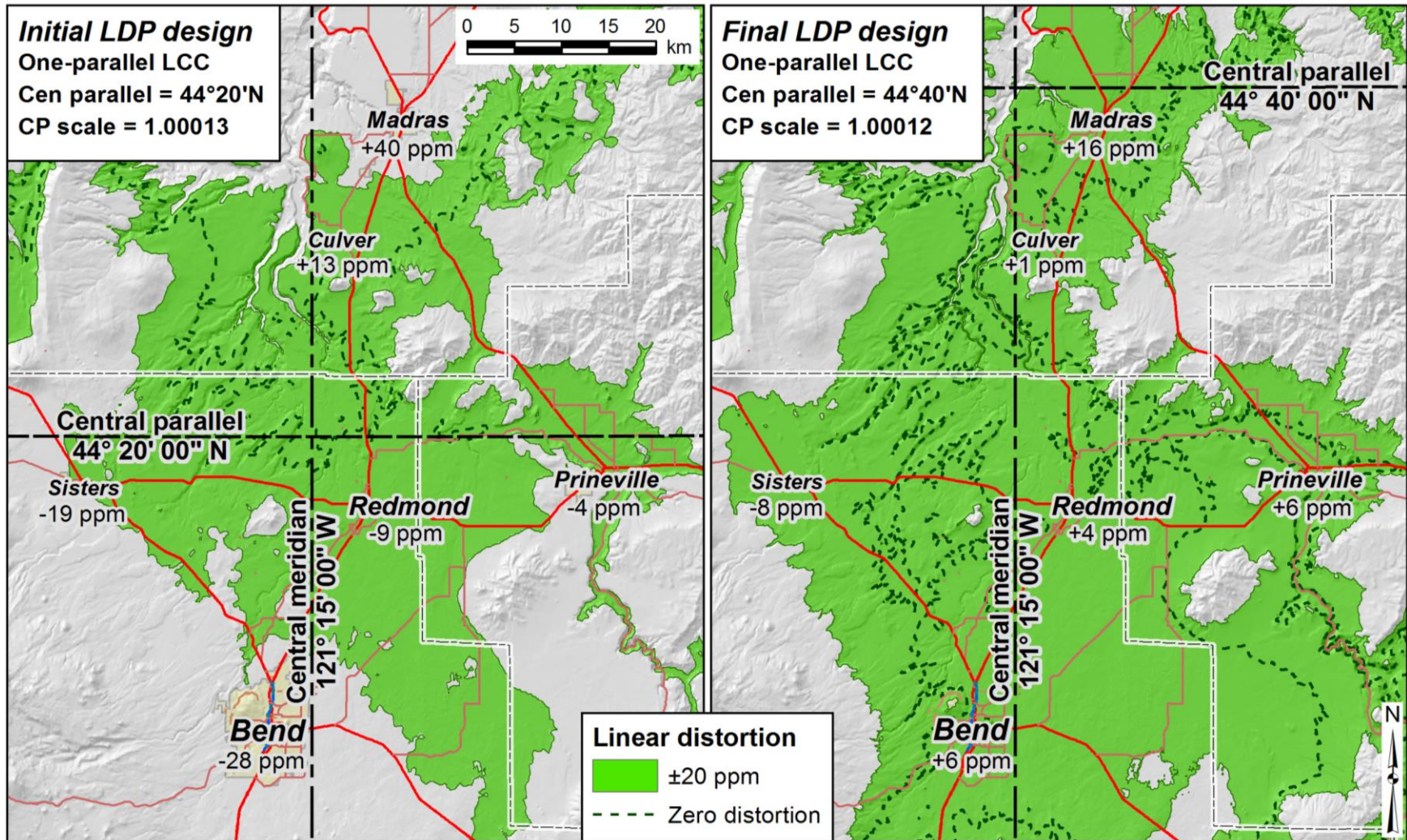


Figure 2.4. Areas with ± 20 ppm linear distortion in example for initial and final LDP designs.

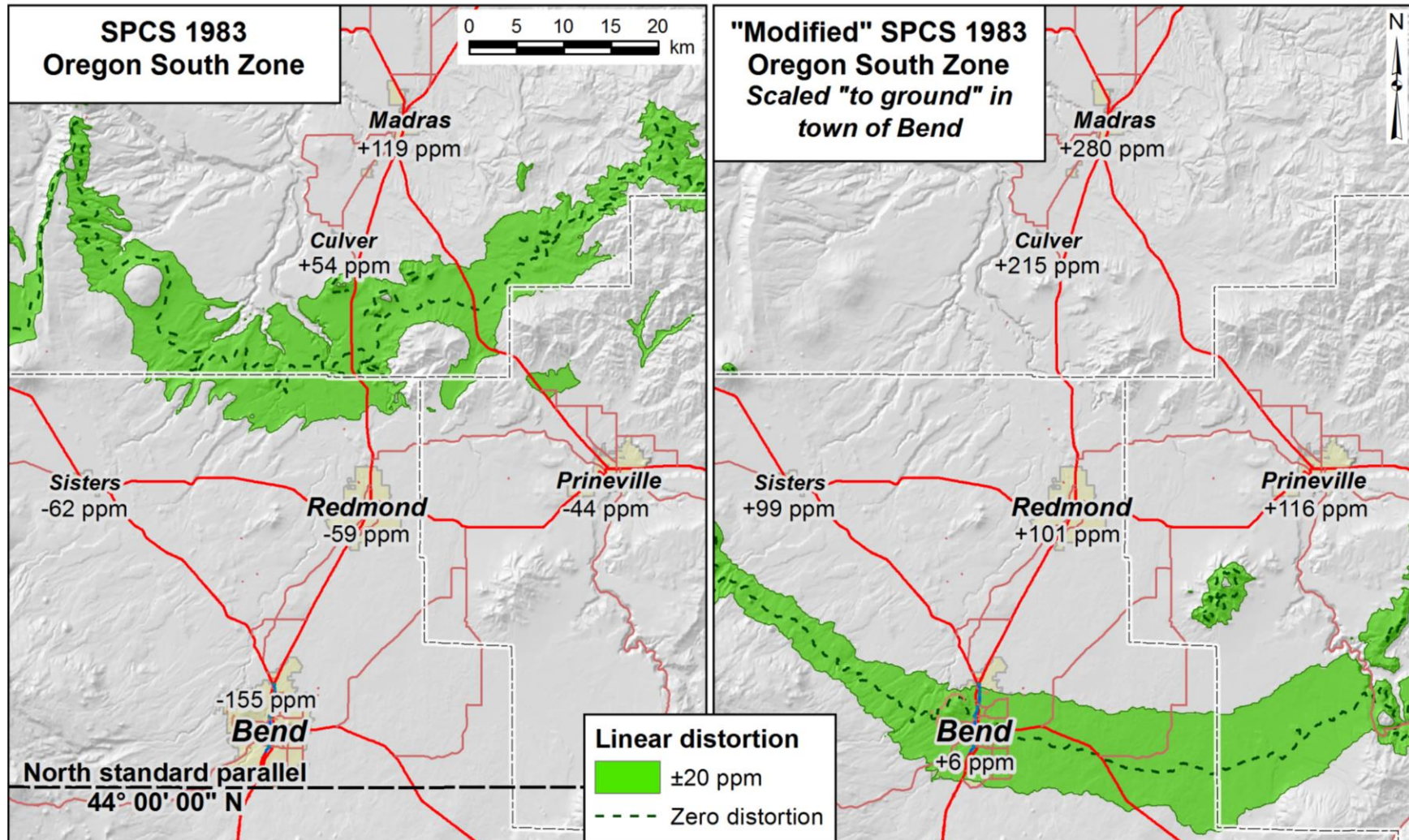


Figure 2.5. Areas with ± 20 ppm linear distortion in design example for original and “modified” SPCS 83 OR South Zone.

Although minimizing linear distortion is the purpose of LDPs, equally important is compatibility with surveying, engineering, GIS, and other geospatial software and datasets. Compatibility is achieved by using rigorously georeferenced and widely available *existing* map projection types (rather than custom specialized projections). Thus the complete set of defining LDP parameters can be used directly to create a Well-Known Text (WKT) mark-up language format (OGC, 2015) which includes Esri's projection (*.prj) WKT format. In contrast, scaled SPCS is not readily compatible because the projection parameters must be back-calculated (which is not always possible). LDP datasets optimally represent conditions "at ground" yet can coexist with other spatial data without resorting to best-fit transformations or other desperate and approximate efforts to align data of dubious pedigree.

2.6 REFERENCES

- Armstrong, M.L., Thomas, J., Bays, K., and Dennis, M.L., 2017. *Oregon Coordinate Reference System Handbook and Map Set*, version 3.01, Oregon Department of Transportation, Geometronics Unit, Salem, Oregon, <ftp://ftp.odot.state.or.us/ORGN/Documents/ocrs_handbook_user_guide.pdf> (Dec 26, 2017)
- Dennis, M.L. (ed.), 2014. *Rocky Mountain Tribal Coordinate Reference System Handbook and User Guide*, v1.0, Rocky Mountain Tribal Transportation Association, <www.neciusa.com/documents/RMTCRS_Manual.pdf> (July 20, 2018).
- Dennis, M.L., Miller, N., and Brown, G., 2014. *Iowa Regional Coordinate System Handbook and User Guide*, v2.10, Iowa Department of Transportation, <www.iowadot.gov/rtn/pdfs/IaRCS_Handbook.pdf> (July 20, 2018).
- Dracup, J.F., 1974. *Fundamentals of the State Plane Coordinate Systems*, National Geodetic Survey, <www.ngs.noaa.gov/PUBS_LIB/FundSPCSys.pdf> (July 20, 2018).
- Gesch, D., Oimoen, M., and Evans, G., 2014. "Accuracy Assessment of the U.S. Geological Survey National Elevation Dataset, and Comparison with Other Large-Area Elevation Datasets—SRTM and ASTER", *U.S. Geological Survey Open File Report 2014-1008*, Washington, D.C. <<https://pubs.usgs.gov/of/2014/1008/pdf/ofr2014-1008.pdf>> (Nov 10, 2108)
- National Geodetic Survey, 2016. *GEOID12B*, <www.ngs.noaa.gov/GEOID/GEOID12B/> (July 20, 2018).

- Open Geospatial Consortium, 2015. *Geographic information – Well-known text representation of coordinate reference systems*, OGC document: 12–063r5, v1.0
<<http://docs.opengeospatial.org/is/12-063r5/12-063r5.html>> (July 20, 2018)
- Snyder, J.P., 1987. “Map Projections — A Working Manual”, *U.S. Geological Survey Professional Paper 1395*, Washington, D.C. <pubs.er.usgs.gov/djvu/PP/PP_1395.pdf> (Nov 12, 2018)
- Stem, J.E., 1990. “State Plane Coordinate System of 1983”, *NOAA Manual NOS NGS 5*, National Geodetic Survey,
<https://geodesy.noaa.gov/library/pdfs/NOAA_Manual_NOS_NGS_0005.pdf> (July 20, 2018).
- Zilkoski, D.B., 2015. Personal communication, National Geodetic Survey Director (retired).

Manuscript #2

A NEW APPROACH FOR DESIGNING STATE PLANE
COORDINATE SYSTEM ZONES

Michael L. Dennis

Target journal: *Journal of Surveying Engineering*, American Society of Civil Engineers

3 A NEW APPROACH FOR DESIGNING STATE PLANE COORDINATE SYSTEM ZONES

3.1 ABSTRACT

A method is proposed for designing conformal projected coordinate systems for zones that cover large areas while minimizing linear distortion (scale error at the topographic surface). Although the approach is intended for the new U.S. State Plane Coordinate System of 2022 (SPCS2022), it is applicable elsewhere. To improve performance (i.e., reduce distortion) in areas of high usage, the design process considers population distribution. A distortion design criterion is established for each zone, based mainly on zone width, with clearly defined performance metrics. The design process is illustrated with three detailed examples using the Transverse Mercator, Lambert Conformal Conic, and Oblique Mercator projections. Results for 28 SPCS2022 zones were compared to State Plane Coordinate System of 1983 (SPCS 83) versions, and 14 additional SPCS2022 zones covering an entire state were compared to the nearest Universal Transverse Mercator (UTM) zone. The approach significantly improved performance for all zones. Mean zone distortion decreased by 59% and 80% compared to SPCS 83 and UTM zones, respectively, and mean distortion weighted by population decreased by 83% and 90%. For SPCS 83 zones, percent within the distortion design criterion increased from 65% to 98% for population, and from 41% to 80% for total area. For UTM zones, the corresponding changes were 14% to 99% for population and 36% to 94% for total area.

3.2 INTRODUCTION AND BACKGROUND

3.2.1 A Brief History of the State Plane Coordinate System

The State Plane Coordinate System of 1927 (SPCS 27) was established in 1934 by the U.S. Coast & Geodetic Survey, the predecessor agency of the National Geodetic Survey (NGS), to

support engineering, surveying, and mapping activities in the U.S. It enabled the use of planar mathematics to perform geodetic work—even for surveys covering large areas—rather than requiring complicated geodetic calculations, a tremendous benefit prior to personal computers. Conformal map projections (with scale error typically limited to 1:10,000 or less) were used for all zones, except one in Guam. Because of conformality, scale error does not vary with direction, which also has the desirable characteristics of locally preserving shapes and angles. The system initially consisted entirely of zones based on the Lambert Conformal Conic (LCC) and Transverse Mercator (TM) projections. The Oblique Mercator (OM) projection was added for the panhandle of Alaska ca. 1960. A total of 134 zones were developed, with 131 in the final 1968 version of SPCS 27.

In 1986, NGS officially adopted the North American Datum of 1983 (NAD 83), replacing NAD 27, along with a concurrent change to SPCS 83 from 27. SPCS 83 consisted of the same three conformal projections: LCC, TM, and OM (still for one Alaska zone). Changes consisted mostly of large shifts in grid origins to avoid confusion with SPCS 27 coordinates. Several other modifications were also made that affected performance, including changes to geodetic parameters, eliminating one zone (American Samoa), and combining multiple zones into a single zone. SPCS 83 reached its current form of 125 zones with the addition of a statewide zone for Kentucky in 2001. The entire SPCS system is shown in Figure 3.1, which summarizes changes from 27 to 83. For more details on SPCS history, see Dennis (2018).

3.2.2 A New State Plane Coordinate System for 2022

In 2022, NGS will transition from its current geometric and vertical datums to new datums (NGS, 2017a; NGS, 2017b). Of particular interest in the context of State Plane are four new

Terrestrial Reference Frames (TRFs) that will replace the current three NAD 83 frames. A new projected coordinate system, SPCS2022, will reference the 2022 TRFs.

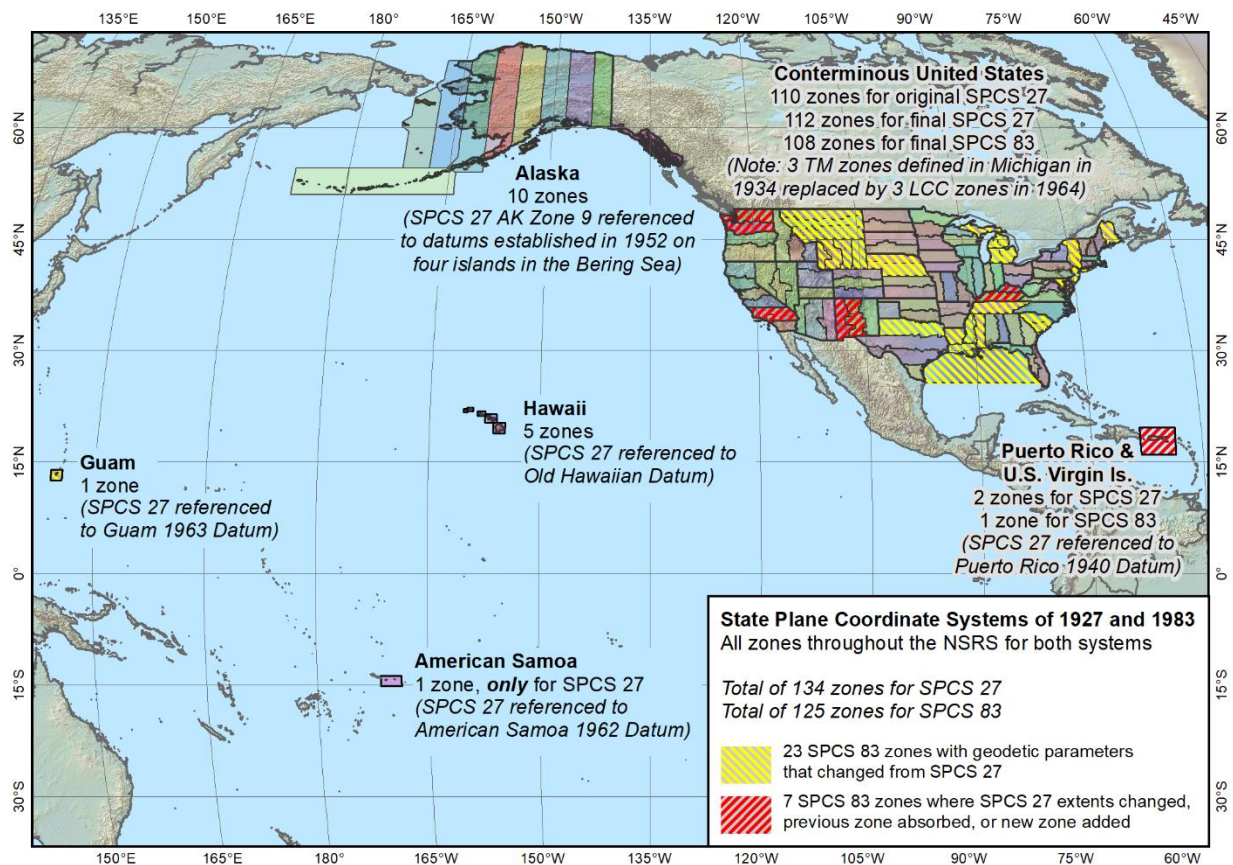


Figure 3.1. Overview map of the State Plane Coordinate Systems of 1927 and 1983.

The four main characteristics of SPCS2022 pertinent to this study are listed below, along with whether and how they differ from SPCS 83. For more details on how SPCS2022 will be defined, see the draft NGS policy and procedures (NGS, 2018a and 2018b).

1. Reference frames and ellipsoid. All SPCS2022 zones will reference one of the four 2022 TRFs and use the Geodetic Reference System of 1980 (GRS 80) ellipsoid (Moritz, 2000), as done for SPCS 83.

2. Projection types. LCC, TM, and OM (same as SPCS 83). However, specific forms of the LCC and OM that differ from existing SPCS are required, as described later in this chapter.
3. Zone design procedure. The projection axis location, orientation, and scale for each zone are defined by considering scale error at the topographic surface (linear distortion), rather than the ellipsoid surface, as done for SPCS 27 and 83 (the terms “linear distortion” and “projection axis” are defined in the next section). The projection axis location is specified to the nearest whole arc-minute, scale to six decimal places or less, and skew azimuth (for OM projections) to the nearest whole degree, positive clockwise ($\pm 90^\circ$).
4. Default and statewide zone designs. Stakeholders within each state can request or propose designs for their SPCS2022 zones. In the absence of such consensus input, NGS will design “default” SPCS2022 zones. Default zones will use the same zone extents and projection type as existing SPCS 83 zones, with a few exceptions (such as Hawaii, as described later in this chapter). For every state that has more than one zone, NGS will also design a single statewide zone (note that a state can simultaneously have both a set of default zones and a statewide zone as distinct SPCS2022 “layers”).

3.3 OBJECTIVES AND DEFINITIONS

This study proposes an approach for designing default and statewide SPCS2022 zones, using the same projections as SPCS 83. The design process differs from SPCS 83, in that linear distortion is minimized at the topographic surface (rather than scale error at the ellipsoid surface), with population distribution taken into account. Three default zone design examples are provided (one for each of the three projection types), including comparison to SPCS 83. Sufficient details

are given for applying the process to other regions, including outside the U.S. To provide a more representative sample for evaluation of the methods, design results for 28 default designs in 25 U.S. states and territories (including the three detailed design examples) are compared to their SPCS 83 counterparts. In addition, statewide SPCS2022 zone designs for 14 states are compared to performance of the nearest Universal Transverse Mercator (UTM) zone.

3.3.1 Linear Distortion and the Projection Axis

Zone design performance is evaluated based on minimizing *linear distortion* at the topographic surface. A zone is designed by selecting the appropriate projection type and specifying its *projection axis* location and scale (and orientation for the OM) to achieve optimal performance. These terms are defined below.

The term “linear distortion” is taken from Stem (1990, p. 18), and Snyder (1987) frequently uses “distortion” in a similar context for conformal projections. In both cases it is similar (and related to) “scale error” and the “combined factor.” It is the difference in horizontal distance represented by a map projection (“grid”) versus its actual value on the *topographic surface* of the Earth (“ground”). It is computed at a point as

$$\delta = k \left(\frac{R_G}{R_G + h} \right) - 1 \quad (3.1)$$

where h is the ellipsoid height in the reference frame of the projection, and k is the *grid point (scale) factor*, which is computed from the map projection equations and is a function of horizontal position only. For this study, k was computed using the algorithms of Stem (1990). For conformal projections, k is the same in all directions from a point (although it generally differs with location). R_G is the geometric mean (or Gaussian) radius of curvature,

$$R_G = \frac{a\sqrt{1-e^2}}{1-e^2\sin^2\varphi} \quad (3.2)$$

where, for the reference ellipsoid used, φ is the geodetic latitude, a is the semi-major axis, and e^2 is the first eccentricity squared. For this chapter, values for the GRS 80 ellipsoid are used: $a = 6,378,137$ m (exact) and $e^2 = 0.0066943800229$.

Linear distortion differs from scale error in that scale error is evaluated on the ellipsoid, i.e., scale error = $k - 1$. In this chapter, the term “scale error” refers specifically to the ellipsoid, and linear distortion to the topographic surface. The combined factor is similar to linear distortion in that it is evaluated at the ground, but it differs numerically. Specifically, the combined factor = $\delta + 1$, and in most cases it is very nearly equal to 1. Thus, linear distortion of $\delta = 0$ corresponds to a combined factor of exactly 1.

The main reason for using linear distortion rather than the combined factor is convenience.

Linear distortion is given here in parts per million (ppm). For a “typical” State Plane zone, the distortion design criterion is 1 part in 10,000 (1:10,000). This criterion is more conveniently expressed as a linear distortion of “ ± 100 ppm” than as combined factor values of “0.9999 to 1.0001” or “ 1 ± 0.0001 ”.

The term “projection axis” is also taken from Stem’s analogous use of the phrase “axis of the projection” (1990), and is used in Chapter 2 (and similarly Dennis, 2016). This axis is the horizontal line or curve along which projection scale error is minimum and constant. It is the central meridian for the TM, the central parallel for the LCC, and the skew axis for the OM (although scale error is not quite constant along the skew axis but changes slowly with distance from its local origin; see Snyder, 1987, p. 70).

3.3.2 Related Work

A vast body of literature exists on development of map projections, with much of the important work on the conformal projections used for SPCS done before the mid-20th century. That work will not be revisited here. For the reader interested in a deeper exploration of map projections, other compendiums exist (e.g., Snyder (1987); Snyder and Steward (1988)). Dennis (2018) gives numerous references to the original projection development work for SPCS.

The approach in this study is to use existing map projection algorithms with the focus on determining parameters that optimally minimize linear distortion for specific versions of TM, LCC, and OM projections. While it is true that different algorithms for each of these projection types can yield slightly different results, most (and perhaps all) will result in the same parameters when used for design. The reason for this approach is practicality: the intent is to make use of projection engines that are already available, and thus can be used immediately. Refinements of those algorithms can and do occur, but that is not of interest here. For this chapter, the algorithms of Stem (1990) were used, although they were modified slightly for negative west longitudes, 1-parallel LCC projections, and local (center) definitions of the OM projection.

Using existing conformal map projections to determine parameters that minimize linear distortion has been investigated to some extent by others, most notably “low distortion projections” (LDPs) in Chapter 2 of this document (i.e., Dennis, 2016). LDPs have also found recent wide usage, for example as documented in Armstrong *et al.* (2017), Badger (2016), Dennis (2017), and WI SCO (2012). However, the objective here creates a different design problem than LDPs, for two reasons. One is that the problem is, to some extent, reversed: rather than define regions where distortion can be minimized to some pre-defined criterion (such as ± 20 ppm for LDPs), the aim here is to minimize distortion for an existing zone. The other is that

the zones are usually much larger than used for LDPs (usually entire states or large, existing SPCS 83 zones within states).

Two cases exist where SPCS zones were developed to minimize linear distortion at the topographic surface rather than the ellipsoid. The first was a system designed for Michigan in 1964 (C&GS 1979; Burkholder 1980; Lusch, 2005). For this system, the three existing TM zones of SPCS 27 were replaced with three LCC zones. To reduce linear distortion, rather than scale the LCC projections, the reference ellipsoid was instead enlarged to coincide with the mean elevation of Michigan. While an approach using an enlarged ellipsoid works, it is no longer considered best practice because it complicates design and implementation, with no improvement in performance. The complications occur because it requires a different ellipsoid for every zone. That increases the number of design parameters and requires a datum transformation when used in practical applications.

The second SPCS zone designed to minimize linear distortion at ground was a statewide LCC zone for Kentucky adopted as part of SPCS 83 in 2001 (Kentucky 2001 and 2002; Bunch, 2018). Interestingly, this statewide zone coexists with the two previously existing LCC zones for Kentucky. Kentucky is the only state with a “layered” zone configuration in SPCS 83, but such layered zones will be common in SPCS2022.

3.3.3 Justification

For SPCS 27 and 83, there was no attempt to minimize linear distortion at the topographic surface, apart from the two exceptions cited above. This is likely due to a lack of elevation data and computer resources. Now, digital elevation models are readily available, and computers are certainly capable of modeling the topographic surface from such models.

There are two advantages to designing zones that reduce linear distortion at the surface: (1) engineering, surveying, and mapping activities are performed at the ground surface, not on the ellipsoid, and (2) the ground surface can be far above the ellipsoid. The conterminous U.S. (CONUS) has a mean topographic ellipsoid height of about 750 m. From the part of Eq. 3.1 in parentheses, this corresponds to distortion due to height of about -120 ppm (becomes more negative with increasing height). This negative distortion of more than -100 ppm is in addition to the -100 ppm already permitted for typical SPCS 83 designs with respect to the ellipsoid. Thus a large part of the U.S. has areas where SPCS 83 distortion exceeds -200 ppm at ground, and in some areas by a very large amount (e.g., the *mean* SPCS 83 distortion in Montana is -588 ppm). Such large distortion magnitudes are at odds with the original intent of SPCS to limit distortion to about ± 100 ppm.

Although there are advantages to designing SPCS zones with respect to the topographic surface, there are challenges as well. One is that SPCS zones are so large that in most cases the distortion range will exceed ± 100 ppm even with negligible topographic relief, which is much greater than what most would consider “low distortion.” Another is that distortion due to height in mountainous regions can vary by more than 100 ppm over horizontal distances of only a few to several km.

To deal with such issues, a philosophy and approach for design is proposed here that differs from that used for LDPs. In addition to minimizing distortion throughout the entire zone, the design process also considers population distribution, to preferentially reduce distortion in cities and towns. Although the resulting distortion might be greater than what is suitable for LDPs, it will be lower (often substantially lower) than distortion for the traditional method of ignoring topography, especially in areas where most people live and work.

3.4 ZONE DESIGN METHODOLOGY

The projected coordinate system design process proposed in this chapter is focused on linear distortion performance and consists of the following four steps:

1. Select a projection type and establish a distortion design criterion, based mainly on maximum zone width perpendicular to the projection axis, and evaluated by proportion of population, cities, and zone area that fall within the design criterion.
2. Determine the projection axis location that gives lowest range of distortion, and select its initial scale such that the mean or median distortion are near zero for the overall zone.
3. Modify projection axis scale based on population distribution, so that lower distortion occurs in areas of high population density and where cities and towns are located.
4. Evaluate and refine the design as necessary by assessing conflicting performance metrics and consideration of other factors, such as balancing distortion, mitigating extreme values, and inspecting distortion maps. Judgment is often required to select the most appropriate parameters for achieving optimal results and to create clean final definitions.

Details of each of these steps are provided in the following four sections. Note that the proposed design process requires that linear distortion be computed “everywhere” in a zone, and that population is known as a function of location. Such data can be represented on a regular grid or at discrete locations representing populated places. There are a variety of ways to acquire and assemble such datasets, and specifics are not given in the following four sections. The datasets used here are instead described with the design examples in this chapter and in Appendix C.

3.4.1 Select a Projection Type and Establish a Distortion Design Criterion

The proposed design approach is based on a known zone geometry (e.g., an existing SPCS 83 zone or an entire state). For default SPCS2022 zone designs, the projection type will usually be what was used for SPCS 83. In other cases, such as for new regions or statewide zones, the

projection type must be selected. Below are the required defining parameters for the three *specific* conformal projection types considered in this chapter.

- **Transverse Mercator (TM).** 2 parameters: central meridian longitude (λ_C) and scale (k_0). Refers specifically to the Gauss-Kruger form of the TM. The origin latitude has no effect on distortion and can be set to any value for the purpose of design (a value for final design can be selected later).
- **Lambert Conformal Conic (LCC).** 2 parameters: central parallel latitude (φ_C) and scale (k_0). A 1-parallel version of the LCC is required (any 2-parallel LCC can be converted into an equivalent 1-parallel; see Appendix A). The origin latitude has no effect on distortion and can be set equal to φ_C (which is required for SPCS2022). The origin longitude (central meridian) also has no effect on linear distortion, although it does effect convergence angles. A central meridian near the center of the zone will keep convergence angles small (if that is of concern during design), and a value for final design can be selected later.
- **Oblique Mercator (OM).** 4 parameters: local (center) latitude and longitude (φ_0 and λ_0), scale (k_0), and skew axis azimuth (α_0). Note that these parameters refer specifically to the local (center) version of the Hotine OM with a defined azimuth (also called “rectified skew orthomorphic”). See Snyder, 1987, p. 74 “Alternate B” for a description of this form of the Hotine OM.

For all projection types, the grid origins (false northing and easting) have no effect on distortion and any value can be used for design, with final values selected later.

The Oblique Stereographic projection is another possible candidate but is not considered here. For large areas, and even for those of modest extent (~50 km), this projection will almost always yield results inferior to the three other types, because its developable surface is a plane that does not curve with the Earth in any direction.

For “large” zones (short dimension greater than about 100 km), the projection type is usually dictated by the orientation of the long axis of the zone. The TM should be used for zones long in the north-south direction, and the LCC for zones long in the east-west direction. For zones elongate in an oblique direction, the OM should be used, although it is not always clear how “oblique” a zone must be to justify this choice. Generally, an OM should not be used if the resulting skew axis azimuth is within $\pm 5^\circ$ of cardinal directions. However, the converse is not necessarily true; an OM may not be the best choice even if its skew axis falls outside the $\pm 5^\circ$ bounds, especially for irregularly-shaped zones.

Likewise, as zones become smaller, the effect of topographic relief becomes more pronounced, and situations can occur where the best-performing projection type is not the one corresponding to the long dimension or orientation of a design area. When in doubt, the best choice for a projection can be determined by evaluating more than one type in the design process. Such a situation is illustrated in the LDP design example in Chapter 2, where an LCC yielded better distortion performance even though the design area was longer north-south than east-west.

For large areas, the appropriate projection type will be obvious in most cases or already determined (e.g., for an existing SPCS 83 zone). Once the projection type is known, a linear distortion design criterion, δ_0 , is needed. This criterion is based on the minimum amount of distortion that can be achieved for a zone of given width w , for the ideal case of no variation in

ellipsoid height. It is desirable to have a simple method for estimating a δ_0 value that is suitable for any of the three projection types used for design, anywhere on Earth. To that end, a simple equation for δ_0 was derived from an equation in Stem, 1990 (p. 37), which is recast as Eq. A.5 in Appendix A. This equation is used to compute the TM grid point scale factor, k , using the projected distance from the central meridian. For a central meridian passing through the zone midpoint, and with the point of interest at the edge of the zone, the projected distance is half the zone width, $w/2$, and Eq. A.5 becomes

$$k = k_0 + \frac{1}{2} \left(\frac{w/2}{k_0 R_G} \right)^2 \quad (3.3)$$

where R_G is the geometric mean radius of curvature (see Eq. 3.2). Scale error on the central meridian is $k_0 - 1$, which is the maximum negative value for the zone. To balance scale error for the zone, the maximum positive value is $1 - k_0$ at the zone edges (perpendicular from the central meridian). The scale at the zone edges is 1 plus the positive scale error, so $k = 1 + (1 - k_0) = 2 - k_0$, and Eq. 3.3 can be written as

$$2(k_0 - 1) = \frac{1}{8} \left(\frac{w}{k_0 R_G} \right)^2 \quad (3.4)$$

Recognizing that the distortion design criterion is the maximum magnitude of scale error, then $\delta_0 = k_0 - 1$, and Eq. 3.4 becomes

$$\delta_0 = \left(\frac{w}{4k_0 R_G} \right)^2 \quad (3.5)$$

Since the equation is intended for any location, R_C can be replaced with a single value R for the entire Earth, for example an arithmetic mean radius of $R = 6371$ km, per Moritz (2000). Using this R value rather than R_C introduces a maximum error in δ_0 of 0.9% at the poles (and only 0.1% at 40° latitude).

However, δ_0 is needed before k_0 is known. The maximum topographic height on Earth is about 8 km, corresponding to $k_0 = 1 + 8 / 6371 = 1.00126$. The reciprocal of this, $k_0 = 0.99874$, corresponds to a zone width of about 905 km, far larger than the nominal UTM zone width of 510 km. A range in k_0 of 1 ± 0.00126 thus covers essentially all possible design scenarios. Based on this range, setting $k_0 = 1$ results in a maximum error in δ_0 of $\pm 0.25\%$. With these assumptions for R and k_0 , Eq. 3.5 can be simplified to compute the distortion design criterion as

$$\delta_0 = \pm \left(\frac{w}{4R} \right)^2 \quad (3.6)$$

where δ_0 is multiplied by 1 million to represent the distortion range in ppm (\pm about zero), and w and R are in consistent units. For $R = 6371$ km, Eq. 3.6 is $\delta_0 = \pm 0.00154w^2$ in ppm.

Although derived for the TM projection, the approximations in Eq. 3.6 make it suitable for the LCC and OM projections as well (where w is the zone width perpendicular to the projection axis in all cases). The *maximum* error of Eq. 3.6 for these projections is a nearly constant 0.7% for zone widths up to at least 1200 km for essentially the entire Earth (between latitudes 70°N and S). Eq. 3.6 was derived for projected distances, but it will also provide correct results if geodesic distances are used. A plot of the equation is shown in Figure 3.2 (with linear distortion on a log scale), for zone widths of up to 800 km (for comparison, the state of Montana is 524 km wide north-south).

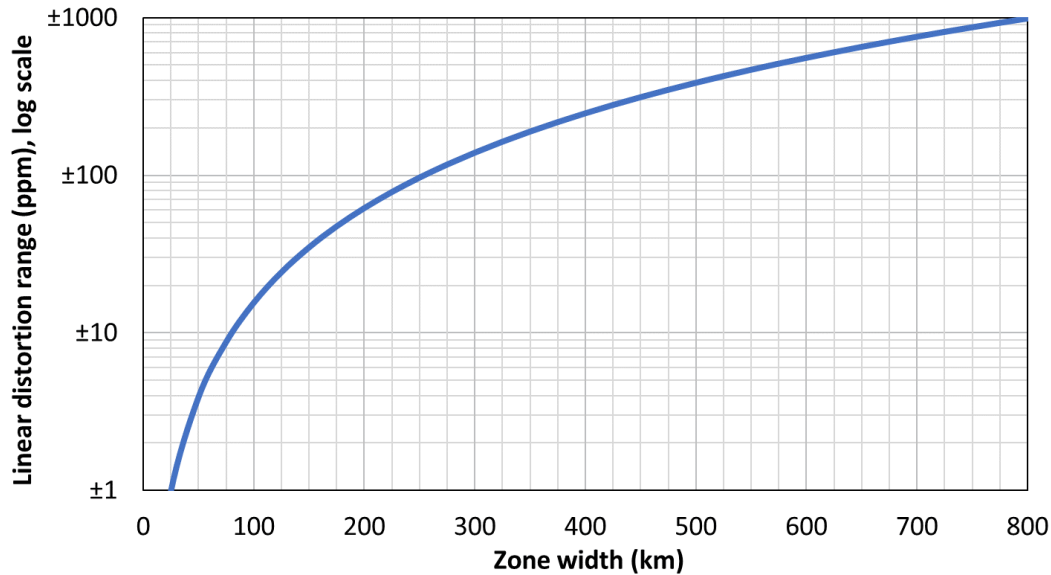


Figure 3.2. Range in linear distortion (log scale) as a function of zone width perpendicular to projection axis (based on Eqs. 3.6 and 3.7). Plot is for constant ellipsoid heights throughout the zone.

For situations where the desired distortion performance range (\pm) is known rather than zone width, Eq. 3.6 can be rearranged to give the zone width:

$$w = 4R \sqrt{\delta_0} \quad (3.7)$$

For Eq. 3.7, the maximum error is a nearly constant 0.3% for linear distortion up to at least ± 2000 ppm, with the same nearly entire Earth coverage as Eq. 3.6.

A distortion range based on Eq. 3.6 (or a width based on Eq. 3.7) gives the performance for the case where ellipsoid height is constant over the entire zone. For example, if $w = 250$ km for a zone, then Eq. 3.6 gives $\delta = \pm 96$ ppm. This means that 100% of the zone will have its distortion within ± 96 ppm—but only if the ellipsoid height is the same everywhere in the zone. In other words, Eqs. 3.6 and 3.7 provide the best that can be expected under the ideal condition of perfect ellipsoid height “flatness.” While this is never true in reality, it provides a useful basis for

establishing a design criterion. The procedure used here is to select a “clean” criterion close to the value computed from Eq. 3.6.

For this study, the following distortion design criteria were used: ± 10 , ± 20 , ± 30 , ± 40 , ± 50 , ± 75 , ± 100 , ± 200 , and ± 400 ppm for default SPCS2022 zones. By far the most commonly used criterion was ± 100 ppm (for 12 of the 28 zones), which is expected since it corresponds to the nominal scale error design criterion of SPCS 27 and 83. Design criteria of ± 100 , ± 200 , ± 300 , ± 400 , ± 500 , ± 1000 , and ± 5000 ppm were used for the statewide SPCS2022 zones, with ± 200 and ± 400 ppm the most commonly used (8 of the 14 zones). Distortion of ± 400 ppm corresponds to the scale error limit of UTM zones. The very large criteria of ± 1000 and ± 5000 ppm were used for the special cases of Texas and Alaska, respectively.

The guiding idea is to use a design criterion that provides a realistic assessment of projection performance where the projection is actually used—at the ground surface. In addition, the design criterion as used here is selected based on zone width to satisfy the following three conditions that at least: (1) 90% of the zone population, (2) 75% of all cities and towns in the zone (irrespective of population), and (3) 50% of the entire zone area all fall within the distortion design criterion. Although admittedly somewhat arbitrary, these thresholds for design performance are reasonable and practical. More importantly, they are based on actual preliminary designs of a large number of SPCS2022 zones distributed throughout the U.S. Many of those designs serve as the example data for this study.

3.4.2 Determine Projection Axis Location and Scale Based on Topography

The projection axis location is determined mainly by minimizing the *range* of linear distortion over the entire zone. Once its location is selected, its scale is assigned such that the mean or

median distortion of the entire zone is near zero. To start the process, initial values must first be iterated to both the location and scale.

For TM and LCC projections, the projection axis is initially placed such that it passes through the mid-longitude or mid-latitude of the zone, respectively. The midpoint is used rather than the centroid so that the positive scale error is balanced (equal) in the parts of the zone most distant from the projection axis.

The process for placing the OM projection axis is similar, but somewhat more involved. It first requires that the minimum bounding geometry by rectangle width be determined for the zone (an example of how this can be done is provided in the design example later in this chapter). The initial projection axis passes through the centroid of the rectangle and is parallel to its long axis.

The projection axis scale can initially be set to $k_0 = 1$ or any arbitrary value. This will provide a set of distortion values for the zone which can then be used to compute an axis scale with a mean or median of zero. Either measure of center will work; one option is to compute both the mean and median and use their average (which was the approach used for this study). This scale value is not critically important, since it will likely be modified when population is considered. In addition, the process for determining projection axis location is very insensitive to k_0 .

The location of the projection axis is then modified to minimize the variability of distortion in the zone, specifically the distortion range (the minimum standard deviation typically does not occur at the same projection axis location). This location can be determined quickly by iteration for TM and LCC zones, as the range minimum is well-defined and unique (as will be shown in the examples). For zones of constant topographic height, the range minimum will always occur at the zone midpoint. Only systematic variation in topographic height will cause it to occur

elsewhere. The concept is illustrated schematically in Figure 3.3, which shows how the variability in distortion over an area (due to systematic change in topographic height) can be decreased by moving the projection axis. Note that such behavior can make existing SPCS 83 zones less than ideal candidates for reducing distortions. In some situations it may improve distortion performance by redefining zone boundaries.

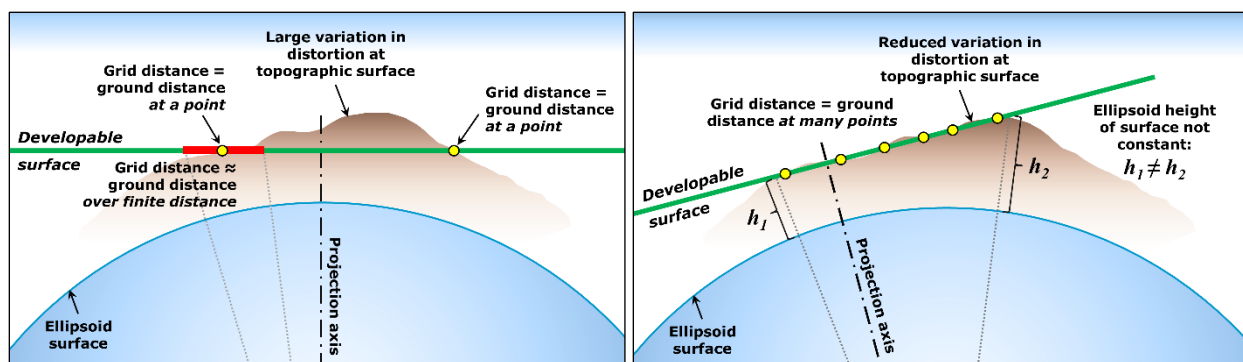


Figure 3.3. Schematic representing how linear distortion can be reduced by changing projection axis location.

Although the range of linear distortion is minimized in the right diagram of Figure 3.3, the ellipsoid heights are not constant (which is true for the left diagram as well). This point is raised because of a common misconception that minimizing linear distortion requires a singular ellipsoid height for design. From the diagrams it is clear that this is not true, because of Earth curvature with respect to the “flat” developable surface. Yet the idea of a single design ellipsoid height persists, most likely because it is approximately true for small areas (less than about 25 km, which corresponds to a distortion range of ± 1 ppm due to Earth curvature alone). But this is manifestly untrue for larger areas. As Eq. 3.6 shows, the contribution of Earth curvature to distortion (independent of ellipsoid height) increases with the square of the zone width.

While the diagrams in Figure 3.3 are useful conceptually, it is important to understand that they do not represent the literal situation regarding the relationship between the ellipsoid and the projection developable surface. That is, conformal projections based on the ellipsoid cannot be constructed geometrically, with lines of perspective that “project” coordinates from the ellipsoid surface to the developable surface, as Figure 3.3 implies (see Snyder, 1987, pp. 5-6 and p. 154-160). Nonetheless such schematic diagrams are useful conceptual tools.

The procedure for OM projections is more complex, because the distortion range is a function of three variables (origin latitude and longitude and skew axis azimuth), rather than only one for TM and LCC projections. Nonetheless the process is similar. The initial estimate of location and orientation based on the minimum bounding rectangle by width is typically quite good, especially for large zones (where Earth curvature strongly dominates distortion). The procedure is to first iterate skew azimuth, and select the one that gives the lowest distortion range. Then iterate the origin latitude, and then the origin longitude (or vice versa), and repeat the process until the minimum distortion range is found.

Using a computer, iteration for design can be done in an automated manner, but it can also be done manually (and in fact that is how it was done for this study). Manual iterative solutions are simplified by limitations in what can be used as parameters for final design. It is good practice to avoid defining projection axis location to a resolution finer than 1 arc-minute, scale to more than 6 decimal places, and skew axis azimuth to less than 1° . In addition, these limitations are specified in SPCS2022 design procedures (NGS, 2018b). For large zones (typical of default and statewide SPCS2022), the scale can usually be rounded to the nearest 5 decimal places. Note that a change of one unit in the 6th decimal place of the scale is only 1 ppm, which corresponds to

the distortion caused by a change in height of about 6 m. The height variation in all SPCS2022 default and statewide zones exceeds 6 m by at least an order of magnitude.

3.4.3 Modify Projection Axis Scale Based on Population Distribution

With the projection axis location set, the next step is refine its scale by considering population, guided by the assumption that more usage of the coordinate system occurs where people live and work, and that the need for low distortion is greater in urban than rural areas. This can be done in part by weighting the mean distortion of a zone by population. To avoid overly biasing the design to large cities at the expense of smaller ones, the distortion at all towns is also considered, irrespective of population. Distortion magnitude must also be considered everywhere (determined in the previous step), because not all surveying and mapping work or geospatial analysis occurs in or near cities and towns.

In this study, the weighted mean distortion was computed using discrete points representing populated places (nominally individual cities and towns), where each point had an ellipsoid height and a population (see Section 3.5.1 and Appendix C for a description of the datasets used for this study). Large metropolitan areas typically consist of several or many points representing individual cities (e.g., 42 cities, towns, and populated places are within the Phoenix metro area).

Using the city or town point position and ellipsoid height, its linear distortion was computed, with its weight being the product of its distortion and population. For a given zone, the weighted mean was the sum of weighted distortion values for all populated cities and town points in the zone, divided by the sum of their populations. A potentially more realistic alternative to discrete points would be to use a rasterized population dataset, where each raster cell has a population, with the weighted mean computed in the same manner.

The projection axis scale that yields zero weighted mean distortion by population will usually not be the same as the scale corresponding to the mean distortion of zero for all cities and towns based on location only (i.e., not considering population). Likewise, the scale will rarely be the same as the scale associated with a mean of zero for the overall zone. It is because of these conflicts that each is given the previously mentioned thresholds: at least 90% of population, 75% of all cities and towns, and 50% of the entire zone area should fall within the distortion design criterion.

3.4.4 Evaluate and Refine Design to Achieve Optimal Performance for Zone

The design process described above is essentially a rules-based algorithm. That is, a zone can be designed by following a recipe without exercising judgment or discretion. But the reality is not quite so clean. In practice, the various design elements often conflict with one another, which can make it difficult to determine which should prevail. While this can be handled with rules, doing so will not always lead to satisfactory results.

In addition to the considering the performance metrics given above, there are other characteristics that warrant consideration in the design process:

- Balancing the areas of positive distortion along zone edges on either side of the projection axis. This can be done by either area or maximum magnitude, or both.
- Minimizing the range in distortion of cities and towns, based only on location.
- Mitigating extreme values in important areas.
- Balancing positive and negative distortion for cities and/or the entire zone. However, in mountainous regions an appropriate design will almost always result in a maximum negative distortion magnitude for the entire zone that is greater than the maximum positive distortion.

Although the above items are secondary in evaluating performance, they can help make design decisions when it is not clear which primary metric should prevail.

An important part of the evaluating a zone design is creation and inspection of a distortion map. There are situations where viewing a map can yield insights that are not apparent through analysis of statistics and plots.

The last step is selecting the final design parameters, including the ones that do not contribute to linear distortion. The parameters affecting distortion were determined in the design process, but in many cases it is prudent to use the simplest and “cleanest” values possible without compromising performance. This includes using the least number of decimal places for scale (5 will usually be sufficient for areas with $w > 100$ km). A projection axis location to the nearest quarter degree is also desirable, or at least evenly divisible by 3, if possible, to obtain exact decimal degree representations. Such efforts were made for the 41 zones designed for this study (the parameters are listed in Appendix D). However, selection of clean final parameters is secondary and should have minimal effect on the optimized performance.

3.5 APPLICATION OF DESIGN METHOD TO STATE PLANE ZONES

Preliminary designs were completed for 28 default SPCS2022 zones in 25 states and territories distributed through the U.S. These default zones correspond to 32 existing SPCS 83 zones, because the five existing zones in Hawaii were replaced with a single SPCS2022 zone. The zones are shown in the maps of Figure 3.4, and their characteristics are listed by state in Table 3.1. *It is important to emphasize that the designs in the figure and table are preliminary and have not been formally adopted for SPCS2022.* In addition, the preliminary designs here are incomplete; they only include the parameters affecting distortion. Note that multiple zones have

been designed for two states, Alaska (three of ten zones) and Florida (all three zones). The SPCS 83 zone for Guam was replaced with an SPCS2022 zone that covers both Guam and the Commonwealth of Northern Mariana Islands, CNMI (which does not have an SPCS 83 zone). An SPCS2022 zone was also designed for American Samoa, which, interestingly, had an SPCS 27 zone, but not an SPCS 83 zone.

In addition to the default zones, statewide SPCS2022 zones were also preliminarily designed for the 14 states that have more than one SPCS 83 zone (including Hawaii, which has a proposed default statewide design). The characteristics of these statewide SPCS2022 zones are given in Table 3.2.

Both Table 3.1 and Table 3.2 give topographic ellipsoid height and population statistics for their coverage areas. The default and statewide zones show large variation in height, with a minimum range of 106 m for the entire state of Florida, and a maximum of 6027 m for Alaska (note that a change in topographic height of 100 m corresponds to a change in linear distortion of 15.7 ppm). The variability in mean topographic height is not as great as the range, but it is still substantial, from a low of -114 m for California to a high of 2087 m for Colorado South Zone.

As examples, details of the SPCS2022 design process are provided for three zones: Arizona Central (TM), California 5 (LCC), and Hawaii (five TMs replaced by a single OM). Hawaii served as both a default and statewide design example. Because of that, it is compared to its five SPCS 83 zones and nearest UTM zone.

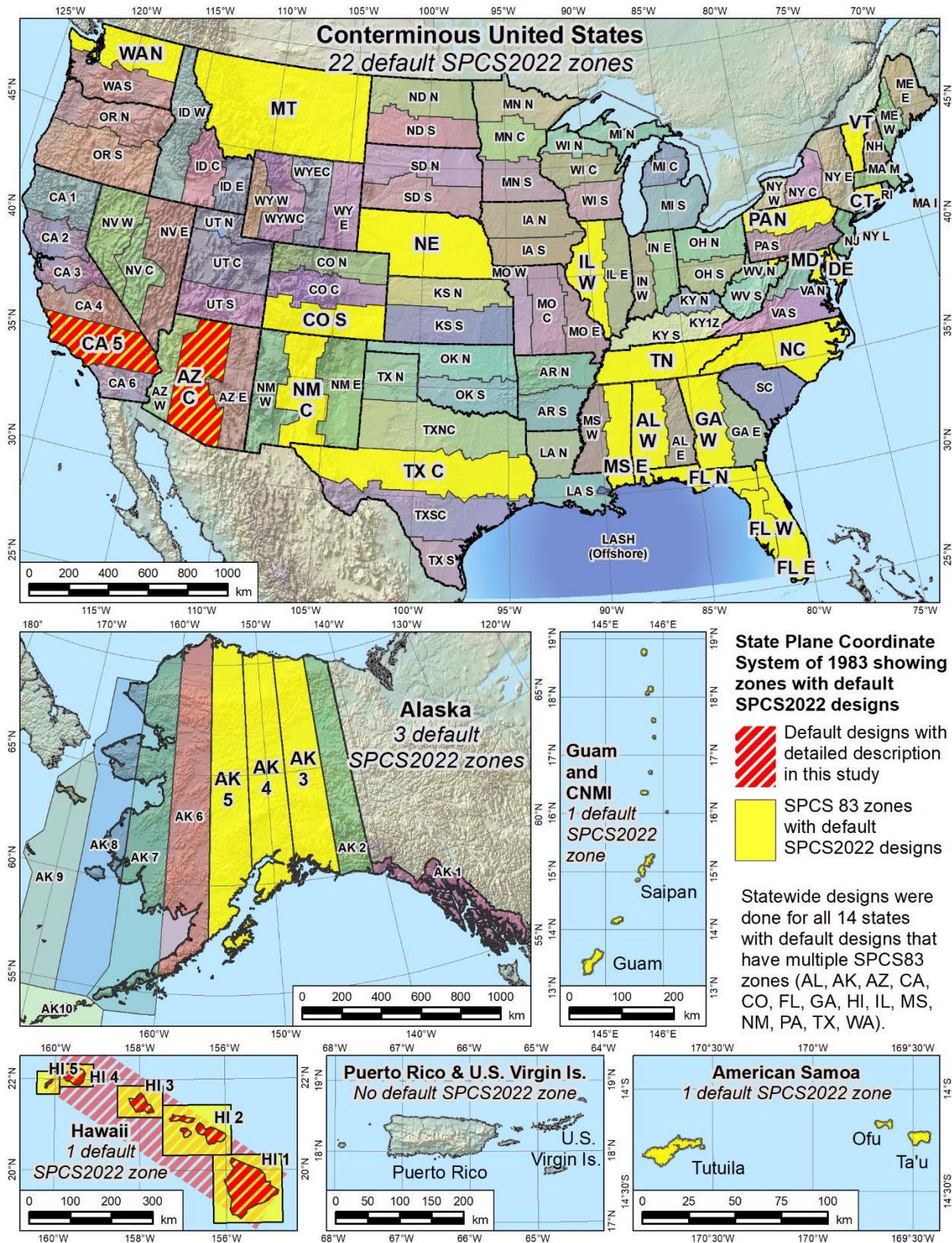


Figure 3.4. Existing SPCS 83 zones used for default SPCS2022 designs. Statewide SPCS2022 designs were done for all states with default designs that have multiple SPCS83 zones.

Table 3.1. Characteristics of SPCS zones used for default designs. Topographic heights are NAD 83 ellipsoid heights. Entries in bold (Arizona, California, and Hawaii) were used as examples for detailed discussion in this study.

State or territory	Zone name	Zone abbrev	Topographic height (m)				City and town populations			
			Min	Max	Range	Mean	Min	Max	Mean	Median
Alabama	West	AL W	-29	402	430	85	22	212,237	5,474	1,049
Alaska*	3-5	AK 3-5	-3	6020	6023	590	4	291,826	4,313	218
American Samoa	Single	AS	19	977	958	220	—	—	—	—
Arizona	Central	AZ C	98	3759	3661	1179	1	1,445,632	29,093	1,899
California	5	CA 5	-39	3431	3470	703	57	3,792,621	46,127	13,147
Colorado	South	CO S	997	4298	3301	2087	12	106,595	2,552	434
Connecticut	Single	CT	-31	551	582	113	43	144,229	16,326	3,746
Delaware	Single	DE	-37	100	137	-21	74	70,851	5,239	1,347
Florida*	All 3	FL (all)	-29	77	106	-8	3	821,784	17,580	4,513
Georgia	West	GA W	-6	1384	1390	184	16	420,003	8,388	1,588
Guam & CNMI**	Single	GU-CQ	-11	962	973	124	—	—	—	—
Hawaii*	All 5	HI (all)	2	4212	4210	919	29	47,698	7,505	3,034
Illinois	West	IL W	60	322	262	159	13	152,871	3,192	701
Maryland	Single	MD	-36	947	983	98	13	620,961	9,327	2,103
Mississippi	East	MS E	-32	185	216	71	90	67,793	3,755	1,146
Montana	Single	MT	552	3735	3183	1241	10	104,170	2,021	324
Nebraska	Single	NE	230	1619	1389	774	1	408,958	2,459	287
New Mexico	Central	NM C	1077	3923	2846	1881	25	545,852	5,620	701
North Carolina	Single	NC	-41	1939	1980	197	13	731,424	7,776	1,350
Pennsylvania	North	PA N	54	735	681	412	10	101,786	2,578	838
Tennessee	Single	TN	27	1804	1776	258	81	646,889	9,258	1,709
Texas	Central	TX C	-27	2333	2361	531	19	790,390	10,407	1,416
Vermont	Single	VT	-5	1177	1182	341	80	42,417	1,999	689
Washington	North	WA N	-23	2996	3019	813	1	608,660	12,641	2,051
		<i>Minimum</i>	<i>-41</i>	<i>77</i>	<i>106</i>	<i>-21</i>	<i>1</i>	<i>42,417</i>	<i>1,999</i>	<i>218</i>
		<i>Maximum</i>	<i>1077</i>	<i>6020</i>	<i>6023</i>	<i>2087</i>	<i>90</i>	<i>3,792,621</i>	<i>46,127</i>	<i>13,147</i>
		<i>Mean</i>	<i>115</i>	<i>1995</i>	<i>1880</i>	<i>540</i>	<i>28</i>	<i>553,439</i>	<i>9,710</i>	<i>2,013</i>

* Statistics are combined for multiple zones (zones 3-5 in AK, all 3 zones in FL, and all 5 zones in HI).

** Guam and Commonwealth of Northern Mariana Islands (CNMI) combined into a single zone.

Table 3.2. Characteristics of statewide SPCS2022 zones designed as part of this study. Topographic heights are NAD 83 ellipsoid heights.

State or territory	Topographic height (m)				City and town populations			
	Min	Max	Range	Mean	Min	Max	Mean	Median
Alabama	-29	673	702	110	22	212,237	5,433	1,046
Alaska	-7	6020	6027	467	4	291,826	2,120	260
Arizona	-12	3759	3771	1263	1	1,445,632	15,703	964
California	-114	4239	4353	829	4	3,792,621	26,354	3,371
Colorado	990	4328	3338	2073	2	600,158	10,265	759
Florida	-29	77	106	-8	3	821,784	17,580	4,513
Georgia	-32	1384	1416	126	16	420,003	6,732	1,321
Hawaii	2	4212	4210	919	29	47,698	7,505	3,034
Illinois	60	322	262	158	13	2,695,598	8,264	1,066
Mississippi	-31	189	220	59	55	173,514	4,373	1,137
New Mexico	840	3923	3083	1742	7	545,852	4,159	465
Pennsylvania	-33	929	962	347	10	1,526,006	4,325	1,131
Tennessee	-28	2333	2361	485	6	2,099,451	12,916	1,524
Washington	-23	4100	4123	678	1	608,660	9,763	1,653
<i>Minimum</i>	<i>-114</i>	<i>77</i>	<i>106</i>	<i>-8</i>	<i>1</i>	<i>47,698</i>	<i>2,120</i>	<i>260</i>
<i>Maximum</i>	<i>990</i>	<i>6020</i>	<i>6027</i>	<i>2073</i>	<i>55</i>	<i>3,792,621</i>	<i>26,354</i>	<i>4,513</i>
<i>Mean</i>	<i>111</i>	<i>2606</i>	<i>2495</i>	<i>661</i>	<i>12</i>	<i>1,091,503</i>	<i>9,678</i>	<i>1,589</i>

The variability of population by point location is much more extreme than height, ranging from 1 person to 3.79 million (these points are usually associated with actual cities or towns, but some are simply named places). This variability is also reflected in the large difference between the mean and median city populations. These extremes show that weighted mean population by itself will tend to skew the design too much toward the large cities, which is why cities and town locations (without population) are also used as part of the design process.

3.5.1 Datasets and Software Used for Analysis and Design

Datasets used for design and analysis of zones for SPCS2022 and SPCS 83 are listed below.

Linear distortion for all datasets was computed using Eqs. 3.1 and 3.2, with k computed using the

algorithms from Stem (1990). Design calculations were performed in Microsoft *Excel* and Esri *ArcGIS* software was also used for creating maps and performing a variety of geoprocessing tasks (although the only specialized one mentioned in this study is the “Minimum Bounding Geometry” tool). The only custom software used for this study was developed to create the linear distortion rasters (for creating maps and providing overall zone statistics at high resolution). The data were obtained from NGS, the U.S. Geological Survey (USGS), the National Aeronautics and Space Administration (NASA), the National Geospatial-Intelligence Agency (NGA), the U.S. Census Bureau, and Esri. What follows is essentially a list; details on these datasets, their sources, and references are given in Appendix C. A key characteristic is that all of the datasets were freely and readily available.

- Digital elevation models (DEMs). DEMs obtained from the USGS 3DEP program were used (resolutions of 1 arc-sec for CONUS and 2 arc-sec for Alaska). For Hawaii, Guam, CNMI, and American Samoa, 3 arc-sec DEMs from the NASA/NGA Shuttle Radar Topography Mission (SRTM) were used.
- Geoid models. Geoid models were used to convert the DEM orthometric heights to ellipsoid heights. The NGS hybrid model GEOID12B was used for CONUS, and the NGA/NASA gravimetric geoid model EGM2008 was used for all other areas.
- Regular grids of points with ellipsoid heights. Point grids were created for use in design computations at various intervals (usually 1- and 2-arc-minute). Ellipsoid heights were determined for each grid point using the highest-resolution DEM available and appropriate geoid model, as stated above.
- City centroids with ellipsoid height and population. Point locations of 38,193 named locations nominally considered cities or towns (compiled by Esri using data from the U.S. Census and USGS). Of those points, 71% have 2010 U.S. Census populations.

- GIS datasets that define the zone geometries. Polygons representing detailed county and state boundaries and shorelines (also compiled by Esri using data from the U.S. Census and USGS).

3.5.2 Design Example 1: Arizona Central Zone (Transverse Mercator)

Input for design was 47,285 points on a 1 arc-minute grid, and 243 cities and towns point locations (174 with population). Final distortion maps and zone statistics were derived from distortion computations at 15 arc-sec resolution. The design process is provided in considerable detail since it is the first of three.

1. Projection type and distortion design criterion. A TM projection was used (same as for SPCS 83), which is appropriate given its north-south elongation and orientation. The maximum east-west width of this zone is 272 km, corresponding to a range of $\delta_0 = \pm 114$ ppm per Eq. 3.6. Thus, a reasonable choice for the distortion design criterion is ± 100 ppm. Note that this is lower than the calculated value, so it is a somewhat ambitious choice, especially considering the large range in topographic height for the zone (3661 m, from Table 3.1). If ellipsoid height was constant throughout the entire zone, and its central meridian was centered, that only 69% of the zone would be within the ± 100 ppm.
2. Projection axis location and scale based on topography. The central meridian, λ_C , was placed at the mid-longitude of the zone, $111^\circ 54' W$ (rounded to the nearest arc-minute). A scale of $k_0 = 1.00012$ was then assigned to λ_C , which is the average of the scale values that yield zero mean and median distortion for the entire zone (rounded to the nearest 5 decimal places). This resulted in an initial design with a distortion range and standard deviation of 748 and ± 119 ppm, respectively, for the entire zone. For all cities and towns, the corresponding range and standard deviation are 549 and ± 95 ppm. These values are shown in Figure 3.5a, along

with those from 17 other iterated central meridian longitudes, all with $k_0 = 1.00012$. Note the clearly defined distortion range minimum is at $\lambda_C = 112^\circ 03' W$ for the entire zone (and very close to that value for all cities). The standard deviation minima are less well defined, do not coincide with the range minima, and are at different meridians for the entire zone and cities. The disagreement between range and standard deviation is typical, as is the more clearly defined minimum for range. Both indicate variability in distortion, but the range is more useful for design because it indicates the maximum magnitudes that can be expected for an entire zone. In contrast, standard deviation gives dispersion about the mean distortion, which is of less importance for design; it is shown in the examples mainly for the sake of completeness.

Figure 3.5b is aligned horizontally with the upper plot and provides secondary information for design analysis, which can aid in selecting the central meridian. It shows the maximum and minimum distortion for the entire zone, as well as for cities. Obviously, the extremes for the entire zone must contain the extremes for the cities within the zone, but there are other features worth noting. The curve shapes are typical, with the maximum positives showing a clear minimum (corresponding to the minimum ranges), but with no such minimum occurring on the maximum negative curves. At $\lambda_C = 112^\circ 03' W$, the negative distortion is of greater magnitude than the positive, and the separation between negative extremes for cities and towns is greater for all λ_C values shown. This behavior is also typical and is particularly pronounced in mountainous areas (such as Arizona) for λ_C near the midpoint of the zone, since the large negative magnitudes represent high topography, which constitutes a smaller proportion of the zone area and has fewer towns.

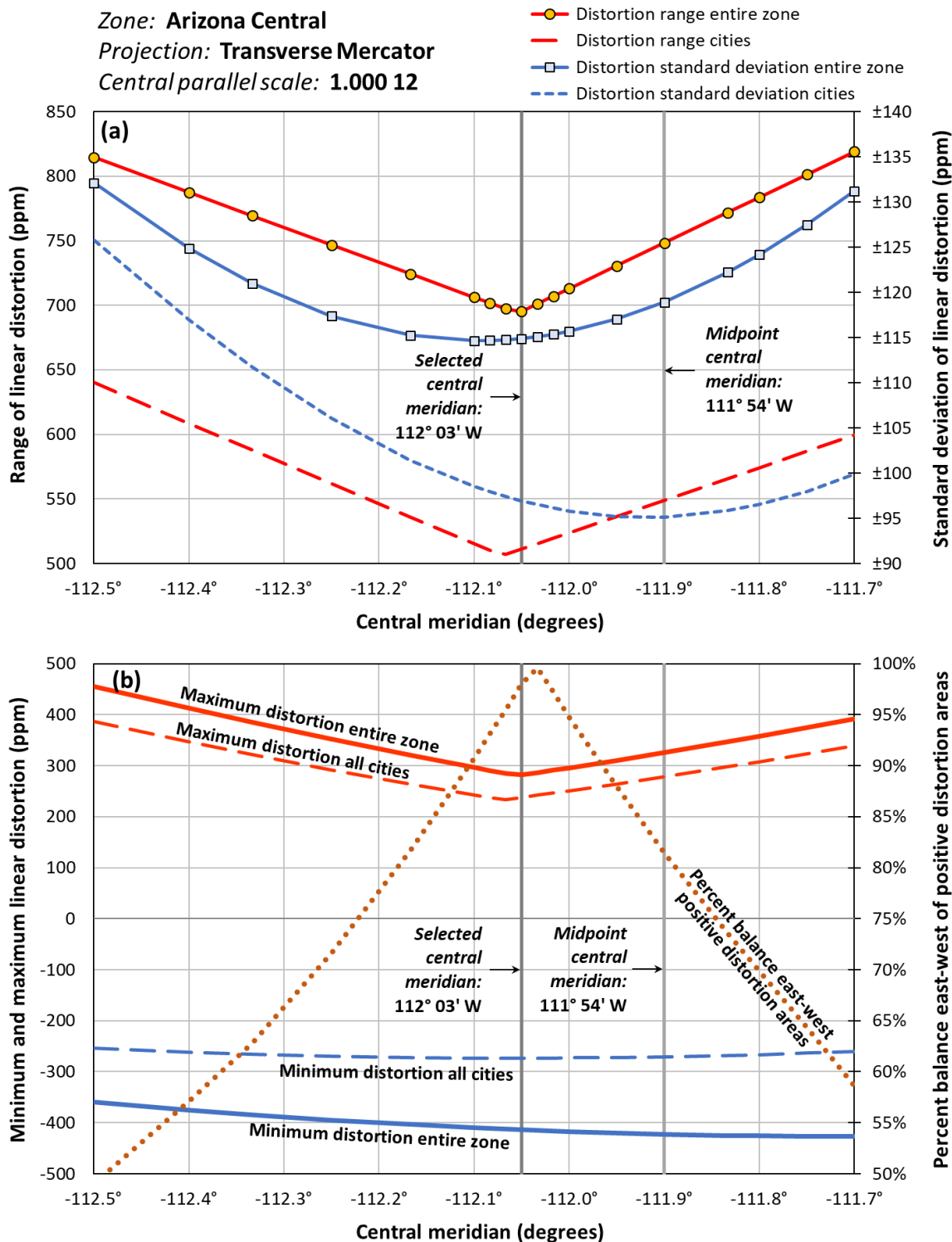


Figure 3.5. Effect of central meridian location on distortion range and standard deviation (top), and on minimum and maximum distortion and percent balance of positive distortion areas east and west of central meridian (bottom), for Arizona Central Zone.

The triangle-shaped dotted curve in Figure 3.5b is the percent balance in area with positive distortion on either side of the projection axis (central meridian in this case). It is computed as 1 minus the ratio of the absolute value of the difference in positive distortion area on either side of the axis to the total positive distortion area. A value of 100% means that the area with positive distortion is the same on either side of the projection axis; 0% means all positive distortion areas are on one side; and 50% means that the difference between sides is half the total, or that there is $(2 - 0.5) / 0.5 = 3$ times as much area with positive distortion on one side than on the other. The purpose of this statistic is to show that the zone positive distortion is balanced, and area is used because the zone edges may be of greatly different shape on either side (as is the case here, as shown by the difference in shape of the east and west edges). Ideally, the balance would be near 100% for a zone design, as occurred here. But that often is not the case, and positive distortion balance, although desirable, is a secondary consideration. In addition, balance is affected by the axis scale, not just its location, and so it can also change when modifying the scale for population.

3. Modification of projection scale based on population distribution. With λ_C selected, its scale is adjusted to account for population distribution (Figure 3.6). In this case the $\lambda_C = 112^\circ 03' W$ is constant but its scale changes, with the initial $k_0 = 1.00012$ shown as a vertical line. In plot (a), the maximum percent total area (60%) occurs near the initial $k_0 = 1.00012$, which is expected since that scale was selected based on a mean and median overall distortion of near zero. This meets the design requirement of 50%. However, this scale corresponds to only 79% of population and 69% of cities and towns within ± 100 ppm, which does not meet their respective design requirements of 90% and 75%. From the curves in Figure 3.6a it can be seen that k_0 must be decreased for these percentages to increase. A

peak value of 76% of cities within ± 100 ppm occurs when $k_0 = 1.00007$, which also corresponds to 95% of population, as well as 55% of total zone area. In addition, the percent balance of positive distortion areas is still high (97%). Thus $k_0 = 1.00007$ satisfies the design criterion for the percent distortion metrics, as well as achieving good distortion balance.

The curve for percent population has an unusual shape. It maintains an essentially constant percentage (92% to 95%) between k_0 values of 0.999955 and 1.000075, but the percentage drops precipitously outside those k_0 values. This behavior is attributed largely to population data at discrete points representing cities and towns. This discretization of the population data causes apparent sudden fall-offs in the percentage within the design criterion, especially for points representing large cities (or group of points clustered in a metropolitan area).

The sudden change in population percentage within a particular distortion band could possibly be ameliorated by rasterizing U.S. Census block data, rather than representing cities by single points. However, it is not clear if such rasterization would alter zone design, since the zones generally cover large areas and so may be insensitive to point discretization of population data. Nonetheless, it would be prudent to investigate rasterized population to determine whether it significantly impacts zone design.

Figure 3.6b includes additional information, most importantly the mean distortion weighted by population and the mean distortion of all cities and towns. Note that the $k_0 = 1.00007$ is about half way between these two metrics, which is reasonable (mean weighted distortion is +24 ppm and mean distortion all cities is -20 ppm). The mean overall distortion (central dotted line) has a mean of zero near the initial $k_0 = 1.00012$ (as it should since that was how that k_0 was determined), but this is of lesser concern.

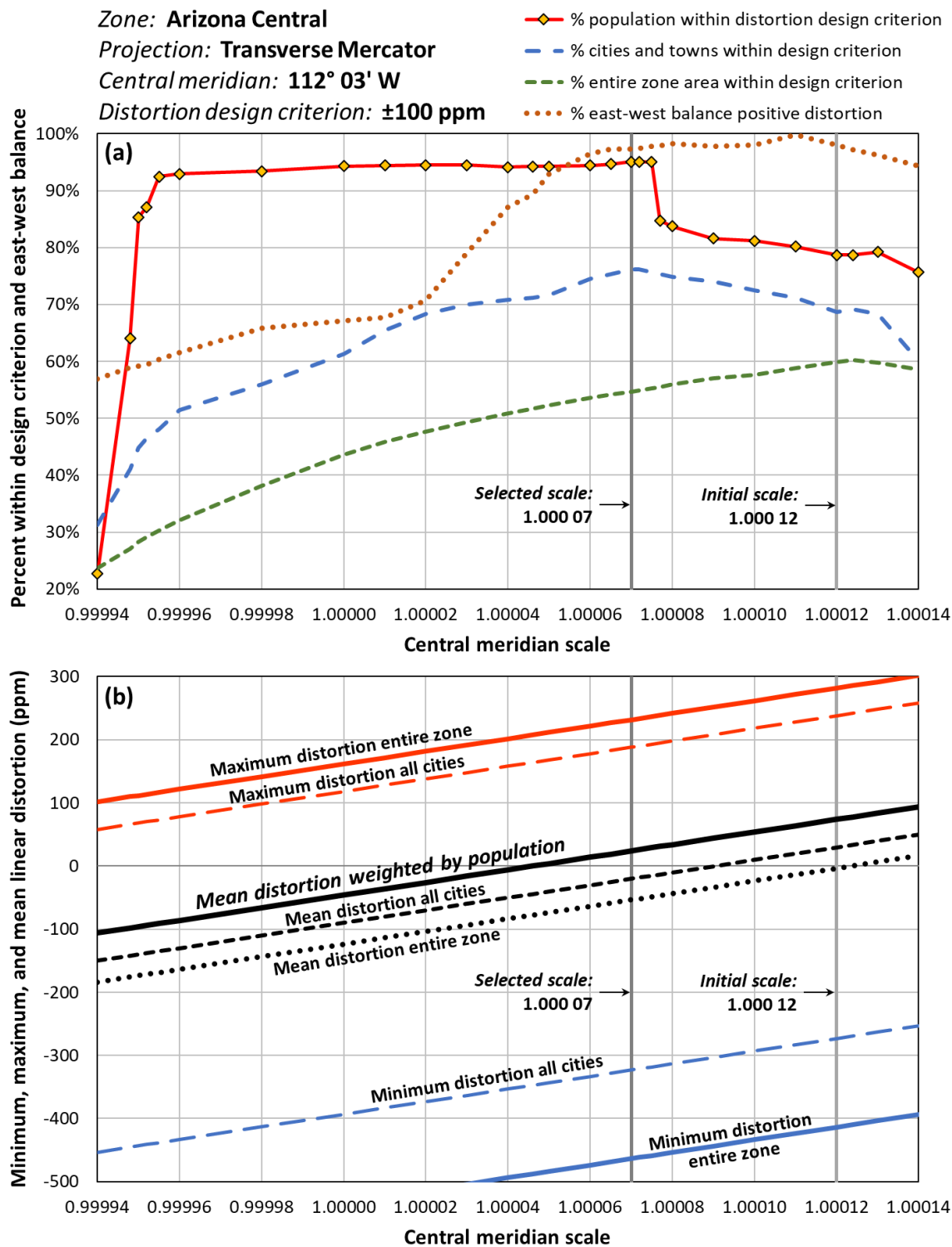


Figure 3.6. Effect of central meridian scale on percent population, cities, and area within design criterion and east-west balance of positive distortion (top), and on min, max, and mean distortion of cities weighted by population, all cities, and entire zone (bottom), for Arizona Central Zone.

Also of secondary concern in Figure 3.6b are the minimum and maximum distortion lines at the top and bottom of the chart (for the entire zone and for cities). Ideally the minimum and maximum distortion for cities should be approximately equal, but that is not the case here (+188 and -323 ppm). From Figure 3.6b, it can be seen that to make them equal would require $k_0 = 1.00014$. But that would give unacceptable results for the more important metrics of percent population and cities, as well as for weighted mean and mean of all cities near zero.

4. Evaluation and refinement of design. The final step is evaluating the design and refining if necessary. Although this can (and perhaps should) include a more careful inspection of the statistics and plots, an important additional tool is plotting a map of the linear distortion, as shown in the upper map of Figure 3.7 (the lower map shows distortion of existing SPCS 83, using the same color ramp to aid comparison). A distortion map allows an immediate overview of distortion performance throughout the entire zone and at specific locations. It is particularly useful for identifying local areas where distortion is excessive, as well as imbalances in distortion at the zone edges, and other unusual behavior that cannot be discerned from statistics and charts. The cities of Tucson (in the south part of the zone) and Flagstaff (in the north) provide an example of using the distortion maps to achieving compromise in design. Because Tucson is the second largest city in Arizona, it was desirable to keep its distortion within ± 100 ppm. On the other hand, excessively large negative distortion in Flagstaff (ellipsoid height of ~ 2100 m) was considered problematic, since it is the largest population center outside the Phoenix and Tucson metro areas. A compromise was struck by keeping Tucson just below +100 ppm, so that Flagstaff did not exceed -240 ppm. This also kept the entire Phoenix metro area below +100 ppm, as can be seen in

the top map of Figure 3.7. It is especially evident in the lower map for SPCS 83, where Tucson distortion is -110 ppm, Phoenix is -145 ppm, and Flagstaff is -420 ppm.

A distortion map should always be created and inspected before finalizing a zone design. It is also useful for comparison to other designs, in this case SPCS 83. The difference is visually striking, showing especially large decreases in the magnitude of distortion in high elevation areas, as well as a significant decrease in the absolute distortion in the Phoenix and Tucson metropolitan areas (where 88% of the zone population resides). Both maps also include statistics on performance. For the SPCS2022 default design, 95% of the population is within ± 100 ppm distortion, versus only 2% for SPCS 83. The weighted mean distortion by population is $+24$ ppm for SPCS2022, versus -151 ppm for SPCS83. Considering the entire zone, 55% of the SPCS2022 zone is within ± 100 ppm (with a mean distortion of -54 ppm) versus 14% for SPCS 83 (with mean distortion of -224 ppm).

Note that a change in k_0 is not the only difference between the SPCS2022 and SPCS 83 versions of the Arizona Central Zone. The central meridian of SPCS2022 is also 8 arc-min further west than SPCS 83. This reduces the distortion range, as shown schematically in Figure 3.3. Although the decrease of 46 ppm (from 784 to 738 ppm) is not large with respect to the overall zone distortion, it is significant. This decrease is the same as shown in Figure 3.5, based on completely different k_0 values, illustrating that distortion range is largely independent of k_0 . This fact can simplify the design process, since a projection axis location can be determined with any k_0 (although a reasonable initial estimate of k_0 helps assess other effects, such as distortion balance and extremes). Based on this analysis, the final design parameters for the *preliminary* default SPCS2022 Arizona Central Zone TM projection are $\lambda_C = 112^\circ 03' W$ and $k_0 = 1.00007$.

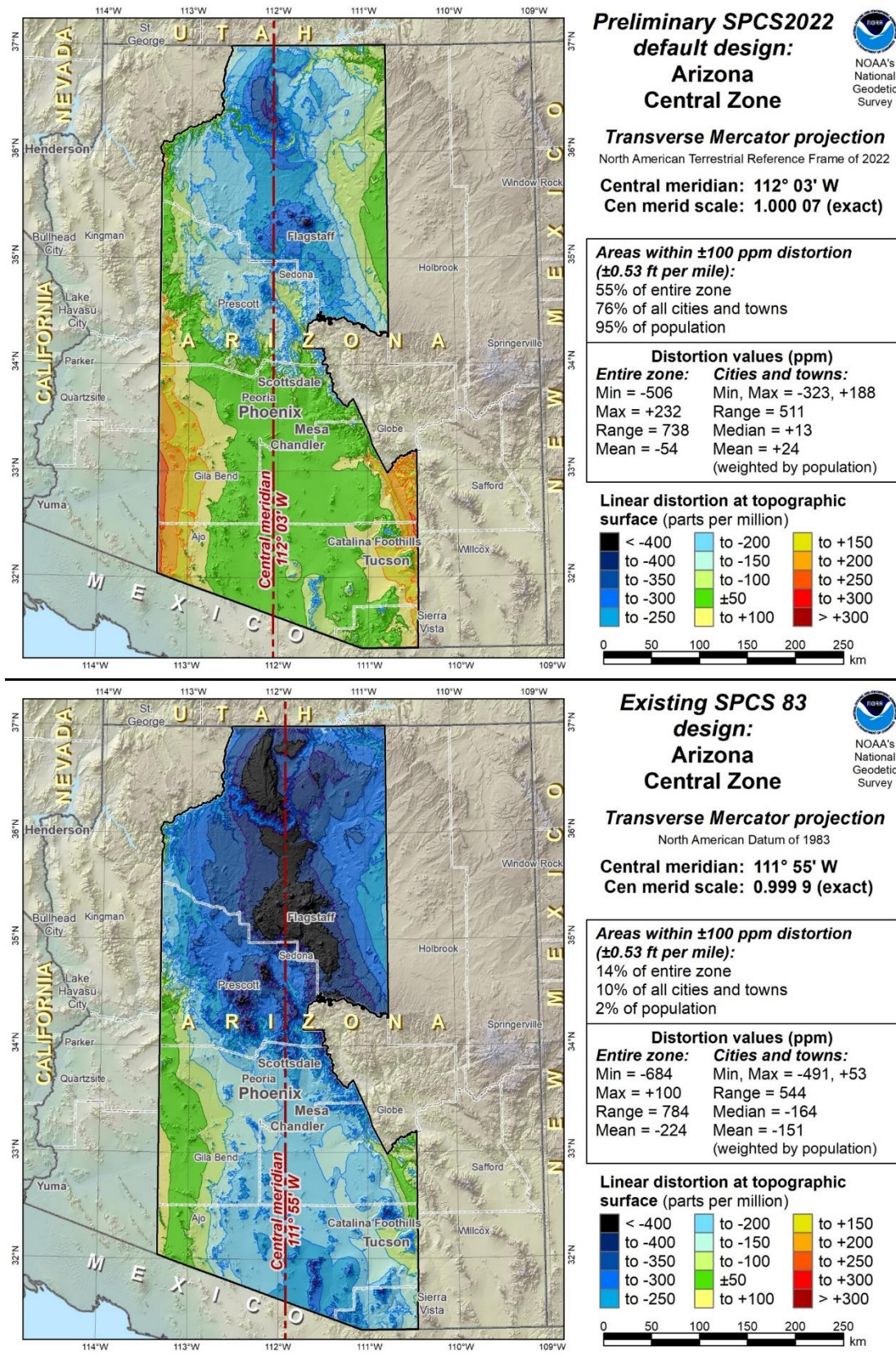


Figure 3.7. Arizona Central Zone linear distortion maps, SPCS2022 (top), SPCS 83 (bottom).

The detailed example of the design process for the SPCS2022 Arizona Central Zone was done to make it clear how the concepts are applied. In practice, the designs can be accomplished more rapidly than the description might imply. That is particularly true if most of the process is automated, leaving mainly just the final step of evaluating and revising the design. With details of the fundamental design concepts covered, the next design example is more streamlined, instead focusing on items where it differs from the Arizona example.

3.5.3 Design Example 2: California Zone 5 (Lambert Conformal Conic)

The input for analysis and design was 36,861 points on a 1 arc-minute grid and 394 cities and towns (289 with population). The following steps are the same as the previous example.

1. Projection type and distortion design criterion. For SPCS 83, an LCC projection was used for California Zone 5, which is appropriate for this zone. The maximum north-south width of this zone is 234 km, corresponding to a range of $\delta_0 = \pm 84$ ppm. Thus again a reasonable choice for the distortion design criterion is ± 100 ppm.
2. Projection axis location and scale based on topography. Placing the central parallel at the mid-latitude of the zone gives $\varphi_C = 34^\circ 45' \text{N}$, and a scale of $k_0 = 1.00007$ results in an average of median and mean distortion of zero for the entire zone. The combination of these values is shown in Figure 3.8a, where φ_C is already at the minimum distortion range for both the entire zone and its cities and towns. However, unlike the Arizona example, in this case the positive distortion area on either side of the projection axis is not as well balanced, at 78% (Figure 3.8b). This occurs even though φ_C is centered, because the north edge of the zone is at a single latitude, whereas the west end of the south edge has a portion that juts south, in the Los Angeles metro region (See Figure 3.4 and Figure 3.10). Thus a larger area

has positive distortion on the north side of the zone. Given the lower priority of such balance, that problem is bypassed for now.

3. Modification of projection scale based on population distribution. With φ_C selected, its scale is modified to account for population distribution. The situation is shown in the upper (a) and lower (b) plots of Figure 3.9, with the initial $k_0 = 1.00007$ shown as a vertical line. In the upper plot, it corresponds to the peak 75% of area within the ± 100 ppm distortion criterion (as well as the peak positive distortion balance of 78%). However, only 28% of the population and 56% of all cities are within ± 100 ppm; thus, there is no choice but to change k_0 , which Figure 3.9 shows must be reduced. A value of $k_0 = 0.99995$ places the central parallel at the peak 76% of cities within ± 100 ppm distortion, and just meets the 90% criterion for population.

Unfortunately, with $k_0 = 0.99995$ the total area within 100 ppm decreases to 41%, below the 50% target. But the plot shows that increasing k_0 will cause the population percentage to fall below 90%. Given the higher priority of population over city locations, it prevails, and the $k_0 = 0.99995$ was selected for design. Figure 3.9b also shows that $k_0 = 0.99995$ corresponds to a weighted mean population of -3 ppm, very close to zero. However, the mean distortion for all cities is -53 ppm, and the mean for the entire zone is -117 ppm. Furthermore, the maximum positive distortion for cities is $+100$ ppm, versus -338 ppm for the minimum, a significant imbalance. These are not desirable characteristics, but whether they lead to a change in φ_C or k_0 (or both) is assessed in the next step.

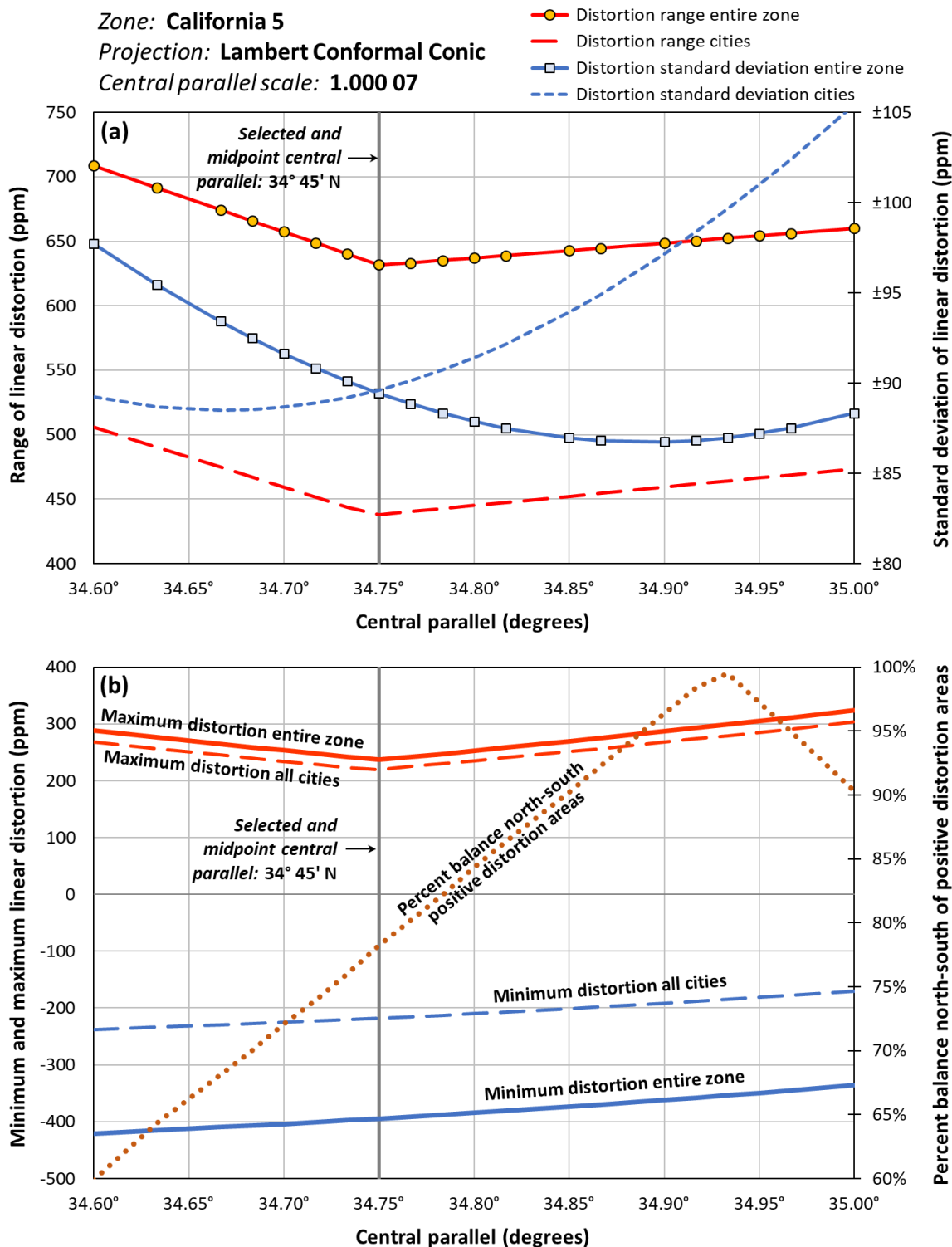
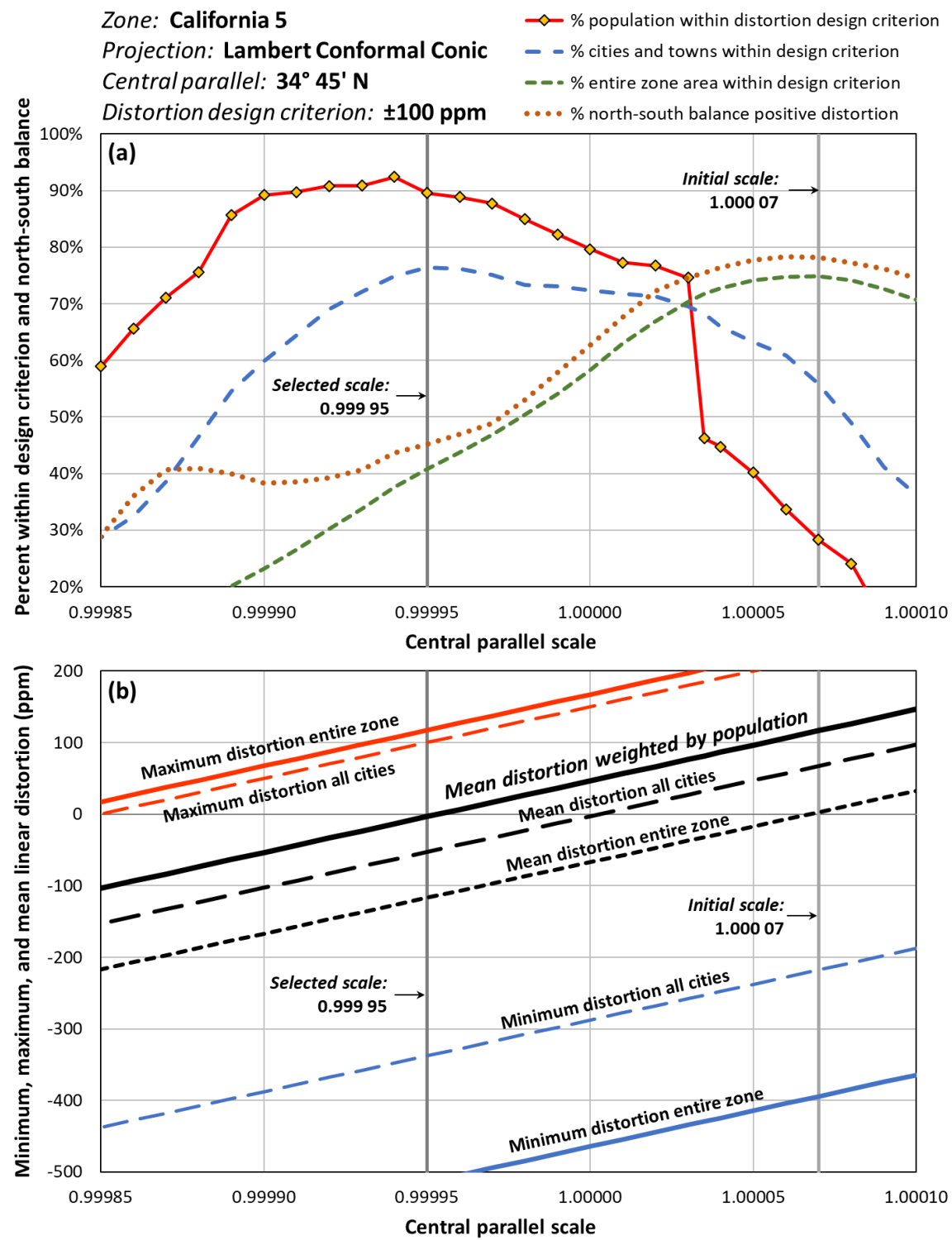


Figure 3.8. Effect of central parallel location (a) on distortion range and standard deviation, and (b) on minimum and maximum distortion and percent balance of positive distortion areas north and south of central parallel (California Zone 5).

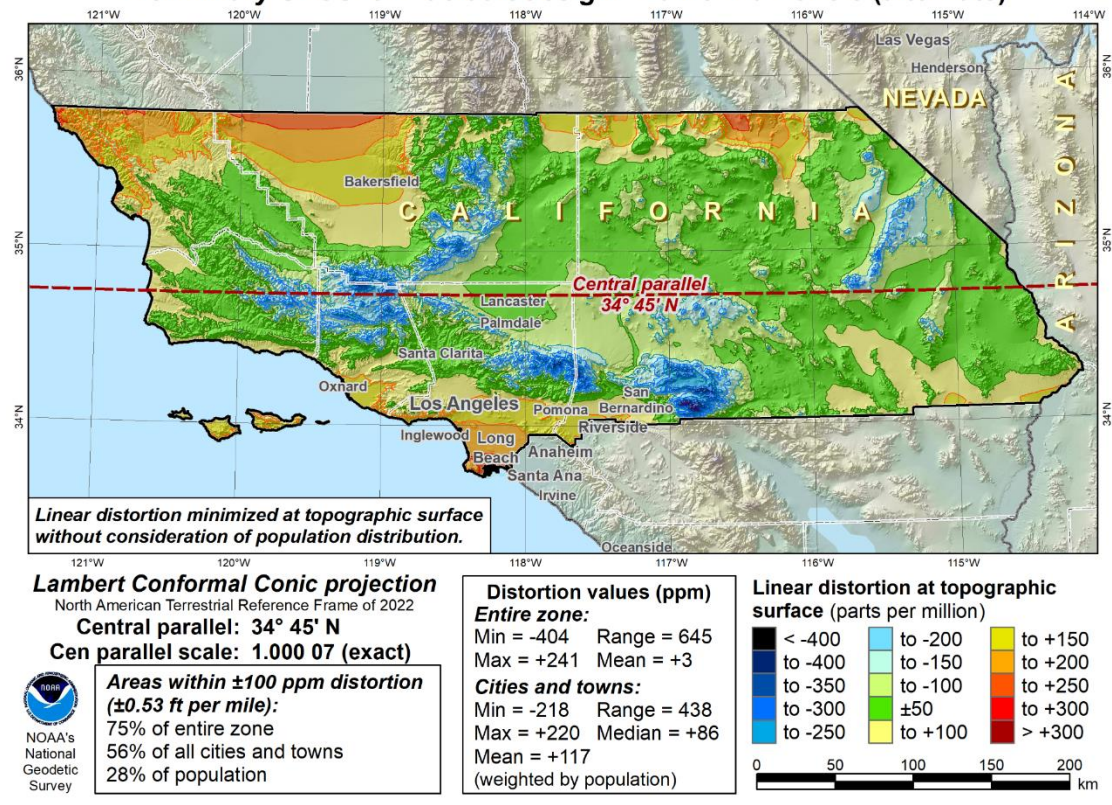


4. Evaluation and refinement of design. Figure 3.10 presents a distortion map of the initial design based on consideration of topography only, with population ignored (top). The bottom map is the final design with population taken into account as described in the previous step. Figure 3.11 shows a distortion map of the existing SPCS 83 zone.

The top map of Figure 3.10 is appealing, because such a large area has low distortion (75% within ± 100 ppm). But the low distortion areas are mostly located in the Mojave Desert, where few people live, and only 28% of the zone population is within ± 100 ppm. A vast majority of the population is at lower elevations along the coast, especially the Los Angeles metro area in the southwest corner of the zone (79% of the zone population). Thus a design based only on topography results in a system that performs best where it will likely be used the least.

The difference here is much greater than that of the Arizona example. In this case, k_0 was decreased by 120 ppm, versus 50 ppm for Arizona. This behavior is typical of zones that include coastal areas, since people tend to live near the coast. It is especially pronounced along the CONUS west coast, since those zones include mountainous areas. Based on this analysis, the final design parameters for the *preliminary* default SPCS2022 California Zone 5 LCC projections are $\varphi_C = 34^\circ 45' \text{N}$ and $k_0 = 0.99995$, despite only 41% of the zone area meeting the distortion design criterion.

Preliminary SPCS2022 default design: California Zone 5 (alternate)



Preliminary SPCS2022 default design: California Zone 5

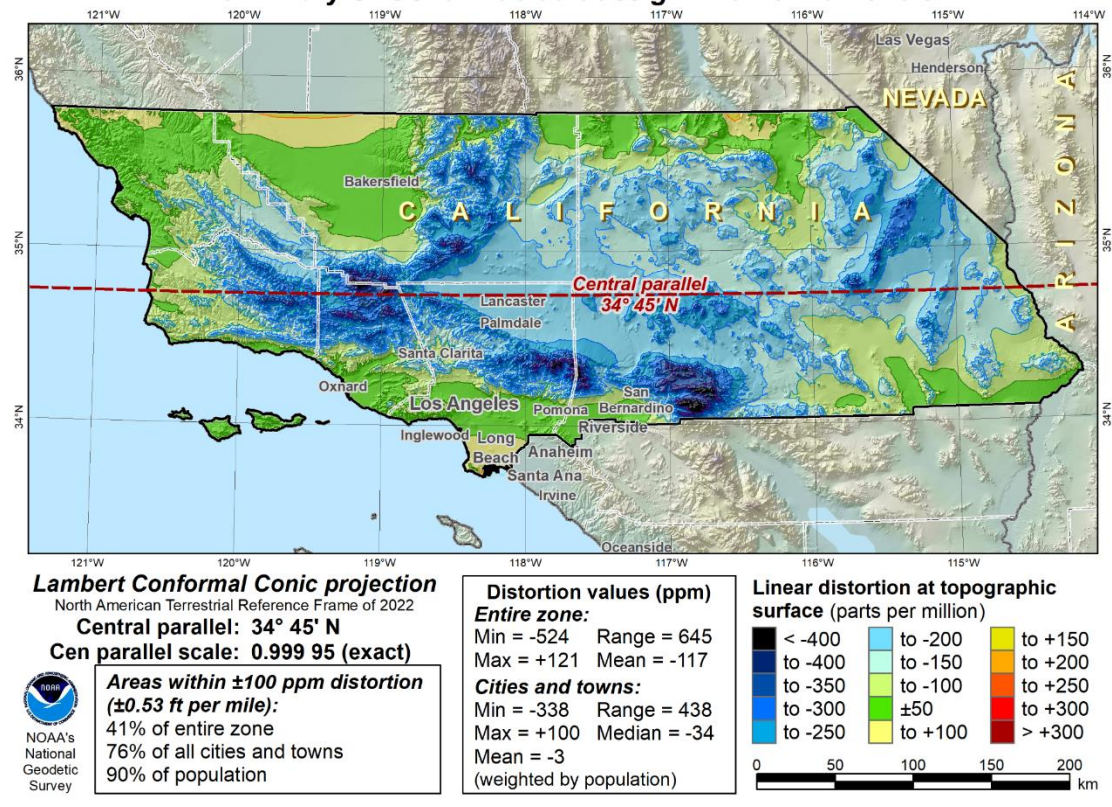


Figure 3.10. California Zone 5 SPCS2022 linear distortion maps: initial (top), final (bottom).

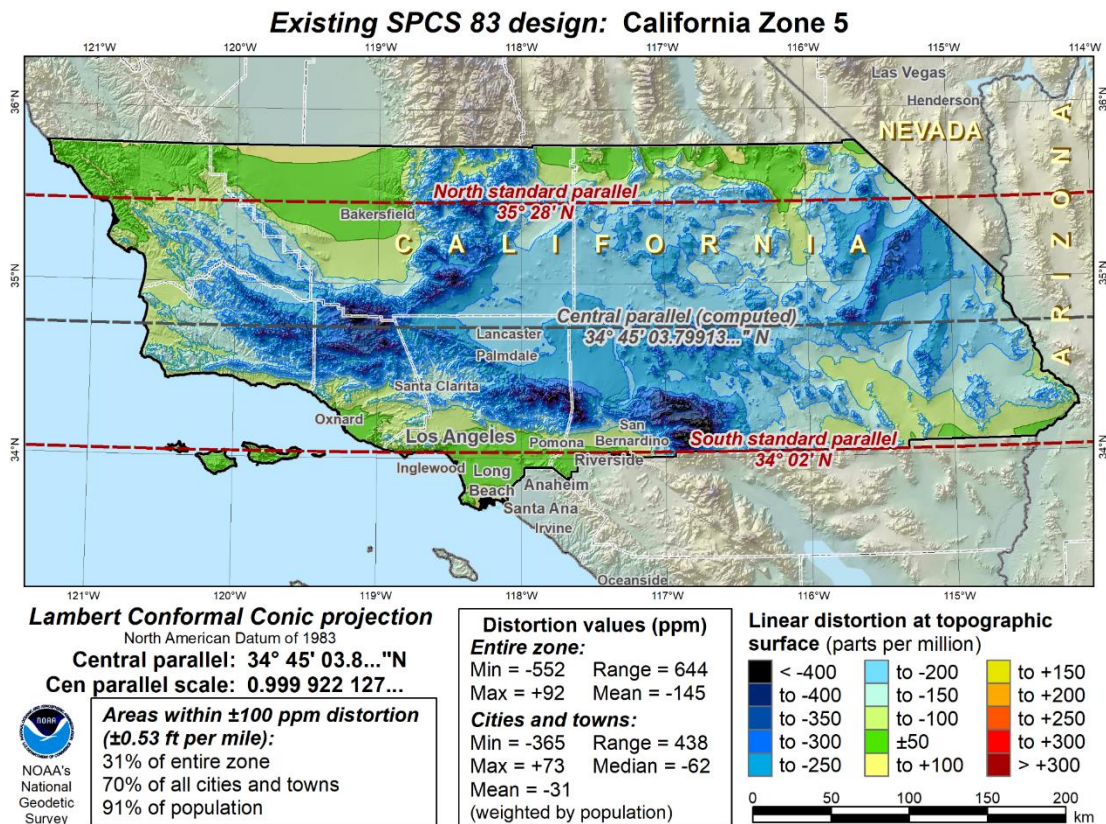


Figure 3.11. California Zone 5 linear distortion map for existing SPCS 83 (2-parallel LCC).

Comparison of the final SPCS2022 design in the bottom of Figure 3.10 to the existing SPCS 83 design in Figure 3.11 shows that the two are very similar. Both have essentially the same ϕ_c (differing by only 3.8 arc-sec) and k_0 (differing by only 28 ppm). Consequently, their performance is similar, both with about 90% of the population within ± 100 ppm. One notable difference is how the parameters are defined: SPCS2022 is based on a 1-parallel LCC (per NGS policy as mentioned previously), whereas all SPCS 83 LCC zones use a 2-parallel definition. Although similar, the SPCS2022 version performs somewhat better overall, with a larger percentage of cities (76% vs. 70%) and total area (41% vs. 31%) within ± 100 ppm. Such similarities in performance between SPCS2022 and SPCS 83 occur in other zones, especially those with a boundary on the coast or at overall low elevation.

3.5.4 Design Example 3: Hawaii Statewide Zone (Oblique Mercator)

Input for analysis and design was 82,960 points on a 15 arc-sec grid (on land areas only) and 108 cities and towns (78 with population).

1. Projection type and distortion design criterion. For SPCS 83, five TM zones were used for Hawaii, with one zone per island or island group (see Figure 3.4 and the bottom map of Figure 3.1). This type of zone layout is a holdover from the past, when classical surveying could not be performed across large expanses of water. Another holdover from that past was the greater computational difficulty in using OM projections. Yet the alignment of the islands most certainly suggests a single OM zone would be a good choice. Thus an OM was selected to provide coverage for or all of the populated islands. The land area of the islands perpendicular to their general alignment is about 155 km wide, which corresponds to a range of $\delta_0 = \pm 37$ ppm. This suggests 40 or 50 ppm for the design criterion. However, these are likely too stringent, given the large range in topographic height for such a small area (4210 m, which is the second largest in Table 3.1, after Alaska). With that in mind, a distortion design criterion of ± 100 ppm was again selected.
2. Projection axis location and scale based on topography. Because an OM was selected, this step is not as simple as for TM and LCC projections. The approach used here (and for all OM designs in this study) was to make use of the “Minimum Bounding Geometry” tool in Esri software (Esri, 2018), using the rectangle by width geometry type. This type gives the rectangle of the smallest width that encloses the input feature. As such it is ideal for determining the location and orientation of the OM projection (skew) axis (especially for large areas), since distortion increased with the square of zone width perpendicular to the skew axis. The tool was applied to the group of polygons representing populated islands of

Hawaii (in geographic coordinates referenced to NAD 83). It yielded a rectangle 154.56 km wide (along a geodesic connecting the midpoints of its long sides), and with a geodetic azimuth of -55.1647° (for the skew axis) between the midpoints of its short sides. Rounding the rectangle centroid coordinates to the nearest arc-minute and the midline axis to the nearest degree gives an initial local origin of $(\varphi_0, \lambda_0) = 20^\circ 51' \text{N}, 157^\circ 25' \text{W}$ and skew azimuth of $\alpha_0 = -55^\circ$. The average median and mean k_0 for zero distortion gives $k_0 = 1.0001$. These initial parameters yielded distortion ranges of 732 and 247 ppm for the entire land area and cities, respectively, with 61% of the island area within ± 100 ppm distortion. Because of the complexity of OM evaluation, it is also useful to evaluate the scale error $(k - 1)$ range, i.e., linear distortion with respect to the ellipsoid, which was 79 ppm for land areas.

Changing α_0 to -56° decreased the overall area and city distortion (and scale error) ranges slightly, to 726 and 243 (and 74 ppm), respectively. The overall range could not be decreased with other combinations of origin and azimuth, and values of $\varphi_0 = 20^\circ 55' \text{N}$, $\lambda_0 = 157^\circ 30' \text{W}$, and $\alpha_0 = -56^\circ$ were selected for design, which gave the same overall range of 726 ppm but a slightly lower range of 241 ppm for cities and 72 ppm for scale error. For this design, 62% of the land area was within ± 100 ppm distortion, but only 55% of the population and 53% of the cities and towns were within that criterion.

3. Modification of projection scale based on population distribution. With the local origin and skew axis azimuth selected, the skew axis scale was modified until optimal performance with respect to population and topography was obtained. The final selected value was $k_0 = 1$ (exact), which resulted in 97% of population, 95% of cities, and 54% of land area within ± 100 ppm.

4. Evaluation and refinement of design. Linear distortion and statistics of the final SPCS2022 OM design for Hawaii are shown in the upper map of Figure 3.12. The lower map shows the five existing SPCS 83 zones. Note that the performance of the single OM zone is slightly better than the five separate zones, with 97% of the population, 95% of cities, and 54% of the land area within the ± 100 ppm distortion design criterion (versus 96% of the population, 94% of cities, and 45% of the land area for the combined five existing SPCS 83 zones). By reducing the number of zones from five to one while improving performance (albeit slightly) demonstrates the advantage of the approach presented here for designing zones.

Figure 3.13 shows linear distortion for UTM 4N, the UTM zone most closely centered on the populated Hawaiian islands, with the same distortion color ramp as Figure 3.12. For this case, the distortion is extreme, with a range of 2608 ppm (vs. 726 for the SPCS2022 OM), and only 0.6% of the population, 2.8% of cities, and 3.6% of the land area are within the ± 100 ppm criterion.

The reason for showing a distortion map and statistics for UTM 4N is that this zone is used by many organizations in Hawaii (including state government) for geospatial applications, such as statewide GIS (Carlson, 2018). Yet it clearly is not an ideal choice. The SPCS2022 single OM zone provides an optimal solution, and one that performs as well as existing SPCS 83. Thus this single zone can simultaneously serve the needs of the engineering, surveying, and GIS communities.

The final design parameters for the *preliminary* default (and statewide) SPCS2022 Hawaii Zone are $\varphi_0 = 20^\circ 55' \text{N}$, $\lambda_0 = 157^\circ 30' \text{W}$, $\alpha_0 = -56^\circ$, and $k_0 = 1$ (exact).

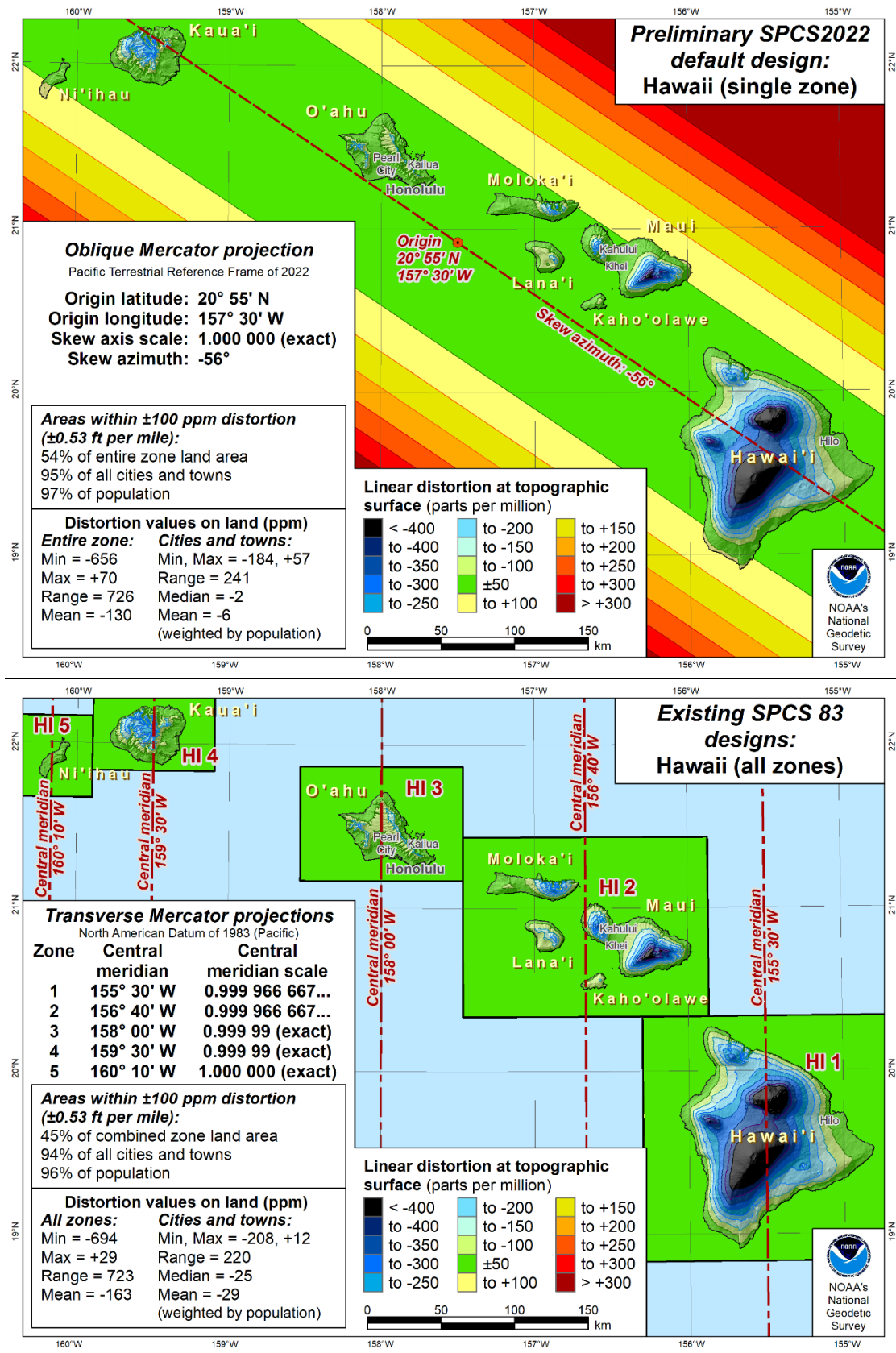


Figure 3.12. Hawaii SPCS linear distortion maps, SPCS2022 (top) and SPCS 83 (bottom).

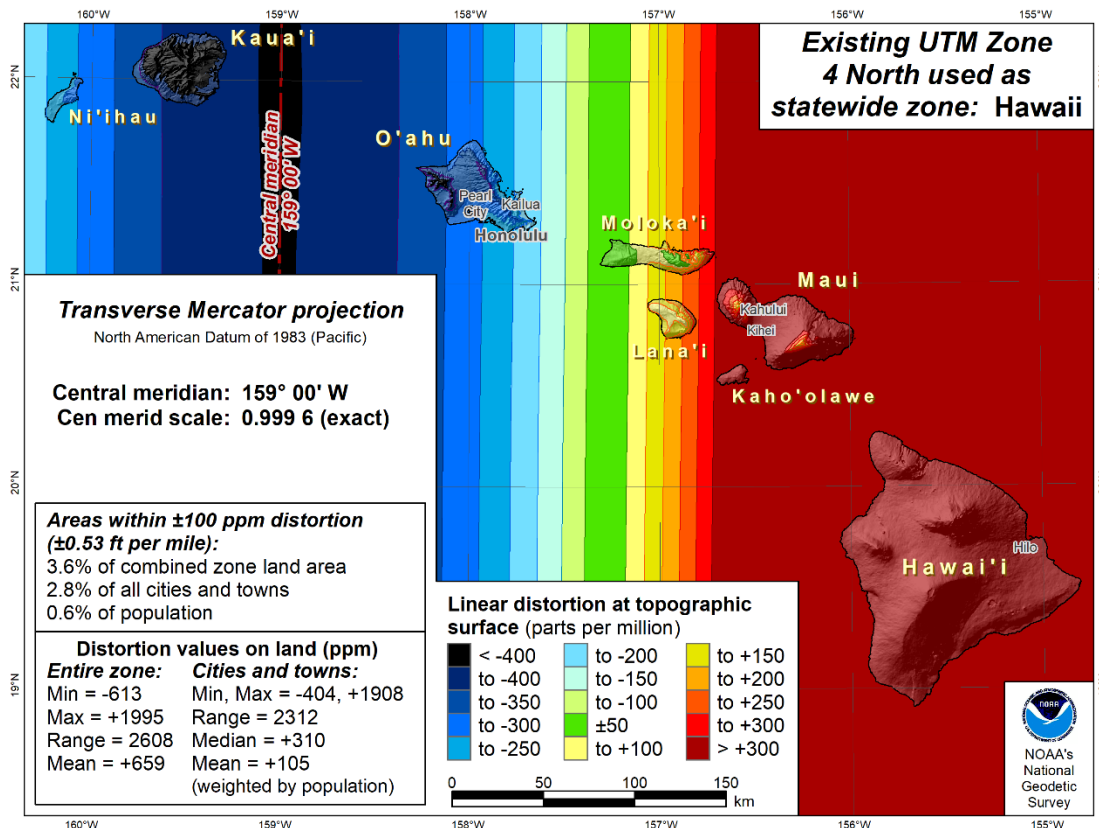


Figure 3.13. Distortion map of UTM Zone 4N used as a statewide zone in Hawaii.

Hawaii is not alone in its use of UTM for statewide applications. States with multiple SPCS 83 zones often do the same thing—even when it performs poorly. The apparent reason for this is convenience; it is easy to select a pre-defined system from an installed software package. It is because of this common practice that statewide SPCS2022 zones are compared to UTM in the next section.

3.6 EVALUATION OF DESIGNS

In the three detailed SPCS2022 design examples, comparisons were made to the corresponding existing SPCS 83 zones, as well as to a UTM zone for the proposed statewide Hawaii zone. In all cases, the SPCS2022 zones performed at least as well as SPCS 83, and significantly better by most distortion metrics. However, three is too small a sample for drawing general conclusions.

Therefore, the SPCS2022 default zone design process as outlined above was applied to SPCS 83 zones in 22 additional states and territories distributed throughout the U.S. (as shown in Figure 3.4). The specific SPCS2022 default and statewide zones designed and analyzed are shown in Figures 3.14 – 3.16, with complete lists in Appendix D (Tables D.1 and D.2).

A summary of distortion performance for the 28 default and 14 statewide SPCS2022 designs is given in Table 3.3. Distortion metrics for SPCS 83 are provided for comparison to the default SPCS2022 designs (upper half of table), and UTM results for comparison to the statewide SPCS2022 designs (lower half of table). Statistics are given for the range and the mean overall zone distortion, and for the mean distortion weighted by population. Statistics are also given for the percent population, cities and towns, and total area within the distortion design criterion.

Change in distortion statistics in Table 3.3 are given from SPCS 83 to the SPCS2022 default designs, and from UTM to SPCS2022 statewide designs. Median values are shown in bold because they are considered better measures of center than the mean when extreme values are present, which occurs often for the metrics on percent within the distortion criterion. For the default SPCS2022 zones, there is little difference in the distortion range statistics (median decrease of only 2%), which indicates the projection type and its axis location did not change much from SPCS 83. The decrease in mean distortion was 59% (both median and mean) for the entire zone area, with a median and mean decrease of 83% and 78%, respectively, when weighted by population. For percent within the distortion design criterion, the maximums are similar but minimums of zero occur only for the SPCS 83 (mainly due to high-elevation zones). Measures of center (median and mean) for all percentages are significantly higher for SPCS2022, especially population. Also notable are SPCS2022 standard deviations, which are substantially lower for all distortion metrics (other than range), showing that there is less distortion variation

for the SPCS2022 designs. The median percent increase was substantial for all three categories: 45% for population, 70% for cities, and 75% for area.

The statewide zone statistics in Table 3.3 show greater change in all median distortion metrics, with large decreases in distortion range (72%), overall mean (80%), and weighted mean (90%), as well as large increases in all percentages within the distortion design criterion (625% for population, 195% for cities, and 167% for area). Variability in comparisons to UTM is greater than SPCS 83, which is not surprising, since UTM zone extents are completely unrelated to state boundaries, and so UTM performance for a state is largely a matter of chance. Note that the Alaska and Texas statewide zones are in their own categories; because of their size they are not representative and so are not included in the statistics. This is shown by their very large distortion design criteria, ± 1000 ppm (0.1%) for Texas and ± 5000 ppm (0.5%) for Alaska.

To provide more detailed information, performance as percentages within the design criterion for each state are plotted in Figure 3.14 and Figure 3.15, for default and statewide zones, respectively. Two zones have no population data, American Samoa (AS) and Guam-CNMI (GU-CQ), although GU-CQ did have a few town locations. For the default designs in Figure 3.14, note that percentages of all metrics are higher for SPCS2022 than SPCS 83, except for percent area in MD and population in CA 5, but these SPCS 83 values are only very slightly greater (by 3% in MD and 1% in CA). In some zones, there is little difference between SPCS2022 and SPCS83, for example in CA, CT, DE, MD, and HI (although it should again be noted that HI has five zones in SPCS83 and only one in SPCS2022). But for most other zones, the difference is substantial. Note in particular that SPCS83 for CO S and NM C have zero (or near zero) percent in all three categories, and that all SPCS 83 percentages are also very low for AZ C, MT, and NE.

Table 3.3. Summary of linear distortion performance for 28 default and 14 statewide preliminary SPCS2022 zone designs, compared to SPCS 83 and UTM, respectively (for 25 states and territories). Median values are bold. Alaska and Texas statewide zones are shown separately because of much greater size.

Distortion design criterion (\pm ppm)	Distortion statistics for entire zone (ppm)				Mean weighted by population (ppm)		Percent within linear distortion design criterion					
	Range		Mean				Population		Cities & towns		Total area	
Default zones	2022	1983	2022	1983	2022	1983	2022	1983	2022	1983	2022	1983
Min 10	32	33	-130	-588	-113	-613	90%	0%	76%	0%	41%	0%
Max 400	1098	1098	10	25	26	1	100%	98%	100%	94%	99%	97%
Median 88	384	391	-22	-90	-4	-46	98%	65%	91%	52%	80%	41%
Mean 90	428	444	-36	-135	-7	-116	96%	54%	90%	51%	78%	41%
Std dev \pm 77	\pm 292	\pm 291	\pm 37	\pm 146	\pm 28	\pm 150	\pm 3%	\pm 35%	\pm 8%	\pm 27%	\pm 17%	\pm 25%
<i>Change from 1983 to 2022</i>	<i>(ppm) (%)</i>		<i>(ppm) (%)</i>		<i>(ppm) (%)</i>		<i>(%)</i>		<i>(%)</i>		<i>(%)</i>	
Min	-95	-36%	-509	-96%	-500	-98%	-1%		+2%		-3%	
Max	+4	+2%	-1	-19%	0	-39%	+5002%		+671%		+628%	
Median	-6	-2%	-34	-59%	-32	-83%	+45%		+70%		+75%	
Mean	-16	-6%	-99	-59%	-100	-78%	+503%		+118%		+129%	
Statewide zones	2022	UTM	2022	UTM	2022	UTM	2022	UTM	2022	UTM	2022	UTM
Min 100	177	531	-250	-323	-244	-578	88%	1%	78%	3%	54%	4%
Max 500	1437	8801	-22	1282	8	1423	100%	93%	100%	80%	100%	78%
Median 250	797	2324	-82	224	-46	-90	99%	14%	98%	33%	94%	36%
Mean 283	846	3156	-95	247	-79	103	97%	32%	95%	31%	89%	32%
Std dev \pm 134	\pm 456	\pm 2125	\pm 60	\pm 474	\pm 81	\pm 534	\pm 4%	\pm 31%	\pm 6%	\pm 21%	\pm 15%	\pm 20%
<i>Change from UTM to 2022</i>	<i>(ppm) (%)</i>		<i>(ppm) (%)</i>		<i>(ppm) (%)</i>		<i>(%)</i>		<i>(%)</i>		<i>(%)</i>	
Min	-7381	-87%	-1148	-93%	-1377	-98%	+7%		+25%		+28%	
Max	-354	-34%	+32	+26%	+148	+153%	+16,147%		+3333%		+1402%	
Median	-1882	-72%	-287	-80%	-242	-90%	+625%		+195%		+167%	
Mean	-2266	-67%	-329	-65%	-324	-63%	+1876%		+577%		+350%	
Alaska 5000	16,834	65,454	-1874	1671	-3976	2095	97%	87%	87%	80%	82%	94%
Texas 1000	4617	6369	-134	443	-223	490	92%	74%	86%	79%	86%	78%

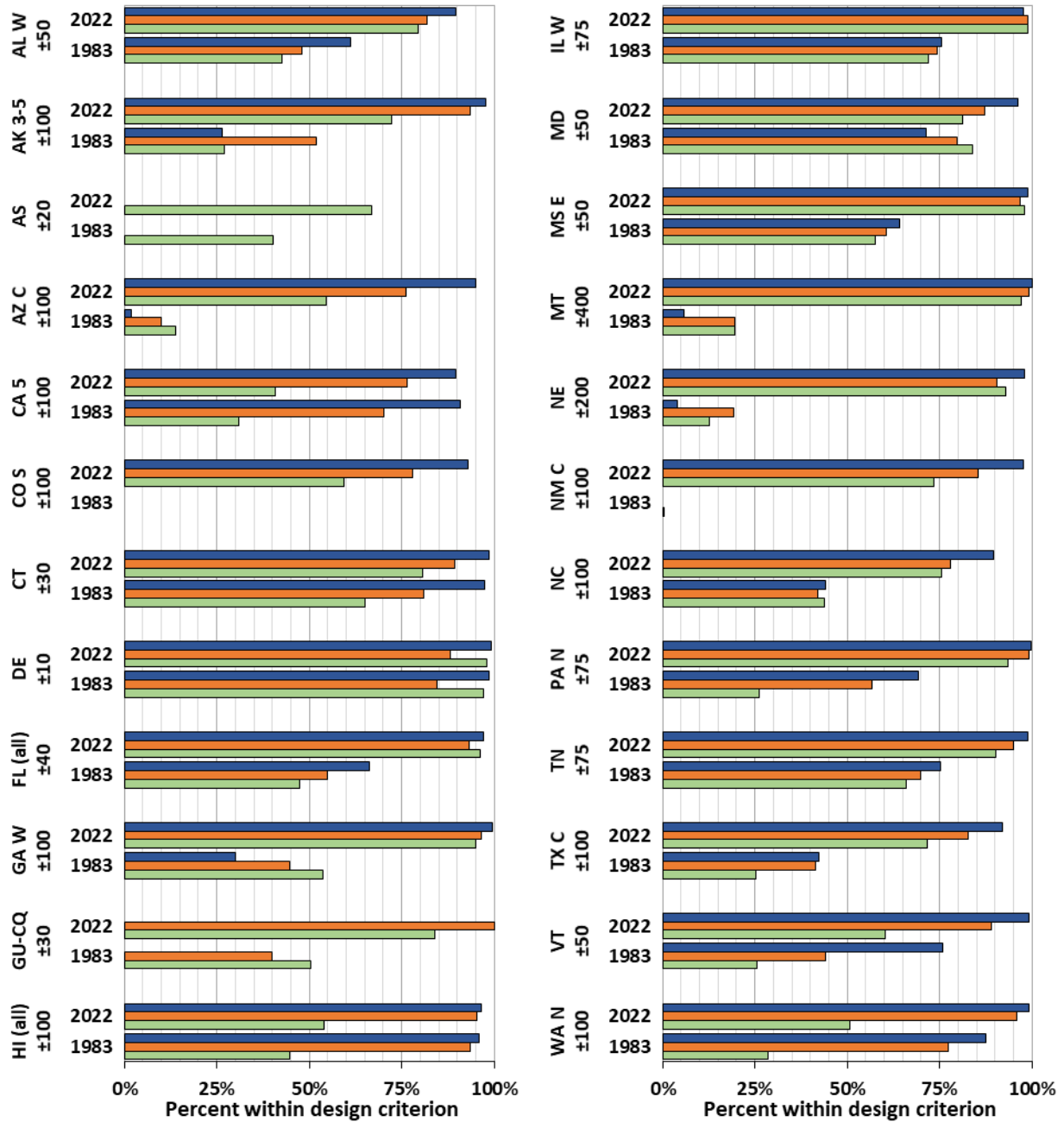
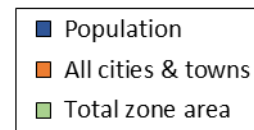


Figure 3.14. Percent of population, all cities and towns, and total zone area within design criterion for 28 SPCS zones. The design criterion is given below the abbreviation for each zone. Labels “2022” and “1983” denote SPC2022 and SPCS 83, respectively.



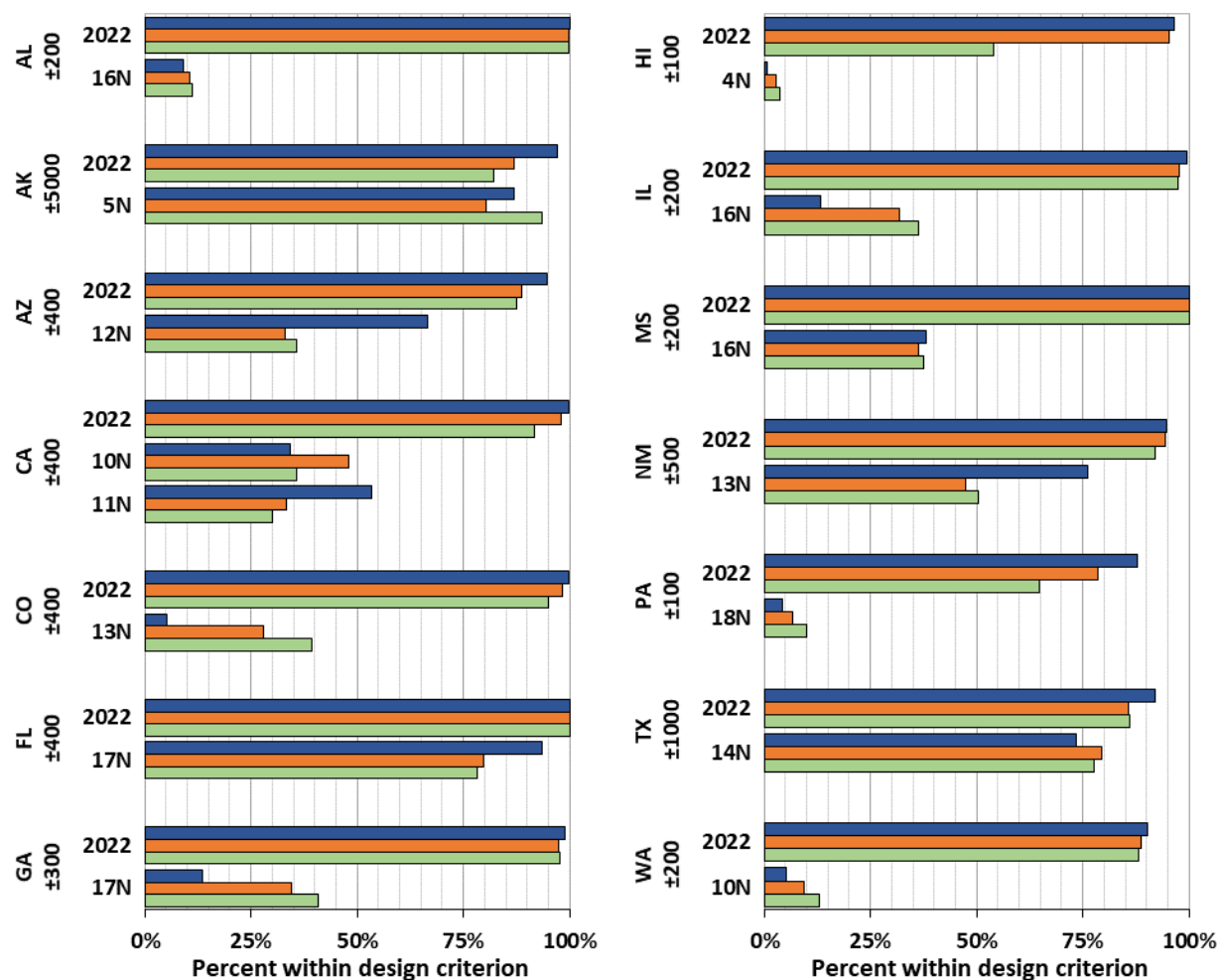
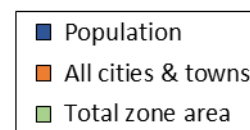


Figure 3.15. Percent of population, all cities and towns, and total zone area within design criterion for 14 SPCS2022 and UTM statewide zones. The design criterion is given below the abbreviation for each state. Labels “2022” denote SPCS2022, and labels *xxN* denote the UTM zone.



The changes of percent within the design criterion for statewide zones in Figure 3.15 is similar to Figure 3.14. The SPCS2022 OM zone for CA is compared to two UTM zones, because that state is nearly evenly split by the 10N and 11N UTM zones (and both are frequently used for statewide geospatial work in California). The difference in AK is somewhat surprising, because a greater percentage of area is within the design criterion of ± 5000 ppm for UTM than the

SPCS2022 design (although the other two percentages are higher for SPCS2022). Regardless of performance, using a TM for the entire state of Alaska is not recommended. TM zones for areas extending more than 10° from the central meridian should be avoided (the AK one extends 25°), because error increases rapidly for many TM algorithms for such wide zones, although more accurate methods are available (see Karney, 2011; NGA, 2014). All other statewide SPCS2022 zones have (often substantially) greater percentages within the distortion design criterion.

Another indicator of performance is comparison of mean distortion (both overall and weighted by population), as well as overall minimum and maximum distortion zone. Such a comparison is shown in Figure 3.16 for SPCS2022 default and corresponding SPCS 83 zones in 25 states. A plot of this type was not prepared for statewide zones, because of the very large range for some zones (especially AK and TX). But from the Table 3.3 and Figure 3.15 it is clear that these zones exhibit similar behavior.

In all cases, Figure 3.16 shows that both the overall mean and weighted mean are closer to zero for SPCS2022 versions of the zones (especially the weighted mean). All SPCS2022 zones also have better balance between positive and negative distortion. Indeed, the SPCS 83 zones AS, CO S, NE, and NM C are entirely negative. In addition, the AK and (especially) MT zones have extremely large ranges, although both show means significantly closer to zero for SPCS2022.

It is also visually apparent that some zones have a smaller range for SPCS2022 than SPCS 83, for example CT, FL, GU-CQ, MS, but this is difficult to assess visually, especially for zones with large distortion ranges. Change in range was small overall (see Table 3.3), but there is variability, and its decrease is greater for the statewide zones.

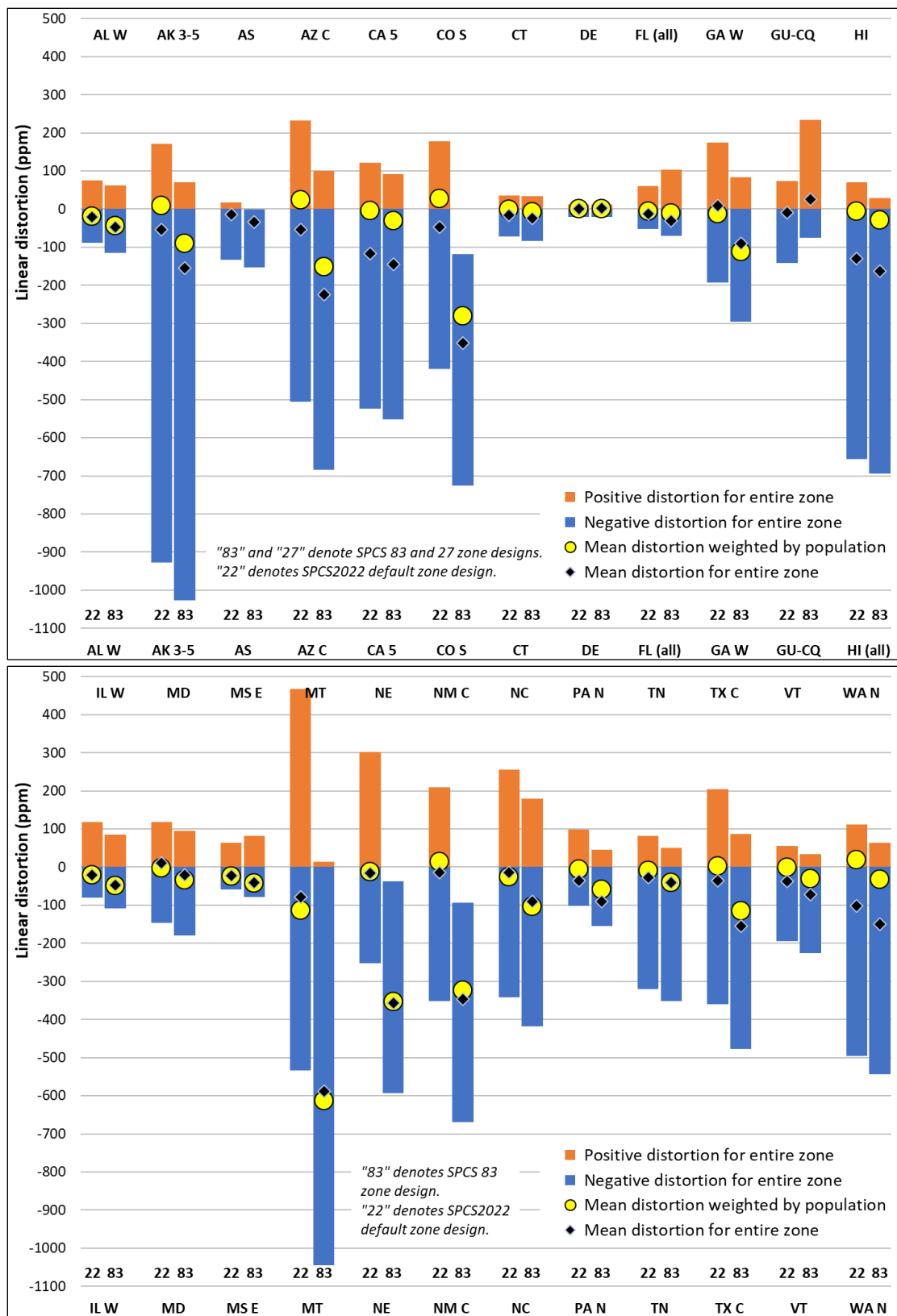


Figure 3.16. Linear distortion range, weighted mean, and overall mean for selected SPCS zones.

For statistics at the individual state level, detailed results are given in Appendix D in Table D.1 for default zones and Table D.2 for statewide zones. These tables also give the defining parameters for each zone (SPCS2022, SPCS 83, and UTM), along with the same distortion metrics as Table 3.3. Note in Appendix D that several SPCS2022 zones use the OM, in addition to the Hawaii statewide zone. This consist of two default Florida zones (on its peninsula) and a statewide zone for Florida and for California. The minimum bounding geometry technique by rectangle width was especially useful for designing these statewide zones, because of the irregular shape of their state boundaries. For SPCS 83 and 27, the OM was only used for a single zone (the Alaska panhandle). Thus, making use of the OM for other zones represents a tremendous expansion of its role, which is timely, since the OM is now widely available in geospatial software packages.

Linear distortion maps for all SPCS2022, SPCS 83, and UTM zones given in this chapter and Appendix D (plus others) are available for download from NGS via anonymous FTP at <ftp://www.ngs.noaa.gov/pub/SPCS/DistortionMaps/>.

3.7 SUMMARY AND CONCLUSIONS

In this chapter, a new method was presented for designing zones of the State Plane Coordinate System of 2022 (SPCS2022). SPCS2022 will be a system of conformal map projections that replaces existing SPCS 83 as part of the transition to from the North American Datum of 1983 (NAD 83) to the 2022 Terrestrial Reference Frames (TRFs). The National Geodetic Survey (NGS) will design default SPCS2022 zones of the same extent as SPCS 83 zones, as well as statewide SPCS2022 zones for those states that have more than one default zone. Although intended for SPCS2022, the design method is suitable for other areas, including those outside the U.S.

The design approach minimizes linear distortion at the topographic surface, rather than by the traditional method of considering only scale error at the ellipsoid surface. In addition, population distribution is taken into account in the design process, based on the assumption that greater use of a national projected coordinate system will occur in populated areas. An important aspect of this approach is that it makes use of current versions of the Transverse Mercator (TM), Lambert Conformal Conic (LCC), and Oblique Mercator (OM) projections. The intent is that the systems designed for SPCS2022 could be immediately put to use with existing projection algorithms. A detail worth noting is that SPCS2022 designs are based on the 1-parallel LCC and the local (center) OM with a specified local skew azimuth. Fortunately, both of these versions are commonly used and are mathematically identical to alternately defined versions.

A challenge with this design approach is that minimizing linear distortion at the topographic surface usually results in different parameters than reducing distortion with respect to population distribution. These apparently conflicting objectives are handled by analysis of distortion behavior with respect to a variety of metrics. Chief among these is establishing a distortion design criterion based largely in the width of the zone perpendicular to the projection axis. The design objective is that 90% of population, 75% of cities and town locations (irrespective of population), and 50% of the zone area fall within the design criterion. Additional primary objectives are that the distortion range be minimized for the entire zone and that the mean distortion weighted by population also be minimized. These primary objectives are augmented by secondary objectives to reduce the distortion range and mean for cities, and to balance positive distortion on both sides of the projection axis. A rules-based approach can be used to apply these design principles, but when selecting final design parameters a more nuanced and global view should be taken. This includes preparing and inspecting linear distortion maps of the

entire zone, and selecting parameters that are as simple and “clean” as possible, if doing so does not adversely impact performance (e.g., minimum number of digits for scale, projection axis location with arc-minutes evenly divisible by 3).

The design approach was applied to 28 default SPCS2022 zones in 25 U.S. states and territories. One of these was also a statewide design, and an additional 13 statewide SPCS2022 zones were designed for states that have more than one default zone. The default SPCS2022 zones were compared to their SPCS 83 counterparts, and the statewide zones were compared to their nearest UTM zone. In all cases the SPCS2022 zones reduced mean distortion (both overall and weighted by population) by a median of 59% and 83%, respectively, for default zones and 80% and 90% for statewide zones. Percentages within the design criterion increased by a median 45% for population, 70% for city location, and 75% for overall area for default zones, and 625% for population, 195% for city location, and 167% for overall area for statewide zones. Only for a few occasional metrics was the SPCS2022 performance worse and then only by a very small amount.

The process described here for designing SPCS2022 default and statewide zones makes it possible to design zones relatively easily. However, the efficiency can be improved in a number of ways, for example by automatically determining initial parameters and performing design iterations based on rule algorithms, as well as by automatically extracting evaluation statistics from datasets as they are created. Doing so would expedite the task of performing final design evaluations and revisions.

Another possible improvement is using a rasterized version of population distribution created directly from U.S. Census blocks (rather than points with populations representing cities and

towns). This would likely reduce the sudden population percentage “fall-offs” with variation in projection axis scale, which is likely due, at least in part, to point-discretized population.

Other possible improvements include use of more accurate DEMs and accounting for the systematic difference in 2022 TRF ellipsoid heights from NAD 83. This difference varies with location, with a maximum of ± 2.2 m anywhere on Earth (NGS, 2018c). This has a small (± 0.3 ppm) but systematic effect on distortion. Similarly, DEMs with (approximate) 5- and 10-m RMSE were used for Alaska and Pacific islands, respectively (see Appendix C). More refined designs may be possible with more accurate height data.

Although the design method proposed here could possibly benefit from refinement (and certainly from improvements in efficiency), this study has demonstrated its effectiveness. It has been shown that this approach will provide improved (lower) distortion for SPCS2022 than SPCS 83 in virtually all cases. More importantly, the SPCS2022 design process allows for fine-tuning zone parameters to achieve the desired performance, something not possible when topography and population are ignored. In addition, by stating the distortion design criterion for a zone, the system user has a more accurate representation of performance than the traditional method of providing scale error limits with respect to the ellipsoid. As such, this design approach is a more flexible way of creating projected coordinate systems that not only have lower distortion, but are also presented in a way that more truly represents their performance.

3.8 REFERENCES

Armstrong, M.L., Thomas, J., Bays, K., and Dennis, M.L., 2017. *Oregon Coordinate Reference System Handbook and Map Set*, version 3.01, Oregon Department of Transportation, Geometronics Unit, Salem, Oregon, ftp://ftp.odot.state.or.us/ORGN/Documents/ocrs_handbook_user_guide.pdf (Dec 26, 2017)

- Badger, M.G. (lead author), 2016. *Indiana Geospatial Coordinate System Handbook and User Guide*, version 1.05, Indiana Department of Transportation and Land & Aerial Survey Office, Indianapolis, Indiana
<http://www.in.gov/indot/files/InGCS_HandbookUserGuide_20160901.pdf> (Dec 26, 2017)
- Bunch, B. 2018. Personal communication, Kentucky Infrastructure Authority.
- Burkholder, E.F., 1980. “The Michigan Scale Factor”, technical paper presented at 40th Annual Meeting of the American Congress on Surveying and Mapping, St. Louis, Missouri, March 1980. <<http://www.globalcogo.com/MichGSF80.pdf>> (Dec 26, 2017)
- C&GS (Coast & Geodetic Survey), 1979 (revised; original 1965). “Plane Coordinate Projection Tables: Michigan (Lambert)”, *Publication 65-3*, U.S. Department of Commerce, Coast and Geodetic Survey.
<https://www.ngs.noaa.gov/library/pdfs/Special_Publication_No_65_3.pdf> (Jan 19, 2018)
- Carlson, E., 2018. Personal communication, NGS Pacific Region Geodetic Advisor.
- Dennis, M.L., 2016. “Ground Truth: Low Distortion Map Projections for Engineering, Surveying, and GIS”, Proceedings of the Pipelines 2016 Conference, Utility Engineering and Surveying Institute of the American Society of Civil Engineers, July 17–20, 2016 Kansas City, Missouri, U.S.A.
- Dennis, M.L., 2017. *The Kansas Regional Coordinate System: A Statewide Multiple-Zone Low-Distortion Projection Coordinate System for the State of Kansas*, Kansas Department of Transportation. <http://data.kansasgis.org/catalog/other/KS_LDP/KRCS_report_2017-11-01.pdf> (Dec 30, 2017)
- Dennis, M.L., 2018. “The State Plane Coordinate System: History, Policy, and Future Directions”, *NOAA Special Publication NOS NGS 13*, National Oceanic and Atmospheric Administration, National Geodetic Survey, Silver Spring, Maryland.
<https://geodesy.noaa.gov/library/pdfs/NOAA_SP_NOS_NGS_0013_v01_2018-03-06.pdf>
- Esri, 2018. “Minimum Bounding Geometry” tool, Esri, Redlands, CA.
<<http://pro.arcgis.com/en/pro-app/tool-reference/data-management/minimum-bounding-geometry.htm>> (Nov 12, 2018)
- Gesch, D., G., Oimoen, M., Greenlee, S., Nelson, C., Steuck, M., and Tyler, D., 2002. “The National Elevation Dataset”, *Photo Eng & Rem Sens*, ASPRS, 68 (1),
<https://www.researchgate.net/publication/273062566_The_National_Elevation_Dataset> (Nov 12, 2018).
- Gesch, D., Oimoen, M., and Evans, G., 2014. “Accuracy Assessment of the U.S. Geological Survey National Elevation Dataset, and Comparison with Other Large-Area Elevation Datasets—SRTM and ASTER”, *U.S. Geological Survey Open File Report 2014-1008*, Washington, D.C. <<https://pubs.usgs.gov/of/2014/1008/pdf/ofr2014-1008.pdf>> (Nov 10, 2108)

- Karney, C., 2011. “Transverse Mercator with an accuracy of a few nanometers,” *J. Geod.*, Vol. 85, No.8, Pp 475-485 <<https://arxiv.org/pdf/1002.1417.pdf>> (Nov 12, 2018)
- Kentucky Geography Network, 2002. *Kentucky State Plane Coordinate System*, Division of Geographic Information, Frankfort, Kentucky <ftp://kygeonet.ky.gov/kygeodata/standards/Ky_StatePlane.pdf> (Dec 15, 2017)
- Kentucky Legislature, 2001. “The Kentucky Single Zone Coordinate System of 1983”, *Kentucky Administrative Regulation 10 KAR 5:010*, Frankfort, Kentucky <<http://www.lrc.ky.gov/kar/010/005/010.htm>> (Dec 15, 2017)
- Lusch, D.P., 2005. “A Primer on Coordinate Systems Commonly Used in Michigan,” Dept. Geography, Remote Sensing & GIS Research and Outreach Services Group, Michigan State University. <http://www.rsgis.msu.edu/pdf/mi_coordinate_systems.pdf> (Dec 26, 2017)
- Moritz, H., 2000, “Geodetic Reference System 1980,” *J. Geod.*, 74(1), pp. 128– 162, doi:10.1007/S001900050278, <<ftp://athena.fsv.cvut.cz/ZFG/grs80-Moritz.pdf>> (Nov 12, 2018)
- Mukul, M., Srivastava, V., and Mukul, M., 2015. “Analysis of the accuracy of Shuttle Radar Topography Mission (SRTM) height models using International Global Navigation Satellite System Service (IGS) Network”, *J. Earth Syst. Sci.*, 124, No. 6, pp. 1343–1357. <<https://www.ias.ac.in/article/fulltext/jess/124/06/1343-1357>> (Nov 10, 2018)
- NGA (National Geospatial-Intelligence Agency), 2014. “The Universal Grids and the Transverse Mercator and Polar Stereographic Map Projections,” version 2.0.0, *NGA.SIG.0012_2.0.0_UTMUPS*, Office of Geomatics, 86 pp. <http://earth-info.nga.mil/GandG/publications/NGA_SIG_0012_2_0_0_UTMUPS/NGA.SIG.0012_2.0.0_UTMUPS.pdf> (Nov 12, 2018)
- NGS (National Geodetic Survey), 2016. *GEOID12B*, <www.ngs.noaa.gov/GEOID/GEOID12B/> (July 20, 2018).
- NGS (National Geodetic Survey), 2017a. “Blueprint for 2022, Part 1: Geometric Coordinates”, *NOAA Technical Report NOS NGS 62*, National Oceanic and Atmospheric Administration, National Geodetic Survey, Silver Spring, Maryland. <https://geodesy.noaa.gov/library/pdfs/NOAA_TR_NOS_NGS_0062.pdf> (Dec 26, 2017)
- NGS (National Geodetic Survey), 2017b. “Blueprint for 2022, Part 2: Geopotential Coordinates”, *NOAA Technical Report NOS NGS 64*, National Oceanic and Atmospheric Administration, National Geodetic Survey, Silver Spring, Maryland. <https://geodesy.noaa.gov/library/pdfs/NOAA_TR_NOS_NGS_0064.pdf> (Nov 12, 2018)
- NGS (National Geodetic Survey), 2018a. “State Plane Coordinate System of 2022 Policy,” (DRAFT), National Oceanic and Atmospheric Administration, National Geodetic Survey, Silver Spring, Maryland <https://geodesy.noaa.gov/INFO/Policy/files/DRAFT_SPCS2022_Policy.pdf> (Nov 12, 2018)

- NGS (National Geodetic Survey), 2018b. “Procedures for Design and Modification of the State Plane Coordinate System of 2022,” (DRAFT), National Oceanic and Atmospheric Administration, National Geodetic Survey, Silver Spring, Maryland <https://geodesy.noaa.gov/INFO/Policy/files/DRAFT_SPCS2022_Procedures.pdf> (Nov 12, 2018)
- NGS (National Geodetic Survey), 2018c. *New Datums: Replacing NAVD 88 and NAD 83*, National Oceanic and Atmospheric Administration, National Geodetic Survey, Silver Spring, Maryland <<https://geodesy.noaa.gov/datums/newdatums/index.shtml>> (Nov 12, 2018)
- Pavlis, N., Holmes, S., Kenyon, S. and Factor, J., 2012. “The development and evaluation of the Earth Gravitational Model 2008 (EGM2008)”, *J. Geophys. Res.*, 117, B04406, American Geophysical Union. <<https://doi.org/10.1029/2011JB008916>> (Nov 10, 2018)
- Snyder, J.P. and Steward, H. (eds.), 1988. “Bibliography of Map Projections”, *U.S. Geological Survey Bulletin 1856*, Washington, D.C. <<https://pubs.usgs.gov/bul/1856/report.pdf>> (Nov 12, 2018)
- Snyder, J.P., 1987. “Map Projections — A Working Manual”, *U.S. Geological Survey Professional Paper 1395*, Washington, D.C. <pubs.er.usgs.gov/djvu/PP/PP_1395.pdf> (Nov 12, 2018)
- Stem, J.E., 1990. “State Plane Coordinate System of 1983”, *NOAA Manual NOS NGS 5*, National Geodetic Survey, <https://geodesy.noaa.gov/library/pdfs/NOAA_Manual_NOS_NGS_0005.pdf> (July 20, 2018).
- WI SCO (Wisconsin State Cartographer’s Office), 2012. *Wisconsin Coordinate Reference Systems*, 2nd Edition, State Cartographer’s Office, Madison, Wisconsin. <<https://www.sco.wisc.edu/pubs/wisconsin-coordinate-reference-systems-second-edition/>> (Dec 26, 2017)

Manuscript #3

INTEGRATION OF GNSS AND DIFFERENTIAL LEVELING
OBSERVATIONS IN A 3D GEODETIC MODEL

Michael L. Dennis, Christopher E. Parrish, and Daniel T. Gillins

Target journal: *Journal of Surveying Engineering*, American Society of Civil Engineers

4 INTEGRATION OF GNSS AND DIFFERENTIAL LEVELING OBSERVATIONS IN A 3D GEODETIC MODEL

4.1 ABSTRACT

The National Geodetic Survey (NGS) will soon adopt the North American-Pacific Geopotential Datum of 2022 (NAPGD2022), with orthometric heights determined primarily using the Global Navigation Satellite System (GNSS) and a gravimetric geoid model. To define the role of differential leveling in NAPGD2022, a method was developed that integrates GNSS and leveling observations into a spatially and stochastically consistent 3D geodetic model for performing simultaneous least squares adjustments. Leveled geopotential differences were transformed to the same geometry as the GNSS vectors, in part by using a modified version of the NGS experimental gravimetric geoid model xGEOID16B. To determine weights for the transformed leveling observations, five geoid slope error models were developed and evaluated, and one was selected for performing the combined GNSS and leveling adjustments. These adjustments yielded ellipsoid heights, which were converted to orthometric heights using (modified) xGEOID16B. Overall adjustment statistics were essentially unchanged after combining the networks, indicating the observations were correctly weighted. Results showed that the high redundancy of GNSS and its accuracy over long distances compensated for the low redundancy of leveling and its rapid error growth with distance. Conversely, the high relative local accuracy of leveling offset the lower vertical accuracy of GNSS over short distances. Precision of the mean GNSS up residuals more than doubled, from 0.6 to 0.2 cm. Median leveling network accuracies decreased from 2.3 to 2.0 cm, and median GNSS local accuracies decreased from 2.7 to 1.1 cm. The combined network also helped identify problems that were otherwise largely undetectable. Although recent GNSS was combined with much older leveling, the two observation types showed remarkable consistency.

4.2 INTRODUCTION AND OBJECTIVES

A movement is underway worldwide wherein Global Navigation Satellite Systems (GNSS) combined with a gravimetric geoid model will be the primary means of determining orthometric heights. In keeping with this trend, the U.S. National Geodetic Survey (NGS) will soon adopt four Terrestrial Reference Frames (TRFs) and a geopotential datum, the North American-Pacific Geopotential Datum of 2022 (NAPGD2022). The four 2022 TRFs will replace the three North American Datum of 1983 (NAD 83) frames. NAPDG2022 will include a gravimetric geoid (GEOID2022) and will replace all current vertical datums of the U.S. National Spatial Reference System (NSRS), including the North American Vertical Datum of 1988 (NAVD 88).

The main advantage of this change is speed and simplicity. Geodetic latitude (φ), longitude (λ), and ellipsoid height (h) can be obtained quickly and easily with GNSS. The orthometric height (H) can then be computed instantaneously with the simple and well-known equation

$$H = h - N \quad (4.1)$$

where N is the geoid height (also called “separation” or “undulation”) obtained directly from a geoid model based on horizontal location. Technically, Eq. 4.1 is approximate, due to deflection of the vertical and curvature of the plumbline along which H is reckoned. However, those effects create less than 1 mm of error anywhere in Earth (Jekeli, 2000)—and much less in most places—so Eq. 4.1 can be considered exact for practical applications.

In contrast, the traditional method for obtaining accurate *differences* in orthometric height, ΔH , is differential leveling. But leveling is a labor-intensive, time-consuming, and therefore expensive process, and it is vulnerable to blunders and accumulation of systematic errors over long distances. In addition, since leveling gives only height differences, it is necessary to

connect to one or more known heights to give an orthometric height with respect to an existing system, such as a national vertical datum. And finally, leveling by itself does not yield change in orthometric height, ΔH . To obtain ΔH requires reductions based on knowledge or assumptions about gravity and how it varies with location and topography.

Despite the liabilities of leveling, it has an advantage over GNSS in one important respect: it can give far more accurate ΔH over short distances. Geodetic leveling can achieve ΔH accuracies of 2 mm (or better) over a distance of 5 km (Zilkoski, 1991). In contrast, typical GNSS applications give absolute (h) and relative (Δh) ellipsoid height accuracies of about 4-6 cm (at 95% confidence), largely independent of distance (Eckl *et al.*, 2001). With great care, multiple independent setups, and long occupation times, ellipsoid height accuracies of 2 cm can be achieved (Gillins and Eddy, 2016; Zilkoski *et al.*, 1997). But the geoid height also has error, which will propagate into the computed orthometric height error, and so the computed orthometric height from GNSS will always have greater error than the ellipsoid height.

For many practical applications, height differences are needed to greater accuracy than can be achieved by GNSS, especially over the short distances typical of engineering, surveying, and construction projects. Thus the transition to a vertical datum defined by a gravimetric geoid and accessed by GNSS leads naturally to questions about the role of leveling in such a system.

Combining GNSS and leveling has been an area of active interest and research for many years. For example, Jiang and Duquenne (1996) discuss a combined adjustment method based on the principle of dealing with short- and long-wavelength gravimetric geoid errors separately. Kotsakis and Sideris (1999) examine adjustment problems and evaluate geoid model accuracy using methods that combine GNSS, leveling, and geoid heights. Khazraei *et al.* (2016),

Fotopoulos *et al.* (2003), and Fotopoulos (2005) consider least-squares variance component estimation in the combined adjustment of ellipsoid, orthometric and geoid height data. Erol and Çelik (2005) and Kim *et al.* (2018) discuss geoid modeling as a surface fitting problem using GNSS and leveling data. Vittuari *et al.* (2016) investigate the ability to estimate deflection of the vertical using a combination of GNSS and geometric leveling, among other methods.

Although such research has made significant contributions, the existing work has largely focused on using ellipsoid, orthometric, and geoid heights directly in 1D adjustments to evaluate or calibrate geoid models, or to compute corrector surfaces. In contrast, this chapter focuses on development of a 3D geodetic model for combining the reduced GNSS and leveling observations into a single network for simultaneous least squares adjustment. Although there has been some research on this topic from an integrated geodesy perspective (e.g., Milbert, 1988), there is overall an apparent lack of recent research using such an approach. Interestingly, it is documented in various text books (e.g., Leick *et al.*, 2015; Ghilani, 2010; Hofmann-Wellenhof and Moritz, 2006) and is incorporated in several commercial software packages, such as *STAR*NET* (used in this research). However, the details of the methods are usually not revealed in commercial software, and there are rarely user options to modify the methods and key parameters, much less the algorithms. This is important, since one aim of this research is to investigate a means of utilizing GNSS observations for NAPGD2022. In such a context it is important to fully understand the details of how the combined observations, uncertainties, and constraints are handled.

This chapter examines the question of appropriately combining GNSS and leveling by presenting a method for combining their observations in a way that leverages the strengths of one to compensate for the weaknesses of the other. The objectives of this research are to:

1. *Represent the input observations in a consistent geometry so that they can be combined into a spatially-coherent network for least-squares adjustment.* The approach pursued was to transform leveling geopotential differences to the same geometry as the GNSS vectors. It further required that the GNSS vectors, leveling observations, and geoid model all be represented in the same reference frame (natively all were different).
2. *Determine appropriate uncertainties for all observation types so that they can be correctly weighted.* This included accounting for overly-optimistic GNSS error estimates and assessing those of leveling based on order and class. The most challenging was to determine an error model for geoid slope (height differences) over short distances. This was essential, since the geoid model was used to transform the leveling, and thus its relative errors became part of the transformed leveling observation error budget.
3. *Perform minimally and fully constrained adjustments of the combined observations.* The goal was to determine the most likely unique heights and their formally propagated uncertainties. This included comparison to results from the separate networks to assess changes in computed heights and accuracies, both network (with respect to the reference frame of the constraints) and local (relative between stations connected by observations).

The research was performed using GNSS and leveling data from Corvallis and the surrounding region in western Oregon. Recently collected GNSS data were used for this project, whereas the leveling data consisted of historical observations obtained from NGS.

4.3 STUDY AREA AND DATASETS

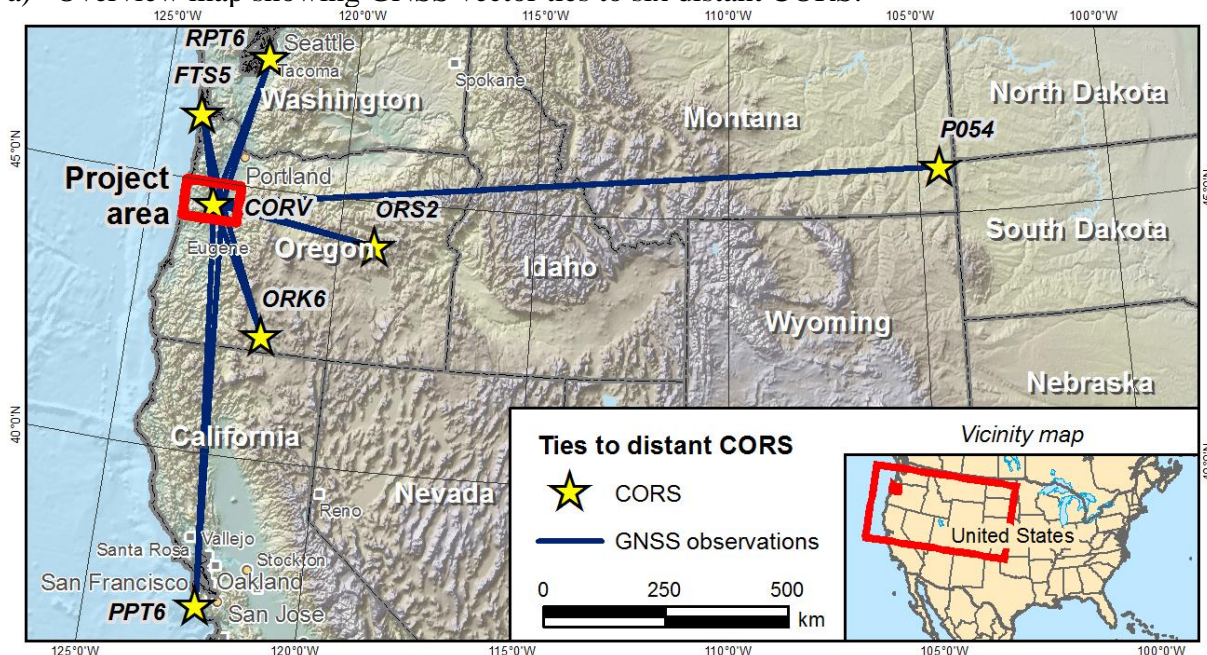
The study area is the region in and around Corvallis, in the southern Willamette Valley of western Oregon. An overview map is shown in Figure 4.1, with details shown in Figure 4.2 for the cities of Corvallis and Albany, and on the campus of Oregon State University (OSU). Three

data types were used for this study: GNSS observations, leveling observations, and a gravimetric geoid model (each described in the following sections). The GNSS and leveling observations are shown as overlapping networks, where leveling consists of short connections, typically less than a few km. GNSS includes ties to distant Continuously Operating Reference Stations (CORS).

4.3.1 GNSS Data

The GNSS data were obtained by OSU faculty and students in fieldwork performed in support of this and other research projects. Data collection was done in three separate campaigns, in July-August 2014, October-November 2014, and June 2015. A total of 157 independent occupations were performed, ranging in duration from 2.1 to 10.0 hours and averaged 8.1 hours. The combined network of GNSS observations from the three campaigns consisted of 40 stations connected by 359 enabled vectors (5 were rejected during the adjustment analyses). Six of the stations are distant CORS, located between 190 and 1480 km from the OSU campus (nominally the project center). These distant CORS were included to improve GNSS processing results by decorrelating tropospheric errors, per NGS guidelines (Armstrong *et al.* 2015); the rationale for selecting these six CORS is described by Gillins and Eddy (2015 and 2016). Of the remaining 34 stations, one is the CORS CORV, and one is the permanent ORGN base LCS1. The other 32 stations are NGS passive control marks distributed throughout the local project area, all within less than 40 km of their processing hubs (CORV or LCS1). Other details of the data, processing, adjustments, and results are given by Dennis *et al.* (2018).

a) Overview map showing GNSS vector ties to six distant CORS.



b) Project area map of GNSS and leveling network in Willamette Valley region of Oregon.

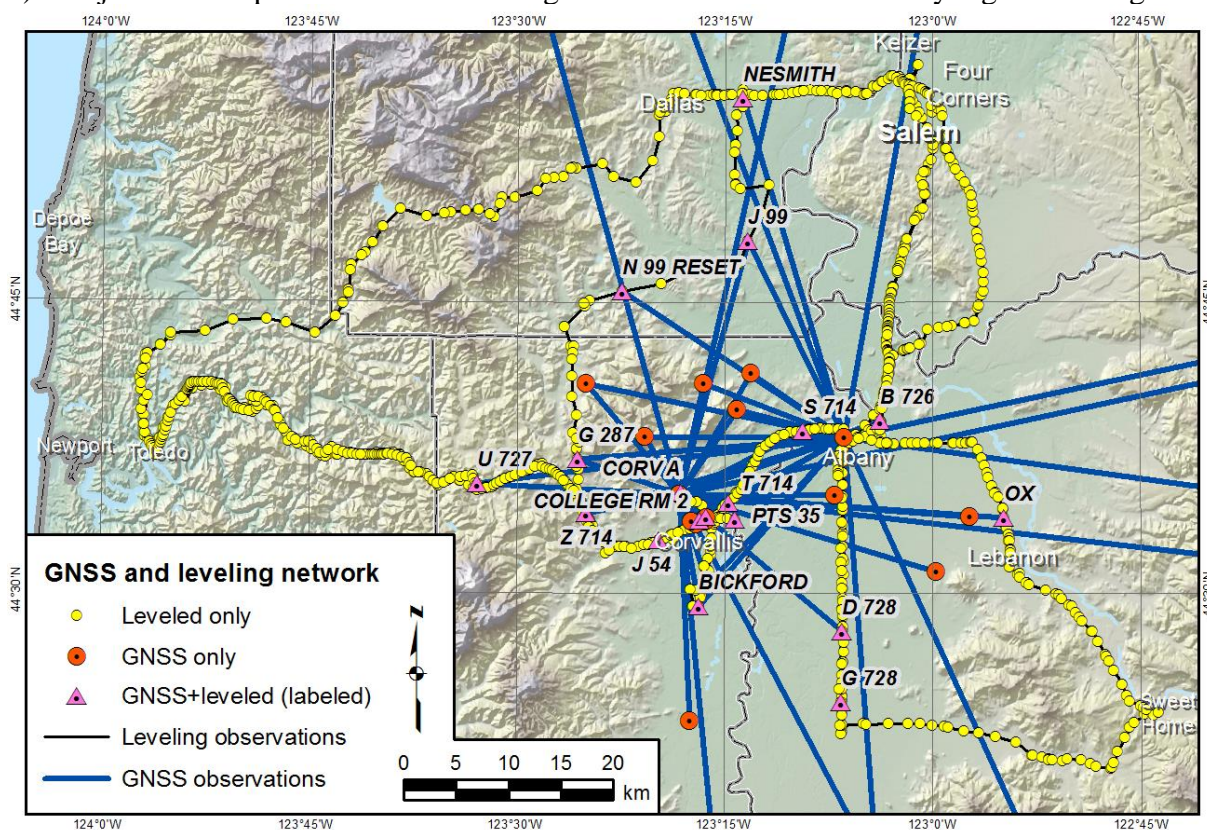
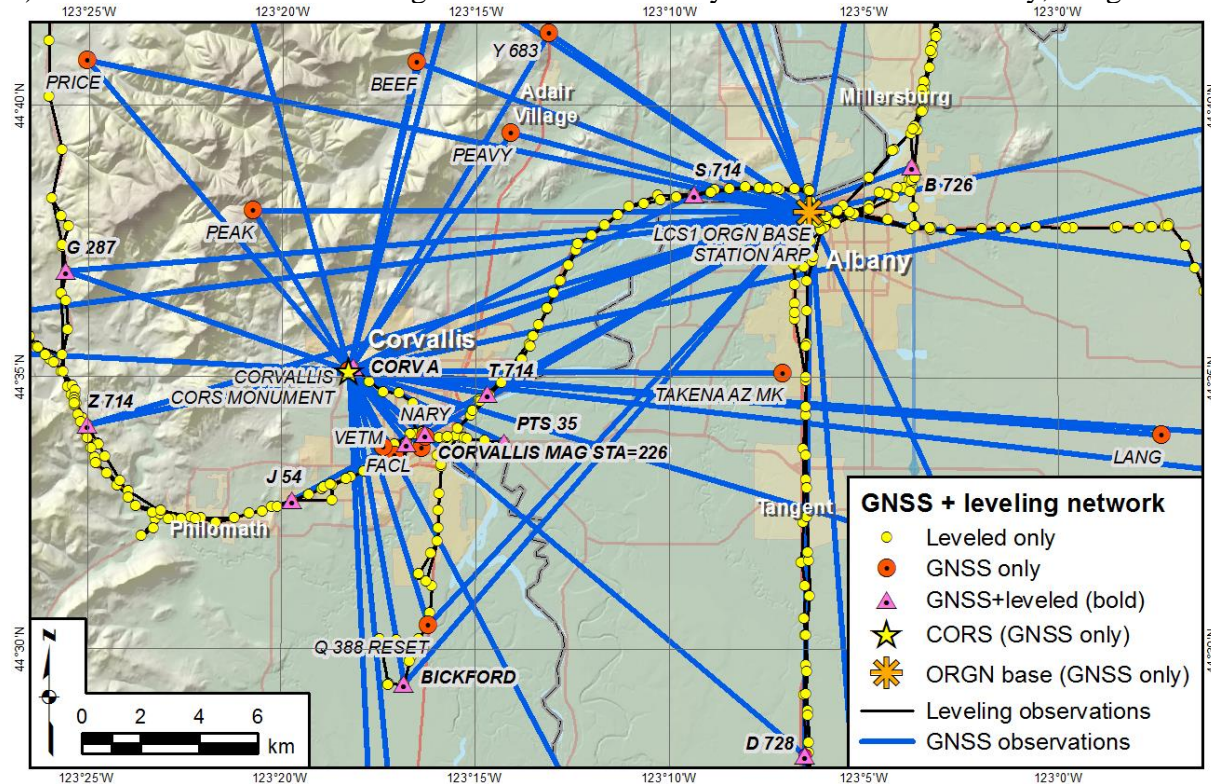


Figure 4.1. a) Overview map showing GNSS vector ties to six distant CORS, and b) project area map of GNSS and leveling networks in Willamette Valley region of Oregon.

a) Detail of GNSS and leveling network in the vicinity of Corvallis and Albany, Oregon.



b) Detail of GNSS and leveling network in the vicinity of Oregon State University (OSU).

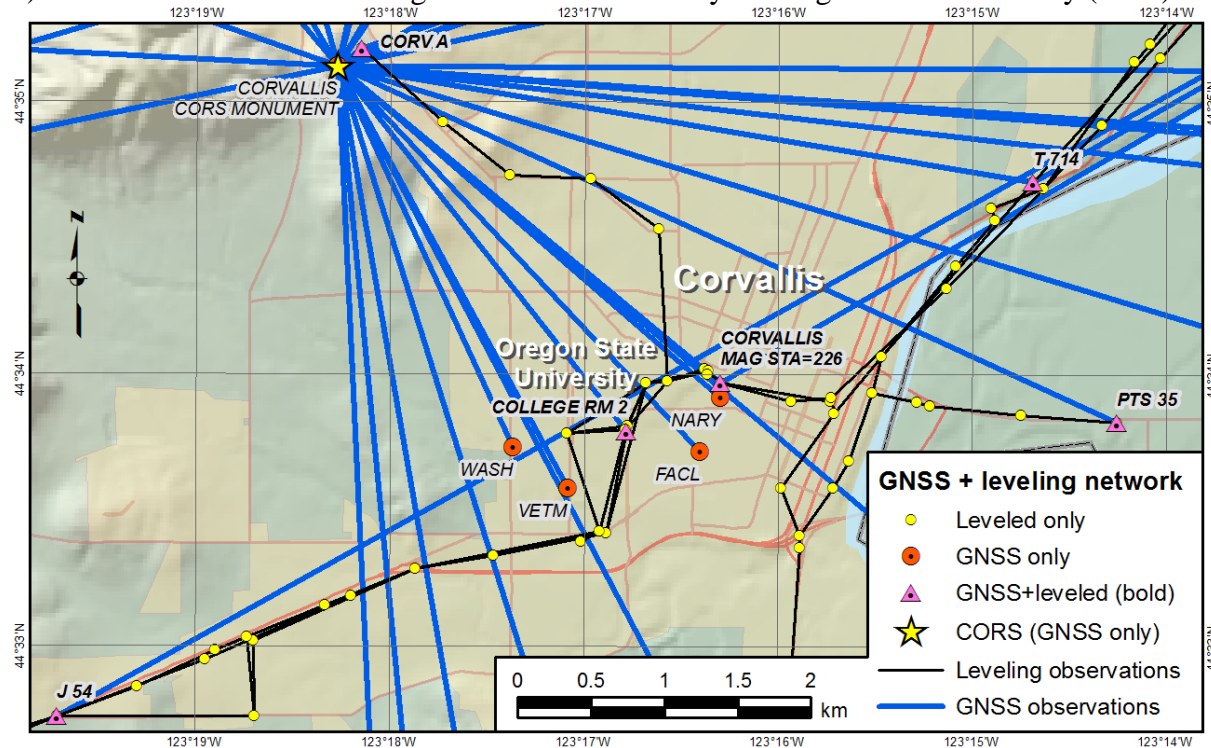


Figure 4.2. GNSS and leveling networks in vicinity of a) Corvallis and Albany and b) OSU.

GNSS data were post-processed using the NGS online *OPUS-Projects (OP)* application (Mader, *et al.*, 2012; Weston, *et al.*, 2007). *OP* uses the NGS program *PAGES* (Blackwell and Hilla, 2000) to perform GPS-only baselines processing, and the results of each processing session are converted to the NGS GNSS Data Transfer Format (“G-file”) vector files. These are fixed-format ASCII files documented in NGS (2018a), commonly known as the “Bluebook.” The GNSS observations are mark-to-mark delta Earth-Centered, Earth-Fixed (ECEF) Cartesian ΔX , ΔY , ΔZ vector components, along with elements of the variance-covariance (v-c) matrix. The v-c matrix consists of the standard deviation of each component (square root of each element of the matrix diagonal) plus the off-diagonal covariance terms (expressed as correlation coefficients).

The processed GNSS network was adjusted using the NGS least-squares adjustment program *ADJUST* (Milbert and Kass, 1987), version 6.4.1. Processing and adjustment procedures were consistent with NGS requirements for “Height Modernization” projects, as described by Zilkoski *et al.* (1997 and 2008). Final adjustment results were loaded into the NGS Integrated Data Base (NGSIDB) in late 2018 and are available to the public. That network is used for this study.

4.3.2 Leveling Data

No new leveling observations were performed for this study; rather, historic leveling data from the NGSIDB were used. Like G-files, the leveling data are fixed-format ASCII files described in the NGS Bluebook (NGS, 2018a, Chapter 6). The NGSIDB leveling data were used to obtain reduced observations between bench marks (BMs), where “reduced” means that corrections were applied, multiple runs in a project were averaged, and the corrected mean leveled differences were converted to geopotential differences using the *NAVD 88 Surface Gravity Model* (NGS, 2016). Corrections were applied for rod scale, temperature, and collimation, as well as

astronomic, refraction, and magnetic effects, as described by Balazs and Young (1982) and Holdahl, *et al.* (1986). Each reduced observation represents the accumulated mean of corrected runs between BMs.

A leveling network for this study was constructed such that all NGSIDB leveling observations passing through the GNSS stations were obtained. Additional leveling observations were included to create closed loops throughout the project (i.e., no “open” spurs existed), and the only spurs allowed were those that ended at a GNSS station. The resulting network is presented in Figure 4.3 and Table 4.1, with the leveling observations classified by order and class, which reveals the heterogeneity of the leveling observations. It consists of 1039 stations connected by 1279 reduced observations with a total leveled distance of 1279 km. Of the 1039 leveled stations, 18 also have GNSS vector ties from the GNSS network. Most of the leveling (77.4%) was 1st order/class II, followed by 2nd order/class 0 (20.6%). Geodetic leveling order and class are defined by Bossler (1984), but that document does not include 2nd order, class 0 leveling, which was defined to create a category between 2nd order/class II and 3rd order. That was done to create an observation group for historical leveling in the NAVD 88 adjustment and was not used for observations made after 1978 (Zilkoski, 1991). The relationship between order/class and observational error is explored in Section 4.5.2 (see Table 4.2).

4.3.3 Gravimetric Geoid Model

The NGS experimental gravimetric geoid model xGEOID16B (NGS, 2018b) was used, which was the latest model available at the time this research was performed. The xGEOID16B model includes all of the conterminous U.S. (CONUS), extending from 24°N to 58°N latitude, and from 60°W to 130°W longitude. It consists of geoid heights (also known as geoid separation or undulations) on a 1 arc-minute grid, with values interpolated between grid cell corners.

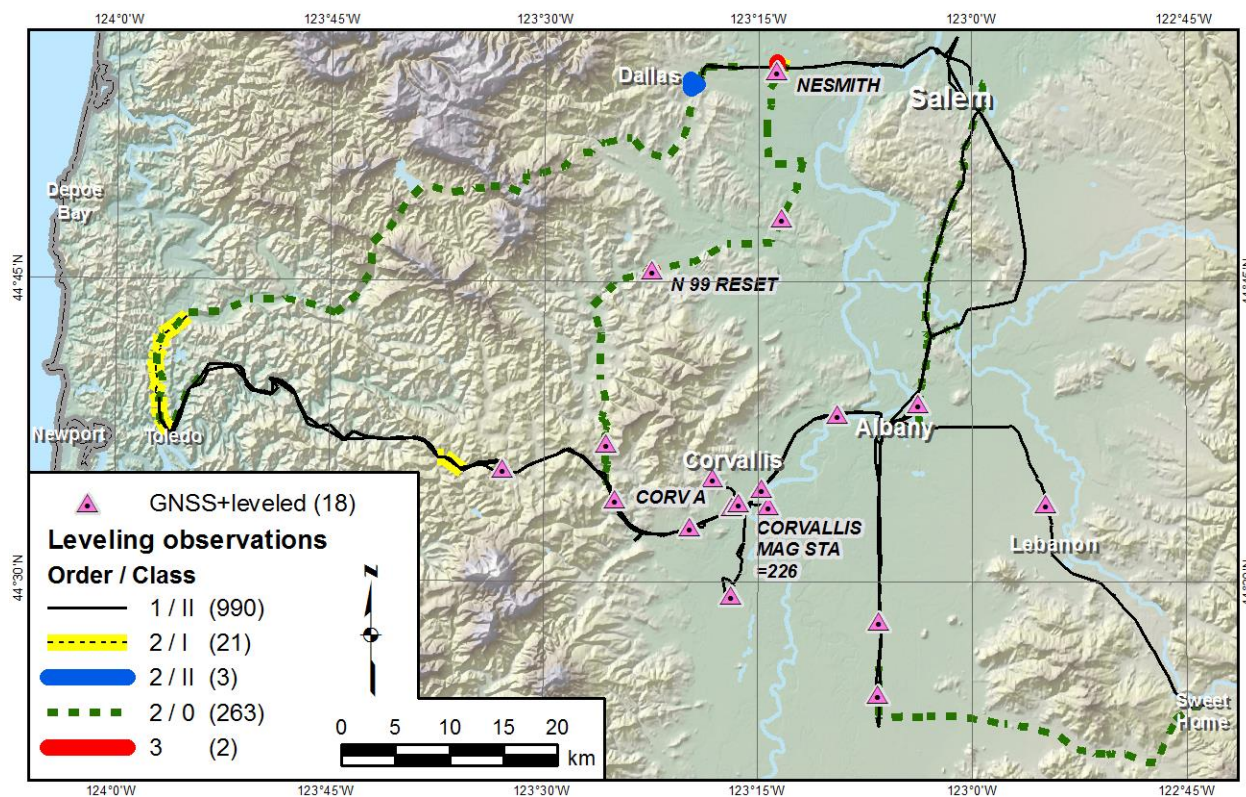


Figure 4.3. Order and class of leveling observation for network used in this study.

Table 4.1. Summary of the leveling observations in the network used for this research.

Observations <i>Total = 1279 (976 km)</i>						
<i>Statistic</i>	<i>Number of runs</i>	<i>Leveled distance (km)</i>	<i>Orthometric ht diff (m)</i>	<i>Year of observations</i>	<i>Standard dev (mm)</i>	
Min	1	0.01	-148.898	1920	0.2	
Max	6	5.34	139.059	2001	6.0	
Median	2	0.58	0.217	1941	0.9	
Mean	1.8	0.76	0.397	1946.5	1.34	
Runs between bench marks			Order and class of observations			
<i>Number of runs</i>	<i>Number of observations</i>	<i>Percent observations</i>	<i>Order / class</i>	<i>Number of observations</i>	<i>Percent observations</i>	
1	419	32.8%	1 / II	990	77.4%	
2	764	59.7%	2 / I	21	1.6%	
3	51	4.0%	2 / II	3	0.2%	
4	40	3.1%	2 / 0	263	20.6%	
5	4	0.3%	3	2	0.2%	
6	1	0.1%				
Total	1279	100.00%	Total	1279	100.00%	

Experimental gravimetric geoid models are created annually by NGS in preparation for NAPGD2022. Two versions of each experimental geoid model are created, one with suffix “A” that does not include any data from the GRAV-D project (NGS, 2007), and one that includes the aerial gravity data, with suffix “B.” Although the xGEOID16B model included GRAV-D aerial gravity data, Corvallis is located just outside the area where aerial gravity data were used.

NGS also produces “hybrid” geoid models, such as GEOID12B (NGS, 2015). Model xGEOID16B was used instead because at the time of this study it was the best estimate of the gravimetric geoid that will be used for NAPGD2022. This choice of geoid model is therefore consistent with a study on combining GNSS and leveling for NAPGD2022. In addition, a hybrid geoid model is problematic because leveling is used to modify the hybrid geoid slope, making it difficult to separate leveling errors from geoid slope errors.

4.3.4 Mixing Old and New Observations

As shown in Table 4.1, there is a great range in the age of the leveling observations, from 1920 to 2001. The distribution of leveling by age is shown in Figure 4.4. None of the leveling observations overlap at all with the GNSS observations performed from 2014-2015. Mixing of old and new observations in combined adjustments is a potential problem, since it is possible that some of the leveled marks have moved in the time between their leveled and GNSS observations. That presents an issue whether the movement was regional or associated with individual marks. Compounding the latter problem is mark stability. Some BM settings are more stable than others, a point that will be revisited later in the analysis of combined adjustment results.

Ideally, a study such as this would make use of concurrent observations, so that mark movement would not introduce another variable, potentially complicating analysis and interpretation of

results. The main reason for using old leveling data was simply one of practicality and opportunity. Geodetic leveling over such a large area is prohibitively time-consuming and expensive. In a study such as this, which seeks to determine feasibility of an untested method, such time and expense cannot be justified. The opportunity here is that OSU had already mobilized to perform campaign-style GNSS surveys for other studies, so there was already a plan to collect current, high-quality GNSS data.

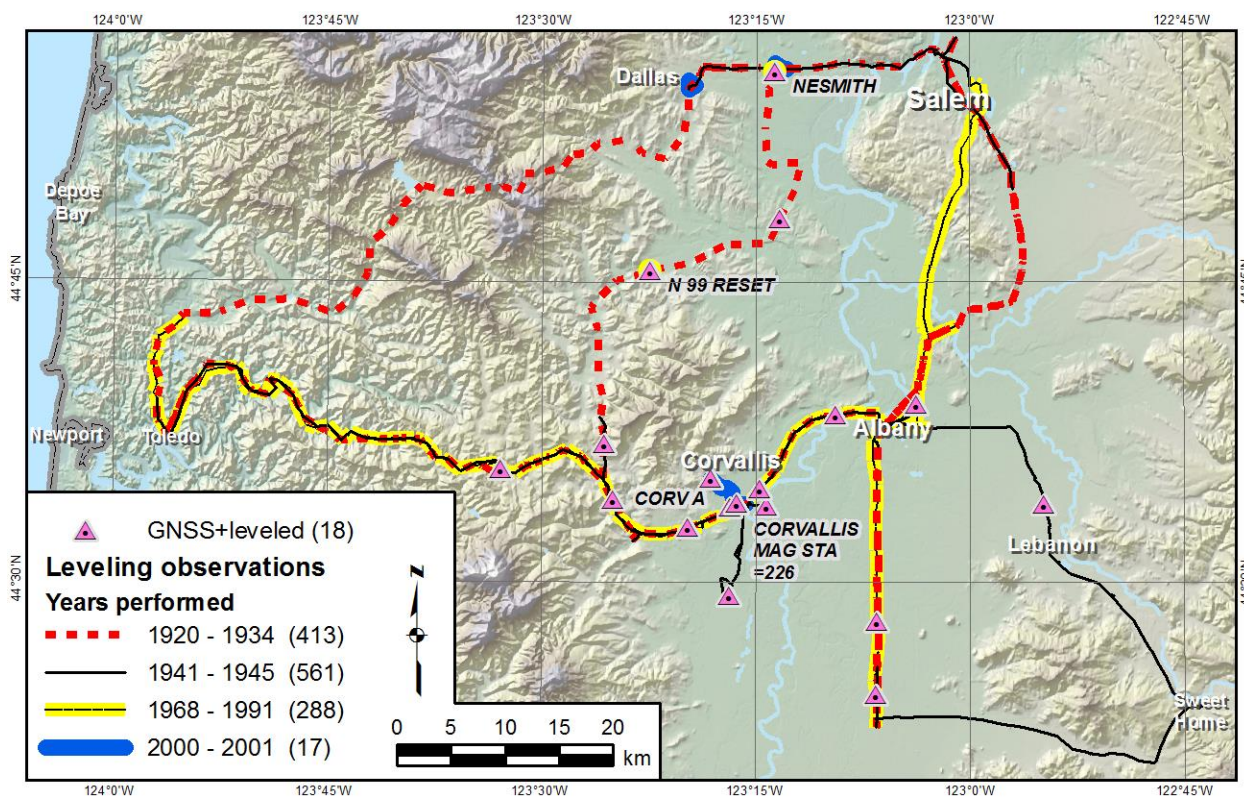


Figure 4.4. Age of leveling observations for network used in this study.

Another reason beyond resource limitations exists for combining old leveling with new GNSS: it is the reality of the situation with these data types in the U.S. The NGSIDB contains over 2 million km of leveling observations covering all of CONUS (and some other regions as well). There is an interest within NGS in making use of at least some of this historic leveling, by readjusting it in NGSIDB using GNSS positions or observations as constraints. Such an

undertaking is an effort to leverage the extremely valuable leveling data and carrying its value into the future. One purpose of this study is to determine whether that is feasible even for very old leveling observations, in a known tectonically active area.

4.4 MATHEMATICAL MODEL FOR COMBINED GNSS AND LEVELING OBSERVATIONS

The approach pursued in this study for integrating leveling and GNSS is through combined least-squares network adjustments of leveling and GNSS observations. Two things are required for such an approach to work. One is that the observations must have a consistent geometry. The second, and more difficult, is that the observations must be correctly weighted. The first of these requirements is discussed in this section. The second is discussed in Section 4.5.

One challenge is that GNSS networks are intrinsically composed of 3D observations whereas leveling networks only contain 1D observations. Moreover, the geometries of the observations are typically not the same (indeed leveling observations can be entirely non-geometric), and the estimated uncertainties of GNSS and leveling are likely inconsistent. Geoid heights provide the essential connection between GNSS- and leveling-derived heights, but the geoid heights must be in the same reference frame as the GNSS and leveling observations, and geoid height errors are not well known. To make all the datasets consistent, so that they could be correctly combined, it was necessary to transform each of them, as described below.

4.4.1 GNSS Observation Geometry and Reference System

As mentioned above, the GNSS observations consist of mark-to-mark ECEF ΔX , ΔY , ΔZ vector components, along with the v-c matrix. The coordinate system of the ECEF vector components is the same as that of the (multiple) CORS constrained during baseline processing, at the weighted mean epoch of the GNSS observations (from 2014.5 to 2015.4): the International

GNSS Service 2008 (IGS08) frame, a GNSS realization of the International Terrestrial Reference Frame of 2008 (ITRF2008); see Rebischung *et al.* (2012).

To maintain consistency with current NGS-published control coordinates on the passive marks observed in this study, the G-files from GNSS processing were transformed from IGS08 to NAD 83 (2011) epoch 2010.00 using the NGS *Horizontal Time Dependent Positioning (HTDP)* software (Pearson and Snay, 2012; Snay *et al.*, 2014). *HTDP* utilizes a 14-parameter Helmert transformation, plus crustal motion models when the input and output epochs differ (as is the case here). Because the vector rotations are extremely small, the effect on the v-c matrix is negligible, and so the v-c matrix is not changed.

4.4.2 Transformation of the Gravimetric Geoid to NAD 83 and NAVD 88

Before discussing leveling observations, it is necessary to first discuss transformation of the geoid model, because the geoid model is required to transform the leveling. Experimental model xGEOID16B is in the IGS08 frame at epoch 2005.00, and it was transformed to the NAD 83 frame at epoch 2010.00 using *HTDP*.

Because the NGS-published orthometric heights for the stations used in this study were referenced to NAVD 88, an additional transformation was needed. The reason is a bias and tilt of the NAVD 88 datum surface with respect to satellite-derived gravity geopotential and local tidal datums, which has been widely documented, e.g., Smith *et al.* (2013); Roman *et al.* (2009); Zilkoski *et al.* (1992). Therefore that bias and tilt was *added* to the NAD 83 version of xGEOID16B to make it consistent with NAVD 88. The bias and tilt trend was determined with planar linear regression using the *ArcGIS* 10.4.1 “Trend” tool (Esri, 2016). The input was the set of GNSS BMs used to create the hybrid model GEOID12B for CONUS. Each GNSS BM has a

NAD 83 GNSS-derived h and an NAVD 88 leveled H . Subtracting the xGEOID16B height from the $h - H$ values for these BMs gives the best available estimate of the tilt and bias of NAVD 88. The resulting regression surface is shown in Figure 4.5. Adding the trend to xGEOID16B (NAD 83) removed a significant portion of the NAVD 88 bias and tilt; the mean difference decreased from +0.584 m to -0.024 m, and the standard deviation from ± 0.258 to ± 0.065 m. Because the trend was determined on a continental scale, it preserved the overall regional and local gradient (slope) of xGEOID16B, as desired. Note that in the remainder of this chapter, a prefix of “T” is used to identify the transformed version as “TxGEOID16B”. It is a combination of the transformation from IGS08 to NAD 83 and the addition of the NAVD 88 trend.

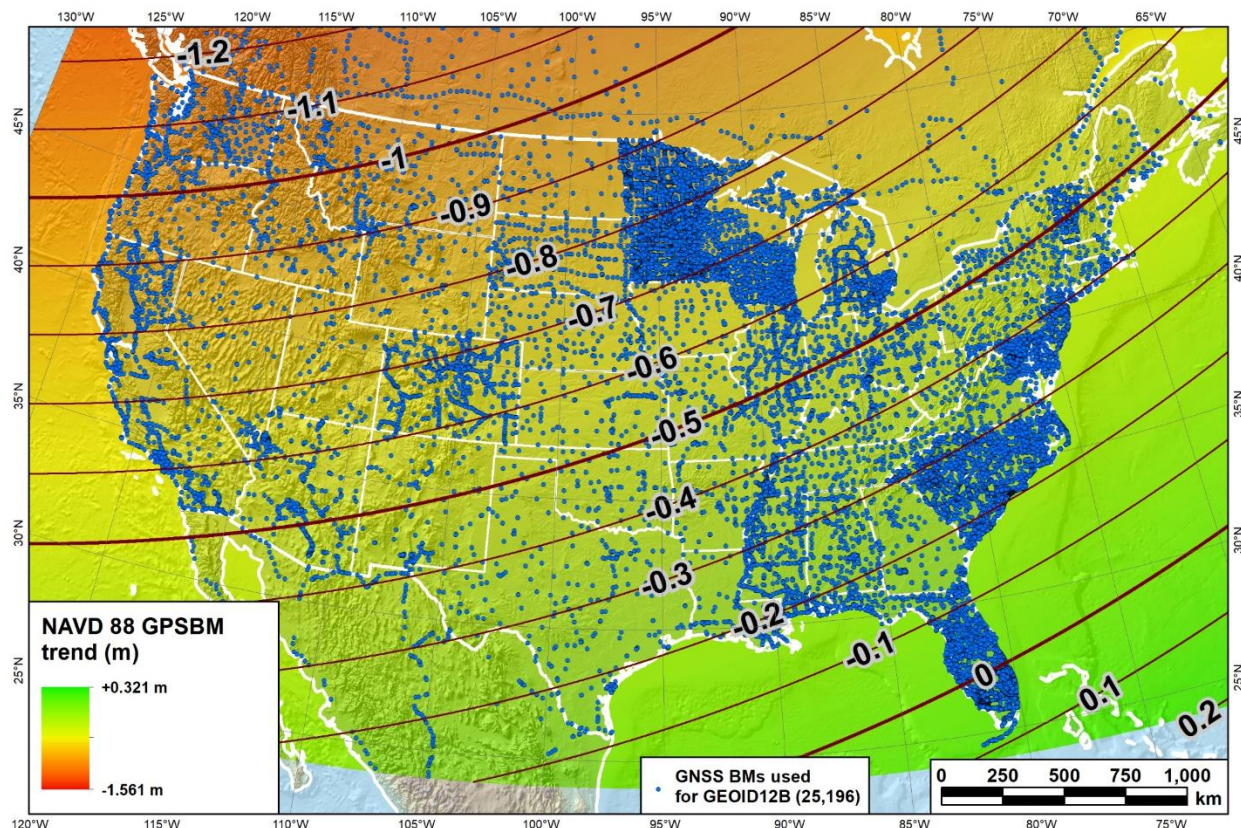


Figure 4.5. NAVD 88 bias and tilt based on linear regression of xGEOID16B (NAD 83) GNSS BM residuals (meters) to create transformed model TxGEOID16B.

4.4.3 Transformed Leveling Observations

The leveling observations were “reduced” mark-to-mark geopotential numbers. A geopotential number difference is the negative difference in gravity potential energy, and it has no geometric meaning (i.e., it does not represent a distance). It can be converted to an orthometric height, which has geometric meaning as the length of the (slightly curved) plumbline from the mark to a geopotential reference surface, nominally the geoid. Specifically, an orthometric height is defined as (Torge and Müller, 2012):

$$H_P = \frac{C_P}{\bar{g}} \quad (4.2)$$

where C_P and H_P are the geopotential number and orthometric height of point P , respectively, and \bar{g} is the mean gravity along the plumbline. For NAVD 88 Helmert orthometric heights, \bar{g} is determined by representing the topography above the geoid as an infinite flat plate of thickness H_P and a constant density (Hofmann-Wellenhof and Moritz, 2006). A model was developed for NAVD 88 that provided surface gravity, g_P , at any location by interpolating observed gravity (Hardy and Nelson, 1986; Fury, 1999). The modeled surface gravity is used to give

$$\bar{g} = g_P + \alpha H_P \quad (4.3)$$

where $\alpha = 4.24 \times 10^{-7} \text{ s}^{-2}$, based on a constant topographic density 2670 kg/m^3 (Zilkoski *et al.*, 1992). Using the relationships in Eqs. 4.2 and 4.3, the change in orthometric height from point A to B can be computed from the change in geopotential number as

$$\Delta H_{AB} = \frac{1}{2\alpha} \left[g_A - g_B + \sqrt{g_B^2 + 4\alpha(C_A + \Delta C_{AB})} - \sqrt{g_A^2 + 4\alpha C_A} \right] \quad (4.4)$$

See Dennis *et al.* (2018) for details on the derivation of Eq. 4.4.

Although ΔH is geometric, it is not consistent with the geometry of the GNSS vectors due to deflection of the vertical. The next step for making the difference consistent is to convert it to an ellipsoid height difference as

$$\Delta h_{AB} = \Delta H_{AB} + \Delta N_{AB} \quad (4.5)$$

where ΔN_{AB} is the geoid height difference between BMs, obtained by interpolation from a high-resolution geoid model. The geoid model must be in the same reference frame as h and H (NAD 83 and NAVD 88, respectively, in this case), as discussed in the previous section.

The final step for making the leveling observations geometrically consistent with the GNSS vectors is to convert them to delta ECEF vectors. Converting 1D leveling observations to 3D delta ECEF vectors also requires horizontal coordinates for the BMs at each end of a leveling observation. Although leveling observations are typically precise to the sub-mm level, most of the horizontal positions were scaled from topographic maps and are often inaccurate by many tens of meters. This creates an obvious disparity, which was handled here by assigning large standard deviations to the positions and constraining the positions in the least squares adjustments, as discussed below.

Using the published horizontal positions of the BMs and Δh_{AB} from Eq. 4.5, the delta ECEF vector components from BM A to B are computed using the well-known relationships between ECEF and ellipsoidal coordinates,

$$\begin{aligned} \Delta X_{AB} &= (R_B + h_A + \Delta h_{AB}) \cos \varphi_B \cos \lambda_B - (R_A + h_A) \cos \varphi_A \cos \lambda_A \\ \Delta Y_{AB} &= (R_B + h_A + \Delta h_{AB}) \cos \varphi_B \sin \lambda_B - (R_A + h_A) \cos \varphi_A \sin \lambda_A \\ \Delta Z_{AB} &= [(1 - e^2) R_B + h_A + \Delta h_{AB}] \cos \varphi_B \cos \lambda_B - [(1 - e^2) R_A + h_A] \cos \varphi_A \cos \lambda_A \end{aligned} \quad (4.6)$$

where, for a given reference ellipsoid, φ is the geodetic latitude, λ is the geodetic longitude, e^2 is the first eccentricity squared, and R is the radius of curvature in the prime vertical. The vector components are mostly dependent on the difference Δh_{AB} and are insensitive to the absolute h_A value; an error of ± 50 m in h_A will cause less than $\pm 0.001\%$ error in the vector components.

Transforming the leveling observations to ECEF vector format also requires the errors be formally transformed using the general law of propagation of variance (GLOPOV):

$$\mathbf{R}^T \Sigma_{\Delta n \Delta e \Delta u} \mathbf{R} = \Sigma_{\Delta X \Delta Y \Delta Z} \quad (4.7)$$

where $\Sigma_{\Delta n \Delta e \Delta u}$ is the original leveling v-c matrix in the delta north-east-up (Δn , Δe , Δu) local geodetic horizon (LGH) and $\Sigma_{\Delta X \Delta Y \Delta Z}$ is the leveling v-c matrix transformed to delta ECEF. \mathbf{R} is the familiar geocentric ECEF to LGH rotation matrix,

$$\mathbf{R} = \begin{bmatrix} -\sin \varphi \cos \lambda & -\sin \varphi \sin \lambda & \cos \varphi \\ -\sin \lambda & \cos \lambda & 0 \\ \cos \varphi \cos \lambda & \cos \varphi \sin \lambda & \sin \varphi \end{bmatrix}. \quad (4.8)$$

Strictly speaking, the leveling variances are in a local astronomic horizon frame, but they were taken as LGH since deflection of the vertical is usually much less than 1 arc-minute and hence would have negligible effect. Zero correlation between all terms was assigned,

$$\mathbf{R}^T \begin{bmatrix} \sigma_{\Delta n}^2 & 0 & 0 \\ 0 & \sigma_{\Delta e}^2 & 0 \\ 0 & 0 & \sigma_{\Delta h}^2 \end{bmatrix} \mathbf{R} = \begin{bmatrix} \sigma_{\Delta X}^2 & \sigma_{\Delta X \Delta Y} & \sigma_{\Delta X \Delta Z} \\ & \sigma_{\Delta Y}^2 & \sigma_{\Delta Y \Delta Z} \\ \text{sym.} & & \sigma_{\Delta Z}^2 \end{bmatrix}. \quad (4.9)$$

Arbitrary values of $\sigma_{\Delta n} = \sigma_{\Delta e} = 1$ m were used for the horizontal components, which is about three orders of magnitude larger than the typical leveling standard deviation of ~ 1 mm. Of

course, because the rotations are large, this causes all terms to be large in the transformed ECEF v-c matrix. As a check, the inverse transformation was performed from $\Delta X \Delta Y \Delta Z$ to $\Delta n \Delta e \Delta u$. The resulting standard deviation (sigma) and off-diagonal zero values exactly matched the original values, and those that differed were within $\pm 10^{-14}$ m².

Most leveled marks had positions scaled from topographic maps, and thus $\sigma_{\Delta n} \approx \sigma_{\Delta e} \approx 100\text{-}200$ m is a more reasonable estimate of uncertainty than 1 m. However, BMs with GNSS-derived horizontal coordinates were accurate to a few mm. Despite such discrepancies, using realistic values for horizontal sigmas is not important since the horizontal coordinates were constrained in all adjustments for the leveled-only marks. To evaluate this, a series of combined GNSS and leveling adjustments were performed with input horizontal sigmas of the leveled observations ranging from 0.1 mm to 1000 m. The results of adjustments became insensitive to input horizontal sigmas once they became greater than about 0.1 m. The results were nearly identical for all horizontal sigmas > 0.1 m, including output coordinates, accuracy estimates, and adjustment statistics. Because of this behavior, $\sigma_{\Delta n} = \sigma_{\Delta e} = 1$ m was used for the leveling G-files in this research, which could be easily scaled to other values if needed.

To some readers it no doubt must seem odd to transform 1D leveling observations into 3D ECEF vectors, especially since the horizontal coordinates can be in error by tens or meters or more. But it is essential that the GNSS and leveling observations have a consistent geometry when combined in a least-squares adjustment, and this is one way to accomplish that. It will not cause problems if the approximate leveled coordinates are constrained, the statistics account for the change in degrees of freedom, and the leveling errors are correctly transformed into ECEF space.

With the leveling observations transformed to NAD 83 delta ECEF vectors, they can simply be appended to the GNSS vector G-file. This creates a single observation input for a combined GNSS and leveling adjustment. But first the observation uncertainties must be reliably estimated, so that the observations are correctly weighted. That is the topic of the next section.

4.5 WEIGHTING OF OBSERVATIONS

4.5.1 GNSS Observation Errors

It is well known that GNSS processing usually yields highly optimistic error estimates (e.g., Gillins and Eddy, 2016; Kashani *et al.*, 2004; Øvstedal, 2000; Weaver *et al.* 2018; Dennis, 2019), although there is significant variation in the amount of optimism across different processors.

The challenge is determining just how optimistic the uncertainty estimates are, especially when determining weights for combining the completely different observations of GNSS and leveling.

The 3D standard deviations (sigmas) output by the *PAGES* baseline processor used for the GNSS data in this study ranged between 0.07 and 0.53 cm, with a mean of 0.14 cm. As will be shown, these values are optimistic by a factor of about 20. Such a large factor is not uncommon for *PAGES*, nor is it uncommon for other popular baseline processing software used by scientists and engineers. As an example, Kashani *et al.* (2004) estimated that the vector sigmas computed from baseline processing in *Bernese GNSS Software* were optimistic by a factor of 23.

The least-squares adjustment program *ADJUST* used for this study includes an option called “VVHU” for estimating the scale factor to apply to GNSS vector standard deviations (sigmas). The mechanics of using this option are described in the supplemental *ADJUST* documentation (NGS, 2018c). Mathematical details are described in Dennis *et al.* (2018) and (comparably) in Dennis (2019), so it is covered only briefly here.

VVHU computes two sigma scalars, one for the horizontal and one for the up component of the vectors. The computation is done by iteratively adjusting the horizontal and up network components separately. The σ values are scaled each time until the standard deviation of unit weight is 1 for both components. The final sigma scalars for the series of adjustments, V_{horz} and V_{up} , are the “variance factors” (NGS terminology). These values are used to compute the *a priori* standard deviations for the GNSS network as

$$\sigma_{\Delta horz} = V_{horz} \sqrt{\sigma_{\Delta n_0}^2 + \sigma_{\Delta e_0}^2 + 2\sigma_{\Delta n_0 \Delta e_0}} \quad (4.10)$$

$$\sigma_{\Delta h} = V_{up} \sigma_{\Delta u_0} \quad (4.11)$$

where:

$\sigma_{\Delta horz}$, $\sigma_{\Delta n}$, and $\sigma_{\Delta e}$ are the horizontal, north, and east standard deviations, respectively;

$\sigma_{\Delta n \Delta e}$ is the horizontal covariance;

$\sigma_{\Delta h} = \sigma_{\Delta u}$ is the standard deviation of delta ellipsoid height and delta up, respectively;

In Eqs. 4.10 and 4.11, the subscript “0” denotes the initial or preliminary values that were scaled to get the actual *a priori* standard deviations used in the adjustments. Variance factors of $V_{horz} = 19.015$ and $V_{up} = 7.709$ were determined for the final version of the GNSS-only network used in the combined GNSS+leveling adjustments for this study.

4.5.2 Leveling Observation Errors

Leveling observation obtained from the NGSIDB included estimated *a priori* error estimates, which were based on the scalars in Table 4.2 (Zilkoski, 1992). The estimated initial *a priori* standard deviation of the leveled orthometric height difference, $\sigma_{\Delta H}$, of each reduced observation (between BM pairs) is computed as

$$\sigma_{\Delta H_0} = \max\{s_{\Delta L} \sqrt{d/n_r}, 0.2 \text{ mm}\} \quad (4.12)$$

where $s_{\Delta L}$ is the scalar from Table 4.2 (i.e., the standard deviation in mm of leveled height differences in 1 km), d is the running distance between BMs (km), and n_r is the number of runs between the BMs used to create the reduced observation. The maximum function in Eq. 4.12 serves to ensure that the minimum value of $\sigma_{\Delta H_0}$ is 0.2 mm regardless of the distance and number of runs between BMs.

Table 4.2. Scalars ($s_{\Delta L}$) used for computing *a priori* standard deviations of leveling observations as a function of square root of distance (units = mm / $\sqrt{\text{km}}$).

Group	Order/Class of leveling observation (mm for 1 km distance)						
	1/0	1/I	1/II	2/I	2/II	2/0	3
Prior to 1971	0.7	1.1	2.0	2.1	2.8	3.0	4.2
From 1971 through 1978	0.7	1.1	1.4	2.1	2.8	3.0	4.2
After 1978	0.7	0.8	1.0	2.1	2.8	3.0	4.2
For Zeiss Nil level data*	—	2.0	2.0	2.8	3.0	—	—

*Almost all Nil data affected by magnetic fields were 1/II and 1/II obtained from 1971-1978.

Although Eq. 4.12 provides a mechanism for estimating leveling observation *a priori* error estimates, it is not known whether they are realistic for the network used in this study. To make that assessment, an iterative approach was used, somewhat similar to the VVHU option in *ADJUST*. It began with a minimally constrained adjustment of the entire leveling network with all observations enabled using $\sigma_{\Delta H_0}$ per Eq. 4.11. The constrained station was S 714, using its NGS-published NAD 83 (2011) epoch 2010.00 coordinates. This station was selected for all minimally constrained adjustments in this project because it has both GNSS and leveled observations (and a published 1st order, class II NAVD 88 height), and it is near the center of the network (see Figure 4.1b and Figure 4.2a). This adjustment yielded a standard deviation of unit weight of $\sigma_0 = 6.57$, much greater than the desired value of 1.

A $\sigma_0 \gg 1$ indicates two likely problems with the adjustment: (1) some of the observations have unusually large residuals, and these observations should be rejected; and (2) the estimated *a priori* standard deviations of the observations were potentially too small (i.e., overly-optimistic), thereby affecting the weight model in the adjustment. Although it was not known how much influence each of the two problems had on the network, there was reason to believe that the observation error should not be scaled by more than about 2 for most leveling in the NGSIDB (Zilkoski, 2016).

The problem was approached by performing a series of minimally constrained adjustments of the leveling network in terms of ellipsoid height differences, Δh , per Eq. 4.5. That equation requires both orthometric and geoid height differences (ΔH and ΔN). It is reasonable to assume that the uncertainty of leveled orthometric and geoid height difference ($\sigma_{\Delta H}$ and $\sigma_{\Delta N}$, respectively) are uncorrelated. In that case the total uncertainty of Δh from leveling can be computed from the special law of propagation of variance (SLOPOV) as

$$\sigma_{\Delta h} = \sqrt{\sigma_{\Delta H}^2 + \sigma_{\Delta N}^2} \quad (4.13)$$

The objective was to determine a realistic value for $\sigma_{\Delta H}$, starting with the initial value $\sigma_{\Delta H_0}$. For this first approach, both ΔN and $\sigma_{\Delta N}$ were taken as zero. Although this treatment yields incorrect adjusted ellipsoid heights and their uncertainties at the marks, it enables evaluation of $\sigma_{\Delta H}$ and otherwise has no detrimental effect on the network because it was minimally constrained.

After each minimally constrained adjustment, the normalized residual (the ratio of the residual to the *a priori* standard deviation of the observation) was computed for each observation. If observations had normalized residuals greater than a selected maximum value, the observation

with the largest residual was rejected. This process was repeated until no observations had normalized residuals that exceeded the maximum. A series of such iterative adjustments were performed for maximum normalized residual criterion values of 10, 5, 4, 3, 2, and 1.7 (the last was the lowest that could be used without the network becoming singular). Final results of this series of adjustments are plotted in Figure 4.6, with σ_0 (left vertical axis) as a function of the percentage of rejected observations in the network, shown as a solid curve. The right vertical axis gives the normalized residual rejection criterion used for each adjustment, corresponding to the upper (dashed) curve.

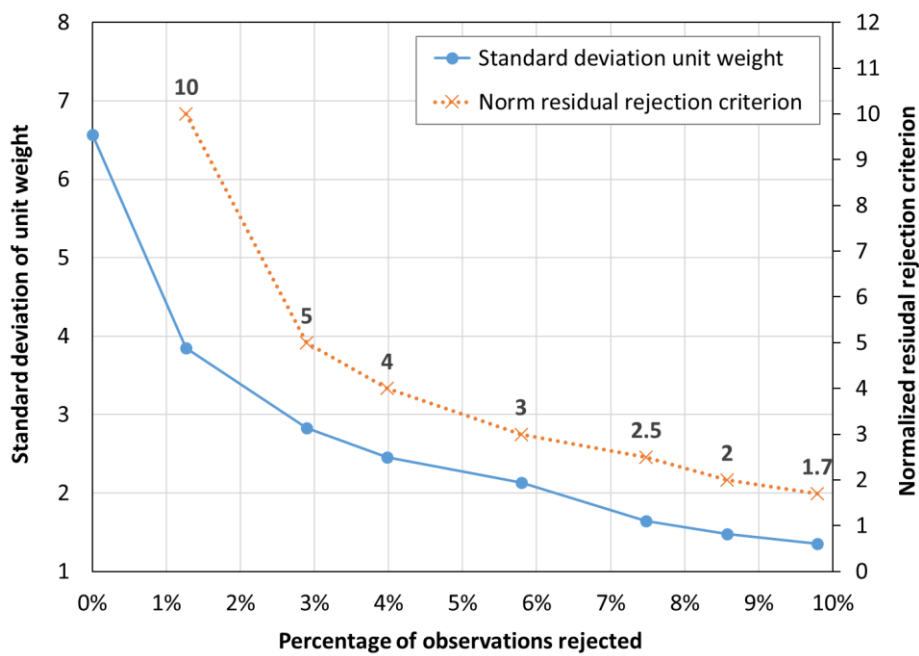


Figure 4.6. Standard deviation of unit weight of minimally constrained adjustments of leveling network corresponding to vector rejections for various normalized residual rejection criteria.

Next, normalized residual rejection criterion values of 2.0, 2.5, and 3.0 were further evaluated to select one rejection criterion value for this project. These values were chosen as they respectively correspond to threshold values for 95.5%, 98.8%, and 99.7% probable error from the standard normal distribution. Data in a normal distribution that exceed these threshold values

are often considered outliers. Using these values, the *a priori* $\sigma_{\Delta H_0}$ values from Eq. 4.12 were scaled and the adjustments were repeated until $\sigma_0 \approx 1$. Observations were re-enabled or rejected as necessary based on the normalized residual rejection criterion. Normalized residuals of 2.0 and 2.5 for the rejection criterion resulted in the same scalar of 1.8 (rounded to the nearest 0.1), corresponding to $\sigma_0 = 0.997$ and 1.020, respectively. The 2.0 and 2.5 criteria also had nearly the same percentage of rejected observations, 6.1 and 6.2%. A more relaxed criterion based on a normalized residual of 3.0 yielded a standard deviation scalar of 2.0 and reduced the rejected vectors to 5.2%. Based on this analysis, a scalar of 1.8 was chosen and multiplied by the preliminary values of $\sigma_{\Delta H_0}$ to estimate *a priori* values for all subsequent adjustments, and Eq. 4.13 becomes

$$\sigma_{\Delta h} = \sqrt{(1.8 \sigma_{\Delta H_0})^2 + \sigma_{\Delta N}^2} \quad (4.14)$$

Once this process was completed, all leveling observations were re-enabled before proceeding to the next task of estimating $\sigma_{\Delta N}$. A normalized residual of 2.5 was used as the nominal rejection criterion for all subsequent adjustments.

4.5.3 Geoid Slope Errors

With estimates of *a priori* errors for both GNSS and leveling observations, the final step was to estimate geoid height difference (geoid slope) errors, $\sigma_{\Delta N}$, for use in Eq. 4.14. Although the error models developed here are referred to as “geoid slope error”, they likely also represent other errors, for example that due to the difference between slope of the geoid surface and deflection of the vertical at the topographic surface. As such, it might be more appropriate to call them “transformation error models.” However, most of the error is in the geoid model itself, and so the term “geoid slope error” is used for $\sigma_{\Delta N}$ throughout this chapter.

Regardless of the name, reliable models or other estimates of $\sigma_{\Delta N}$ are not readily available. Recent research indicates an uncertainty in geoid slope of 1 cm over distances from 0.4 to 325 km for new gravimetric geoids that used GRAV-D data, and 1-3 cm for other modern geoid models (Smith *et al.*, 2013). However, part of the error budget is the uncertainty in adjusted GNSS-derived ellipsoid height differences, which were about 0.4 cm (~68% confidence) at all distances in the study. This implies that $\sigma_{\Delta N}$ is likely less than 1 cm for short distances and presumably is much less than 1 cm. Indeed, it is likely that geoid slope error approaches zero (or near zero) as the distance between marks approaches zero, due to autocorrelation alone.

Correctly modeling geoid slope error over short distances is important, because most leveled height differences are for distances of about 1 km. Referring to Table 4.1, the network used in this research has a median leveled distance of 0.58 km, mean of 0.76 km, and a maximum of 5.34 km. Note that these actual leveled distance are generally longer than the straight-line horizontal distance between marks, since leveling is performed along a clear path on the ground (usually along a road). Because of this, for most leveling observations the horizontal length of the ECEF leveling vector was used for computing distance-dependent geoid slope errors.

4.5.3.1 *Development of Geoid Slope Error Models*

Since a geoid slope error model was not available, models for $\sigma_{\Delta N}$ were developed and tested using variance component estimation procedures. Three geoid slope error model types considered in this project are listed below. These model types were selected in an attempt to use the simplest possible (so that their parameters could be reliably estimated), and yet provide reasonably realistic modeling (for example by allowing distance-dependence).

1. Constant error model. $\sigma_{\Delta N}$ is set to a constant value, c , in mm. This is the simplest case because only one parameter was varied until $\sigma_0 \approx 1$.
2. Error model increasing linearly with distance. $\sigma_{\Delta N} = c + md$, where m is the slope in parts per million (mm/km) and d is the horizontal distance between marks (km).
3. Error increasing with the square root of distance. $\sigma_{\Delta N} = c + s\sqrt{d}$, where s is a constant in mm/ $\sqrt{\text{km}}$. This is likely more realistic than the linearly increasing case, because it conforms to observed random walk error that occurs when (uncorrelated) random errors accumulate, as is the case for terrestrial surveying errors. Such error models are proportional to the square root of time or distance and can be found in published literature in geodesy, geophysics, and inertial navigation (e.g., Herring, 2009; Hartman, 1995; Hackl, 2012; and Langbein, 2004).

The parameters in the geoid slope error models were estimated by iteration. First, for a given error model, values of $\sigma_{\Delta N}$ were computed based on assumed parameters and inserted in Eq. 4.14 to find $\sigma_{\Delta h}$. Then a minimally constrained adjustment of only the ECEF leveling vectors (derived from Eqs. 4.5 and 4.6 using values of ΔN from TxGEOID16B) was performed in *ADJUST*. The parameters in the $\sigma_{\Delta N}$ models were then refined, and these steps were repeated until the adjustment resulted in $\sigma_0 \approx 1$.

As the geoid slope error models and the resulting *a priori* standard deviations of the observations were refined, the percentage of observations exceeding a normalized residual of 2.5 was about 1-2% (much less than ~6% in the preceding section). Although the rejections for the geoid slope error model evaluations were similar, they were not identical. For the sake of consistency, the same rejections were used for the development of the final leveling network used in for analysis. After close inspection, it was decided to reject 23 observations (1.8% of the total network of

leveling observations). Most of the rejected observations had normalized residuals greater than 2.5 after a minimally constrained adjustment using any of the geoid slope error models.

However, four observations were rejected, because their residuals were unusually high (although their normalized residuals were less than 2.5). Sufficient redundancy still existed in the leveling network so that none of the rejections created spurs.

Once the 23 observations were identified and rejected, the parameters in the geoid slope error models were further refined until a minimally constrained adjustment of the final leveling network yielded $\sigma_0 \approx 1$. For distance-dependent error models with the y -intercept (c) not set to zero, all parameters were determined to the nearest 0.5 mm to avoid over-specification, since they could not be determined uniquely by consideration of just one statistic, σ_0 . The following final parameters were derived for a five geoid slope error models:

Model 1. Constant error: $c = 2.9$ mm for all distances.

Model 2. Linear distance-dependent error: $c = 0$ and $m = 6.8$ mm/km

Model 3. Linear distance-dependent error: $c = 2$ mm and $m = 1.5$ mm/km

Model 4. Square root distance-dependent error: $c = 0$ and $s = 4.3$ mm/ $\sqrt{\text{km}}$

Model 5. Square root distance-dependent error: $c = 1.5$ mm and $s = 2$ mm/ $\sqrt{\text{km}}$

A plot of constant error Model 1 is shown in Figure 4.7, and plots of distant-dependent Models 2-5 are presented in Figure 4.8. All plots show the *a priori* leveling errors with $\sigma_{\Delta H} = 1.8 \sigma_{\Delta H_0}$, the geoid slope error model, and the total $\sigma_{\Delta h}$ error per Eq. 4.14. The $\sigma_{\Delta H}$ values are symbolized by order and class groups, which shows how each accuracy category falls along curves based on the square root of distance.

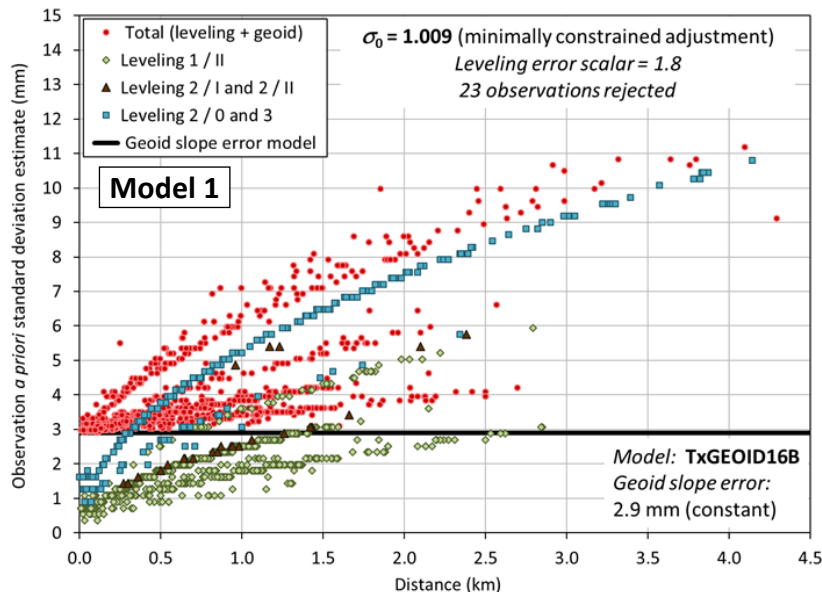


Figure 4.7. Observation *a priori* error estimates for the constant geoid slope error model.

4.5.3.2 Evaluation of Geoid Slope Error Models

The geoid slope error models were assessed by comparison of minimally and fully constrained adjustments. These adjustments were performed using *ADJUST*, with leveling observations represented by delta ECEF vectors as described above. As a check, the adjustments were also performed with *STAR*NET* using orthometric height differences (Dennis *et al.*, 2018). The two programs yielded nearly identical results, but only the results from *ADJUST* are given here.

Table 4.3 summarizes results of minimally constrained leveling network adjustments for the five geoid slope error models, as well as for no geoid slope error model and for no geoid model at all.

An *a priori* leveling errors of $\sigma_{\Delta H} = 1.8 \sigma_{\Delta H_0}$ was used for all adjustments. The networks consist of 1039 stations connected by 1256 enabled leveling observations, with 218 degrees of freedom, and σ_0 is given for each adjustment. Also given are: 1) adjustment residuals, 2) network and local accuracies, and 3) differences with NGS-published NAD 83 ellipsoid heights and NAVD 88 orthometric heights. Each of these three adjustment metrics is discussed below:

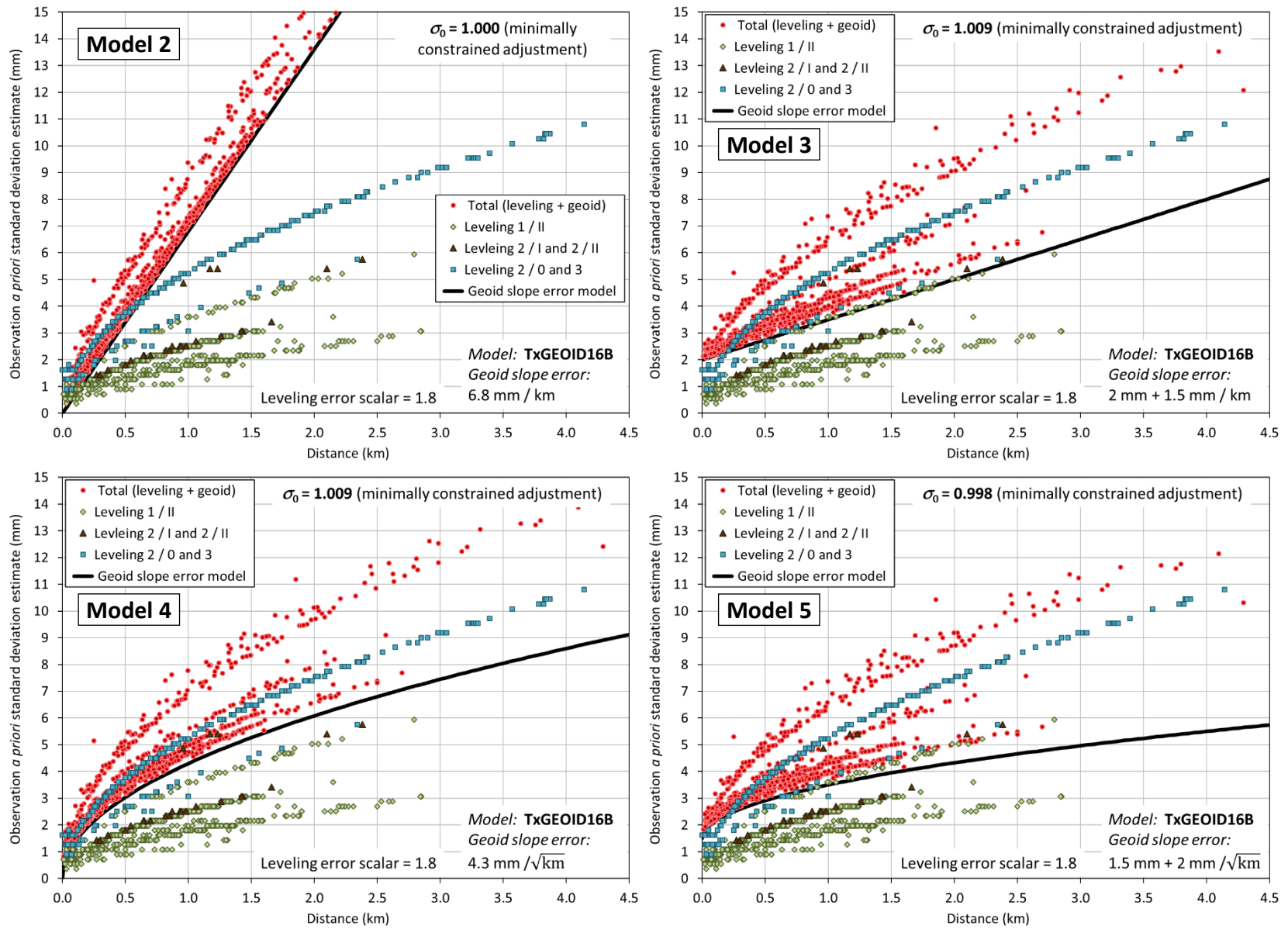


Figure 4.8. Observation *a priori* error estimates for distance-dependent geoid slope error models.

Table 4.3. Results of minimally constrained adjustments of the leveling network with no geoid model and with geoid model TxGEOID16B using no geoid slope error model and the five proposed geoid slope error models. Constrained to the NGS-published NAD 83 (2011) epoch 2010.00 ellipsoid height of NGS station S 714.

Geoid model	None	TxGEOID16B					
Geoid slope error model	n/a	None	Model 1	Model 2	Model 3	Model 4	Model 5
Error at zero distance	n/a	n/a	2.9 mm	0 mm	2 mm	0 mm	1.5 mm
Error model distance dependence	n/a	n/a	Constant	6.8 mm /km	1.5 mm /km	4.3 mm / $\sqrt{\text{km}}$	2 mm / $\sqrt{\text{km}}$
Std dev unit weight	2.021	2.020	1.009	1.000	1.009	1.009	0.998
<i>Residuals (cm) for 1256 enabled observations</i>							
Max ABS	1.05	1.05	0.81	1.68	0.93	0.97	0.81
Mean ABS	0.1151	0.1151	0.1123	0.1155	0.1129	0.1130	0.1126
RMS	± 0.1842	± 0.1841	± 0.1655	± 0.2010	± 0.1715	± 0.1759	± 0.1695
<i>Normalized residuals (unitless) for 1256 enabled observations</i>							
Max ABS	6.30	6.30	1.79	4.85	1.83	2.58	1.78
Mean ABS	0.53	0.53	0.29	0.23	0.29	0.28	0.28
RMS	± 0.838	± 0.838	± 0.420	± 0.421	± 0.420	± 0.420	± 0.416
<i>Network accuracies (cm) at 95% confidence for 1038 stations (constrained station excluded)</i>							
Min	0.42	0.42	0.59	0.95	0.62	0.72	0.63
Max	9.96	9.96	5.92	10.26	6.44	6.88	6.22
Median	3.536	3.535	2.936	5.211	3.219	3.552	3.123
Std dev	± 1.651	± 1.651	± 1.025	± 1.629	± 1.083	± 1.154	± 1.058
<i>Local accuracies (cm) at 95% confidence (cm) for all 1039 stations (median)</i>							
Min	0.16	0.16	0.36	0.11	0.29	0.16	0.29
Max	4.06	4.06	2.12	5.29	2.52	2.60	2.26
Median	0.687	0.687	0.646	0.790	0.646	0.686	0.649
Std dev	± 0.626	± 0.626	± 0.255	± 0.681	± 0.316	± 0.364	± 0.293
<i>Adjusted ellipsoid height minus published NAD 83 (cm) for 22 GNSS stations (constrained excluded)</i>							
Range	185.1	10.4	9.0	10.4	9.3	9.4	9.2
Mean	-30.24	-2.95	-3.18	-2.71	-3.08	-3.13	-3.16
Std dev	± 45.86	± 2.07	± 1.94	± 2.16	± 1.98	± 2.01	± 1.98
<i>Adjusted orthometric height minus published NAVD 88 (cm) for 528 leveled stations</i>							
Range	7.8	7.8	7.9	7.9	7.8	7.9	7.8
Mean	-2287.87	1.40	1.18	1.77	1.31	1.27	1.20
Std dev	± 0.88	± 0.88	± 1.00	± 0.75	± 0.91	± 0.88	± 0.94

1. Residuals. For adjustments that used a geoid slope error model (except for Model 2 with $c = 0$ and $m = 6.8$ mm/km), all residuals were within ± 1 cm. As expected, residuals were larger for adjustments that did not use a geoid slope error model or a geoid model at all (and much larger for normalized residuals). Although the distinction is slight, overall the smallest residuals and least dispersion occurs for geoid slope error Model 5.
2. Network and local accuracies. Network accuracies represent the uncertainty of the adjusted station coordinates with respect to the network control, and local accuracies represent the uncertainty of a station with respect to other stations to which it is connected by observations (i.e., the uncertainty of the adjusted observations). Both are given in cm at 95% confidence and are computed from post-adjustment v-c matrices and scaled by the adjustment σ_0 . Thus for each station in an adjusted network, there is one network accuracy but there can be (and usually are) multiple local accuracies, one for each adjusted observation. The NGS convention uses the median to give a single local accuracy for each station, and that convention is followed here. For the original definition of these accuracies, see FGDC (1998, parts 1 and 2), and later modifications described by Milbert (2009) and Dennis (2019). The network and local accuracies in Table 4.3 are fairly consistent for geoid slope error Models 3-5. The median for these three models is about 3.3 and 0.66 cm with standard deviations of about ± 1.1 and ± 0.3 cm for network and local accuracies, respectively. Overall, the accuracies and their dispersion are smallest for Model 5, although the differences are slight.
3. Differences with published heights. Apart from the adjustment with no geoid model, all adjustments in Table 4.3 show fairly consistent differences with the published NAD 83 ellipsoid and NAVD 88 orthometric heights (the adjusted orthometric heights were derived

directly from the adjusted ellipsoid heights using TxGEOID16B). Although the adjustments were constrained to the published ellipsoid height of station S 714, the best overall agreement was with the 528 published NAVD 88 orthometric heights, with a range of about 8 cm and a standard deviation of about ± 0.9 cm for all adjustments with a geoid model. Differences with the 22 published NAD 83 ellipsoid heights were also consistent for all adjustments using a geoid model, but they did not agree quite as well, with a range of about 9 cm and standard deviation of about ± 2.0 cm overall. Although these results show fairly good agreement with published values, they do not help in determining which geoid slope error model performs best. Comparisons to published control will be revisited in Section 4.6.

Constrained leveling-only adjustments were also performed, but final versions were only done for geoid slope error Models 3-5 (the reason for limiting it to these three is discussed in Section 4.5.3.3). One set of adjustments was constrained to 16 published (or known) ellipsoid heights, another to 18 published leveled orthometric heights. The weights used for the constrained ellipsoid heights were based on their published formal sigmas (ranged from 0.31 to 0.97 cm). Since these values are not available for published orthometric heights, a (tight) sigma of 0.1 cm was used. As expected, σ_0 increased for all of these constrained adjustments, but all passed the statistical F-test at 95% confidence, indicating the constraints were consistent with the observations (even for the tight orthometric height constraints). Because of this consistency, the residuals and *a posteriori* accuracies exhibited little change, and so these adjustments provided little if any additional insight into which of the three geoid slope error models was most appropriate. These constrained adjustments did, however, provide reassurance that the ECEF leveling mathematical model was performing correctly.

4.5.3.3 Selection of a Geoid Slope Error Models for Combined GNSS and Leveling

As can be seen from the preceding results and discussion, the adjustments by themselves were not definitive in determining an appropriate geoid slope error model for use in combined GNSS and leveling adjustments. Performance of Model 5 was overall somewhat better than the other models, in terms of residuals and accuracies, but the improvement was slight and not conclusive. Other criteria and judgment was necessary.

Of the five geoid slope error models tested in this study, the first two models seemed quite unrealistic. Model 1 resulted in a constant geoid slope error value of only 2.9 mm. Such a small error value is 4.4 to 13 times smaller than the constant geoid slope error value of 1-3 cm over any distance as estimated by Smith *et al.* (2013). Model 2, a linear model with no error at zero distance (i.e., y-intercept of zero) is even more unrealistic, as is readily apparent in Figure 4.8. To achieve $\sigma_0 \approx 1$ from a minimally constrained adjustment required a slope of 6.8 mm/km, corresponding to geoid slope errors that exceeds 1 cm at a distance of only 1.5 km. In addition, this model had the worst performance of all models (including those with no geoid error model), in terms of residual statistics and estimated accuracies (see Table 4.3).

Estimating more than one parameter, such as c and s or m , from a single variable, σ_0 , is mathematically intractable without simplifying assumptions or additional information. Models 1 and 2 suggest bounds for the y-intercept, with Model 1 indicating $c < 2.9$ mm and Model 2 providing evidence for $c > 0$. In addition, hybrid geoid models suggest that a linear slope of 1-2 mm/km is reasonable (e.g., Smith and Milbert, 1999; Roman *et al.*, 2004; NGS, 2014). Guided by this information, values of $m = 1.5$ mm/km and $c = 2$ mm were selected for Model 3 to give $\sigma_0 \approx 1$. For this model, geoid slope error was about 1 cm at 5.3 km and 2 cm at 12 km, as shown in Figure 4.8. Since the maximum (straight line) leveling observation distance in this study was

4.3 km, geoid slope errors for larger distances could not be evaluated. Assuming the geoid slope error estimated by Smith *et al.* (2013) of 1-3 cm over any distance represents a maximum amount of geoid slope error, then by setting the maximum geoid slope error to the midpoint of this range (2 cm) on Model 3 would require a change in slope from $m = 1.5$ to $m = 0$ mm/km at a distance of only 12 km.

The need for a change in slope in the error model to limit the maximum error leads logically to a model with slope that decreases with distance. The simplest of these is a square root of distance model, which is the type of model used for estimating accumulation of leveling error (and is consistent with random walk error models commonly used in geodesy, geophysics, and inertial navigation). As with the linear model, if $c = 0$ the distance coefficient can be estimated directly by using the value that yields $\sigma_0 \approx 1$ in a minimally constrained adjustment. Using that approach gives Model 4, with coefficient $s = 4.3$ mm/ $\sqrt{\text{km}}$. As shown in Table 4.2, this value is nearly identical to the estimated error of 3rd order leveling (4.2 mm / $\sqrt{\text{km}}$), which is not unreasonable. Yet the equation still seems somewhat pessimistic, since it reaches an error of 2 cm at a distance of only 22 km. Yet this model is tempting because its single parameter can be easily estimated.

Adding a second parameter, such as a y-intercept, to a model based on the square root of distance allows reduction of the accumulation of geoid slope error over distance. For Model 5, using $c = 1.5$ mm and $s = 2$ mm/ $\sqrt{\text{km}}$ gives $\sigma_0 \approx 1$ for a minimally constrained adjustment. Geoid slope error from this model reaches 2 cm at 86 km rather than at 22 km per Model 4. The coefficient $s = 2$ mm/ $\sqrt{\text{km}}$ is nearly the same as 2nd order, class I leveling (2.1 mm/ $\sqrt{\text{km}}$), as shown in Table 4.2. But because $c = 1.5$ mm for the model, its error is greater than 2nd order, class I leveling for distances of less than $[1.5 / (2.1 - 2.0)]^2 = 225$ km. Similarly, the model error is greater than 2nd

order, class II leveling for distances of less than $[1.5 / (2.8 - 2.0)]^2 = 3.5$ km. The model error is never better than 1st order, class II leveling (note that an error of 2 cm corresponds to a distance of 400 km for 1st order, class II leveling). Such geoid slope error model performance with respect to leveling seems reasonable, which is part of the justification for selecting parameters $c = 1.5$ mm and $s = 2$ mm/ $\sqrt{\text{km}}$ (in addition to the $\sigma_0 \approx 1$ criterion).

Of the geoid slope error models discussed, only Models 3, 4, and 5 are viable, which is why those were the only models used in the constrained leveling-only adjustments. There remains some question as to whether it is appropriate to assume a minimum nonzero (positive y-intercept) error for the geoid slope error models. Certainly, including this additional constant makes it more difficult to estimate model parameters, since there are many more permutations possible if two parameters can vary rather than only one. Values of $c = 2$ and 1.5 mm were determined previously for the linear and square root of distance models, respectively. Additional analysis of this and other datasets may provide a better means for estimating these values. That can include determining whether $c > 0$ is appropriate or whether a different decay rate is warranted (e.g., power < 0.5 , logarithmic, etc.). Such efforts are left to future work.

There may be a question as to why we are concerned with geoid slope errors for long distances in a leveling adjustments, since the distance between leveled marks is typically less than a few km. The reason is that combined adjustments of GNSS and leveling observations do not necessarily have to use all the actual (reduced) leveling observations between marks. Instead, leveling observations can be accumulated into single orthometric height differences between junctions in a leveling network, which could represent many km of leveling. Such an approach could be used, for example, to adjust a regional leveling framework to determine heights at junctions (and other marks of interest) rather than at every bench mark. In such cases, geoid slope error

estimates for large distances would be necessary. In addition, accumulating orthometric height differences between junctions and stations at specified distances may provide a means for estimating geoid slope errors at longer distances. Doing so may reveal whether there is a distance above which geoid slope errors become essentially constant. Although that approach is not pursued in this study, it could be investigated in future research.

Based on the foregoing analysis and discussion, geoid slope error Model 5 appears the most realistic, at least for this particular leveling dataset. In addition, Models 3 and 4 both give $\sigma_{\Delta N} > 1$ cm for distances of more than 5.4 km, and $\sigma_{\Delta N} > 3$ cm at distances of more than 19 and 49 km, respectively. These error estimates are not compatible with the findings in Smith *et al.* (2013) where it was reported that the relative geoid height error is 1 to 3 cm at a distance up to 325 km. For Model 5, $\sigma_{\Delta N} = 1$ cm at a distance of 18.1 km reaches 3.8 cm at 325 km, which agrees reasonably well with Smith *et al.* (2013).

Applying geoid slope error Model 5 to Eq. 4.14 gives the following *a priori* standard deviation of leveling observations, transformed to ellipsoid height differences (in cm)

$$\sigma_{\Delta h} = \sqrt{(1.8 \sigma_{\Delta H_0})^2 + (0.15 + 0.2 \sqrt{d})^2} \quad (4.15)$$

where the variables are as defined previously, except that Model 5 parameters are given in cm, and d is the straight-line horizontal distance between marks (km), rather than the leveling path.

Using Eq. 4.15 for the combined leveling and geoid slope errors, along with Eqs. 4.10 and 4.11 for GNSS errors, provides a means for appropriately weighting these very different observation types. With that done, the GNSS and leveling observations can be combined into a single

network to perform simultaneous adjustments. That is the overarching goal of this study and topic of the next section.

4.6 COMBINED 3D ADJUSTMENTS OF GNSS AND LEVELING OBSERVATIONS

Many separate GNSS- and leveling-only adjustments were performed for this study, as described in previous sections. Those separate adjustments were performed again for this section, to provide a basis of comparison for combined 3D adjustments of GNSS and leveling observations. For the sake of consistency, there were slight changes to these adjustments, as follows:

- GNSS-only adjustments. For the minimally constrained GNSS-only adjustments, station S 714 was constrained (rather than the CORV CORS), since S 714 was also minimally constrained for the leveling-only network. Another minor change was in the computed variance factors. Initial values of $V_{horz} = 18.985$ and $V_{up} = 7.702$ were determined using the original set of five rejected vectors. These values changed slightly for the GNSS-only network in this section, to $V_{horz} = 19.015$ and $V_{up} = 7.709$ because an additional GNSS vector was rejected, based on analysis of the minimally constrained combined GNSS+leveling network, as described below.
- Leveling-only adjustments. The only difference is that an up variance factor of $V_{up} = 0.998$ was used rather than exactly 1. This change has negligible impact on the results in Table 4.3. The reason for $V_{up} = 0.998$ was consistency with the GNSS-only network, so that both minimally constrained adjustments had a standard deviation of unit weight (σ_0) of exactly 1.
- Constraints. The fully constrained leveling-only adjustment used a different set of ellipsoid height constraints than in Section 4.5.3. The heights constrained in this section were limited to those with published values *before* the fieldwork was performed. They were therefore not

available to use as constraints for the GNSS-only network. Because they could not be constrained in the GNSS-only network, it was also appropriate to not constrain them in the leveling-only network, since the two networks were combined and adjusted simultaneously. The reason all available GNSS-derived ellipsoid heights were used for leveling constraints in Section 4.5.3 was to validate the use of delta ECEF vectors for leveling, and to assess the geoid slope error models. Recall that orthometric heights are not constrained, because it is not consistent with the objective of combining GNSS and leveling observations for determining heights for a vertical datum based on a gravimetric geoid model.

The stations used for all fully constrained adjustments in this section are shown in the map in Figure 4.9 and are listed in Table E.1 (in Appendix E). The list of stations gives the (NGS-published) constrained ellipsoid height and the north, east, and up standard deviations (which were inverted and squared to weight the constraints). The nine marks constrained for leveling are GNSS stations that also had leveling observations (the leveled order and class is given for each of these BMs). Note that leveled stations J 54 and PTS 35 are not included (as mentioned in Section 4.5.3.2), even though they both have published ellipsoid heights and leveling observations. These two stations will be revisited in this chapter, as an illustration of how combining observations into a single network can help identify problems.

4.6.1 Minimally Constrained Separate and Combined Adjustments

Using the *a priori* standard deviations for GNSS observations (Eqs. 4.10 and 4.11) and leveling observations with geoid slope error Model 5 (Eq. 4.15), minimally constrained adjustments were performed of the GNSS-only, leveling-only, and combined GNSS+leveling networks. The published NAD 83 ellipsoid height (and horizontal coordinates) of station S 714 were held fixed. Results of these adjustments are summarized in the upper part of Table 4.4.

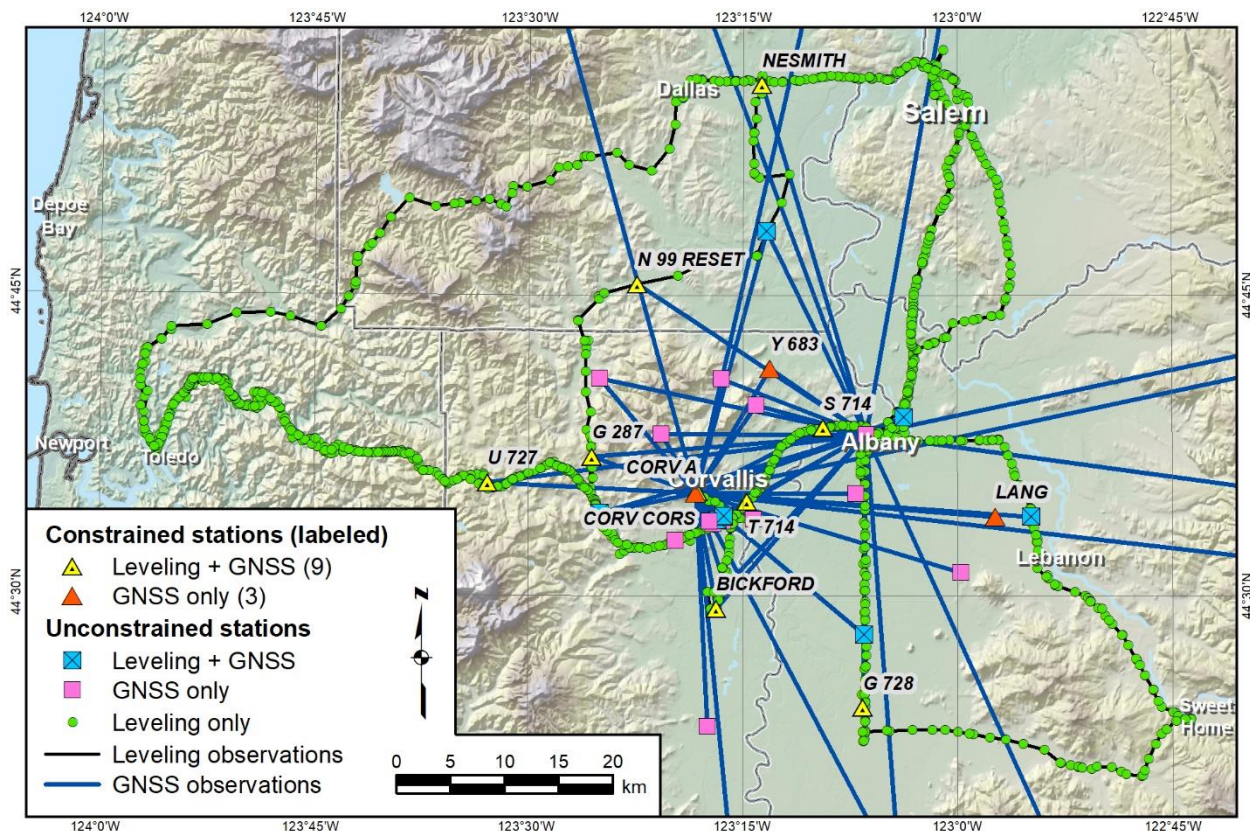


Figure 4.9. Combined leveling and GNSS network in main project area, showing stations constrained for adjustments (labeled). See also Figure 4.1 and Figure 4.2.

Because of the variance component estimation methods, the minimally constrained adjustments of the GNSS-only and leveling-only networks resulted in $\sigma_0 = 1.000$ for both. However, as shown in the third row of Table 4.4, the first minimally constrained simultaneous GNSS+leveling adjustment resulted in $\sigma_0 = 1.111$, which is statistically not equal to 1 at the 5% significance level, based on the χ^2 test. Upon inspection, one of the leveling observations to a mark at the end of a leveling spur (PTS 35) had a normalized residual magnitude of 6.6 (recall that the rejection criterion was 2.5). At PTS 35, the ellipsoid height from the constrained adjustment of the GNSS-only network was 14.0 cm lower than the adjusted ellipsoid height from

the leveling-only network. Apparently, this mark was disturbed or settled since it was leveled (in 1941). Note this is the only GNSS+leveling station in the network classified as stability D, which is the lowest ranking used by NGS (defined as “questionable or unknown stability”).

Table 4.4. Summary of minimally constrained and fully constrained GNSS-only, leveling-only, and GNSS+leveling network adjustments.

Adjustment	Number observations		Observation up residuals (cm)		Normalized up residuals		Std dev unit weight, σ_0
	Leveling	GNSS	Leveling	GNSS	Leveling	GNSS	
<i>Minimally constrained</i>							
GNSS only	—	359	—	-3.2 to 2.7	—	-2.4 to 2.3	1.000
Leveling only	1256	—	-0.8 to 0.8	—	-1.8 to 1.6	—	1.000
GNSS+leveling	1256	359	-2.4 to 1.2	-4.8 to 4.4	-6.6 to 3.5	-4.7 to 2.3	1.111
GNSS+leveling*	1255	359	-1.0 to 1.1	-2.7 to 3.1	-1.8 to 2.0	-2.3 to 2.3	1.006
GNSS+leveling**	1255	358	-1.0 to 1.1	-2.7 to 2.7	-1.8 to 2.0	-2.3 to 2.3	1.005
<i>Fully constrained</i>							
GNSS only	—	359	—	-3.2 to 2.7	—	-2.4 to 2.3	1.013
Leveling only	1256	—	-0.9 to 1.1	—	-1.8 to 2.1	—	1.039
GNSS+leveling	1255	358	-1.0 to 1.1	-2.7 to 2.7	-1.8 to 2.1	-2.4 to 2.3	1.017

* Rejected leveling observation to spur station PTS 35 with normalized up residual magnitude = 6.6

** Rejected one of six GNSS vectors to station CORVALLIS MAG with up residual magnitude = 3.1 cm

After rejecting the leveling observation to PTS 35, another minimally constrained adjustment was performed (fourth row in Table 4.4), resulting in $\sigma_0 = 1.006$, which is statistically equal to 1 at the 5% significance level. However, one of the GNSS vectors had a residual of 3.1 cm, whereas all others (both leveling and GNSS) were within ± 2.7 cm. This vector was one of six tied to station CORVALLIS MAG, and the other five were all within 1.5 cm. Thus, this single vector was considered an outlier and rejected.

It is notable that the problem at PTS 35 was not detectable in the leveling-only network, since it was on a spur that was leveled only once. The combined observations additionally revealed a misfit with one GNSS vector to station CORVALLIS MAG. Only by combining the observations into a single network were these discrepancies found. The locations of these stations and their connecting observations are shown in the map presented in Figure 4.2b.

Unlike rejecting the leveling spur to PTS 35, rejection of the GNSS vector to CORVALLIS MAG altered the redundancy of the GNSS network (which is always the case if the observations are correlated, as they are for this GNSS network). That rejection thus altered the results of the VVHU variance estimation, yielding the new values $V_{horz} = 19.015$ and $V_{up} = 7.709$. Using these updated variance factors, a final minimally constrained adjustment of the combined network was performed, resulting in $\sigma_0 = 1.005$ (the last minimally constrained entry in Table 4.4). The improvement in residuals is evident, especially from the first to second GNSS+leveling adjustment (when the spur to PTS 35 was rejected), where the maximum magnitude of the normalized residuals decreased from 6.6 to 2.3.

Histograms of GNSS only, leveling only, and GNSS+leveling up residuals are shown for the final minimally constrained adjustments in Figure 4.10. This plot clearly shows the greater precision of leveling as compared to GNSS. The residuals for the leveling-only network were approximately 4 times more precise than the residuals for the GNSS-only network. By including the leveling observations with the GNSS vectors in the network adjustment, the precision of the up residuals nearly doubled for the GNSS+ leveling network versus the GNSS-only network.

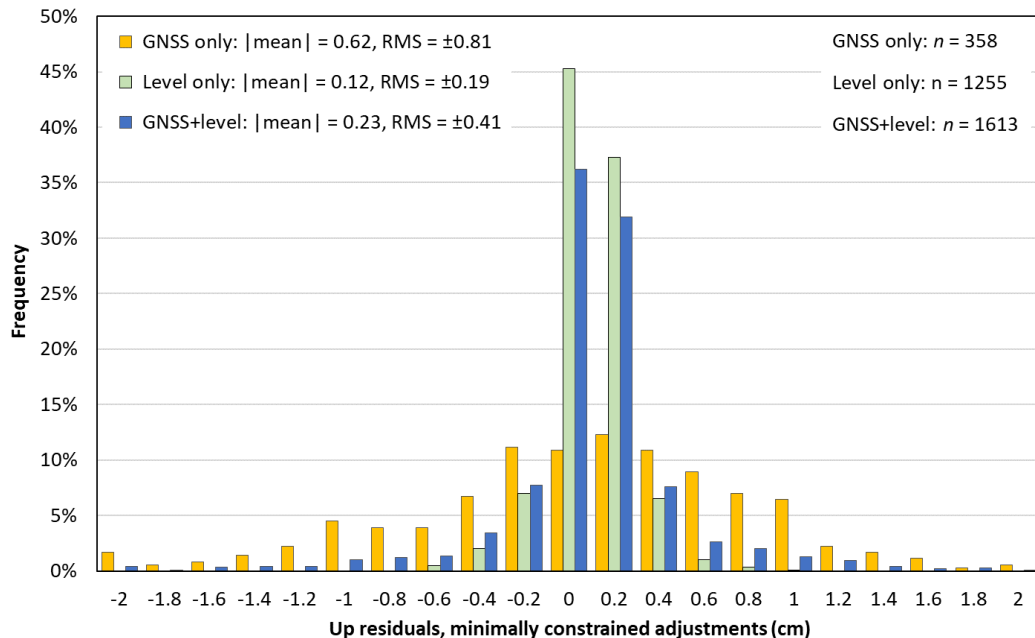


Figure 4.10. Up residuals for minimally constrained adjustments of GNSS-only, leveling-only, and GNSS+leveling networks.

Although not shown in Figure 4.10, the difference by observation type is less marked for normalized residuals, because the residuals were divided by their *a priori* error estimates. Although normalizing decreases the difference in residuals between observation types, the normalized leveling residuals were nearly twice as precise as the GNSS residuals, and the combined adjustment normalized residuals were about 1.5 times more precise those of the GNSS-only network.

4.6.2 Fully Constrained Separate and Combined GNSS+Leveling Adjustments

Using the networks from the final minimally constrained adjustments, fully constrained GNSS-only, leveling-only, and GNSS+leveling adjustments were performed. These adjustments were constrained stochastically to the stations listed in Table E.1: 18 stations (including 7 CORS) for the GNSS-only and GNSS+leveling networks, and 9 stations for the leveling-only network.

A summary of the three constrained adjustment results is shown in the lower part of Table 4.4. All had $\sigma_0 \approx 1.0$ and passed the χ^2 and F statistical hypothesis tests at the 5% significance level. This finding provides evidence that the estimated *a priori* variances and covariances for the observations and constraints were reasonable. Importantly, this demonstrates that the *combined* GNSS and leveling observations were appropriately weighted with respect to one another.

Table 4.5 provides height accuracies for the final minimally and fully constrained combined adjustments. It gives results for all 1062 stations, as well as for 1022 stations with only leveling observations, 23 stations with only GNSS observations, and 17 stations with both leveling and GNSS observations. Although ellipsoid height accuracies for the minimally constrained adjustment are included, they are of limited use since they were a function of observation error propagation from a single tightly constrained station (assigned a standard deviation of 0.01 cm in all components). Despite this, there was only slight change in the accuracies from the minimally to the fully constrained adjustment. The median network accuracy of the entire combined constrained network was 1.973 cm (at 95% confidence), due mostly to the large number of stations with only leveling observations (1022), compared to 40 stations with GNSS observations. The 1022 stations with only leveling observations had a median network accuracy of 2.023 cm, versus about half that (~ 0.9 cm) for the 40 stations with GNSS observations. Although leveling-only stations had worse accuracies than those with GNSS, stations with both GNSS and leveling had slightly better accuracies than those with only GNSS.

As observed in previous adjustments, the situation with local accuracies was reversed: leveled-only stations had local accuracies about twice as good (median of 0.661 cm) as those with GNSS observations (median of about 1.1 cm). Not surprisingly, the local accuracy was somewhat better (lower) for GNSS with leveling (1.007 cm) than GNSS alone (1.210 cm).

Table 4.5. Adjusted ellipsoid height accuracies for final minimally and fully constrained combined leveling and GNSS adjustments. The fully constrained stations are listed in Table E.1.

Adjustment	Final minimally constrained				Fully constrained			
Number of stations	All	GNSS-only	Level-only	GNSS+level	All	GNSS-only	Level-only	GNSS+level
Total	1062	23	1022	17	1062	23	1022	17
<i>Constrained</i>	1	0	0	1	18	9	0	9
Network and local accuracies, cm (95% confidence)								
<i>Network accuracies</i>								
Number	1061*	23	1022	16*	1062	23	1022	17
Min	0.61	0.68	0.61	0.85	0.46	0.46	0.71	0.61
Max	5.74	2.66	5.74	1.54	5.75	2.65	5.75	1.46
Median	2.031	1.106	2.061	1.056	1.973	0.925	2.023	0.844
Std dev	±0.990	±0.590	±0.985	±0.165	±1.017	±0.668	±1.007	±0.197
<i>Local accuracies (maximum distance 100 km; distant CORS excluded)</i>								
Number	1056	17	1022	17	1056	17	1022	17
Min	0.28	0.92	0.28	0.90	0.28	0.81	0.28	0.88
Max	2.66	2.66	2.22	1.75	2.69	2.69	2.25	1.72
Median	0.653	1.237	0.653	1.126	0.661	1.210	0.661	1.007
Std dev	±0.313	±0.527	±0.287	±0.184	±0.314	±0.576	±0.290	±0.193

* Minimally constrained station excluded.

Median network and local accuracies (at 95% confidence) are summarized in Figure 4.11 for all permutations of constrained adjustments (GNSS only, leveling only, and GNSS+leveling), with accuracies grouped by connecting observation type. Local accuracies were not computed for vectors longer than 100 km, so the six distant CORS were excluded. Median leveling network accuracies improved (decreased) when their observations were included in a network adjustment with GNSS observations. This occurred even for the 1022 leveled marks that had no GNSS observations (decreased from 2.26 to 2.02 cm), but it was especially marked for the 17 leveled stations with GNSS (from 1.36 to 0.84 cm). For leveled marks with no GNSS ties, the leveled local accuracies were scarcely affected at all by including GNSS (they improved slightly, from

0.68 to 0.66 cm), but the local accuracies got noticeably larger for the 17 leveled stations with GNSS ties (increased from 0.74 to 1.01 cm).

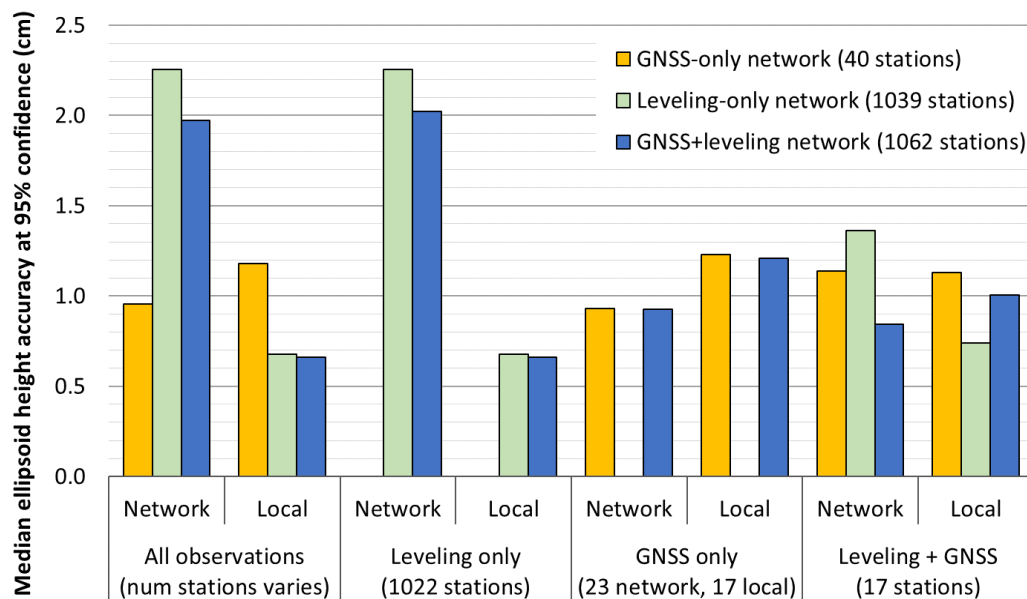


Figure 4.11. Median ellipsoid height network and local accuracies from constrained adjustments for stations in GNSS-only, leveling-only, and GNSS+leveling networks, grouped by connecting observation type.

For GNSS stations with no connecting leveling observations, adding leveling observations to the network caused essentially no change in median network accuracy, and only a very slight decrease in median local accuracy. But median accuracies noticeably improved (got smaller) at GNSS stations in a combined adjustment when leveling observations were connected, decreasing from 1.14 to 0.84 cm for network accuracies, and from 1.13 to 1.01 cm for local accuracies.

Network and local accuracies for individual stations exhibit the same overall characteristics as the aggregated median results in Figure 4.11. All 16 stations with leveled ties had a decrease (improvement) in both leveled and GNSS network accuracies (average decrease 0.8 cm for leveling and 0.2 cm for GNSS). The decrease was especially pronounced for the two leveled

accuracies at stations J 99 and OX (decreased by 2.3 and 2.7 cm, respectively); see Figure 4.12 for their locations. These two stations had large leveled network accuracies (3.7 and 3.8 cm, respectively) because they are far away from constrained stations. Network accuracies of 18 GNSS stations with no leveled ties were largely unaffected in the combined adjustment; some increased slightly, some decreased slightly, but overall there was effectively no change

Local accuracies of all leveled stations increased in the combined adjustment, except for constrained station G 287 and station J 99. Both of these stations are the only 2nd order, class 0 leveled marks in the network that have GNSS ties. Conversely, the GNSS local accuracies decreased (improved) for all stations in the combined network, whether or not the station had leveled ties. The local accuracy decrease was typically more pronounced for GNSS stations with leveled observations (average decrease of 0.2 cm vs. 0.09 cm for stations without leveling observations), but they all decreased nonetheless. This illustrates the beneficial effect that leveling has on GNSS local accuracies when they are combined in a simultaneous adjustment.

For all 1022 leveled-only stations, the network accuracy decreased (improved) by -0.09 to -2.58 cm, with an average of -0.33 cm. Except for a single station, TBM 173 (AZ9323), all local accuracies changed by -0.004 to -0.226 cm, with an average of -0.02 cm (nearly zero). The local accuracy of TBM 173 increased by 0.45 cm because it was the station connected to end-of-spur station PTS 35. When that connection was rejected, TBM 173 became the end of the spur, and its local accuracy increased due to loss of one of its two connecting observations.

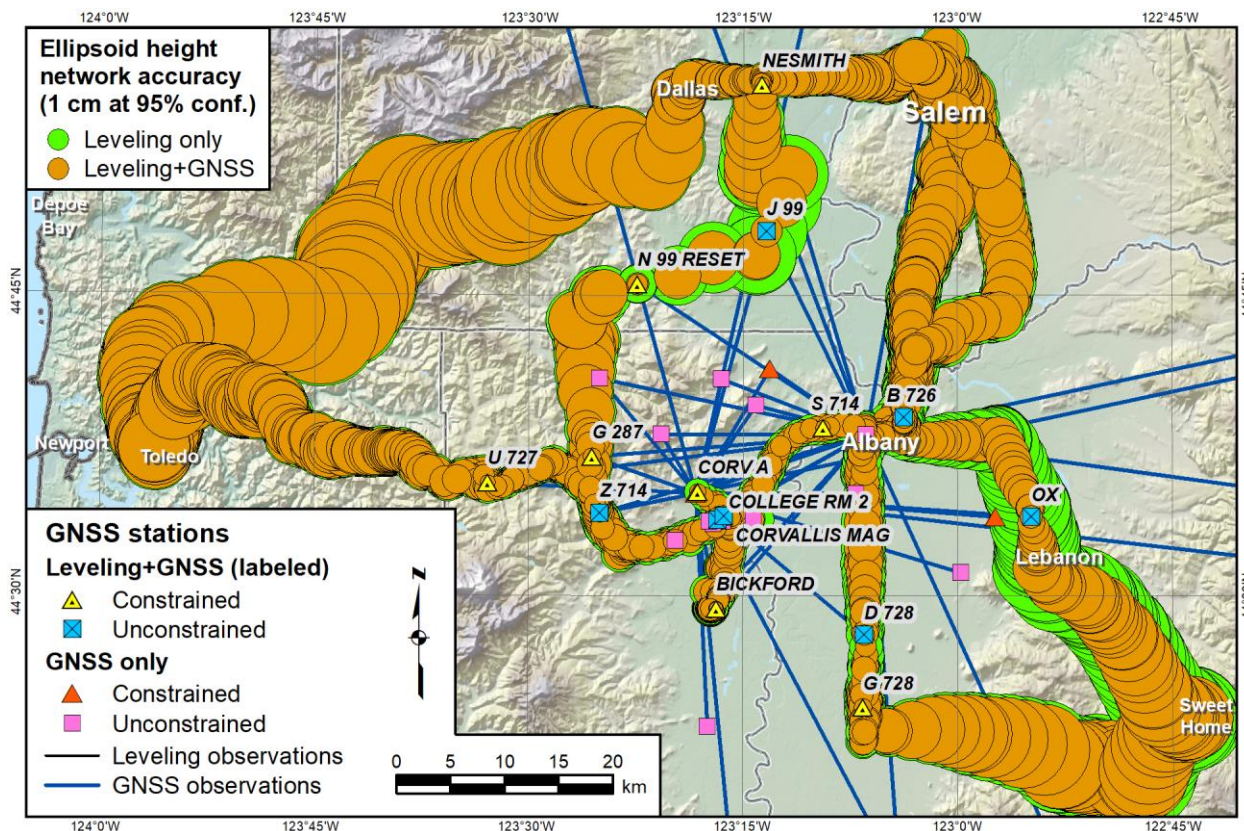


Figure 4.12. Map showing leveling network ellipsoid height accuracies for leveling-only (green) and GNSS+leveling (orange) constrained adjustments. Leveling station symbol sizes are proportional to accuracy (legend shows symbol size for 1 cm accuracy).

The spatial distribution of the change in leveling network accuracies due to adding GNSS observations is shown symbolically in the map in Figure 4.12. Without GNSS, the lack of redundancy in leveling caused the errors to increase systematically through a chain of leveling observations. The leveling observation error accumulated until either a constrained station or a connecting leg of leveling observations increased the redundancy. When GNSS observations were introduced, the GNSS station—even when not constrained—added redundancy that suppressed the growth of error. This is particularly evident at unconstrained GNSS+leveling stations J 99 and OX. Note the substantial decrease (improvement) in accuracy simply due to the additional redundancy provided by GNSS. At other locations, the leveling-only and

GNSS+leveling accuracies were about the same, since both networks used the same constraints (with the same weights). Additional redundancy also improves the robustness of the overall network, making it less susceptible to blunders and other systematic errors.

The network and local ellipsoid height accuracies of the final constrained GNSS+leveling adjustment are shown in the top map of Figure 4.13 for the 34 local GNSS stations. There are too many leveling-only stations (1022) to depict on a map or table on a printed page, so a selected subset of 37 is provided in the bottom map of Figure 4.13. The network and local accuracy values for all 34 GNSS stations and the selected 37 leveling-only stations are given in Tables E.2 and E.3, respectively (in Appendix E), along with the final adjusted ellipsoid heights (and orthometric heights based on TxGEOID16B). The accuracies are *a posteriori* values derived from the adjustment by formal error propagation and scaled by the adjustment in $\sigma_0 = 1.017$ (as shown in Table 4.4), and further scaled to 95% confidence.

The maps in Figure 4.13 show ellipsoid height network and local accuracies sized proportionally by their magnitudes, with the same scale for both maps. In the top map, the network accuracies are slightly smaller than the local accuracies for all 34 GNSS stations. The ratio of network to local accuracy ranges from 0.53 (CORV CORS) to 0.98 (J 54), with mean ratio of 0.84. Hence, for GNSS stations, the network accuracy symbols are shown on top of those for local accuracies.

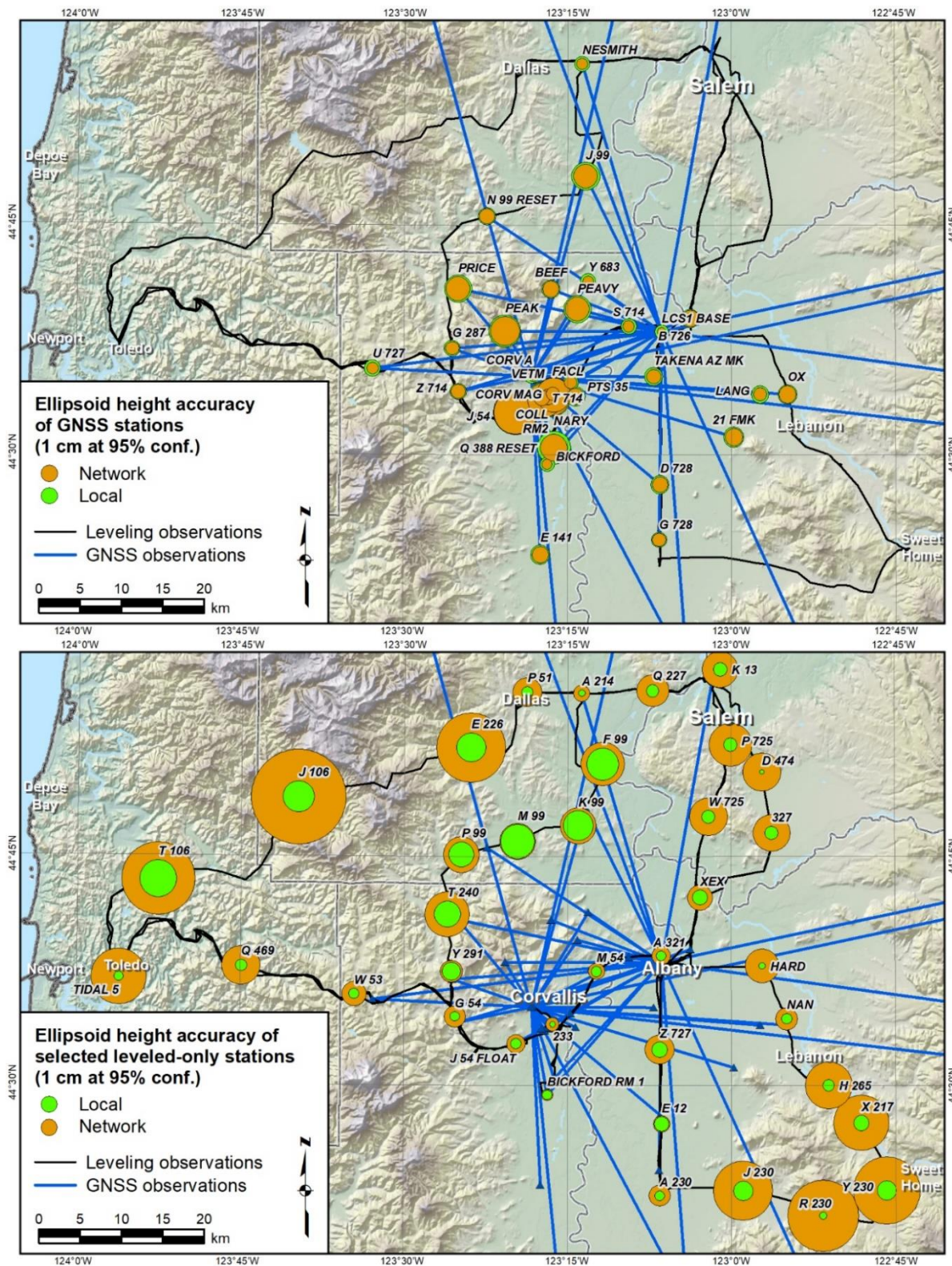


Figure 4.13. Network and local accuracies of the 34 local GNSS station in Table 6.12 (top map) and 37 (of 1022) selected leveled-only stations in Table 6.13 (bottom map).

The bottom map of Figure 4.13 shows the subset of 37 leveled-only stations. For this map, the local accuracy symbols are shown on top of the network accuracy symbols, since local accuracies are smaller for all stations (opposite of the relationship for GNSS stations). These stations were selected to show representative accuracy distributions, along with the extremes.

Up to this point, the discussion has focused on the vertical component of accuracies. But horizontal local and network accuracies were also determined by formal error propagation for GNSS stations in the GNSS-only and GNSS+leveling adjustments. The expectation is that combining the leveling and GNSS observations should have no effect on horizontal accuracies (or coordinates). However, that is not entirely clear because of the correlation between horizontal and vertical components of GNSS observations. Dennis *et al.* (2018) conclude it is likely that combining leveling with GNSS in the manner done for this study had negligible effect on the estimated horizontal network and local accuracies.

4.6.3 Final Heights from Combined GNSS and Leveling Adjustments

Combining the leveling and GNSS observations into a single simultaneously-adjusted network yielded ellipsoid heights different from those of the separately adjusted networks, even when the same heights were constrained using the same weights. The changes in ellipsoid heights are summarized in Table 4.6 for minimally and fully constrained adjustments. Station PTS 35 is not included in the leveling statistics because its (single) leveled observation was rejected in the combined adjustment, as described previously. If it was included, it would overwhelm the statistics for leveling-only change in Table 4.6, since its height decreased by 14.0 cm.

Even with PTS 35 excluded, the change in ellipsoid heights are in general greater for the leveling-only network. As expected, this was especially the case for the minimally constrained

adjustment, with leveling-only differences from -0.7 to +7.0 cm (mean +1.73 cm), versus from -1.3 to +1.5 cm (mean +0.26 cm) for the constrained adjustment differences. In contrast, the change in GNSS-only network heights remained about the same for both minimally and fully constrained adjustments. Both had a difference range of about 1.2 to 1.3 cm, with only a slight vertical shift of +0.32 cm (the difference of the mean differences). The large discrepancy in differences between the minimally and full constrained adjustments for leveling-only and GNSS-only networks was a result of the much greater redundancy of GNSS, which provided multiple “anchor points” that were missing from the minimally constrained leveling-only network.

Table 4.6. Change in ellipsoid height and horizontal coordinates from separate to combined minimally and fully constrained adjustments (GNSS+leveling minus GNSS- and leveling-only).

	Change in ellipsoid height (cm)		Change in horizontal coordinates (cm)		
	GNSS-only	Leveling-only	Δ North	Δ East	Δ Horizontal
<i>Minimally constrained adjustments</i>					
Number	39*	1037*†	39*	39*	39*
Minimum	-1.3	-0.7	-0.03	0.00	0.00
Maximum	0.0	7.0	0.09	0.09	0.09
Mean	-0.39	1.73	0.019	0.013	0.029
Std deviation	± 0.24	± 1.66	± 0.023	± 0.018	± 0.023
<i>Fully constrained adjustments</i>					
Number	40	1038†	40	40	40
Minimum	-0.9	-1.3	-0.03	-0.02	0.00
Maximum	0.3	1.5	0.09	0.02	0.09
Mean	-0.07	0.26	0.005	-0.002	0.008
Std deviation	± 0.20	± 0.52	± 0.018	± 0.008	± 0.018

* Minimally constrained station S 714 not included.

† Station PTS 35 omitted because leveling observation rejected from final combined adjustment.

Table 4.6 also presents change in horizontal GNSS coordinates from the separate to combined adjustments, even though the expectation is that there should be no change. Indeed, the

horizontal changes were essentially negligible, with a maximum of 0.09 cm for both the minimally and fully constrained networks. The maximum occurred at station CORVALLIS MAG (which included level ties). The change was zero for 11 and 31 of the 40 GNSS stations for the minimally and fully constrained networks, respectively. These changes may have been due to computational numerical precision, or small correlation between up and horizontal, or both. In any event, they were small enough to ignore, as was the case for change in horizontal network accuracies.

Figure 4.14 presents two maps of the change from leveling-only to GNSS+leveling results. The top map is for minimally constrained adjustments, and the bottom for fully constrained adjustments. The largest changes occurred for the leveling-only heights, especially for the minimally constrained (free) adjustment, as shown in the top map. The largest change (+7.0 cm) for level-only ellipsoid heights to GNSS+leveling heights was at station NESMITH. This station is at the north end of the network and had by far the longest leveling path length from the single constrained station, S 714 (near the center of the leveling network), and thus it had the largest number of leveling observations for accumulating differences. The next largest (+3.3 cm) was at J 99, near NESMITH and also with a long path length. After that, the correlation between path length and difference is less clear, in part because of the large number of overlapping observations in and around Corvallis and Albany. Nearly all of the differences are positive, the only exception being part of the large loop on the southeast side of the network that includes station OX, where the maximum negative difference occurred (only -0.7 cm). All of the GNSS-only differences with the combined network were negative and quite uniform (mean -0.39 cm, standard deviation ± 0.24 cm), especially for the GNSS station with no leveling ties.

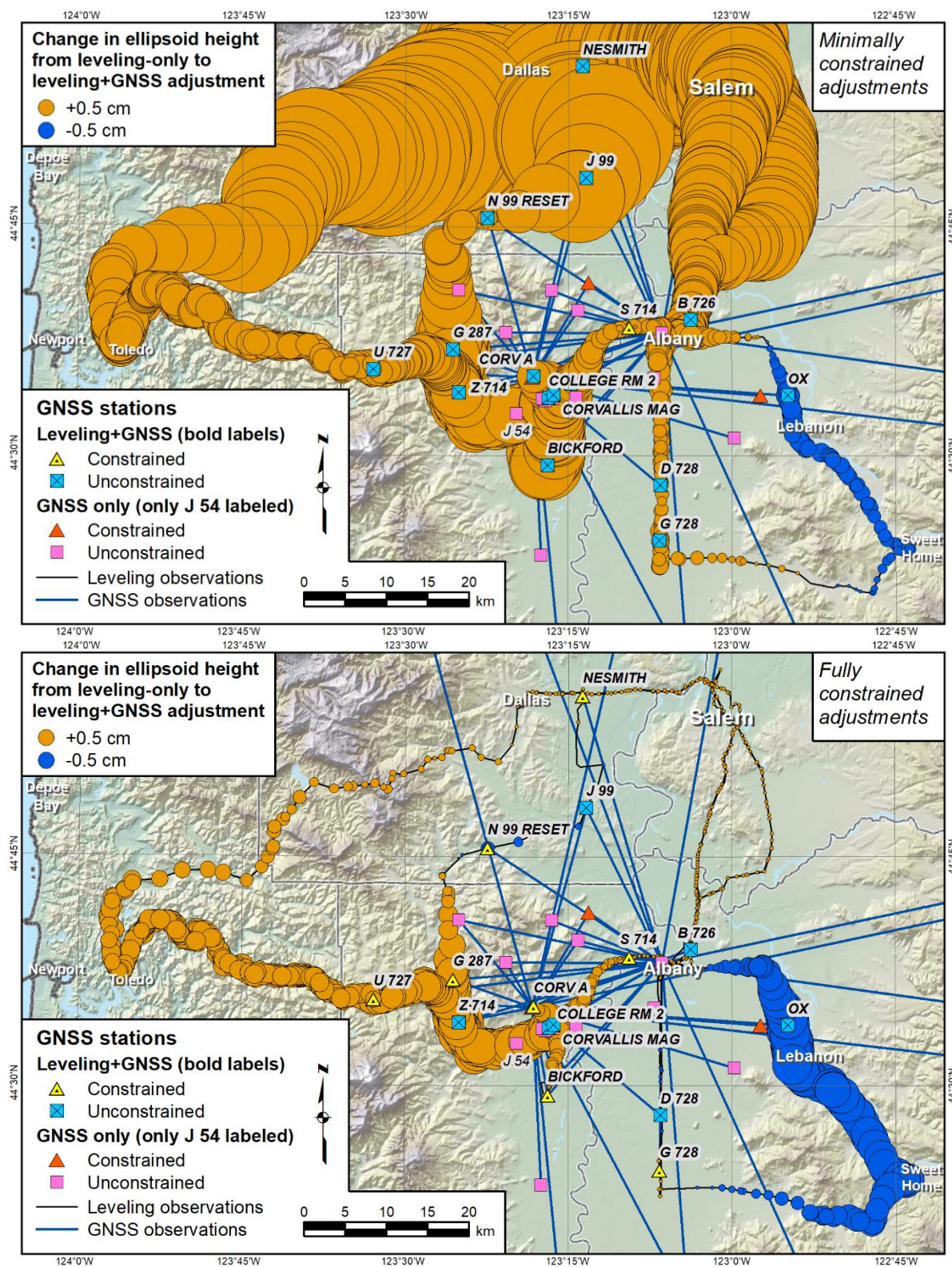


Figure 4.14. Changes in adjusted ellipsoid heights from leveling-only to GNSS+leveling network for minimally (top) and fully (bottom) constrained adjustments.

The change in ellipsoid height difference between separate and combined networks for fully constrained adjustments in Figure 4.14 is striking. Nine of the GNSS with leveling stations were constrained, but all GNSS- or leveling-only heights changed. The largest change in constrained station height was +1.0 cm for the leveled-only height of G 287. The largest change in GNSS-only height was +0.3 cm for S 714, which was the constrained station for all minimally constrained adjustments in this chapter (but its change in leveled-only height was zero).

The maps in Figure 4.14 clearly show that the greatest difference in changes between the minimally and fully constrained comparisons was in the northern part of the network.

Constraining NESMITH (and to a lesser degree N 99 RESET) made the constrained leveling-only and GNSS+leveling networks very consistent for stations in the northern area. This is the expected behavior in areas where the leveled height differences are consistent with the GNSS height differences. This is illustrated at unconstrained station J 99, which is between NESMITH and N 99 RESET. Even though it was not part of the leveling-only network, its difference with the combined network decreased from +3.3 to -0.1 cm once both networks were constrained.

This conforming behavior at J 99 did not occur everywhere. Figure 4.14 shows that the largest changes in adjusted ellipsoid heights occurred at unconstrained GNSS+leveling stations Z 714 (+1.5 cm) and OX (-1.3 cm). Despite the large change at OX, its level loop still behaves as expected, with the magnitude of differences decreasing away from OX to near zero at GNSS+leveling constrained stations. Note by comparison to the top map that the magnitude of change in this loop increased in the constrained adjustment. This resulted from constraining stations at the west side of the loop, which forced height differences to increase at the unconstrained OX anchor point. A difference of 1.3 cm at OX is not surprising, given that its GNSS-only ellipsoid height network accuracy was 1.11 cm at 95% confidence.

Unfortunately, the situation in the vicinity of Z 714 does not quite comport with expectation. It is only about 5 km from constrained station G 287, and there are four other constrained stations in the general area (U 727, CORV A, BICKFORD, and T 714). Yet many of the leveled stations in the vicinity of Z 714 are about 1 cm higher than those of the leveling-only adjustment using the same constraints. The reason for the unexpectedly large differences is that the leveled-only and GNSS+leveling heights at constrained stations G 287 itself differs by +1.0 cm (and by +0.5 cm at nearby U 727 and T 714). At first blush, these appear to be excessively large differences at constrained stations, especially since the typically low redundancy of leveling allows it to “fit” control. But the situation in this area is not quite what it seems. There are actually a large number of leveling lines that crisscross one another, from leveling campaigns widely separated in time (as indicated in Figure 4.3 and Figure 4.4), resulting in more leveling redundancy than is apparent. In addition, the leveling observations have high relative accuracies over the short distances in this area. And finally, the shifts are not necessarily large in comparison to the *a priori* uncertainties (e.g., published standard deviation of 0.82 cm for G 287).

Of course, all of the constrained adjustments could have been forced to better match the coordinates of the constrained stations by assigning them greater weights (i.e., by using smaller *a priori* errors). This was not pursued because it was not deemed realistic, and there was no other known source for uncertainty estimates better than what was obtained from the NGSIDB. Moreover, the constrained adjustments passed the F-test, which indicates the constraints were realistic (likewise for constraint ratios discussed below). Much tighter constraints would almost certainly not pass such statistical tests. Finally, since the constraints for GNSS stations were 3D, if the ellipsoid height constraints were tightened, the horizontal constraints would have to be

tightened as well. Somewhat large height shifts at a few constrained stations does not justify tightly constraining all components of all constrained GNSS stations.

There is a possibility that the ~1 cm shifts observed in the west Corvallis area indicate uplift relative to the northeast part of the network (and perhaps 2-3 cm relative to the east part of the network, where shifts were downward by 1-2 cm). This is not unreasonable, given the large time span between the leveling and GNSS observations (virtually all of the leveling was done before 1988, and most was done before 1942; see Figure 4.4). However, relative uplift of 1-2 cm is on par with the estimated 95% accuracies of these marks, and such a small uplift would be extremely difficult to reliably detect. Nonetheless, this points to one of the weaknesses of the data used for this study: the large time difference between the leveling and GNSS observations.

For GNSS-only stations, the combined constrained adjustment change in height was overall much less than for GNSS with leveling observations. Changes for 8 of the 17 stations were zero (including the three constrained stations), and all others were negative, with none exceeding -0.2 cm. The largest change for GNSS+leveling stations from the GNSS-only adjustment was -0.9 cm for CORVALLIS MAG, followed by -0.6 cm for COLLEGE RM 2; the change in leveled heights were also fairly large for both stations, but in the opposite direction (about +1.0 cm).

Station J 54 changed by only -0.1 cm, but this result is based only on GNSS observations. Recall that this station also had level ties, but it was “floated” (i.e., treated as a different station) for the leveling, because it appears to have moved since the leveling was performed (most recently in 1987). Interestingly, its leveled height in the level-only network matched its GNSS height in the GNSS-only network (to the nearest mm), yet its leveled-only height in the combined

GNSS+leveling network changed by +1.1 cm. This change probably has little (if anything) to do with this station specifically, but rather is consistent with the change of other marks in its vicinity, as discussed above and illustrated in Figure 4.14. The changes are about +1 cm in the vicinity of J 54 (labeled), corresponding to the observed change of +1.1 cm at J 54 FLOAT.

The minimally constrained adjusted ellipsoid heights match the published ellipsoid heights quite well, with a difference range of 2.9 cm (excluding the six distant CORS). This range decreased to 2.5 cm in the constrained adjustment, and the bias also decreased (as represented by the mean difference) from -1.29 to +0.25 cm. Such behavior is expected, since all of the ellipsoid heights being compared were constrained.

Although ellipsoid heights are the output of the network adjustments performed in this chapter, the ultimate objective is combining leveling and GNSS observations to obtain orthometric heights. Ellipsoid heights were output from the adjustments, because it was considered simpler to transform leveling observations to a geometry consistent with GNSS observations than vice versa. Regardless of the method used, it was essential to make the observation types geometrically consistent to perform simultaneous least-squares adjustments.

With the final adjusted ellipsoid heights obtained, all that is required to compute orthometric heights is to subtract the geoid height, per Eq. 4.1, where h is the NAD 83 (2011) epoch 2010.00 ellipsoid height and N is the TxGEOID16B geoid height (i.e., xGEOID16B transformed to NAD 83 with the NAVD 88 trend for all of CONUS incorporated).

For estimating network accuracies of the orthometric heights, it is reasonable to assume that the leveling, GNSS, and TxGEOID16B errors are uncorrelated. Therefore, determining the network orthometric heights accuracies can be done using SLOPOV:

$$\sigma_H = \sqrt{\sigma_h^2 + \sigma_N^2}. \quad (4.16)$$

The estimated uncertainty (standard deviation) of the adjusted ellipsoid height, σ_h , was obtained from the final constrained adjustment of the GNSS+leveling network through formal error propagation. As stated earlier, an estimated uncertainty of the geoid height, σ_N , is apparently about 1-3 cm for “modern” geoid models, based on work done using data from 2011 (Smith *et al.*, 2013). In addition, it is the objective of NGS to develop a gravimetric geoid model for NAPGD2022 with $\sigma_N = 1$ cm (or better) in most areas of the NSRS. Although σ_N is not known for TxGEOID16B, knowing it is not of great importance for this study, since it can simply be accounted for with SLOPOV.

Relative or “local” orthometric height accuracy (of height differences), $\sigma_{\Delta H}$, is another matter entirely. Although $\sigma_{\Delta H}$ is likely of greater interest in most practical surveying and engineering applications, it is a more difficult problem because unlike $\sigma_{\Delta h}$ (local ellipsoid height error), $\sigma_{\Delta H}$ is not an output of the formal error propagation of the network adjustment. Therefore some other method must be used to estimate $\sigma_{\Delta H}$. An approach using GLOPOV was developed and discussed by Dennis *et al.* (2018), but it is quite involved and somewhat tentative, so it is not presented here. However, determination of a method for reliably estimating $\sigma_{\Delta H}$ is important and a worthwhile topic for future research.

4.7 SUMMARY AND CONCLUSIONS

GNSS is increasingly being used to determine orthometric heights. That trend will accelerate when NGS replaces NAVD 88 with NAPGD2022. When that occurs, the primary means of determining orthometric heights will be through the use of Eq. 4.1, by measurement of ellipsoid heights with GNSS and obtaining geoid heights from the associated gravimetric geoid model,

GEOID2022. This approach is in stark contrast to NAVD 88, which was defined by, and primarily accessed through, differential leveling. Leveling can give height differences that are much more accurate than GNSS over short distances (a few to several km), so there is no question that leveling will still be used after the adoption of NAPGD2022. The question instead is how leveling can be most effectively used in the NAPGD2022 paradigm.

In an attempt to answer that question, a method was developed to integrate GNSS and leveling observations into a spatially and stochastically consistent 3D geodetic model. The purpose was to create a single network of the combined observations for performing simultaneous least squares adjustments. This approach requires that the observations have a consistent geometry and be correctly weighted. How these two requirements were met is summarized below.

1. Mathematical transformation of observations to a consistent geometry. The GNSS vectors, leveled geopotential differences, and NGS experimental geoid model xGEOID16B were transformed to a common geometric frame, in this case the current realization of NAD 83. The GNSS delta ECEF vectors were transformed from IGS08 at the epochs of data collection (2014-2015) to NAD 83 at epoch 2010.00 using the NGS program *HTDP*.

After transforming xGEOID16B from IGS08 to NAD 83, the bias and tilt trend of the NAVD 88 datum surface was estimated and added to the NAD 83 version of xGEOID16B to create a transformed version, called TxGEOID16B. The intent was for TxGEOID16B to be consistent with NAVD 88 and yet preserve the local slope of xGEOID16B itself.

Using the NAVD 88 surface gravity model and TxGEOID16B, the leveling geopotential differences were converted to ellipsoid height differences. These height differences (and their uncertainties) were then rotated into the same ECEF geometry as the GNSS vectors.

2. Appropriate weighting of observations. Because GNSS observations are typically highly optimistic, the VVHU option in the NGS program *ADJUST* was used to scale the vector uncertainties such that they are consistent with the geometric closure of the minimally constrained GNSS network. The horizontal and vertical components were evaluated through iterative adjustments, until both components (and the entire network) have a standard deviation of unit weight of $\sigma_0 = 1$.

Leveling a priori errors were evaluated and scaled in a similar manner, through iterative adjustments with successive observation rejections, until $\sigma_0 = 1$ for a specific combination of error scalar and observation rejection criterion.

An essential but difficult part of the process was determining geoid slope error, $\sigma_{\Delta N}$. This was necessary because $\sigma_{\Delta N}$ was part of the error budget of the transformed leveling observations. Five geoid slope error models were empirically developed by performing minimally constrained adjustments of the ECEF leveling network to determine parameters corresponding $\sigma_0 = 1$. After evaluation, one (Model 5) was selected for use in the combined GNSS and leveling network adjustments. This model estimated the increase in $\sigma_{\Delta N}$ as a function of the square root of distance between leveled marks.

After the observations and their uncertainties had been transformed into a common geometry, combined adjustments were performed. These adjustments yielded ellipsoid heights (and their formally propagated uncertainties) that compared favorably with results from leveling-only and GNSS-only adjustments. The combined leveling and GNSS and leveling network adjustment had several advantages over separately adjusted networks, as summarized below.

- The approach was useful for identifying marks with published leveled heights that were inaccurate or outdated; for example, one mark (PTS 35) that had been disturbed since it was leveled was easily identified because its adjusted leveling residual was six times bigger than its estimated *a priori* standard deviation. A GNSS outlier (to mark CORVALLIS MAG) was also exposed by combining the observations into a single network.
- Since leveling over short distances is highly precise, combining leveling with GNSS more than doubled the precision of the adjusted residuals in the up component in the network, from a mean absolute value of 0.60 cm for GNSS alone to 0.23 cm for GNSS+leveling.
- Adding GNSS to leveling helped tie the network to the reference frame and reduce (improve) network accuracies. The ellipsoid height network accuracies estimated from the GNSS+leveling network adjustment were consistently smaller and more precise than the network accuracies from the leveling-only network. The median network accuracy of the leveling observations decreased from 2.3 to 2.0 cm from the leveling-only to GNSS+leveling adjustment. The additional redundancy especially improved network accuracy at leveled stations with GNSS ties, even for stations that were not constrained (e.g., from 3.8 to 1.1 cm at unconstrained station OX).
- Conversely, adding leveling to GNSS decreased (improved) the GNSS local accuracies, with no detrimental impact on the leveling local accuracies. The median local accuracy of GNSS observations decreased from 2.7 to 1.1 cm from the GNSS-only to the GNSS+leveling adjustment. Yet the median local accuracies of the leveling observations were essentially unchanged (and actually decreased slightly), from 0.68 cm in the leveling-only adjustment to 0.66 cm in the combined adjustment.

- The method enables computation of final orthometric heights directly from the adjusted ellipsoid height and the geoid model using Eq. 4.1. If the geoid height uncertainty is known, orthometric height network accuracy can be computed from the ellipsoid height uncertainty using SLOPOV (Eq. 4.16). A method for estimating orthometric height local accuracy was not proposed, although work has been done on this by Dennis *et al.* (2018) using GLOPOV.

In summary, the approach presented here for combining properly weighted leveling and GNSS observations into a single, integrated geodetic framework appears viable and robust. The strength of one observation type makes up for the weakness of the other: the high redundancy of GNSS and its largely distance-independent errors compensates for the low redundancy of leveling and its relatively rapid error growth with distance. Likewise, the high relative local accuracy of leveling compensates for the lower vertical accuracy of GNSS over short distances.

This study combined recent GNSS observations with much (decades) older leveling observations. Encouragingly, despite the large time difference, the leveling data overall showed remarkable consistency with the recent GNSS observations. This demonstrates that even “old” leveling observations may still have utility in NAPGD2022. However, there were some apparent systematic differences with GNSS, with both the mark-to-mark leveling observations and published heights. It is not clear how much these differences are due to the relative movement of marks within the study area, and that ambiguity somewhat clouds the interpretation of the results. For that reason, it is recommended that future work include analysis of networks with (near) simultaneous leveling and GNSS observations, to remove the time difference variable. Nonetheless, analysis of other networks combining “old” leveling with “new” GNSS is also recommended. This would be particularly useful in tectonically stable areas, to see whether

behavior occurs that is similar to what was observed in the (relatively tectonically active) western Oregon study area used here. Given the enormous volume of existing leveling data in the NGSIDB (over 2 million leveling observations), evaluation of temporal effects would help NGS determine the role of historic leveling observations in NAPGD2022. A final, but noteworthy, benefit of additional studies using the method presented here is that it can serve as a comparison or validation of other methods being considered by NGS to combine GNSS and leveling for NAPGD2022.

4.8 REFERENCES

- ADJUST* [Computer software]. National Oceanic and Atmospheric Administration, National Geodetic Survey, Silver Spring, MD.
- Armstrong, M.L., Schenewerk, M.S., Mader, G., Martin, D., Stone, B., and Foote, R., 2015. *OPUS Projects: Online Positioning User Service Baseline Processing and Adjustment Software User Instructions and Technical Guide*, Ver. 2.5, National Oceanic and Atmospheric Administration, National Geodetic Survey, Silver Spring, MD.
- Balazs, E.I., and Young, G.M., 1982. “Corrections Applied by the National Geodetic Survey to Precise Leveling Observations”, *NOAA Technical Memorandum, NOS NGS 34*. National Oceanic and Atmospheric Administration, National Geodetic Survey, Silver Spring, MD. <https://www.ngs.noaa.gov/PUBS_LIB/NOAA-TM-NOS-NGS-34.pdf> (Oct 1, 2016).
- Blackwell, J. and Hilla, S., 2000. *PAGE-NT User’s Manual*. National Oceanic and Atmospheric Administration, National Geodetic Survey, Silver Spring, MD. <<ftp://ftp.ngs.noaa.gov/pub/pnt6/>> (Oct. 1, 2016).
- Bossler, J.D., 1984. *Standards and Specifications for Geodetic Control Networks*, Federal Geodetic Control Committee (now the Federal Geodetic Control Subcommittee), USA, 25 pp. <http://www.ngs.noaa.gov/FGCS/tech_pub/1984-stds-specs-geodetic-control-networks.pdf> (Oct. 1, 2016).
- Dennis, M.L., 2019. (in review) “The National Adjustment of 2011: Alignment of passive GNSS control with the three frames of the North American Datum of 1983 at epoch 2010.00: NAD 83 (2011), NAD 83 (PA11), and NAD 83 (MA11).” *NOAA Technical Report NOS NGS 65*, National Oceanic and Atmospheric Administration, National Geodetic Survey, Silver Spring, MD.
- Dennis, M.L., Gillins, D.T., Parrish, C.E., Olsen, M., Park, J., and Kim, S.K., 2018. *Towards Optimizing the Determination of Accurate Heights using GNSS, Volume 2: Integration of Differential Leveling and GNSS*, Oregon State University, Cooperative Institute for Marine

- Resources Studies, volume 2 of report for National Oceanic and Atmospheric Administration, National Geodetic Survey, Silver Spring, MD.
- Eckl, M.C., Snay, R.A., Soler T., Cline, M.W., and Mader G.L., 2001. "Accuracy of GPS-derived relative positions as a function of interstation distance and observing-session duration." *J. Geod.*, 75(12), 633-640.
- Erol, B., and Çelik, R., 2005. "Modelling local GPS/leveling Geoid with the assessment of inverse distance weighting and geostatistical kriging methods." Proc., ISPRS Congress, Istanbul, Turkey, Citeseer.
- Esri, 2016. "A quick tour of geoprocessing tool references." Esri, Redlands, CA. <<http://desktop.arcgis.com/en/arcmap/latest/tools/main/a-quick-tour-of-geoprocessing-tool-references.htm>> (Oct. 10, 2016).
- FGDC (Federal Geographic Data Committee), 1998. *Geospatial Positioning Accuracy Standards*, FGDC-STD-007.2-1998, Federal Geographic Data Committee, Reston, Virginia, USA, 128 pp., <www.fgdc.gov/standards/projects/FGDC-standards-projects/accuracy/> (Oct 3, 2018) [includes Reporting Methodology (Part 1), Standards for Geodetic Networks (Part 2), National Standard for Spatial Data Accuracy (Part 3), Standards for Architecture, Engineering, Construction (A/E/C) and Facility Management (Part 4), and Standards for Nautical Charting Hydrographic Surveys (Part 5)].
- Fotopoulos, G., 2005. "Calibration of geoid error models via a combined adjustment of ellipsoidal, orthometric and gravimetric geoid height data." *J. Geod.*, 79(1-3), 111-123.
- Fotopoulos, G., Kotsakis, C., and Sideris, M. G., 2003. "How accurately can we determine orthometric height differences from GPS and geoid data?" *J. Surv. Eng.*, 10.1061/(ASCE)0733-9453(2003)129:1(1), 1-10.
- Fury, R.J., 1999. "National Geodetic Survey (NGS) Gravity Prediction Methodology." National Oceanic and Atmospheric Administration, National Geodetic Survey, Silver Spring, MD. <http://www.ngs.noaa.gov/TOOLS/Gravity/grav_method.html> (Dec. 12, 2016).
- Ghilani, C.D., 2010. *Adjustment Computations*, 5th Ed., John Wiley & Sons, Inc., Hoboken, NJ.
- Gillins, D.T., and Dennis, M.L., 2017. "Inclusion of Leveling with GNSS Observations in a Single, 3-D Geodetic Survey Network Adjustment." In: *Proc. of FIG (International Federation of Surveyors) Working Week*, FIG, Helsinki, Finland.
- Gillins, D.T., and Eddy, M. J., 2016. "Comparison of GPS Height Modernization Surveys Using OPUS-Projects and Following NGS-58 Guidelines." *J. Surv. Eng.*, 10.1061/(ASCE)SU.1943-5428.0000196 , 05016007.
- Gillins, D.T., and Eddy, M.J., 2015. "An evaluation of NGS-58 and OPUS Projects: Methods for determining accurate ellipsoidal heights with GPS." National Oceanic and Atmospheric Administration, National Geodetic Survey, Silver Spring, MD.

- Hackl, M., 2012. "GPS analysis: strain, transients, and colored noise." Ph.D. dissertation, Ludwig Maximilian University of Munich, Germany. <https://edoc.ub.uni-muenchen.de/14627/3/Hackl_Matthias.pdf> (Sep 25, 2018)
- Hardy, R.L. and Nelson, S.A., 1986. "A multiquadric-biharmonic representation and approximation of disturbing potential." *Geophysical Research Letters*, 13(1), pp. 18-21.
- Hartman, K.R., 1995. "Flight Mechanics/Estimation Theory Symposium." *NASA Conference Publication 3299*, NASA Technical Archives. <<https://ntrs.nasa.gov/archive/nasa/casi.ntrs.nasa.gov/19950021342.pdf>> (Sep 25, 2018)
- Herring, T., (ed.), 2009. *Treatise on Geophysics, Volume 3: Geodesy*. Elsevier.
- Hofmann-Wellenhof, B., and Moritz, H., 2006. *Physical Geodesy*, Springer Science & Business Media, New York.
- Holdahl, S.R., Strange, W.E., and Harris, R.J., 1986. "Empirical Calibration of Zeiss Nil Level Instruments to Account for Magnetic Errors." *NOAA Technical Memorandum, NOS NGS 45*. National Oceanic and Atmospheric Administration, National Geodetic Survey, Silver Spring, MD.
- Jekeli, C., 2000. "Heights, the geopotential, and vertical datums." Rep. 459, Ohio State Univ., Geodetic Science and Surveying, Dept. of Civil and Environmental Engineering and Geodetic Science, Columbus, OH.
- Jiang, Z., and Duquenne, H., 1996. "On the combined adjustment of a gravimetrically determined geoid and GPS levelling stations." *J. Geod.*, 70(8), 505–514.
- Kashani, I., Wielgosz, P., and Grejner-Brzezinska, D.A., 2004. "On the reliability of the VCV Matrix: A case study based on GAMIT and Bernese GPS Software." *GPS Solutions*, (2004)8:193-199. DOI 10.1007/s10291-004-0103-9.
- Khazraei, S., Nafisi, V., Amiri-Simkooei, A., and Asgari, J., 2016. "Combination of GPS and Leveling Observations and Geoid Models Using Least-Squares Variance Component Estimation." *J. Surv. Eng.*, 10.1061/(ASCE)SU.1943-5428.0000205 , 04016023.
- Kim, S-K., Park, J., Gillins, D., and Dennis, M., 2018. "On determining orthometric heights from a corrector surface model based on leveling observations, GNSS, and a geoid model." *Journal of Applied Geodesy*, Published Online: 2018-08-21 <<https://doi.org/10.1515/jag-2018-0014>> (Sep 24, 2018).
- Kotsakis, C., and Sideris, M. G., 1999. "On the adjustment of combined GPS/levelling/geoid networks." *J. Geod.*, 73(8), 412–421.
- Langbein, J., 2004. "Noise in two-color electronic distance meter measurements revisited." *Journal of Geophysical Research: Solid Earth*, 109(B4). <<https://agupubs.onlinelibrary.wiley.com/doi/10.1029/2003JB002819>> (Sep 25, 2018)
- Leick, A., Rapoport, L., and Tatarnikov, D., 2015. *GPS Satellite Surveying* (4th Edition), John Wiley & Sons, New York, New York.

- Mader, G., Schenewerk, M., Weston, N., Evjen, J., Tadepalli, K., and Neti, J., 2012. “Interactive web-based GPS network processing and adjustment using NGS’ OPUS-Projects.” In: *Proceedings of the FIG working week 2012*, Rome, Italy.
- Milbert, D.G., 1988. “Treatment of Geodetic Leveling in the Integrated Geodesy Approach, *OSU Report 396*, Ph.D. dissertation, Ohio State Univ., Columbus, OH.
- Milbert, D.G., 2009. *An Analysis of the NAD 83 (NSRS2007) National Readjustment*, National Geodetic Survey, Silver Spring, MD, <www.geodesy.noaa.gov/PUBS_LIB/NSRS2007/NSRS2007Analysis.pdf> (Oct. 24, 2016).
- Milbert, D.G., and Kass, W.G., 1987. *NOAA Technical Memorandum NOS NGS-47: ADJUST: The Horizontal Observation Adjustment Program*. National Oceanic and Atmospheric Administration, National Geodetic Survey, Silver Spring, MD <https://www.ngs.noaa.gov/PUBS_LIB/Adjust_TheHorizontalObservationAdjustmentProgram_TM_NOS_NGS_47.pdf> (Sep 24, 2018).
- NGS (National Geodetic Survey), 2007. *The GRAV-D Project: Gravity for the Redefinition of the American Vertical Datum*. National Oceanic and Atmospheric Administration, National Geodetic Survey, Silver Spring, MD <http://www.ngs.noaa.gov/GRAV-D/pubs/GRAV-D_v2007_12_19.pdf> (Oct. 1, 2016).
- NGS (National Geodetic Survey), 2014. *GEOID12B Readme File*. National Oceanic and Atmospheric Administration, National Geodetic Survey, Silver Spring, MD. <<http://www.ngs.noaa.gov/GEOID/GEOID12B/g2012Brme.txt>> (Sept. 27, 2016).
- NGS (National Geodetic Survey), 2015. “Technical Details for GEOID12/12A/12B.” National Oceanic and Atmospheric Administration, National Geodetic Survey, Silver Spring, MD. <http://www.ngs.noaa.gov/GEOID/GEOID12B/GEOID12B_TD.shtml> (Oct. 1, 2016).
- NGS (National Geodetic Survey), 2016. *NAVD 88 Gravity Computations*. National Oceanic and Atmospheric Administration, National Geodetic Survey, Silver Spring, MD. <<http://www.geodesy.noaa.gov/TOOLS/Navdgrav/navdgrav.shtml>> (Oct. 10, 2016).
- NGS (National Geodetic Survey), 2018a. *Input Formats and Specifications of the National Geodetic Survey Data Base* (the NGS “Bluebook”), three volumes and eleven annexes. National Oceanic and Atmospheric Administration, National Geodetic Survey, Silver Spring, Maryland. <<http://www.ngs.noaa.gov/FGCS/BlueBook/>> (Oct. 1, 2016).
- NGS (National Geodetic Survey), 2018b. “Technical Details for xGEOID16 Models.” National Oceanic and Atmospheric Administrations, National Geodetic Survey, Silver Spring, MD. <https://beta.ngs.noaa.gov/GEOID/xGEOID16/xGEOID16_technical_details.shtml> (Jan. 4, 2018).
- NGS (National Geodetic Survey), 2018c. *ADJUST Supplemental Documentation*. National Oceanic and Atmospheric Administration, National Geodetic Survey, Silver Spring, MD. <http://www.ngs.noaa.gov/PC_PROD/ADJUST/adjust_supplemental.txt> (Sept. 27, 2016).

- OPUS-Projects* [Computer software]. National Oceanic and Atmospheric Administration, National Geodetic Survey, Silver Spring, MD.
- Øvstedal, O., 2000. "Single Processed Independent and Trivial Vectors in Network Analysis", *Journal of Surveying Engineering*, Vol. 126, No. 1, pp. 18-25.
- Pearson, C. and Snay, R., 2012. "Introducing HTDP 3.1 to transform coordinates across time and spatial reference frames", *GPS Solut*, 10.1007/s10291-012-0255-y. <www.ngs.noaa.gov/TOOLS/Htdp/Pearson_Snay_2012.pdf> (Apr. 9, 2017)
- Rebischung, P., Griffiths, J., Ray, J., Schmid, R., Collilieux, X, and Garayt, B., 2012. "IGS08: the IGS realization of ITRF2008." *GPS Solut*, 16:483–494, DOI 10.1007/s10291-011-0248-2. <ftp://igs.cb.igs.org/pub/resource/pubs/IGS08_The_IGS_Realization_of_ITRF2008.pdf> (Oct. 22, 2018)
- Roman, D.R., Wang, Y.M., Henning, W., and Hamilton, J., 2004. "Assessment of the New National Geoid Height Model, GEOID03." *Proceedings of the American Congress on Surveying and Mapping 2004 Conference and Technology Exhibition*, Nashville, Tennessee, April 16-21.
- Roman, D.R., Wang, Y.M., Saleh, J., and Li, X., 2009. "Final National Models for the United States: Development of GEOID09." National Oceanic and Atmospheric Administration, National Geodetic Survey, Silver Spring, MD. <http://www.ngs.noaa.gov/GEOID/GEOID09/GEOID09_tech_details.pdf> (Oct. 1, 2016).
- Smith, D.A., and Milbert, D.G., 1999. "The GEOID96 high-resolution geoid height model for the United States." *J. Geod.*, 73:219–236.
- Smith, D.A., Holmes, S.A., Li, X., Guillaume, S., Wang, Y.M., Bürki, B., Roman, D.R., and Damiani, T.M., 2013. "Confirming regional 1 cm differential geoid accuracy from airborne gravimetry: the Geoid Slope Validation Survey of 2011." *J. Geod.*, 87: 885. doi:10.1007/s00190-013-0653-0.
- Snay, R., Pearson, C., and Saleh, J., 2014. *HTDP User's Guide*, Version 3.2.5. National Oceanic and Atmospheric Administration, National Geodetic Survey, Silver Spring, MD. <<http://www.geodesy.noaa.gov/TOOLS/Htdp/HTDP-user-guide.pdf>> (Sept. 27, 2016).
- Torge, W. and Müller, J., 2012. *Geodesy* (4th Edition), W. de Gruyter, Berlin.
- Vittuari, L., Tini, M. A., Sarti, P., Serantoni, E., Borghi, A., Negusini, M., & Guillaume, S., 2016. A Comparative Study of the Applied Methods for Estimating Deflection of the Vertical in Terrestrial Geodetic Measurements. *Sensors*, 16(4), 565.
- Weaver, B., Gillins, D.T., and Dennis, M., 2018. "Hybrid Survey Networks: Combining Real-Time and Static GNSS Observations for Optimizing Height Modernization," *J. Surv. Eng.* (ASCE), 05017006 <[10.1061/\(ASCE\)SU.1943-5428.0000244](https://doi.org/10.1061/(ASCE)SU.1943-5428.0000244)> (Nov 19, 2018)
- Weston, N.D., Mader, G.L., and Soler, T., 2007. "OPUS Projects – A Web-based application to administer and process multi-day GPS campaign data." *Proc. of FIG (International Federation of Surveyors) Working Week*, FIG, Hong Kong, China.

- Zilkoski, D.B., 1991. "A Priori Estimates of Standard Errors of Leveling Data." *Proceedings of the 1991 ACSM/ASPRS Annual Convention*, Baltimore, Maryland.
- Zilkoski, D.B., 2016. Personal communication. National Geodetic Survey Director (retired).
- Zilkoski, D.B., Carlson, E.E., and Smith, C.L., 2008. *NOAA Technical Memorandum NOS NGS-59, Guidelines for Establishing GPS-Derived Orthometric Heights*, Version 1.5. National Oceanic and Atmospheric Administration, National Geodetic Survey, Silver Spring, MD.
- Zilkoski, D.B., D'Onofrio, J.D., and Frakes, S.J., 1997. *NOAA Technical Memorandum NOS NGS-58, Guidelines for Establishing GPS-Derived Ellipsoid Heights (Standards: 2 cm and 5 cm)*, Version 4.3. National Oceanic and Atmospheric Administration, National Geodetic Survey, Silver Spring, MD.
- Zilkoski, D.B., Richards, J.H., and Young, G.M., 1992. "Results of the General Adjustment of the North American Vertical Datum of 1988." *Surveying and Land Information Systems*, 52(3), 133-149. <http://www.ngs.noaa.gov/PUBS_LIB/NAVD88/navd88report.htm> (Oct. 2, 2016).

5 CONCLUSIONS AND FUTURE WORK

5.1 CONCLUSIONS

The research performed for this dissertation focused on two important topics to surveying and mapping: 1) reducing conformal map projection linear distortion, and 2) integrating GNSS and leveling observations. These topics are unified in that together they contribute to defining a set of topocentric 3D coordinates as northing, easting, and orthometric height (N, E, H). The N, E components are obtained from map projections, and the H component from GNSS combined with a geoid model and leveling, to produce 3D coordinates of great practical relevance. That is especially the case for applications in engineering and surveying, where it is often required that the coordinates:

- Preserve the high relative (local) accuracy of the original observations, both horizontally and vertically.
- Provide values in a topocentric system with a practical representation of “horizontal” and “vertical.”
- Give conditions “at ground”, i.e., very similar to what would be measured directly using terrestrial methods.
- Allow integration of GNSS with leveling to leverage the strengths of each.
- Are fully and rigorously georeferenced, as reflected in the formal network accuracies.

The topics in this dissertation were further unified in their applicability to the modernization of the National Spatial Reference System (NSRS) currently underway at the National Geodetic Survey (NGS). This will result in replacing the existing datums and State Plane Coordinate System of 1983 (SPCS 83) with four Terrestrial Reference Frames, the North American-Pacific

Geopotential Datum (NAPGD2022), and the State Plane Coordinate System of 2022 (SPCS2022).

The research was presented in three chapters, each focusing on a particular problem. Chapter 2 (manuscript #1) presented a method for designing conformal projections that optimally minimize linear distortion at the topographic surface. Such “low distortion projections” (LDPs) provide a way to essentially eliminate the “grid to ground” problem by generating projected (grid) coordinates that differ from true horizontal distances at the topographic surface (ground) by an amount below some small threshold. A commonly used threshold is ± 20 parts per million (ppm), meaning a grid distance differs from a horizontal ground distance by 2 cm/km or less. As an example, an LDP was defined for the Bend-Redmond-Prineville area in the Deschutes Valley of central Oregon. For that design, distortion within ± 10 ppm was obtained for the three major cities defining the region, and ± 20 ppm elsewhere. The low-distortion performance was achieved over a surprisingly large area (70 by 60 km) with height change of over 420 m, by using a design process that took advantage of the overall topographic slope to increase coverage extent. This coverage and reduction in distortion far exceeded what was achieved using the traditional method of simply scaling existing SPCS 83 coordinates.

Map projection linear distortion was also the topic of Chapter 3 (manuscript #2), but in a different context than LDPs in Chapter 2. In this case, a method was presented for designing conformal projections covering large regions, usually much larger than could be covered by LDPs. The intent was to develop a design approach that could be used for replacing the zones of existing SPCS 83 with new zones for SPCS2022, including zones that cover entire states. As with LDPs, the design objective was to minimize linear distortion, but in a different way. Rather than consider only distortion across the entire zone, population distribution was taken into

account, so that distortion was preferentially reduced more in populated areas. Results for SPCS2022 version of SPCS83 zones were compared to SPCS 83, and results for entire states were compared to the nearest UTM zone. Distortion dramatically decreased, both in considering mean overall distortion as well as mean distortion weighted by population.

Chapter 4 (manuscript #3) investigated the integration of GNSS and leveling observations into a single 3D geodetic network for combined simultaneous least-squares adjustments. The research was done to investigate the role of leveling in NAPGD2022, which will be accessed primarily using GNSS with a gravimetric geoid model. Combining these two very different observation types required they be in the same geometry. To accomplish that, the leveling was transformed to the 3D geometry of GNSS, as delta Earth-Centered, Earth-Fixed Cartesian coordinates. Such a transformation required accounting for deflection of the vertical, which was done using an NGS experimental gravimetric geoid model. Equally important as geometry were error estimates, because they were used to weight the observations. Error estimates were determined for the GNSS and the leveling, and a significant part of the research was concerned with determining an error model for geoid slope. The geometrically consistent and appropriately weighted observations were combined into networks and adjusted with minimal and full (stochastically weighted) constraints. Results indicated that the weighting was realistic, and furthermore that each observation type contributed to results superior to those obtained when adjusted separately. This was manifested in smaller residuals and height errors and higher redundancy in the combined networks than the separate networks.

5.2 FUTURE WORK

All three research topics provide opportunities for additional work, which could lead to significant improvement in efficiency, results, methods and perhaps all three.

The chapters on low distortion map projections relied on initial parameter estimates and manual iteration to achieve the optimal designs. This process could be improved by automating aspects of the initialization and iteration steps. Doing so could possibly reduce the need to create and visually assess distortion maps as part of finalizing zone designs.

The map projection design process could likely benefit from a solution that computes projection parameters by solving a constrained optimization problem (for example using least-squares). Such an approach would be especially useful for designs using the Oblique Mercator projection, since its distortion variation is a function of three variables rather than only one (as it is for Transverse Mercator and Lambert Conformal Conic projections). This seems particularly useful for designing LDPs in situations where the topographic slope is more-or-less uniform in an oblique direction.

In Chapter 3 (manuscript #2), designs that accounted for population distribution used cities and towns represented by points, where each point was assigned a population (and ellipsoid height). Concentrating a city population into a single point is clearly unrealistic (especially large cities), although it may have little impact on designs covering large regions. Nonetheless it seems likely that a better approach would be to rasterize U.S. Census block data to create an essentially continuous representation of population distribution. This would require creating a raster from block (polygon) data, which is not necessarily a simple exercise, but still likely worth pursuing.

The geoid slope error model in Chapter 4 (manuscript #3) on integrating GNSS and leveling was determined empirically. It therefore could benefit greatly from additional investigations using other datasets to see if it can be more generally applied. In addition, the GNSS and leveling observations used in this study were collected at much different times (a span of decades), and,

therefore, it is of interest to perform additional analyses using observations acquired at the same time. Doing so would remove possible temporal effects as a variable, simplifying analysis and model development. In addition, a more careful consideration of geoid slope error modeling should be pursued, for example by considering the case of zero error at zero distance (which seems more realistic because of auto-correlation alone), along with revisiting modeling of leveling errors (perhaps also with zero error at zero distance). A final, but important, area of investigation would be to compare the method developed in this research with other methods used for combine GNSS and leveling. Doing so would help make more informed decision on adopting a method for using both GNSS and leveling in NAPGD2022.

6 BIBLIOGRAPHY

- Armstrong, M.L., Schenewerk, M. S., Mader, G., Martin, D., Stone, B., and Foote, R., 2015. *OPUS Projects: Online Positioning User Service Baseline Processing and Adjustment Software User Instructions and Technical Guide*, Ver. 2.5, National Oceanic and Atmospheric Administration, National Geodetic Survey, Silver Spring, MD.
- Armstrong, M.L., Thomas, J., Bays, K., and Dennis, M.L., 2017. *Oregon Coordinate Reference System Handbook and Map Set*, version 3.01, Oregon Department of Transportation, Geometronics Unit, Salem, Oregon, <ftp://ftp.odot.state.or.us/ORGN/Documents/ocrs_handbook_user_guide.pdf> (Dec 26, 2017)
- Badger, M.G. (lead author), 2016. *Indiana Geospatial Coordinate System Handbook and User Guide*, version 1.05, Indiana Department of Transportation and Land & Aerial Survey Office, Indianapolis, Indiana <http://www.in.gov/indot/files/InGCS_HandbookUserGuide_20160901.pdf> (Dec 26, 2017)
- Balazs, E.I., and Young, G.M., 1982. “Corrections Applied by the National Geodetic Survey to Precise Leveling Observations”, *NOAA Technical Memorandum, NOS NGS 34*. National Oceanic and Atmospheric Administration, National Geodetic Survey, Silver Spring, MD. <https://www.ngs.noaa.gov/PUBS_LIB/NOAA-TM-NOS-NGS-34.pdf> (Oct 1, 2016).
- Blackwell, J. and Hilla, S., 2000. *PAGE-NT User’s Manual*. National Oceanic and Atmospheric Administration, National Geodetic Survey, Silver Spring, MD. <<ftp://ftp.ngs.noaa.gov/pub/pnt6/>> (Oct. 1, 2016).
- Bossler, J.D., 1984. *Standards and Specifications for Geodetic Control Networks*, Federal Geodetic Control Committee (now the Federal Geodetic Control Subcommittee), USA, 25 pp. <http://www.ngs.noaa.gov/FGCS/tech_pub/1984-stds-specs-geodetic-control-networks.pdf> (Oct. 1, 2016).
- Burkholder, E.F., 1980. “The Michigan Scale Factor”, technical paper presented at 40th Annual Meeting of the American Congress on Surveying and Mapping, St. Louis, Missouri, March 1980. <<http://www.globalcogo.com/MichGSF80.pdf>> (Dec 26, 2017)
- C&GS (Coast & Geodetic Survey), 1979 (revised; original 1965). “Plane Coordinate Projection Tables: Michigan (Lambert)”, *Publication 65-3*, U.S. Department of Commerce, Coast and Geodetic Survey. <https://www.ngs.noaa.gov/library/pdfs/Special_Publication_No_65_3.pdf> (Jan 19, 2018)
- Dennis, M.L. (ed.), 2014. *Rocky Mountain Tribal Coordinate Reference System Handbook and User Guide*, v1.0, Rocky Mountain Tribal Transportation Association, <www.neciusa.com/documents/RMTCRS_Manual.pdf> (July 20, 2018).
- Dennis, M.L., 2016. “Ground Truth: Low Distortion Map Projections for Engineering, Surveying, and GIS”, Proceedings of the Pipelines 2016 Conference, Utility Engineering and

Surveying Institute of the American Society of Civil Engineers, July 17–20, 2016 Kansas City, Missouri, U.S.A.

- Dennis, M.L., 2017. *The Kansas Regional Coordinate System: A Statewide Multiple-Zone Low-Distortion Projection Coordinate System for the State of Kansas*, Kansas Department of Transportation. <http://data.kansasgis.org/catalog/other/KS_LDP/KRCS_report_2017-11-01.pdf> (Dec 30, 2017)
- Dennis, M.L., 2018. “The State Plane Coordinate System: History, Policy, and Future Directions”, *NOAA Special Publication NOS NGS 13*, National Oceanic and Atmospheric Administration, National Geodetic Survey, Silver Spring, Maryland. <https://geodesy.noaa.gov/library/pdfs/NOAA_SP_NOS_NGS_0013_v01_2018-03-06.pdf>
- Dennis, M.L., 2019. (in review) “The National Adjustment of 2011: Alignment of passive GNSS control with the three frames of the North American Datum of 1983 at epoch 2010.00: NAD 83 (2011), NAD 83 (PA11), and NAD 83 (MA11).” *NOAA Technical Report NOS NGS 65*, National Oceanic and Atmospheric Administration, National Geodetic Survey, Silver Spring, MD.
- Dennis, M.L., Gillins, D.T., Parrish, C.E., Olsen, M., Park, J., and Kim, S.K., 2018. *Towards Optimizing the Determination of Accurate Heights using GNSS, Volume 2: Integration of Differential Leveling and GNSS*, Oregon State University, Cooperative Institute for Marine Resources Studies, volume 2 of report for National Oceanic and Atmospheric Administration, National Geodetic Survey, Silver Spring, MD.
- Dennis, M.L., Miller, N., and Brown, G., 2014. *Iowa Regional Coordinate System Handbook and User Guide*, v2.10, Iowa Department of Transportation, <www.iowadot.gov/rtn/pdfs/IaRCS_Handbook.pdf> (July 20, 2018).
- Dracup, J.F., 1974. *Fundamentals of the State Plane Coordinate Systems*, National Geodetic Survey, <www.ngs.noaa.gov/PUBS_LIB/FundSPCSys.pdf> (July 20, 2018).
- Eckl, M.C., Snay, R.A., Soler T., Cline, M.W., and Mader G.L., 2001. “Accuracy of GPS-derived relative positions as a function of interstation distance and observing-session duration.” *J. Geod.*, 75(12), 633-640.
- Erol, B., and Çelik, R., 2005. “Modelling local GPS/leveling Geoid with the assessment of inverse distance weighting and geostatistical kriging methods.” Proc., ISPRS Congress, Istanbul, Turkey, Citeseer.
- Esri, 2016. “A quick tour of geoprocessing tool references.” Esri, Redlands, CA. <<http://desktop.arcgis.com/en/arcmap/latest/tools/main/a-quick-tour-of-geoprocessing-tool-references.htm>> (Oct. 10, 2016).
- Esri, 2018. “Minimum Bounding Geometry” tool, Esri, Redlands, CA. <<http://pro.arcgis.com/en/pro-app/tool-reference/data-management/minimum-bounding-geometry.htm>> (Nov 12, 2018)

- FGDC (Federal Geographic Data Committee), 1998. *Geospatial Positioning Accuracy Standards*, FGDC-STD-007.2-1998, Federal Geographic Data Committee, Reston, Virginia, USA, 128 pp., <www.fgdc.gov/standards/projects/FGDC-standards-projects/accuracy/> (Oct 3, 2018) [includes Reporting Methodology (Part 1), Standards for Geodetic Networks (Part 2), National Standard for Spatial Data Accuracy (Part 3), Standards for Architecture, Engineering, Construction (A/E/C) and Facility Management (Part 4), and Standards for Nautical Charting Hydrographic Surveys (Part 5)].
- Fotopoulos, G., 2005. “Calibration of geoid error models via a combined adjustment of ellipsoidal, orthometric and gravimetric geoid height data.” *J. Geod.*, 79(1–3), 111–123.
- Fotopoulos, G., Kotsakis, C., and Sideris, M. G., 2003. “How accurately can we determine orthometric height differences from GPS and geoid data?” *J. Surv. Eng.*, 10.1061/(ASCE)0733-9453(2003)129:1(1), 1–10.
- Fury, R. J., 1999. “National Geodetic Survey (NGS) Gravity Prediction Methodology.” National Oceanic and Atmospheric Administration, National Geodetic Survey, Silver Spring, MD. <http://www.ngs.noaa.gov/TOOLS/Gravity/grav_method.html> (Dec. 12, 2016).
- Gesch, D., G., Oimoen, M., Greenlee, S., Nelson, C., Steuck, M., and Tyler, D., 2002. “The National Elevation Dataset”, *Photo Eng & Rem Sens*, ASPRS, 68 (1), <https://www.researchgate.net/publication/273062566_The_National_Elevation_Dataset> (Nov 12, 2018).
- Gesch, D., Oimoen, M., and Evans, G., 2014. “Accuracy Assessment of the U.S. Geological Survey National Elevation Dataset, and Comparison with Other Large-Area Elevation Datasets—SRTM and ASTER”, *U.S. Geological Survey Open File Report 2014-1008*, Washington, D.C. <<https://pubs.usgs.gov/of/2014/1008/pdf/ofr2014-1008.pdf>> (Nov 10, 2108)
- Ghilani, C. D., 2010. *Adjustment Computations*, 5th Ed., John Wiley & Sons, Inc., Hoboken, NJ.
- Gillins, D.T., and Dennis, M.L., 2017. “Inclusion of Leveling with GNSS Observations in a Single, 3-D Geodetic Survey Network Adjustment.” In: *Proc. of FIG (International Federation of Surveyors) Working Week*, FIG, Helsinki, Finland.
- Gillins, D.T., and Eddy, M.J., 2015. “An evaluation of NGS-58 and OPUS Projects: Methods for determining accurate ellipsoidal heights with GPS.” National Oceanic and Atmospheric Administration, National Geodetic Survey, Silver Spring, MD.
- Gillins, D.T., and Eddy, M.J., 2016. “Comparison of GPS Height Modernization Surveys Using OPUS-Projects and Following NGS-58 Guidelines.” *J. Surv. Eng.*, 10.1061/(ASCE)SU.1943-5428.0000196 , 05016007.
- Hackl, M., 2012. “GPS analysis: strain, transients, and colored noise.” Ph.D. dissertation, Ludwig Maximilian University of Munich, Germany. <https://edoc.ub.uni-muenchen.de/14627/3/Hackl_Matthias.pdf> (Sep 25, 2018)

- Hardy, R.L. and Nelson, S.A., 1986. "A multiquadric-biharmonic representation and approximation of disturbing potential." *Geophysical Research Letters*, 13(1), pp. 18-21.
- Hartman, K.R., 1995. "Flight Mechanics/Estimation Theory Symposium." *NASA Conference Publication 3299*, NASA Technical Archives.
<<https://ntrs.nasa.gov/archive/nasa/casi.ntrs.nasa.gov/19950021342.pdf>> (Sep 25, 2018)
- Herring, T., (ed.), 2009. *Treatise on Geophysics, Volume 3: Geodesy*. Elsevier.
- Hofmann-Wellenhof, B., and Moritz, H., 2006. *Physical Geodesy*, Springer Science & Business Media, New York.
- Holdahl, S.R., Strange, W.E., and Harris, R.J., 1986. "Empirical Calibration of Zeiss Nil Level Instruments to Account for Magnetic Errors." *NOAA Technical Memorandum, NOS NGS 45*. National Oceanic and Atmospheric Administration, National Geodetic Survey, Silver Spring, MD.
- Jekeli, C., 2000. "Heights, the geopotential, and vertical datums." Rep. 459, Ohio State Univ., Geodetic Science and Surveying, Dept. of Civil and Environmental Engineering and Geodetic Science, Columbus, OH.
- Jiang, Z., and Duquenne, H., 1996. "On the combined adjustment of a gravimetrically determined geoid and GPS levelling stations." *J. Geod.*, 70(8), 505–514.
- Karney, C., 2011. "Transverse Mercator with an accuracy of a few nanometers," *J. Geod.*, Vol. 85, No.8, Pp 475-485 <<https://arxiv.org/pdf/1002.1417.pdf>> (Nov 12, 2018)
- Kashani, I., Wielgosz, P., and Grejner-Brzezinska, D.A., 2004. "On the reliability of the VCV Matrix: A case study based on GAMIT and Bernese GPS Software." *GPS Solutions*, (2004)8:193-199. DOI 10.1007/s10291-004-0103-9.
- Kentucky Geography Network, 2002. *Kentucky State Plane Coordinate System*, Division of Geographic Information, Frankfort, Kentucky
<ftp://kygeonet.ky.gov/kygeodata/standards/Ky_StatePlane.pdf> (Dec 15, 2017)
- Kentucky Legislature, 2001. "The Kentucky Single Zone Coordinate System of 1983", *Kentucky Administrative Regulation 10 KAR 5:010*, Frankfort, Kentucky
<<http://www.lrc.ky.gov/kar/010/005/010.htm>> (Dec 15, 2017)
- Khazraei, S., Nafisi, V., Amiri-Simkooei, A., and Asgari, J., 2016. "Combination of GPS and Leveling Observations and Geoid Models Using Least-Squares Variance Component Estimation." *J. Surv. Eng.*, 10.1061/(ASCE)SU.1943-5428.0000205 , 04016023.
- Kim, S-K., Park, J., Gillins, D., and Dennis, M., 2018. "On determining orthometric heights from a corrector surface model based on leveling observations, GNSS, and a geoid model." *Journal of Applied Geodesy*, Published Online: 2018-08-21 <<https://doi.org/10.1515/jag-2018-0014>> (Sep 24, 2018).
- Kotsakis, C., and Sideris, M. G., 1999. "On the adjustment of combined GPS/levelling/geoid networks." *J. Geod.*, 73(8), 412–421.

- Langbein, J., 2004. "Noise in two-color electronic distance meter measurements revisited." *Journal of Geophysical Research: Solid Earth*, 109(B4).
<<https://agupubs.onlinelibrary.wiley.com/doi/10.1029/2003JB002819>> (Sep 25, 2018)
- Leick, A., Rapoport, L., and Tatarnikov, D., 2015. *GPS Satellite Surveying* (4th Edition), John Wiley & Sons, New York, New York.
- Lusch, D.P., 2005. "A Primer on Coordinate Systems Commonly Used in Michigan," Dept. Geography, Remote Sensing & GIS Research and Outreach Services Group, Michigan State University. <http://www.rsgis.msu.edu/pdf/mi_coordinate_systems.pdf> (Dec 26, 2017)
- Mader, G., Schenewerk, M., Weston, N., Evjen, J., Tadeballi, K., and Neti, J., 2012. "Interactive web-based GPS network processing and adjustment using NGS' OPUS-Projects." In: *Proceedings of the FIG working week 2012*, Rome, Italy.
- Milbert, D.G., 1988. "Treatment of Geodetic Leveling in the Integrated Geodesy Approach, *OSU Report 396*, Ph.D. dissertation, Ohio State Univ., Columbus, OH.
- Milbert, D.G., 2009. *An Analysis of the NAD 83 (NSRS2007) National Readjustment*, National Geodetic Survey, Silver Spring, MD,
<www.geodesy.noaa.gov/PUBS_LIB/NSRS2007/NSRS2007Analysis.pdf> (Oct. 24, 2016).
- Milbert, D.G., and Kass, W.G., 1987. *NOAA Technical Memorandum NOS NGS-47: ADJUST: The Horizontal Observation Adjustment Program*. National Oceanic and Atmospheric Administration, National Geodetic Survey, Silver Spring, MD
<https://www.ngs.noaa.gov/PUBS_LIB/Adjust_TheHorizontalObservationAdjustmentProgram_TM_NOS_NGS_47.pdf> (Sep 24, 2018).
- Moritz, H., 2000, "Geodetic Reference System 1980," *J. Geod.*, 74(1), pp. 128– 162, doi:10.1007/S001900050278, <<ftp://athena.fsv.cvut.cz/ZFG/grs80-Moritz.pdf>> (Nov 12, 2018)
- Mukul, M., Srivastava, V., and Mukul, M., 2015. "Analysis of the accuracy of Shuttle Radar Topography Mission (SRTM) height models using International Global Navigation Satellite System Service (IGS) Network", *J. Earth Syst. Sci.*, 124, No. 6, pp. 1343–1357.
<<https://www.ias.ac.in/article/fulltext/jess/124/06/1343-1357>> (Nov 10, 2018)
- National Geodetic Survey, 2016. *GEOID12B*, <www.ngs.noaa.gov/GEOID/GEOID12B/> (July 20, 2018).
- NGA (National Geospatial-Intelligence Agency), 2014. "The Universal Grids and the Transverse Mercator and Polar Stereographic Map Projections," version 2.0.0, *NGA.SIG.0012_2.0.0_UTMUPS*, Office of Geomatics, 86 pp. <http://earth-info.nga.mil/GandG/publications/NGA_SIG_0012_2_0_0_UTMUPS/NGA.SIG.0012_2.0.0_UTMUPS.pdf> (Nov 12, 2018)
- NGS (National Geodetic Survey), 2007. *The GRAV-D Project: Gravity for the Redefinition of the American Vertical Datum*. National Oceanic and Atmospheric Administration, National

- Geodetic Survey, Silver Spring, MD <http://www.ngs.noaa.gov/GRAV-D/pubs/GRAV-D_v2007_12_19.pdf> (Oct. 1, 2016).
- NGS (National Geodetic Survey), 2014. *GEOID12B Readme File*. National Oceanic and Atmospheric Administration, National Geodetic Survey, Silver Spring, MD. <<http://www.ngs.noaa.gov/GEOID/GEOID12B/g2012Brme.txt>> (Sept. 27, 2016).
- NGS (National Geodetic Survey), 2015. “Technical Details for GEOID12/12A/12B.” National Oceanic and Atmospheric Administration, National Geodetic Survey, Silver Spring, MD. <http://www.ngs.noaa.gov/GEOID/GEOID12B/GEOID12B_TD.shtml> (Oct. 1, 2016).
- NGS (National Geodetic Survey), 2016. *GEOID12B*, <www.ngs.noaa.gov/GEOID/GEOID12B/> (July 20, 2018).
- NGS (National Geodetic Survey), 2016. *NAVD 88 Gravity Computations*. National Oceanic and Atmospheric Administration, National Geodetic Survey, Silver Spring, MD. <<http://www.geodesy.noaa.gov/TOOLS/Navdgrav/navdgrav.shtml>> (Oct. 10, 2016).
- NGS (National Geodetic Survey), 2017a. “Blueprint for 2022, Part 1: Geometric Coordinates”, *NOAA Technical Report NOS NGS 62*, National Oceanic and Atmospheric Administration, National Geodetic Survey, Silver Spring, Maryland. <https://geodesy.noaa.gov/library/pdfs/NOAA_TR_NOS_NGS_0062.pdf> (Dec 26, 2017)
- NGS (National Geodetic Survey), 2017b. “Blueprint for 2022, Part 2: Geopotential Coordinates”, *NOAA Technical Report NOS NGS 64*, National Oceanic and Atmospheric Administration, National Geodetic Survey, Silver Spring, Maryland. <https://geodesy.noaa.gov/library/pdfs/NOAA_TR_NOS_NGS_0064.pdf> (Nov 12, 2018)
- NGS (National Geodetic Survey), 2018a. “State Plane Coordinate System of 2022 Policy,” (DRAFT), National Oceanic and Atmospheric Administration, National Geodetic Survey, Silver Spring, Maryland <https://geodesy.noaa.gov/INFO/Policy/files/DRAFT_SPCS2022_Policy.pdf> (Nov 12, 2018)
- NGS (National Geodetic Survey), 2018b. “Procedures for Design and Modification of the State Plane Coordinate System of 2022,” (DRAFT), National Oceanic and Atmospheric Administration, National Geodetic Survey, Silver Spring, Maryland <https://geodesy.noaa.gov/INFO/Policy/files/DRAFT_SPCS2022_Procedures.pdf> (Nov 12, 2018)
- NGS (National Geodetic Survey), 2018c. *Input Formats and Specifications of the National Geodetic Survey Data Base* (the NGS “Bluebook”), three volumes and eleven annexes. National Oceanic and Atmospheric Administration, National Geodetic Survey, Silver Spring, Maryland. <<http://www.ngs.noaa.gov/FGCS/BlueBook/>> (Oct. 1, 2016).
- NGS (National Geodetic Survey), 2018d. “Technical Details for xGEOID16 Models.” National Oceanic and Atmospheric Administrations, National Geodetic Survey, Silver Spring, MD. <https://beta.ngs.noaa.gov/GEOID/xGEOID16/xGEOID16_technical_details.shtml> (Jan. 4, 2018).

- NGS (National Geodetic Survey), 2018e. *ADJUST Supplemental Documentation*. National Oceanic and Atmospheric Administration, National Geodetic Survey, Silver Spring, MD. <http://www.ngs.noaa.gov/PC_PROD/ADJUST/adjust_supplemental.txt> (Sept. 27, 2016).
- NGS (National Geodetic Survey), 2018f. *New Datums: Replacing NAVD 88 and NAD 83*, National Oceanic and Atmospheric Administration, National Geodetic Survey, Silver Spring, Maryland <<https://geodesy.noaa.gov/datums/newdatums/index.shtml>> (Nov 12, 2018)
- Open Geospatial Consortium, 2015. *Geographic information – Well-known text representation of coordinate reference systems*, OGC document: 12–063r5, v1.0 <<http://docs.opengeospatial.org/is/12-063r5/12-063r5.html>> (July 20, 2018)
- Øvstedal, O, 2000. “Single Processed Independent and Trivial Vectors in Network Analysis”, *Journal of Surveying Engineering*, Vol. 126, No. 1, pp. 18-25.
- Pavlis, N., Holmes, S., Kenyon, S. and Factor, J., 2012. “The development and evaluation of the Earth Gravitational Model 2008 (EGM2008)”, *J. Geophys. Res.*, 117, B04406, American Geophysical Union. <<https://doi.org/10.1029/2011JB008916>> (Nov 10, 2018)
- Pearson, C. and Snay, R., 2012. “Introducing HTDP 3.1 to transform coordinates across time and spatial reference frames”, *GPS Solut*, 10.1007/s10291-012-0255-y. <www.ngs.noaa.gov/TOOLS/Htdp/Pearson_Snay_2012.pdf> (Apr. 9, 2017)
- Rebischung, P., Griffiths, J., Ray, J., Schmid, R., Collilieux, X, and Garayt, B., 2012. “IGS08: the IGS realization of ITRF2008.” *GPS Solut*, 16:483–494, DOI 10.1007/s10291-011-0248-2. <ftp://igs.cb.igs.org/pub/resource/pubs/IGS08_The_IGS_Realization_of_ITRF2008.pdf> (Oct. 22, 2018)
- Roman, D.R., Wang, Y.M., Henning, W., and Hamilton, J., 2004. “Assessment of the New National Geoid Height Model, GEOID03.” *Proceedings of the American Congress on Surveying and Mapping 2004 Conference and Technology Exhibition*, Nashville, Tennessee, April 16-21.
- Roman, D.R., Wang, Y.M., Saleh, J., and Li, X., 2009. “Final National Models for the United States: Development of GEOID09.” National Oceanic and Atmospheric Administration, National Geodetic Survey, Silver Spring, MD. <http://www.ngs.noaa.gov/GEOID/GEOID09/GEOID09_tech_details.pdf> (Oct. 1, 2016).
- Smith, D.A., and Milbert, D.G., 1999. “The GEOID96 high-resolution geoid height model for the United States.” *J. Geod.*, 73:219–236.
- Smith, D.A., Holmes, S.A., Li, X., Guillaume, S., Wang, Y.M., Bürki, B., Roman, D.R., and Damiani, T.M., 2013. “Confirming regional 1 cm differential geoid accuracy from airborne gravimetry: the Geoid Slope Validation Survey of 2011.” *J. Geod.*, 87: 885. doi:10.1007/s00190-013-0653-0.
- Snay, R., Pearson, C., and Saleh, J., 2014. *HTDP User’s Guide*, Version 3.2.5. National Oceanic and Atmospheric Administration, National Geodetic Survey, Silver Spring, MD. <<http://www.geodesy.noaa.gov/TOOLS/Htdp/HTDP-user-guide.pdf>> (Sept. 27, 2016).

- Snyder, J.P. and Steward, H. (eds.), 1988. “Bibliography of Map Projections”, *U.S. Geological Survey Bulletin 1856*, Washington, D.C. <<https://pubs.usgs.gov/bul/1856/report.pdf>> (Nov 12, 2018)
- Snyder, J.P., 1987. “Map Projections — A Working Manual”, *U.S. Geological Survey Professional Paper 1395*, Washington, D.C. <pubs.er.usgs.gov/djvu/PP/PP_1395.pdf> (Nov 12, 2018)
- Stem, J.E., 1990. “State Plane Coordinate System of 1983”, *NOAA Manual NOS NGS 5*, National Geodetic Survey, <https://geodesy.noaa.gov/library/pdfs/NOAA_Manual_NOS_NGS_0005.pdf> (July 20, 2018).
- Torge, W. and Müller, J., 2012. *Geodesy* (4th Edition), W. de Gruyter, Berlin.
- Vittuari, L., Tini, M. A., Sarti, P., Serantoni, E., Borghi, A., Negusini, M., & Guillaume, S., 2016. A Comparative Study of the Applied Methods for Estimating Deflection of the Vertical in Terrestrial Geodetic Measurements. *Sensors*, 16(4), 565.
- Weaver, B., Gillins, D.T., and Dennis, M., 2018. “Hybrid Survey Networks: Combining Real-Time and Static GNSS Observations for Optimizing Height Modernization,” *J. Surv. Eng.* (ASCE), 05017006 <[10.1061/\(ASCE\)SU.1943-5428.0000244](https://doi.org/10.1061/(ASCE)SU.1943-5428.0000244)> (Nov 19, 2018)
- Weston, N.D., Mader, G.L., and Soler, T., 2007. “OPUS Projects – A Web-based application to administer and process multi-day GPS campaign data.” *Proc. of FIG (International Federation of Surveyors) Working Week*, FIG, Hong Kong, China.
- WI SCO (Wisconsin State Cartographer’s Office), 2012. *Wisconsin Coordinate Reference Systems*, 2nd Edition, State Cartographer’s Office, Madison, Wisconsin. <<https://www.sco.wisc.edu/pubs/wisconsin-coordinate-reference-systems-second-edition/>> (Dec 26, 2017)
- Zilkoski, D.B., 1991. “A Priori Estimates of Standard Errors of Leveling Data.” *Proceedings of the 1991 ACSM/ASPRS Annual Convention*, Baltimore, Maryland.
- Zilkoski, D.B., Carlson, E.E., and Smith, C.L., 2008. *NOAA Technical Memorandum NOS NGS-59, Guidelines for Establishing GPS-Derived Orthometric Heights*, Version 1.5. National Oceanic and Atmospheric Administration, National Geodetic Survey, Silver Spring, MD.
- Zilkoski, D.B., D’Onofrio, J.D., and Frakes, S.J., 1997. *NOAA Technical Memorandum NOS NGS-58, Guidelines for Establishing GPS-Derived Ellipsoid Heights (Standards: 2 cm and 5 cm)*, Version 4.3. National Oceanic and Atmospheric Administration, National Geodetic Survey, Silver Spring, MD.
- Zilkoski, D.B., Richards, J.H., and Young, G.M., 1992. “Results of the General Adjustment of the North American Vertical Datum of 1988.” *Surveying and Land Information Systems*, 52(3), 133-149. <http://www.ngs.noaa.gov/PUBS_LIB/NAVD88/navd88report.htm> (Oct. 2, 2016).

APPENDICES

APPENDIX A. PROJECTION SCALE FACTOR AND CONVERGENCE ANGLE COMPUTATION

The projection grid point scale factor, k , is required to compute map projection distortion for a point on the ground. Because some surveying, engineering, and GIS software does not provide k , formulas for computing it are given below for the Transverse Mercator and Lambert Conformal Conic projections. These equations were derived from those provided in *NOAA Manual NOS NGS 5 “State Plane Coordinate System of 1983”* by James Stem (1990). Equations for computing the convergence angle of these projections are also provided.

Lambert Conformal Conic (LCC) projection

The grid scale factor at a point can be computed as follows (modified from Stem, 1990, pp. 26-29):

$$k = k_0 \frac{\cos \varphi_C}{\cos \varphi} \sqrt{\frac{1 - e^2 \sin^2 \varphi}{1 - e^2 \sin^2 \varphi_C}} \times \exp \left\{ \frac{\sin \varphi_C}{2} \left[\ln \frac{1 + \sin \varphi_C}{1 - \sin \varphi_C} - \ln \frac{1 + \sin \varphi}{1 - \sin \varphi} + e \left(\ln \frac{1 + e \sin \varphi}{1 - e \sin \varphi} - \ln \frac{1 + e \sin \varphi_C}{1 - e \sin \varphi_C} \right) \right] \right\} \quad (\text{A.1})$$

where k_0 = projection grid scale factor applied to central parallel (tangent to ellipsoid if $k_0 = 1$)

φ_C = geodetic latitude of central parallel = standard parallel for one-parallel LCC

$e = \sqrt{e^2} = \sqrt{2f - f^2}$ = first eccentricity of the reference ellipsoid

f = geometric flattening of the reference ellipsoid

To use this equation for a two-parallel LCC, the two-parallel LCC must first be converted to an equivalent one-parallel LCC by computing φ_C and k_0 . For a two-parallel LCC, the central parallel is

$$\varphi_C = \sin^{-1} \left[\frac{2 \ln \frac{\cos \varphi_S}{\cos \varphi_N} \sqrt{\frac{1 - e^2 \sin^2 \varphi_N}{1 - e^2 \sin^2 \varphi_S}}}{\ln \frac{1 + \sin \varphi_N}{1 - \sin \varphi_N} - \ln \frac{1 + \sin \varphi_S}{1 - \sin \varphi_S} + e \left(\ln \frac{1 + e \sin \varphi_S}{1 - e \sin \varphi_S} - \ln \frac{1 + e \sin \varphi_N}{1 - e \sin \varphi_N} \right)} \right] \quad (\text{A.2})$$

and the central parallel scale factor is

$$k_0 = \frac{\cos \varphi_N}{\cos \varphi_C} \sqrt{\frac{1 - e^2 \sin^2 \varphi_C}{1 - e^2 \sin^2 \varphi_N}} \times \exp \left\{ \frac{\sin \varphi_C}{2} \left[\ln \frac{1 + \sin \varphi_N}{1 - \sin \varphi_N} - \ln \frac{1 + \sin \varphi_C}{1 - \sin \varphi_C} + e \left(\ln \frac{1 + e \sin \varphi_C}{1 - e \sin \varphi_C} - \ln \frac{1 + e \sin \varphi_N}{1 - e \sin \varphi_N} \right) \right] \right\} \quad (\text{A.3})$$

where φ_N and φ_S are the geodetic latitude of the northern and southern standard parallels, respectively, and all other variables are as defined previously.

Transverse Mercator (TM) projection

The grid scale factor at a point can be computed as follows (modified from Stem, 1990, pp. 32-35):

$$k = k_0 \left\{ 1 + \frac{(\Delta\lambda \cos \varphi)^2}{2} \left(1 + \frac{e^2 \cos^2 \varphi}{1 - e^2} \right) \left[1 + \frac{(\Delta\lambda \cos \varphi)^2}{12} \left(5 - 4 \tan^2 \varphi + \frac{e^2 \cos^2 \varphi}{1 - e^2} (9 - 24 \tan^2 \varphi) \right) \right] \right\} \quad (\text{A.4})$$

where $\Delta\lambda = \lambda_0 - \lambda$ (in radians, for negative west longitude)

λ = geodetic longitude of point

λ_0 = central meridian longitude

and all other variables are as defined previously.

The following equation can be used to approximate k for the Transverse Mercator projection using the grid coordinate easting value. For k_0 between 0.9996 and 1.0004, it is accurate to within about ± 0.1 part per million (7 decimal places) if the computation point is within 100 km of the central meridian:

$$k \approx k_0 + \frac{(E_0 - E)^2}{2(k_0 R_G)^2} \quad (\text{A.5})$$

where E = Easting of the point where k is computed (in same units as R_G)

E_0 = False easting (on central meridian) of projection definition (in same units as R_G)

R_G = Earth geometric mean radius of curvature; see Eq. 2.2 or 3.2(2.2)

Note that this equation may not be sufficiently accurate for computing k throughout wide zones (such as UTM), e.g., at a UTM zone edge of $\pm 3^\circ$ from the central meridian, the error can exceed 0.3 ppm, depending on latitude.

Convergence angles

For any LCC projection, the convergence angle is exactly $\gamma = -\Delta\lambda \sin \varphi_C$ (where all variables are as defined previously; the units of γ are the same as the units of $\Delta\lambda$). For the TM, the convergence angle for a point at latitude φ can be approximated as $\gamma = -\Delta\lambda \sin \varphi$. This equation is accurate to better than 00.2'' if the computation point is within $\sim 1^\circ$ of the central meridian.

APPENDIX B. METHODS FOR COMPUTING HORIZONTAL “GROUND” DISTANCE

Two methods are given below for computing horizontal “ground” distances using geodetic information. The first method is done by scaling the ellipsoid distance (geodesic) using the average of the ellipsoid heights at the endpoints, as follows:

$$D_{grnd} = s \left(1 + \frac{\bar{h}}{\bar{R}_G} \right) \quad (\text{B.1})$$

where s is the ellipsoid distance (geodesic)

\bar{h} is the average ellipsoid height of the two points

\bar{R}_G is the geometric mean radius of curvature at the midpoint latitude of the two points

The NGS Geodetic Tool Kit inverting tools can be used to compute the ellipsoid distance (https://geodesy.noaa.gov/TOOLS/Inv_Fwd/Inv_Fwd.html).

The second method for computing a horizontal ground distance can be done by using a GPS (GNSS) vector directly. Neglecting Earth curvature, this distance can be computed as:

$$D_{grnd} = \sqrt{\Delta X^2 + \Delta Y^2 + \Delta Z^2 - \Delta h^2} \quad (\text{B.2})$$

where $\Delta X, \Delta Y, \Delta Z$ are the GPS vector components, as Earth-Centered, Earth-Fixed (ECEF) Cartesian coordinate deltas

Δh = change in ellipsoid height between vector end points

Note that this method can also be used with end point coordinates (rather than a GPS vector), by converting the latitude, longitude, and ellipsoid heights to X, Y, Z ECEF coordinates, and then

using the difference in ECEF coordinates. The NGS Geodetic Tool Kit *XYZ Conversion* tool can be used for this purpose (<https://geodesy.noaa.gov/TOOLS/XYZ/xyz.shtml>).

Curvature increases the horizontal ground distance, but for distances of less than 30 km (about 20 miles), the error due to the increase is less than 1 part per million (ppm), i.e., less than 3 cm (0.1 ft). The straight-line horizontal distance can be multiplied by the following curvature correction factor to get the approximate curved horizontal ground distance:

$$C_c = \frac{2\bar{R}_G \sin^{-1}\left(\frac{D_{grnd}}{\bar{R}_G}\right)}{D_{grnd}} \quad (\text{B.3})$$

where all variables are as defined previously. With the curvature correction, for distances of less than 160 km (100 miles) the error is less than 0.005 ppm, i.e., less than 1 mm (0.003 ft). The mean Earth radius of curvature can be computed using Eq. 2.2 or 3.2(2.2).

APPENDIX C. DATASETS USED FOR SPCS ZONE DESIGN AND ANALYSIS

Datasets used for design and analysis of zones for SPCS2022 and SPCS 83 are listed below, including descriptions of how they were used, spatial accuracy (where applicable), and citation of sources. The data were obtained from the U.S. Geological Survey (USGS), the National Geodetic Survey (NGS), the National Aeronautics and Space Administration (NASA), the National Geospatial-Intelligence Agency (NGA), the U.S. Census Bureau, and Esri

- **Digital elevation models.** DEMs were obtained from two sources, depending on location. For CONUS and Alaska, the USGS 3DEP data repository was used, formerly National Elevation Dataset (Gesch *et al.*, 2002), at 1 arc-sec resolution for CONUS and 2 arc-sec for Alaska. These DEMs provide North American Vertical Datum of 1988 elevations (orthometric heights). For Hawaii, Guam, CNMI, and American Samoa, the 3 arc-sec DEMs from the NASA/NGA Shuttle Radar Topography Mission (SRTM) were used. The SRTM DEMs are based on global mean sea level as defined by the Earth Gravitational Model 1996 (EGM96) geopotential models (see <https://lta.cr.usgs.gov/SRTM>).

The different DEMs were used in different ways, depending on the type of analysis and size of the design area. For extracting heights to grid and city points, the highest-resolution version of each DEM was used. To create distortion rasters of large areas for distortion maps and computing overall zone statistics, the DEMs were aggregated to lower resolution (usually 15 arc-sec) by taking the mean of the aggregated cells.

The vertical accuracy of the 3DEP DEMs were about 2 m root means square error (RMSE) in CONUS (1 arc-sec) and about 5 RMSE in Alaska (2 arc-sec), per Gesch, *et al.* (2014). The 3-sec SRTM DEM accuracy was about 10 m RMSE (Mukul *et al.*, 2015). Recall that 6 m

error in height causes 1 ppm error in distortion. Given that large zone designed here are concerned with distortion resolution of a few ppm at most, DEMs of 10 m accuracy are considered sufficient.

- **Geoid models.** Geoid models were used to convert the DEM orthometric heights to ellipsoid heights. The NGS hybrid model GEOID12B (NGS, 2016) was used to obtain NAD 83 ellipsoid heights for CONUS. The NGA/NASA gravimetric geoid model EGM2008 (Pavlis, *et al.*, 2012) was used for all other areas, which gives WGS 84 ellipsoid heights. NAD 83 and WGS 84 ellipsoid heights differ by 2 m or less (depending on location), which is much less than the estimated accuracy of the DEMs to which it was applied. In the areas where they were used, both geoid models were far more accurate than the DEMs, about 0.1 m RMSE or better. GEOID12B was not used in Alaska because of its known large tilt with respect to the gravimetric geoid (exceeding 3 m in some locations); see NGS, 2017b.
- **Regular grids of points with ellipsoid heights.** Point grids were created for use in design computations using Microsoft *Excel*. Grids were generated at 1- and 2-arc-minute intervals for CONUS; at 1, 2, 3, and 5 arc-minutes for Alaska, and at 3 arc-minutes for islands (Hawaii, Guam, etc.). Ellipsoid heights were determined for each grid point using the highest-resolution DEM available and appropriate geoid model, as stated above. Different spacings were used to keep the number of grid points to less than 100,000 for each zone, in order to avoid excessive computation burden in *Excel*. Several tens of thousands of points were also considered sufficient representation for design. This was augmented by distortion computations based on higher-resolution DEM-derived rasters, usually at 15 arc-sec resolution, which typically yielded from a few hundred thousand to a few million computation points.

- **City centroids with ellipsoid height and population.** Point locations were obtained from the standard map datasets provided by Esri (*Data and Maps for ArcGIS*). These locations and their 2010 Census populations were compiled by Esri from the National Atlas (<https://catalog.data.gov/dataset/national-atlas-of-the-united-states>) and U.S. Census cities and towns (<https://www.census.gov/data/tables/2017/demo/popest/total-cities-and-towns.html>). The points consisted of 38,193 named locations nominally considered cities or towns, although 11,125 (29%) were not assigned a population. These null population locations were nonetheless considered valid for design because it is likely they actually have non-zero population (and include private property). Most were probably not given a population not because of lack of people, but rather because of how Census block (polygon) data are assigned to points. Ellipsoid heights were computed at each point in the same manner as the grid points. Population data were not obtained for the islands of American Samoa, Guam, and CNMI, because the islands are so small that it was considered more practical and useful to design for the entire land area of the islands.
- **GIS datasets that define the zone geometries.** Polygons representing detailed county and state boundaries and shorelines were obtained from Esri. The polygon datasets were compiled and created by Esri from U.S. Census Bureau data and other sources. Zones not corresponding to state and county boundaries (in Alaska and Washington state) were created from their NGS definitions for this project.

APPENDIX D. SPCS2022 ZONE PARAMETERS AND COMPARISONS TO EXISTING SYSTEMS

Table D.1. Design results and performance statistics for SPCS zones in 25 states and territories (28 default *preliminary* SPCS2022 zone designs and 32 existing SPCS 83 zones). Ellipses (...) for projection axis location and scale indicate infinite continuation of digits.

State zone abrv	Distortion criterion (ppm)		Ref frame	Proj type	Projection axis		Distortion (ppm)			Pct within design criterion		
	Design	Calc'd			Location	Scale	Overall		Wtd mean	By pop	Cities & towns	Total area
							Range	Mean				
AL W	±50	±62	2022	TM	87°27'W	0.99996	164	-21	-19	90%	82%	79%
			1983		87°30'W	0.99993...	177	-48	-44	61%	48%	43%
*AK 3-5	±100	±76	2022	TM	Varies	1	1098	-54	9	98%	94%	72%
			1983		Varies	0.9999	1098	-154	-91	26%	52%	27%
AS	±20	±1	2022	LCC	14°15'S	1.00002	152	-14	—	—	—	67%
			1927		14°16'S	1	152	-34	—	—	—	40%
AZ C	±100	±114	2022	TM	112°03'W	1.00007	738	-54	24	95%	76%	55%
			1983		111°55'W	0.9999	784	-224	-151	2%	10%	14%
CA 5	±100	±84	2022	LCC	34°45'N	0.99995	645	-117	-3	90%	76%	41%
			1983		34°45'...N	0.99992...	644	-145	-31	91%	70%	31%
CO S	±100	±55	2022	LCC	37°48'N	1.00025	598	-48	26	93%	78%	60%
			1983		37°50'...N	0.99994...	607	-351	-280	0%	0%	0%
CT	±30	±40	2022	LCC	41°30'N	0.99999	107	-16	-1	99%	89%	81%
			1983		41°32'...N	0.99998...	118	-24	-8	97%	81%	65%
DE	±10	±6	2022	TM	75°24'W	0.999994	32	1	0	99%	88%	98%
			1983		75°25'W	0.999995	33	2	1	98%	85%	97%
*FL (all)	±40	±40	2022	Mult.	Varies	Varies	112	-13	-6	97%	93%	96%
		±52	1983		Varies	Varies	174	-30	-10	66%	55%	48%
GA W	±100	±90	2022	TM	84°12'W	1	367	9	-12	99.6%	96%	95%
			1983		84°10'W	0.9999	380	-90	-111	30%	45%	54%
†GU -CQ	±30	±37	2022	TM	144°15'E	0.99999	215	-9	—	—	100.0%	84%
			1983		144°45'E	1	310	25	—	—	40%	50%
*HI (all)	±50	±37	2022	OM	20°55'N	1	726	-130	-6	97%	95%	54%
		Varies	1983		157°30'W	az = -56°	Varies	Varies	723	-163	-29	96%
IL W	±75	±77	2022	TM	90°09'W	0.99997	198	-20	-20	98%	99%	99%
			1983		90°10'W	0.99994...	194	-48	-48	76%	74%	72%
MD	±50	±62	2022	LCC	38°51'N	0.99998	264	10	-2	96%	87%	81%
			1983		38°52'...N	0.99994...	274	-21	-34	71%	80%	84%

Table D.1. (continued)

State zone abrv	Distortion criterion (ppm)		Ref frame	Proj type	Projection axis		Distortion (ppm)			Pct within design criterion		
	Design	Calc'd			Location	Scale	Overall		Wtd mean	By pop	Cities & towns	Total area
							Range	Mean				
MS E	±50	±45	2022	TM	89°00'W	0.99997	123	-23	-24	99%	97%	98%
			1983		88°50'W	0.99995	160	-40	-42	64%	61%	58%
MT	±400	±423	2022	LCC	46°55'N	0.9999	1001	-79	-113	100.0%	99%	97%
			1983		47°00'...N	0.99939...	1059	-588	-613	6%	19%	20%
NE	±200	±175	2022	LCC	41°30'N	1	554	-15	-12	98%	91%	93%
			1983		41°30'...N	0.99965...	556	-357	-353	4%	19%	13%
NM C	±100	±110	2022	TM	106°09'W	1.00023	560	-14	14	98%	86%	73%
			1983		106°15'W	0.9999	576	-346	-323	0%	0%	0%
NC	±100	±143	2022	LCC	35°15'N	0.99995	597	-14	-25	90%	78%	76%
			1983		35°15'...N	0.99987...	597	-91	-103	44%	42%	44%
PA N	±75	±53	2022	LCC	41°25'N	1.00001	201	-36	-5	99.8%	99%	93%
			1983		41°25'...N	0.99995...	200	-90	-58	69%	57%	26%
TN	±75	±55	2022	LCC	35°50'N	0.99998	401	-28	-8	99%	95%	90%
			1983		35°50'...N	0.99994...	401	-40	-40	75%	70%	66%
TX C	±100	±110	2022	LCC	31°00'N	1	565	-36	3	92%	83%	72%
			1983		31°00'...N	0.99988...	565	-154	-115	42%	41%	25%
VT	±50	±36	2022	TM	72°36'W	1	249	-38	-1	99%	89%	60%
			1983		72°30'W	0.99996...	260	-72	-31	76%	44%	25%
WA N	±100	±72	2022	LCC	48°09'N	0.99999	606	-102	19	99%	96%	51%
			1983		48°07'...N	0.99994...	606	-150	-33	87%	77%	29%

* Statistics are combined for multiple zones (zones 3-5 in AK, all 3 zones in FL, and all 5 SPCS 83 zones in HI). The SPCS2022 parameters for Alaska and Florida are:

Alaska. TM central meridians: 146°00'W (Zone 3), 150°00'W (Zone 4), 154°00'W (Zone 5).

Florida. LCC (west): $\varphi_c = 31^\circ 18'N$, $k_0 = 0.99998$; OM (central): $\varphi_0 = 28^\circ 00'N$, $\lambda_0 = 82^\circ 00'W$, $k_0 = 0.99996$, $\alpha_0 = -16^\circ$; OM (east): $\varphi_0 = 28^\circ 00'N$, $\lambda_0 = 81^\circ 06'W$, $k_0 = 0.99999$, $\alpha_0 = -16^\circ$.

For Hawaii SPCS 83 parameters of its 5 TM zones, see Figure 3.12 (and Appendix A of Dennis, 2018).

† Single SPCS2022 zone used for Guam and CNMI; SPCS 83 zone is for Guam only.

Table D.2. Design results and performance statistics for 14 statewide *preliminary* SPCS2022 zone designs and 15 nearest UTM zones within state boundaries (two UTM zones shown for California).

State	Distortion criterion (ppm)		2022 or UTM	Proj or UTM zone	Projection axis		Distortion (ppm)			Pct within design criterion		
	Design	Calc'd			Location	Scale	Overall		Wtd mean	By pop	Cities & towns	Total area
							Range	Mean				
AL	±200	±175	2022	TM	86°42'W	0.99985	177	-74	-100	100.0%	99.9%	99.8%
		±175	UTM	16N	87°00'W	0.9996	531	-323	-342	9%	11%	11%
AK	±5000	±5997	2022	LCC	62°00'N	0.995	16834	-1874	-3976	97%	87%	82%
		±21269	UTM	5N	153°00'W	0.9996	65454	1671	2095	87%	80%	94%
AZ	±400	±452	2022	TM	112°03'W	0.99985	1409	-79	-148	95%	89%	88%
		±450	UTM	12N	111°00'W	0.9996	2130	-300	-318	67%	33%	36%
CA	±400	±399	2022	OM	37°00'N 119°30'W	0.99985 <i>az</i> = -34°	1420	-134	-46	99.7%	98%	92%
		±1341	UTM	10N	123°00'W	0.9996	8801	1282	1423	34%	48%	36%
		±1217	UTM	11N	117°00'W	0.9996	5390	666	470	53%	33%	30%
CO	±400	±307	2022	LCC	39°00'N	1.0001	1128	-22	-46	99.9%	98%	95%
		±592	UTM	13N	105°00'W	0.9996	2036	-320	-578	5%	28%	39%
FL	±400	±357	2022	OM	29°00'N 83°00'W	0.99965 <i>az</i> = -41°	714	-250	-244	100.0%	100.0%	100.0%
		±816	UTM	17N	81°00'W	0.9996	4971	218	-96	93%	80%	78%
GA	±300	±297	2022	TM	83°00'W	0.9998	868	-69	-26	99%	97%	98%
		±289	UTM	17N	81°00'W	0.9996	2143	356	581	14%	35%	41%
HI	±100	±37	2022	OM	20°55'N 157°30'W	1 <i>az</i> = -56°	726	-130	-6	97%	95%	54%
		±498	UTM	4N	159°00'W	0.9996	2608	659	105	1%	3%	4%
IL	±200	±182	2022	TM	89°24'W	0.99983	425	-111	-35	99.5%	98%	97%
		±178	UTM	16N	87°00'W	0.9996	1810	88	-219	13%	32%	36%
MS	±200	±167	2022	TM	89°55'W	0.99984	362	-90	-101	100.0%	100.0%	100.0%
		±179	UTM	16N	87°00'W	0.9996	2324	434	427	38%	36%	37%
NM	±500	±493	2022	TM	106°03'W	0.99987	1437	-85	-199	95%	94%	92%
		±494	UTM	13N	105°00'W	0.9996	2223	-226	-294	76%	48%	50%
PA	±100	±124	2022	LCC	40°57'N	0.99993	356	-58	-6	88%	78%	65%
		±382	UTM	18N	75°00'W	0.9996	2811	452	277	4%	7%	10%
TX	±1000	±2146	2022	LCC	31°10'N	0.9992	4617	-134	-223	92%	86%	86%
		±2377	UTM	14N	99°00'W	0.9996	6369	443	490	74%	79%	78%
WA	±200	±231	2022	LCC	47°15'N	0.99995	1125	-33	8	90%	89%	88%
		±547	UTM	10N	123°00'W	0.9996	3251	224	-90	5%	9%	13%

APPENDIX E. ADJUSTMENT CONSTRAINTS AND FINAL ADJUSTED HEIGHTS AND ACCURACIES

Table E.1. Station ellipsoid heights for the GNSS, leveling, and combined networks. (including standard deviations used for weights). The only stations constrained are those that had NGS-published GNSS-derived coordinates prior to the fieldwork performed for this project.

PID*	Designation	Ellipsoid height (m)	Constraint standard dev			Constrained leveled mark order/class
			North (cm)	East (cm)	Up (cm)	
QE0656	BICKFORD	52.329	0.21	0.15	0.61	Yes (1/II)
AI6289	CORV A	103.471	0.13	0.10	0.74	Yes (1/II)
QE0742	G 287	179.939	0.50	0.43	0.82	Yes (2/0)
QE1488	G 728	61.309	0.27	0.22	0.62	Yes (1/II)
QE2671	LANG	70.978	0.25	0.19	0.62	
QE2734	N 99 RESET	53.344	1.00	0.69	0.93	Yes (3)
QE2664	NESMITH	41.519	0.18	0.13	0.44	Yes (3)
QE1579	S 714	43.603	0.45	0.37	0.76	Yes (1/II)
QE1576	T 714	46.752	0.32	0.35	1.77	Yes (1/II)
QE1564	U 727	204.742	0.24	0.21	0.53	Yes (1/II)
AI2011	Y 683	71.990	0.23	0.19	0.48	
AH2488	CORVALLIS CORS MONUMENT	105.978	0.48	0.33	1.58	
DK4499	FORT STEVENS 5 CORS ARP	-13.444	0.25	0.18	0.79	
DK4175	KLAMATH FALLS 6 CORS ARP	1258.821	0.72	0.53	2.53	
DI0900	PIGEON POINT 6 CORS ARP	6.448	0.77	0.59	2.85	
DK4105	ROBINSON POINT 6 CORS ARP	-9.425	0.68	0.47	2.15	
DG9793	SENECA 2 CORS ARP	1439.014	0.29	0.21	0.96	
DI2262	TEREKALAKAMT2006 GRP	1093.845	0.46	0.32	1.61	

* *PID* is the NGS Permanent *ID*entifier used to uniquely identify all stations in the NGSIDB.

** N 99 RESET is an offset of 2nd order, class 0 station N 99 (QE0726) established using NGS reset procedures. Reset BMs are always classified 3rd order, regardless of the order/class of the parent BM.

Table E.2. Final adjusted ellipsoid and orthometric heights for the 34 local GNSS stations (6 distant CORS excluded), with network and median local accuracies(at 95% confidence).

Constrained stations are denoted with an asterisk (*).

Station	Final adjusted height (m)		Ellipsoid height accuracies (cm)	
	NAD 83 ellipsoid	Quasi-NAVD 88 orthometric**	Network	Median local
<i>GNSS stations with leveling</i>				
B 726	42.416	65.521	0.97	1.09
*BICKFORD	52.325	75.127	0.61	0.89
COLLEGE RM 2	50.225	72.927	0.94	1.02
*CORV A	103.470	126.055	0.78	1.01
CORVALLIS MAG STA=226	47.417	70.134	0.81	0.88
D 728	56.099	79.217	0.93	1.12
*G 287	179.944	202.117	0.80	1.00
*G 728	61.311	84.446	0.84	0.96
J 99	53.911	76.506	1.46	1.71
*N 99 RESET	53.345	75.463	0.95	1.07
*NESMITH	41.515	63.984	0.70	0.92
OX	76.037	99.366	1.08	1.17
*S 714	43.616	66.509	0.70	0.95
*T 714	46.764	69.529	0.76	0.96
*U 727	204.751	226.799	0.70	0.97
Z 714	148.840	171.165	0.86	1.02
<i>GNSS stations with no leveling</i>				
21 FMK	69.812	93.084	1.04	1.21
BEEF	120.522	142.989	1.01	1.13
*CORVALLIS CORS MONUMENT	105.966	128.548	0.46	0.86
E 141	58.935	81.756	1.01	1.15
FACL	47.773	70.494	2.13	2.22
J 54	63.693	86.312	2.65	2.69
*LANG	70.988	94.314	0.81	1.05
LCS1 ORGN BASE STATION ARP	59.421	82.436	0.52	0.81
NARY	47.281	70.000	2.04	2.13
PEAK	585.312	607.619	1.74	1.96
PEAVY	106.049	128.702	1.48	1.63
PRICE	113.621	135.692	1.49	1.62
PTS 35	45.570	68.377	1.02	1.17
Q 388 RESET	51.909	74.717	1.64	1.98
TAKENA AZ MK	47.314	70.362	0.89	1.10
VETM	48.646	71.343	2.08	2.17
WASH	50.569	73.249	0.93	1.10
*Y 683	71.989	94.655	0.65	0.95

Table E.3. Final adjusted ellipsoid and orthometric heights for 37 (of 1022) selected leveling-only stations, with network and median local accuracies (at 95% confidence).

Station	Final adjusted height (m)		Ellipsoid height accuracies (cm)	
	NAD 83 ellipsoid	Quasi-NAVD 88 orthometric**	Network	Median local
233	49.681	72.394	0.82	0.29
327	78.122	101.293	2.26	0.81
A 214	43.042	65.504	0.97	0.41
A 230	63.850	87.000	1.27	0.60
A 321	37.656	60.661	1.09	0.54
BICKFORD RM 1	52.322	75.124	0.71	0.55
D 474 (single spur observation)	65.456	88.513	2.29	0.28
E 12	58.403	81.525	1.00	0.85
E 226	104.838	126.709	4.21	1.76
F 99	30.869	53.529	2.65	1.92
G 54	189.454	211.749	1.28	0.58
H 265	97.909	121.142	2.83	0.72
HARD	58.027	81.351	2.05	0.38
J 106	387.400	408.897	5.75	1.89
J 230	80.330	103.542	3.63	1.18
J 54 FLOAT	63.705	86.324	1.14	0.65
K 13	29.098	52.054	2.21	0.84
K 99	48.132	70.695	2.17	1.81
M 54	47.685	70.478	1.02	0.62
M 99	49.704	71.963	2.21	2.05
NAN	73.846	97.181	1.36	0.63
P 51	84.610	106.718	1.77	0.71
P 725	102.788	125.777	2.57	0.80
P 99	58.641	80.656	2.20	1.54
Q 227	39.859	62.644	1.94	0.74
Q 469	16.153	38.477	2.33	0.69
R 230 (single spur observation)	112.880	136.088	4.32	0.44
T 106	24.431	47.100	4.43	2.24
T 240	85.507	107.549	2.69	1.59
TIDAL 5	-17.584	5.622	3.34	0.56
W 53	178.905	200.941	1.45	0.63
W 725	57.462	80.456	2.30	0.80
X 217	124.819	148.024	3.36	0.92
XEX	43.747	66.826	1.56	0.92
Y 230	240.696	263.913	4.05	1.18
Y 291	222.113	244.264	1.35	1.09
Z 727	52.456	75.557	1.74	0.94

** Term “quasi-NAVD 88” is used because orthometric heights were obtained by simply applying TxGEOID16B model without any ties to published leveled NAVD 88 height.